

On Turbulent Swirling Jets: Vortex Breakdown, Coherent Structures, and their Control

von
Diplom-Ingenieur
Kilian Oberleithner
aus Innsbruck

Von der Fakultät V – Verkehrs- und Maschinensysteme
der Technischen Universität Berlin
zur Erlangung des akademischen Grades

Doktor der Ingenieurwissenschaften
– Dr.-Ing. –

genehmigte Dissertation

Promotionsausschuss:

Vorsitzender: Prof. Dr. sc. techn. Jörn Sesterhenn
Gutachter: Prof. Dr.-Ing. Christian Oliver Paschereit
Gutachter: Prof. Dr. Israel J. Wygnanski

Tag der wissenschaftlichen Aussprache: 18. Juni 2012

Berlin 2012
D 83

Danksagung

Diese Dissertation entstand während meiner Tätigkeit als Wissenschaftlicher Mitarbeiter am Institut für Strömungsmechanik und Technische Akustik des Fachgebiets Experimentelle Strömungsmechanik der TU Berlin. An dieser Stelle möchte ich allen denen danken, die durch ihre Unterstützung zum Gelingen dieser Arbeit beigetragen haben.

Herzlich danken möchte ich meinem Doktorvater Christian Oliver Paschereit, der mir durch eine ausgewogene Mischung aus Freiraum und Führung optimale Arbeitsbedingungen schuf. Das mir entgegengebrachte Vertrauen ermöglichte mir eine freie, durch Neugierde und persönliche Neigung gelenkte Entwicklung.

Mein besonderer Dank richtet sich an meinen Mentor Israel Wagnanski, der alle meine wissenschaftlichen Tätigkeiten während der letzten sechs Jahre verfolgte. Seine kompromisslose Durchdringung fachlicher Probleme und sein unbedingter Wille, die Physik hinter den Dingen zu verstehen, haben mich von Anfang an stark geprägt. Die immerwährende persönliche Hingabe, die er mir und meiner Arbeit entgegenbrachte war für mich sehr wichtig. Ich danke ihm für die Übernahme der Gutachtertätigkeiten im Rahmen des Promotionsverfahrens und dafür, dass er die Mühen auf sich genommen hat, für die Verteidigung dieser Arbeit nach Berlin zu reisen. Außerdem möchte ich Navid Nayeri danken. Für große wie kleine Probleme war er für mich meist der erste Ansprechpartner. Ob bei der Betreuung von Diplomanden, der Planung von Versuchskampagnen oder größeren Investitionen in Laborgerät, man konnte sich immer auf seinen einfühlsamen und pragmatischen Ratschlag verlassen.

Bernd Noack möchte ich hier ausdrücklich für die gute Zusammenarbeit danken. Sein verlässlicher Führungsstil, seine exakte und schnelle Beurteilung des wissenschaftlichen Potentials der erbrachten Resultate und der Fähigkeit diese Resultate zu bündeln und zu präsentieren waren essentiell für unsere gemeinsamen Veröffentlichungen.

Des Weiteren bedanke ich mich herzlich für die gute Zusammenarbeit bei Christoph Petz, Roman Seele und Stephan Kallweit, ohne deren Beiträge diese Arbeit so nicht hätte verfasst werden können.

Außerdem will ich den Studenten danken, die für mich als studentische Hilfskräfte gearbeitet haben oder deren Diplom-/Master-/Bachelorarbeit ich betreut habe. Meinem ersten Diplomanden, Martin Lück, sei gedankt für seine strukturierte Arbeitsweise und die wunderbaren PIV-Daten, die er aufgenommen hat. Phoebe Kuhn sei ausdrücklich gedankt für die unglaubliche Geduld während der Hitzdraht-Messungen und der sauberen Auswertung, auf die sie wirklich sehr stolz sein kann. Moritz Sieber danke ich sehr für die mehrjährige Unterstützung als studentische Hilfskraft, die gute Zusammenarbeit während der Anfertigung unserer gemeinsamen Veröffentlichungen und der selbstständigen Arbeitsweise während seiner Diplomarbeit. Genauso möchte ich Lothar Rukes danken, für die Weiterentwicklung des Stabilitätslösers. Es hat mich besonders gefreut, dass aus der von mir begonnenen Arbeit an Drallstrahlen nun zwei Folgeprojekte entstehen zu denen Moritz Sieber und Lothar Rukes promovieren. Meinen beiden letzten Master-Absolventen Amir-Reza Afkhami und Schaham Schoar sei gedankt für die professionellen Umbauten des Drallkanals.

Ausdrücklicher Dank gebührt auch den Mitarbeitern der Metallwerkstatt, unserem Elektroingenieur Heiko Stolpe, unserer Systemadministratorin Angela Pätzold sowie Kristin

Halboth, Sandy Meinecke und Lilli Lindemann aus dem Sekretariat. Die Letztere konnten mir, durch leichtfertiges Negieren gewisser bürokratischer Regeln in Bedrängnis gekommen, stets mit geschickten Manövern aus der Patsche helfen.

Außerdem möchte ich hier Stefan Vey danken, mit dem ich mir über Jahre das Büro geteilt habe. Trotz eines sehr unterschiedlichen Empfindens der Raumtemperatur und der daraus folgenden Differenzen im Heizbedürfnis, habe ich diese Zeit mit ihm sehr genossen. Ebenso möchte ich Jonas Moeck danken, mit dem ich mir im letzten Jahr das Büro teilte. Sein analytischer Verstand, seine wissenschaftliche Neugierde und seine Hilfsbereitschaft machen ihn zu einem sehr wertvollen Kollegen.

Danken möchte ich auch Sebastian Göke für die das tägliche Stelldichein am Kickertisch, auf das ich mich jeden Tag aufs Neue gefreut habe. Zuletzt möchte ich noch den Mitarbeitern danken, die diese Arbeit Korrektur gelesen haben.

Finanzielle Unterstützung erhielt ich in dieser Zeit durch ein Auslandsstipendium der Gottlieb Daimler- und Karl Benz-Stiftung, durch ein NaFöG-Stipendium des Landes Berlin, durch eine Anschubfinanzierung der Technischen Universität Berlin und durch die Deutsche Forschungsgemeinschaft im Rahmen der Projekte PA-PA920/10-1 und PA-PA920/10-2. Den Geldgebern sei für ihre Unterstützung gedankt.

Berlin, im Juni 2012

Zusammenfassung

Diese Arbeit umfasst die experimentelle und theoretische Untersuchung der Entstehung großskaliger kohärenter Strukturen in turbulenten Drallstrahlen. Die untersuchte Strömungskonfiguration zeichnet sich durch eine hohe Komplexität aufgrund gleichzeitig auftretender axialer und azimuthaler Scherschichten aus. Darüber hinaus tritt ab einer gewissen Drallintensität ein Phänomen auf, was zu einer abrupten Änderung der gesamten Strömung führt. Durch das sogenannte Aufplatzen des Wirbelkerns (vortex breakdown) entsteht eine Rückstromblase auf der Strahlachse wodurch sich eine innere und eine äußere Scherschicht manifestiert. Die Analyse und Kontrolle dieser komplexen Strömungskonfiguration stellt allgemein eine große Herausforderung für die Grundlagenforschung dar und ist darüber hinaus von großem Nutzen für die Optimierung drallstabilisierter Verbrennung in Gasturbinen.

Die Arbeit ist im Wesentlichen in vier Untersuchungen unterteilt. Im ersten Teil werden die verschiedenen Strömungszustände bei ansteigender Drall charakterisiert. Dieser rein experimentelle Teil gibt einen Überblick über die wesentlichen Strömungsphänomene, mit dem Augenmerk auf das Aufplatzen des Wirbels und das damit verbundene Einsetzen einer globalen Instabilität. Die Experimente zeigen, dass eine globale Oszillation dann einsetzt, wenn die Rückstromblase eine kritische Größe erreicht hat. Das diesem Vorgang vorangehende Einsetzen des Wirbelaufplatzens wird anhand stehender Wellen im Wirbelkern erklärt. Die zweite Untersuchung geht detailliert auf die Charakteristik räumlich anwachsender kohärenter Strukturen im global stabilen Drallstrahl ein. Die hydrodynamischen Instabilitäten, welche die Entstehung dieser Strukturen antreiben, werden mittels räumlicher Stabilitätsanalyse systematisch untersucht. Es wird gezeigt, dass trotz des Einsetzens einer Zentrifugalininstabilität mit ansteigendem Drall, die Kelvin-Helmholtz-Instabilität dominiert. Jedoch beeinflusst der Drall die Phasengeschwindigkeit der helikalen Instabilitätsmoden und erhöht dabei die Dispersivität der Scherschicht. Außerdem sorgt zunehmender Drall für eine Destabilisierung stehender Moden, was dazu führen kann, dass die mittlere Strömung ihre Axialsymmetrie verliert. Diese Ergebnisse werden durch Experimente des harmonisch und des gepulst angeregten Strahls bestätigt. Im dritten Teil dieser Arbeit werden die kohärenten Strukturen der globalen Mode untersucht. Basierend auf der proper orthogonal decomposition, wird die phasengemittelte Geschwindigkeit bezüglich der globalen Oszillationsfrequenz aus zeitlich unkorrelierten Daten extrahiert. Die resultierenden kohärenten Strukturen werden mit der globalen Eigenmode verglichen, die mittels räumlicher Stabilitätsanalyse berechnet werden kann. Die globale Mode zeichnet sich durch einen präzedierenden Wirbelkern (precessing vortex core) stromauf der Rückstromblase aus, der als der Taktgeber ('wavemaker') interpretiert wird. Von dort wird die Oszillation auf die gesamte Strömung aufgeprägt, was zu einem synchronen Anwachsen helikaler Strukturen in der äußeren Scherschicht führt. Die vierte Untersuchung geht auf die Kontrolle der globalen Stabilitätsmode mittels sinusförmiger Anregung ein. Aus den Ergebnissen der ersten drei Untersuchungen lässt sich eine Kontrolltechnik ableiten, die bei geringer Anregungsamplitude größtmögliche Wirkung erzielt. Die Anregung konvektiv instabiler Moden am Düsenaustritt führt dabei zu einer Änderung des mittleren Strömungsfeldes und zu einer Unterdrückung der Rückkopplung in Strahlinnenen, was zu einer Dämpfung des präzedierenden Wirbelkerns führt.

Abstract

This thesis provides an experimental and theoretical investigation of turbulent swirling jets with the emphasis on the formation of large-scale coherent flow structures. The involved mechanisms are highly three-dimensional due to the coexistence of an axial and an azimuthal shear layer. Moreover, swirling jets are prone to a unique flow phenomenon that causes an abrupt change of the entire flow. The so-called vortex breakdown is manifested in the appearance of an internal recirculation bubble, which creates an inner and an outer shear layer. The complexity of this flow configuration poses a great challenge to fundamental research and deals as a benchmark for recent theoretical concepts. Furthermore, the present work is of great importance for the gas turbine industry, where swirling flows are frequently applied to improve combustion processes.

The work consists of four major investigations. First, the dominant flow dynamics are characterized at different swirl intensities via time-resolved stereo particle image velocimetry. This experimental work provides an overview of the main flow features with particular focus on the formation of vortex breakdown and the onset of global instability. A self-excited single-helical mode is found to arise from the axisymmetric breakdown state when the recirculation bubble reaches a sufficient streamwise extent. The preceding onset of breakdown is explained by the criticality of the rotating base flow. The second investigation consists of a detailed examination of the coherent flow structures that amplify in the swirled shear layer. The impact of swirl on the driving instabilities is addressed theoretically by means of spatial stability analysis based on the mean turbulent flow. The most dominant instability is of Kelvin–Helmholtz type, similar to the non-swirling jet. However, swirl effects the phase velocity of the helical instability waves and renders the shear layer as strongly dispersive. Moreover, the azimuthal shear destabilizes steady modes that gain significant amplitudes, which may lead to a breaking of the mean flow symmetry. The theoretical predictions are confirmed by hot-wire measurements of the pulsed and the single-mode actuated swirling jet. The third investigation focuses on the coherent structures associated with the swirling jet’s global mode that arises from the axisymmetric vortex breakdown state. A method based on the proper orthogonal decomposition is developed that allows to reconstruct the phase-averaged velocity field of the dominant coherent structures from uncorrelated flow snapshots. The obtained coherent structures are compared to the global eigenmode derived theoretically from a local spatial stability analysis. The global mode is characterized by a precessing vortex core located upstream of the breakdown bubble. It is interpreted as the global wavemaker that imposes its frequency onto the highly receptive outer shear layer, causing large-scale helical flow structures to evolve in the periphery of the jet. The last investigation focuses on the control of the swirling jet undergoing vortex breakdown. By combining the findings of the preceding studies, it is possible to derive a control scheme that enables to dampen the natural global mode at low amplitude forcing. The natural flow is shown to be globally unstable to a single-helical mode resulting in the precession of the vortex core. Convectively unstable modes forced at the nozzle lip lead to an enhanced growth of the outer shear layer. The resulting change of the mean flow leads to a global stabilization of the single-helical mode and to the suppression of the internal feedback that causes the precession of the vortex core.

Contents

Zusammenfassung	v
Abstract	vii
List of Figures	xiii
Nomenclature	xvii
1 Introduction	1
1.1 Overview of the Thesis	4
2 Theoretical Concepts	9
2.1 Triple Decomposition as the Basis for Coherent Structure Extraction	9
2.2 Coordinate Systems	10
2.3 Normal Mode Ansatz and Sign Convention	10
2.4 Linear Stability Analysis	12
2.4.1 Eigenvalue Problem of the Parallel Flow	12
2.4.2 Temporal, Spatial, and Spatio-temporal Analysis	13
2.4.3 Numerical Method	15
2.4.4 Modeling Small-scale Turbulence	18
2.5 Proper Orthogonal Decomposition	19
3 Experimental Arrangements and Measurement Techniques	21
3.1 The Swirling Jet Water Facility	21
3.2 The Swirling Jet Air Facility	21
3.3 Stereo-PIV Measurements	24
3.3.1 Measurements in Water	24
3.3.2 Measurements in Air	24
3.4 Hot-wire Measurements in the Moderately Swirling Jet	25
3.4.1 Coherent Velocity Extraction of the Excited Flow	26
3.4.2 Ensemble Average of the Pulsed Experiments	26
4 The Onset of Vortex Breakdown and Global Instability	29
4.1 Literature Review	29
4.2 Objective and Approach	31
4.3 The Mean Flow Configuration	32
4.4 Momentum Balance and Swirl Number Discussion	34
4.5 Onset of Vortex Breakdown	35

4.6	Vortex Core Criticality	43
4.7	Coherent Structures	46
4.7.1	Local Examination of Azimuthal Waves	46
4.7.2	The Onset of the Global Mode	49
4.8	Summary and Discussion	54
5	Instabilities in the Moderately Swirling Jet	59
5.1	Background and Scope	60
5.2	The Mean Flow Configuration	61
5.2.1	Analytic Representation of the Mean Flow	62
5.2.2	The Velocity Distribution at the Nozzle	62
5.2.3	Quantification of Swirl at the Nozzle Exit	63
5.2.4	Streamwise Distribution of Mean Velocities and Turbulent Stresses	64
5.2.5	Parametrization of the Divergent Mean Flow	65
5.2.6	Streamwise Distribution of the Eddy Viscosity	68
5.3	Stability at the Nozzle Exit	68
5.3.1	Shear Instability	69
5.3.2	Centrifugal Instability	75
5.4	Streamwise Evolution of Instability	80
5.4.1	Shear Instability	80
5.4.2	Centrifugal Instability	85
5.5	Single-mode Actuation	85
5.5.1	Streamwise Growth of the Co-rotating Single-helical Mode	87
5.5.2	Streamwise Phase Velocity in the Swirling Jet	90
5.6	Impulse Response	92
5.6.1	Trajectory of the Wave Packet Envelope	93
5.6.2	Modal Decomposition of the Wave Packet	96
5.6.3	Morphology of the Wave Packet	98
5.7	Summary and Discussion	100
5.7.1	The Purpose of the Present Investigation	100
5.7.2	The Main Observations	101
5.7.3	Final Remarks	103
6	Coherent Structures in the Strongly Swirling Jet	105
6.1	Motivation, and Approach	105
6.2	A Brief Survey on Empirical Mode Construction	106
6.3	Description of the Flow Configuration	107
6.3.1	Characteristic Numbers	107
6.4	Mean Flow Properties	107
6.4.1	Analytic Representation of the Mean Flow	109
6.4.2	Self-excited Oscillations	111
6.5	Empirical Construction of the Global Mode	113
6.5.1	Spatial and Temporal POD Modes	113
6.5.2	Linking the POD Modes to the Coherent Velocity	117
6.5.3	Construction of Three-dimensional Coherent Structures	119
6.6	Most Unstable Spatial Modes	119
6.7	Three-dimensional Shape of the Global Mode	123

6.8	Summary and Discussion	124
7	Open-loop Control of the Self-excited Swirling Jet	127
7.1	Objectives and Approach	127
7.2	Description of the Unforced Flow	129
	7.2.1 Characteristic Numbers	129
	7.2.2 Flow Features	130
7.3	Open-loop Control	132
	7.3.1 Amplitude Variation	133
	7.3.2 Frequency Variation	136
7.4	Impact of Forcing on the Flow Characteristics	137
7.5	Impact of Forcing on Global Instability	141
7.6	Summary and Discussion	142
8	Concluding Remarks	145
A	Flow Properties of the Swirling Water Jet	147
A.1	Mean Flow Properties	147
	A.1.1 Velocity Profiles	147
	A.1.2 Characteristic Velocity and Length Scales	149
A.2	Turbulent Fluctuations	150
	A.2.1 Turbulent Normal Stress	150
	A.2.2 Turbulent Shear Stress	152
B	Supplemental Information of the Swirling Air Jet Facility	155
B.1	The Swirling Jet Facility	155
B.2	The Actuation Device	156
B.3	Actuator Calibration	162
C	Visualization of the Global Mode	163
	Bibliography	165

List of Figures

1.1	Smoke visualization of the laminar jet at increasing swirl	2
1.2	Smoke visualization of the laminar and turbulent vortex breakdown	4
2.1	Coordinate systems	10
2.2	Normal mode sign convention	11
2.3	Comparison of the stability analysis with previous work	17
3.1	Sketch of the swirling jet water facility	22
3.2	Sketch of the swirling jet air facility	23
3.3	Hot-wire traversing system	25
3.4	Hot-wire signal of a traveling wave packet	27
4.1	Streamlines of the jet at increasing swirl	33
4.2	Streamwise distribution of axial momentum flux with swirl	36
4.3	Development of the swirl number S with rotation rate Ω of the honeycomb	37
4.4	Decay of axial velocity at a local minimum with increasing swirl	37
4.5	Mean location of the breakdown bubble with increasing swirl	38
4.6	Azimuthal vorticity contours at increasing swirl	39
4.7	Statistic evaluation of onset of vortex breakdown	42
4.8	Criticality of the vortex core at increasing swirl	45
4.9	PSD of azimuthal modes derived at $x/D = 1.1$	47
4.10	Total energy distributed among azimuthal modes at $x/D = 1.1$	48
4.11	Turbulent kinetic energy captured in the POD modes ($S = 1.37$)	50
4.12	Comparison of POD and Fourier analysis	52
4.13	Phase-locked vorticity distribution of the global mode	53
4.14	Limit-cycle amplitude versus swirl number	54
4.15	Conceptual drawing summarizing the experimental results.	56
5.1	Mean velocity profiles at the nozzle for different swirl intensities	63
5.2	Mean flow of the non-swirling jet S_1	65
5.3	Mean flow of the swirling jet S_3	66
5.4	Streamwise distribution of mean flow parameters	67
5.5	Streamwise distribution of eddy viscosity and turbulent Reynolds number	68
5.6	Growth rate of the shear instability at the nozzle exit	70
5.7	α_r , α_i , and c_{ph} of the shear instability at the nozzle exit	72
5.8	Amplitude distribution of the shear instability at the nozzle exit	74
5.9	Axial wavenumber and frequency selection at the nozzle exit	75
5.10	Radial stratification of angular momentum	76
5.11	Growth rate of the centrifugal instability at the nozzle exit	77

5.12	α_r , α_i , and c_{ph} of the centrifugal instability at the nozzle exit	78
5.13	Amplitude distribution of the centrifugal instability at the nozzle exit . . .	79
5.14	Streamwise evolution of spatial growth rate of the shear mode in the non-swirling jet	81
5.15	Streamwise development of the maximum growth rate of the shear mode in the non-swirling jet	82
5.16	Streamwise evolution of spatial growth rate in the swirling jet	84
5.17	Streamwise evolution of spatial growth rate of the centrifugal instability in the swirling jet	86
5.18	Radial amplitude distribution of the $m = 1$ mode	88
5.19	Streamwise amplitude distribution of actuated co-winding $m = 1$ mode for various swirl configurations	88
5.20	Streamwise development of spatial growth rate of actuated co-winding $m = 1$ mode	89
5.21	Phase distribution of mode $m = 1$ for the swirling jet	91
5.22	Streamwise evolution of the phase delay with swirl	91
5.23	Streamwise evolution of the phase velocity with swirl	92
5.24	Trajectory of the wave packet envelope for the swirling and non-swirling jet	95
5.25	Modal amplitude distribution derived from linear stability analysis	97
5.26	Modal amplitude distribution derived from hot-wire measurements	99
5.27	3D-wireframe visualization of the traveling wave packet	100
6.1	Profiles of the mean axial and plane-normal velocity	108
6.2	Velocity profiles of the approximated mean flow	110
6.3	Peak in the PSD from the global mode	111
6.4	Hopf bifurcation diagram	112
6.5	Lock-in regime	113
6.6	POD spectrum	114
6.7	First five POD modes of the crossflow plane of measurement	114
6.8	Phase portrait of the POD for the crossflow plane	115
6.9	First four POD modes of the streamwise measurement plane	116
6.10	Phase portrait of the POD for the streamwise plane	116
6.11	Comparison of streamwise and crosswise coherent data	118
6.12	Schematic diagram of the 3D flow construction	120
6.13	Spatial amplification rate of the mode $m = 1$	121
6.14	Streamwise evolution of the spatial amplification rate and axial wavelength	122
6.15	Coherent velocity of the most amplified normal mode	123
6.16	Three-dimensional flow field visualizing the global mode	125
7.1	Swirl number versus axial distance	130
7.2	Natural flow at $S = 1$ and $Re_D = 20000$	131
7.3	Cross-section of the jet undergoing vortex breakdown	134
7.4	Linear growth and nonlinear saturation of the forced mode	135
7.5	Streamwise distribution of kinetic energy of the forced and natural mode	135
7.6	Spatial linear stability analysis for $m = 2$	136
7.7	Streamwise development of coherent energy at varying forcing frequency	137
7.8	Contours of coherent energy for the natural and actuated flow	138
7.9	Impact of forcing on the momentum thickness of the outer shear layer	139

7.10	Impact of forcing on location and size of the recirculation bubble	140
7.11	Spatio-temporal analysis of the natural flow	143
A.1	Mean profiles of the swirling jet	148
A.2	Characteristic velocity and length scales versus axial distance.	149
A.3	Profiles of turbulent normal stresses	151
A.4	Profiles of turbulent shear stresses.	153
B.1	Sketch of the swirling jet facility (first state)	156
B.2	Photographs of the swirling jet facility (second state)	157
B.3	Photographs of the actuation device	158
B.4	Technical drawing of the complete excitation device	158
B.5	Technical drawing of the nozzle plate with details on the wave guide geometries.	159
B.6	Technical drawing of the nozzle front plate with details.	160
B.7	Technical drawing of the nozzle adapter.	161
B.8	Technical drawing of the nozzle ring.	161
B.9	Speaker calibration at no-flow condition	162
C.1	3D-Visualization of the global mode in swirling jets	163

Nomenclature

$(\cdot)'$	stochastic part of the Reynolds decomposition
$(\cdot)^c$	coherent part of the triple decomposition
$(\cdot)^P$	phase-averaged part
$(\cdot)^s$	stochastic part of the triple decomposition
$(\cdot)_{x,y,\dots}$	vector components
$\alpha = \alpha_r + i\alpha_i$	complex axial wavenumber
α_i^{\max}	maximum spatial growth rate
α_r^{\max}	real axial wavenumber at maximum growth rate
δ_x	momentum thickness
\dot{Q}_x	axial flux of axial momentum
\dot{Q}_θ	axial flux of tangential momentum
γ	intermittency factor
$\hat{(\cdot)}$	complex Fourier coefficient
λ_i	i th POD eigenvalue
Re_D	global Reynolds number
Re_t	turbulent Reynolds number
RMS	root mean square
ν	kinematic viscosity
ν_t	eddy viscosity
Ω	rotation rate of the honeycomb
$\omega = \omega_r + i\omega_i$	complex angular frequency
Ω^e	rotation rate of the wave packet envelope
$\omega_0 = \omega_{0,r} + i\omega_{0,i}$	complex absolute angular frequency
ω_r^{\max}	real angular frequency at maximum growth rate
$\omega_s = \omega_{s,r} + i\omega_{s,i}$	complex angular frequency at the saddle point
Ω_{cl}	rotation rate on the jet centerline
$\omega_{\theta,\text{cl}}$	azimuthal vorticity near the jet centerline
ϕ_c	Benjamin's test function
Π	all control parameters of the mean flow
φ_m	azimuthal mode phase angle
Φ_i	i th spatial POD mode
\mathbf{V}	mean velocity vector
\mathbf{v}	time-dependent velocity vector
$\mathbf{x} = x, r, \theta$	cylindrical coordinates
$\mathbf{x} = x, y, z$	Cartesian coordinates
$\boldsymbol{\omega}$	vorticity vector

\tilde{K}_{tot}	total coherent energy
$A_{\text{spk}}^* = A_{\text{spk}}/A_{\text{spk},0}$	normalized speaker input voltage
A^e	amplitude of wave packet envelope
a_i	i th temporal POD mode
A_m	mode amplitude integrated across the shear layer
A_{max}^e	maximum amplitude of wave packet envelope
A_{sat}	global mode limit-cycle amplitude
$A_{\text{spk},0}$	critical speaker input voltage of mode $m = 2$
A_{spk}	speaker input voltage
B	shape parameter of reversed flow
$b_{1,2}$	fit parameters of axial velocity profile
$b_{3,4}$	fit parameters of azimuthal velocity profile
D	nozzle diameter
f	frequency
f_s	PIV acquisition sampling frequency
f_{act}	single mode actuation frequency
H, F, G, P	complex disturbance Eigenfunctions
K	turbulent kinetic energy (TKE)
m	azimuthal mode number
N	number of PIV snapshots
N_x, N_θ	shape parameter of axial and azimuthal shear layers
$N_{1,2}$	shape parameters of axial inner and outer shear layers
$N_{3,4}$	shape parameters of azimuthal inner and outer shear layers
P_{RF}	probability of reversed flow
P_{VB}	probability of vortex breakdown
$R_{.05}$	radial location where $V_x = 0.05V_{\text{cl}}$
$R_{.5}$	radial location where $V_x = 0.5V_{\text{cl}}$
$R_{.95}$	radial location where $V_x = 0.95V_{\text{cl}}$
R_{core}	radial position where $\omega_x = 0$
R_{crit}	Benjamin's critical radius
R_{max}	radial location of maximum axial velocity
R_θ	radial location of maximum mean azimuthal velocity
R_v	vortex core radius
S	integral swirl number
S_i	i th swirl configuration
S_{VB}	minimum integral swirl number for vortex breakdown
S_{crit}	critical integral swirl number of Hopf bifurcation
S_{loc}	local swirl number
$St = fD/V$	Strouhal number
T	period time
t	time
T_{ens}	duration of measurement ensemble
V	axial bulk velocity at the nozzle exit
V_{cl}	axial velocity on the jet centerline
V_{max}	maximum axial velocity
$X_s = X_{s,r} + iX_{s,i}$	complex axial coordinate at the saddle point

Z	number of Chebyshev points
PDF	probability density function
PSD	power spectral density

Chapter 1

Introduction

Swirling jets represent a flow configuration that is both easy to generate in an experiment and astonishingly rich in physical problems. It often serves as a benchmark for new theoretical concepts in the field of unbounded shear flows. Moreover, swirling jets are of great importance for the combustion industry, due to their ability to stabilize flames and enhance turbulent mixing. The scientific work presented here focuses on the fundamental aspects of swirling jets with the prospect of gaining deeper insights into the dynamics of turbulent, three-dimensional shear flows and to derive analysis and control strategies that are applicable to industrial flows.

The swirling jet considered in this work emanates from a round nozzle into an unconfined domain of quiescent fluid. The investigations described in this thesis target the flow dynamics in the jet nearfield that are dominated by the following two flow phenomena. (i) Streamwise growing waves emerge in the thin shear layer between the jet and the steady surrounding fluid. These waves cause the shear layer to roll-up to large-scale eddies that entrain quiescent fluid from the surrounding and pump it towards the jet center. This causes the jet diameter to increase continuously in downstream direction. (ii) Vortex breakdown occurs when a critical swirl level is exceeded and the jet switches to a completely different flow state. This flow phenomenon occurs abruptly and is characterized by the appearance of flow reversal on the jet axis. This leads to the formation of a recirculation bubble located on the jet center that transforms the flow into that of an annular jet.

The smoke visualizations of a laminar jet depicted in figure 1.1 illustrate these flow phenomena and may serve as an intuitive introduction to the dominant features of swirling jets. The photographs represent snapshots of jets emanating from a circular nozzle that is located near the left image margin. The plane along the jet axis is made visible by mixing smoke particles to the jet, which are illuminated by a vertical laser sheet coming from downstream. The different gray levels along the jet cross-section are due to an inhomogeneous smoke distribution in the jet. The steady surrounding fluid was not filled with smoke and appears white.

Figure 1.1a represents a non-swirling jet. The shear layer between the jet and the steady fluid rolls up and forms into ring-like axisymmetric vortices that propagate in the downstream direction at approximately half the jet velocity. These orderly eddy-like structures are caused by the well-known Kelvin–Helmholtz instability. With increasing distance from the nozzle these vortices merge, causing the shear layer to spread radially until it reaches

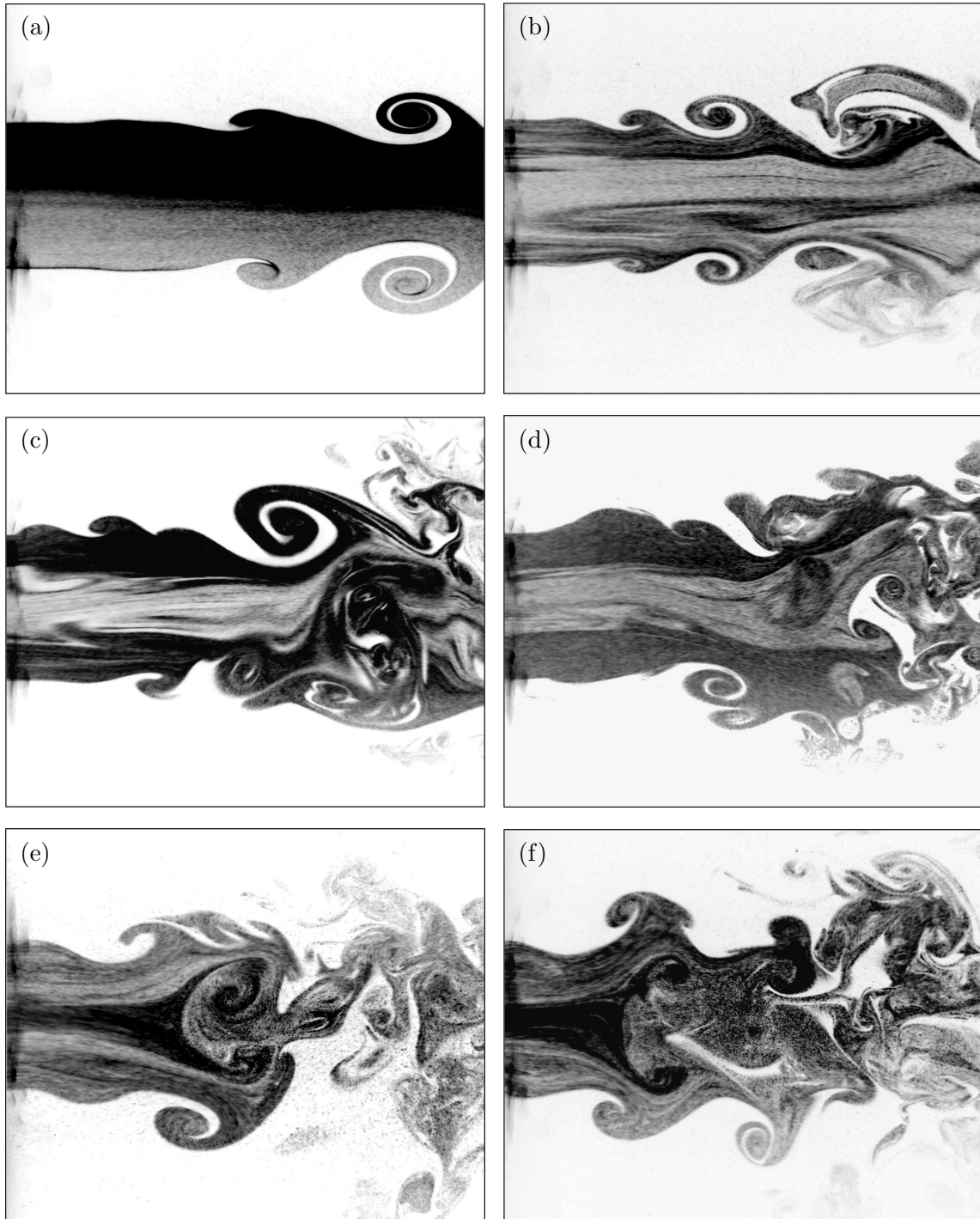


Figure 1.1: Experimental smoke visualization of the plane aligned to the jet axis of laminar non-swirling (a) and swirling jets (b-f). The swirl intensity is successively increased from image a to f.

the jet axis. By introducing swirl to the jet (figures 1.1b-c), the roll-up of the shear layer occurs closer to the nozzle and the eddies break down to irregular structures at an earlier state. At sufficiently strong swirl, the axisymmetry of the eddy-like structures is lost. Flow structures on the upper boundary of the jet appear at different streamwise locations than on the bottom boundary, indicating the existence of inclined, spiral-shaped vortices that replace the axisymmetric, ring-like vortices of the non-swirling jet (compare figure 1.1a with figure 1.1c). Hence, swirl effects the development of the shear layers and the dynamics of the eddies that form therein. The understanding of these phenomena is of crucial importance to predict the mixing characteristic of swirling jets. A detailed experimental and theoretical investigation on this topic is given in chapter 5 of this thesis.

Vortex breakdown occurs when the swirl intensity exceeds a certain threshold. Figure 1.1d displays a snapshot of a swirling jet undergoing vortex breakdown, visible by a small mushroom-shaped white structure in the center of the right half of the image. This structure indicates fluid that is sucked from downstream to the jet center, creating reversed flow on the jet axis for a short instant of time. At that swirl intensity, vortex breakdown occurs intermittently and at a varying streamwise position. Furthermore, the image shows that the entire jet column is deformed to a wave-like shape, indicating traveling waves in the jet column. The onset of vortex breakdown and its connection to the formation of standing waves in the vortex core is discussed in detail in chapter 4.

By further increasing swirl, vortex breakdown becomes more orderly and a recirculation bubble stabilizes near the nozzle. For instance figure 1.1e depicts a steady bubble located in the center of the image. Its upstream end is bounded by a dark trident-shaped flow pattern that rolls up into two inwardly-directed opposing eddies. In fact, these internal eddies are synchronized to the large rollers that are visible at the periphery of the jet (e.g., see bottom half of figure 1.1e). Hence, swirling jets undergoing vortex breakdown exhibit large-scale flow structures that reside in the center of the jet and in the outer shear layers, thereby, dominating the entire nearfield dynamics. These structures are analyzed in chapter 6, while their active control is discussed in chapter 7.

The smoke visualizations depicted in figure 1.1 have been conducted for laminar jets at a very low Reynolds number (inertia to viscosity ratio). The photographs clearly depict how flow structures grow in the downstream direction, saturate, and break down into small-scale structures, thereby, marching along the classical road from an orderly laminar flow to chaos and turbulence. The growth of the (laminar) flow structures near the nozzle are determined by the linearized Navier–Stokes equations providing the theoretical framework of linear stability analysis.

Figure 1.2 displays snapshots of a laminar and a turbulent swirling jet undergoing vortex breakdown. Both flows correspond to the same flow states, although the turbulent flow refers to a Reynolds number that is an order of magnitude higher than for the laminar flow. By carefully comparing these two images, one may find similarities, such as the recirculation zone in the center of the image or the periodic waves in the periphery of the jet. For the turbulent flow, these large-scale flow features are covered with small-scale turbulent ‘noise’ due to the high Reynolds number that causes the laminar-to-turbulent transition to occur already upstream of the nozzle exit. The existence of so-called coherent structures in turbulent flows and their similarity to the orderly laminar structures is of immense importance for the theoretical approach presented in this thesis. The linear stability analysis, a well

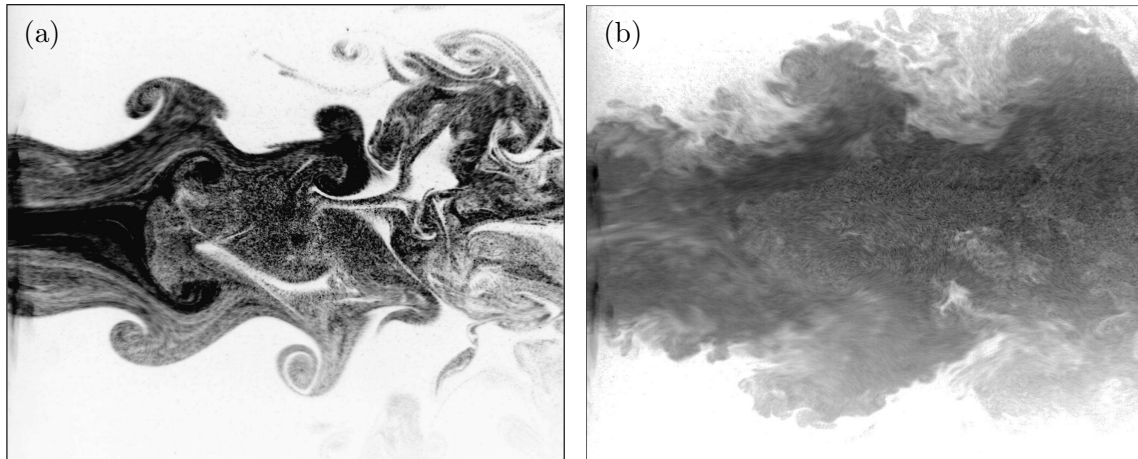


Figure 1.2: Experimental smoke visualization of the plane aligned to the jet axis of a laminar (a) and a turbulent (b) swirling jet undergoing vortex breakdown.

established theoretical framework for laminar flows, is applied to turbulent flows, yielding an effective analytical tool.

The present work focuses exclusively on fully turbulent flows. Their stochastic nature requires statistical methods in order to separate the random turbulent noise from the coherent structures. In chapter 6 of this thesis, a method is derived to reconstruct the three-dimensional shape of such flow structures from an uncorrelated sequence of flow snapshots. The experimental description of the coherent structures is always compared to the results from linear stability analysis of the turbulent mean flow. The experimental and theoretical methods used throughout this work turn out to complement one another allowing for a comprehensive analysis of the flow dynamics in turbulent swirling jets.

1.1 Overview of the Thesis

A detailed description of the underlying theoretical concepts and definitions is given in chapter 2. Therein, the triple decomposition as the corner stone of coherent structure extraction and the decomposition of the coherent velocity in normal modes is introduced first, followed by an outline of the theoretical concept of the linear stability analysis and its numerical implementation. The chapter ends with a brief introduction to the proper orthogonal decomposition (POD) used in this work.

Chapter 3 contains a detailed description of the two experimental setups used in this work. Experiments were conducted at the swirling jet water facility at the University of Arizona and the swirling jet air facility at the TU Berlin. The chapter provides details of the conducted experiments and the applied measurement techniques.

The main part of this thesis is organized in four chapters, which correspond to four independent investigations (chapters 4–7). Each chapter begins with a short abstract, followed by a brief introductory section, a comprehensive result section, and a summary and discussion of the major results.

In the following, the major concepts and outcome of the four investigations are summarized and the connections between them are pointed out.

- **Chapter 4:** This investigation focuses on the formation of vortex breakdown at increasing swirl and the onset of global instability. The swirling jet water facility described in section 3.1 is used and the flow field at increasing swirl is mapped via time-resolved PIV. A consistent swirl number definition is proposed in section 4.4 that is based on the full equation of motion. The commonly used swirl number based on boundary layer approximations results in inaccurate values within the region of vortex breakdown. The formation of vortex breakdown in the turbulent jet is observed by increasing the swirl number incrementally at very small steps.

Breakdown occurs first intermittently thereby heavily oscillating in streamwise direction (section 4.5). Thereby, the location of vortex breakdown coincides with the super-to-subcritical transition of the mean flow in excellent agreement with the inviscid theory of Benjamin (section 4.6). By further increasing the swirl, vortex breakdown stabilizes and the axial extent of the recirculation region increases. At a critical swirl number, the swirling jet undergoes a supercritical Hopf bifurcation to a global mode. The global oscillations is manifested in a precession of the vortex core and the roll-up of the outer shear layer to helix-like eddies (section 4.7.2). The experiments provide clear evidence that vortex breakdown occurs at a lower swirl number than the onset of global instability.

- **Chapter 5:** This chapter deals with the swirling jet below the onset of vortex breakdown. As shown in chapter 4, this flow configuration is globally stable. The shear layers act as amplifiers to upstream perturbations. The investigation discussed in chapter 4 already reveals a breaking of the rotational symmetry of the mode selection with increasing swirl (section 4.7.1). The impact of swirl on the convectively unstable modes is investigated in more detail in chapter 5. A spatial stability analysis is conducted employing the mean turbulent flow of the swirling jet below the threshold of vortex breakdown. Details to the applied stability analysis are given in section 2.4, whereas the mean flow configuration is described in section 5.2.1. Results are compared to the instabilities in a non-swirling jet.

At the nozzle, the swirling jet is unstable to a centrifugal and a Kelvin–Helmholtz instability (section 5.3). Due to the rotational motion, the symmetry breaks and the phase velocity of the helical instabilities depends on the frequency and the azimuthal mode number. It is concluded that this affects the ability of the swirling jets to promote subharmonic resonance and intermodal interactions of helical instability waves, which is a prominent feature of non-swirling jets. With increasing streamwise distance, only co-winding shear modes remain unstable. The swirling jet inherits a double-helical co-winding mode as the preferred mode in the nearfield that decelerates and becomes nearly steady at the end of the potential core (section 5.4).

The theoretical results are validated by experimental investigations. A wave packet is generated at the nozzle lip and its streamwise development is mapped via ensemble-averaged hot-wire measurements (section 5.6). The theoretically derived mode selection is validated by decomposing the wave packet into Fourier modes. Details on the experimental procedure are given in 3.4. The existence of steady modes is clearly confirmed by the pulsed experiments (section 5.6). The impact of swirl on the streamwise phase velocity is validated by forcing the flow at a single mode. Phase-averaged hot-wire measurements clearly support the theoretical findings (section 5.5).

Furthermore, this investigation shows that the streamwise growth of instabilities in a swirling jet is much lower than in a non-swirling jet due to the rapid increase of the thickness of the axial shear layer. The swirl component had only a marginal effect on the growth rates for the considered flow configurations.

- **Chapter 6:** As shown in chapter 4, the axisymmetric vortex breakdown state bifurcates to a global mode when a certain swirl number is exceeded. Chapter 6 focuses on the description of the coherent structures associated with the global mode at its limit-cycle oscillations. PIV measurements are conducted at a swirl number beyond the threshold of the Hopf bifurcation. Details to the considered flow configuration are given in section 6.3. The phase-averaged velocity field of the global mode is derived from uncorrelated PIV snapshots employing a POD-based phase reconstruction procedure. Although the method has already been used in chapter 4 to obtain the critical swirl number of the Hopf bifurcation (section 4.7), its application is described in section 6.5 in a more general scope.

The dynamics associated with the global mode of the swirling jet is characterized by a precession of the vortex core upstream of the breakdown bubble and the roll-up of large-scale coherent structures in the outer shear layer (section 6.5). The three-dimensional shape of this global mode is reconstructed from the two-dimensional PIV snapshots (section 6.5.3) and compared to the global mode derived from a local spatial stability analysis (section 6.7). The stability eigenmodes and the phase-averaged velocities indicate that the coherent kinetic energy of the global mode is concentrated in the periphery of the jet where coherent structures grow rapidly with downstream distance.

- **Chapter 7:** This chapter deals with the open-loop control of the global mode. A swirling jet is generated using the same swirling air facility as in chapter 5 and 6. The swirl is adjusted to a level where vortex breakdown occurs with the jet-to-wake transition to be located downstream of the nozzle. Details to the flow configuration are given in section 7.2. A spatio-temporal stability analysis employing the natural mean flow reveals that the single-helical mode is the only mode that exhibits a pocket of absolutely unstable flow. The analysis further reveals that the wavemaker of this mode is located upstream of the breakdown bubble, which coincides with the location where the precessing vortex core is most energetic. Forcing of the flow at the azimuthal mode number of the global mode results in a global lock-in (section 6.4.2). Forcing the flow at a different azimuthal wavenumber leads to the amplification of convectively unstable modes in the outer shear layer (section 7.4). These excited modes saturate nonlinearly, which results in a significant mean flow correction. This has a stabilizing effect on the natural global mode, revealing an effective suppression of the precession of the vortex core (section 7.5).

While the investigation of the moderately swirling jet of chapter 5 is rather self-contained, the results from the chapters 4, 6, and 7 can be condensed to the following statements. Spiral-shaped vortex breakdown is a consequence of a globally unstable axisymmetric vortex breakdown. The associated large-scale coherent structures are most energetic in the periphery of the jet due to the thin outer axial shear layer that enables strong streamwise amplification of upstream perturbations. The pacemaker of these perturbations is located

upstream the breakdown bubble and is characterized by a precessing vortex core that represents the wavemaker of the global mode. This wavemaker can be controlled indirectly by forcing the outer shear layer at a different mode, thereby utilizing the amplifier dynamics in the outer axial shear layer.

Chapter 2

Theoretical Concepts

2.1 Triple Decomposition as the Basis for Coherent Structure Extraction

Large-scale organized structures in turbulent flows were investigated for more than 40 years. For a comprehensive summary of earlier work, the reader is referred to [Laufer \(1975\)](#), [Roshko \(1977\)](#), [Cantwell \(1981\)](#) and [Ho & Huerre \(1984\)](#). A variety of definitions and techniques have been developed to reveal these so-called coherent structures. These include statistical approaches, pattern recognition methods, stability theory, conditional sampling and averaging and topological methods from dynamical system theory.

Some of these methods are based on a triple decomposition introduced by [Hussain & Reynolds \(1970\)](#). Accordingly, the time and space dependent flow $\mathbf{v}(\mathbf{x}, t)$ is decomposed into a time-averaged part $\mathbf{V}(\mathbf{x})$, a coherent part $\mathbf{v}^c(\mathbf{x}, t)$, and a randomly fluctuating (stochastic) part $\mathbf{v}^s(\mathbf{x}, t)$, yielding

$$\mathbf{v}(\mathbf{x}, t) = \mathbf{V}(\mathbf{x}) + \mathbf{v}^c(\mathbf{x}, t) + \mathbf{v}^s(\mathbf{x}, t), \quad (2.1)$$

The coherent part is assumed to be periodic in time and space and may be decomposed into normal modes. The triple decomposition method represents a refinement of the classical Reynolds decomposition

$$\mathbf{v}(\mathbf{x}, t) = \mathbf{V}(\mathbf{x}) + \mathbf{v}'(\mathbf{x}, t), \quad (2.2)$$

with $\mathbf{v}'(\mathbf{x}, t)$ simply representing the fluctuating part of the velocity.

The triple decomposition has become a conventional tool in active flow control experiments that distill coherent disturbances by means of phase-locked averaging. Its application to experiments is easy when the coherent structure is tagged by external excitation where a simple synchronization of the data acquisition with the forcing signals is required. Without such external phase trigger, POD-based techniques can provide another means for phase identification ([Depardon et al. 2007](#)). The triple decomposition method has been implicitly used in a number of theoretical articles where the stability analysis was applied for turbulent flows (e.g., see [Crighton & Gaster 1976](#); [Gaster et al. 1985](#)). [Liu \(1989\)](#) has developed a local turbulence model for many shear flows utilizing the triple decomposition.

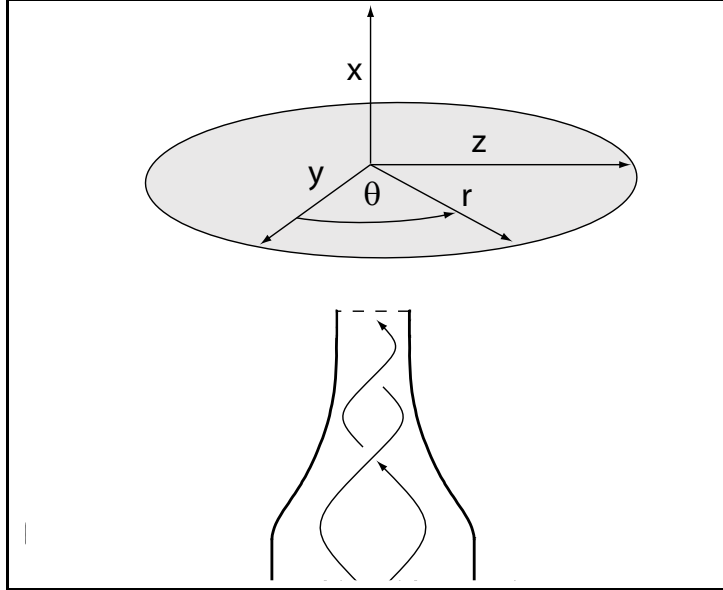


Figure 2.1: Coordinate systems used throughout this work displayed with the nozzle.

2.2 Coordinate Systems

The orientation of the two coordinate systems used in the present work is shown in figure 2.1. Cylindrical coordinates are used to describe the flow quantities in the crossflow plane whereas Cartesian coordinates are used for data shown in the streamwise plane. The two coordinate systems are necessary, as the latter does not cause a singularity along the jet axis. On the other hand, in the crossflow plane, cylindrical velocity components are necessary to correctly describe the flow quantities of the axisymmetric flow. Furthermore, the normal mode decomposition, necessary for the linear stability analysis, is strictly based on an axisymmetric flow given in cylindrical coordinates. In order to compare theoretical results with experimental data we will switch between the two coordinate systems.

2.3 Normal Mode Ansatz and Sign Convention

In order to avoid confusion during the discussion of the spatio-temporal characteristics of the instabilities, it is important to clarify the sign conventions used in this work. The coherent velocity of a disturbance traveling in an axisymmetric shear layer can be decomposed in normal modes in the following form (e.g., see [Gallaire & Chomaz 2003](#)):

$$\mathbf{v}^c(x, r, \theta, t) = \hat{\mathbf{v}}(r)e^{i(\alpha x + m\theta - \omega t)} + \hat{\mathbf{v}}^*(r)e^{-i(\alpha^* x + m\theta - \omega^* t)} \quad (2.3)$$

where α is the complex axial wavenumber, ω is the complex frequency, m is the real azimuthal wavenumber, and the asterisk $*$ denotes the complex conjugate. Hence, instability modes are equally represented by

$$(\alpha, m, \omega) \quad \text{or} \quad (-\alpha^*, -m, -\omega^*). \quad (2.4)$$

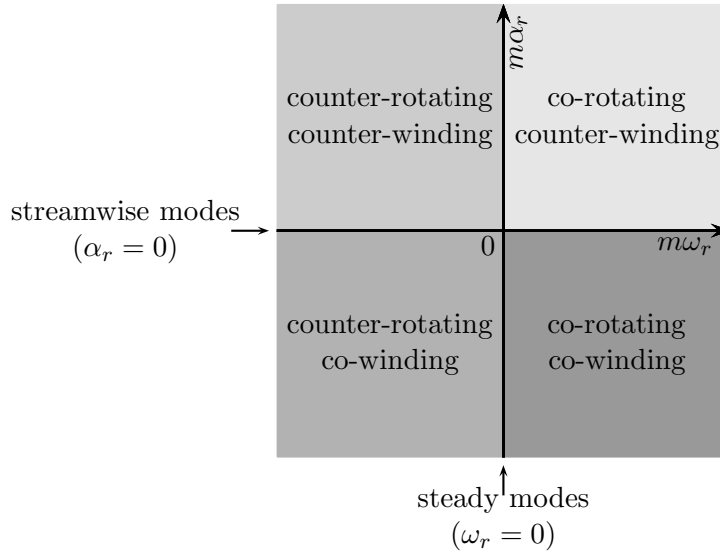


Figure 2.2: Schematic drawing of the six non-axisymmetric variants of mode alignments in swirling jets; m , ω_r , and α_r may take both signs and are equally expressed by (α_r, m, ω_r) or $(-\alpha_r, -m, -\omega_r)$.

Without loss of generality, we consider only mean flows with $V_\theta \geq 0$. Cases with negative V_θ can be deduced by the following symmetry (Gallaire & Chomaz 2003; Olendraru & Sellier 2002)

$$(V_\theta, m) \rightarrow (-V_\theta, -m). \quad (2.5)$$

In experimental studies, it is common to let ω_r and α_r only take positive values (e.g., see Liang & Maxworthy 2005; Panda & McLaughlin 1994). The phase function $(\alpha_r x + m\theta - \omega_r t)$ then implies that at a fixed axial location x modes with $m > 0$ rotate in time in the direction of the basic flow and are called *co-rotating*, while modes with $m < 0$ are called *counter-rotating*. The phase function further implies that at fixed time t and increasing x , modes with $m > 0$ have a line with constant phase that winds in opposite direction to the basic flow rotation and are called *counter-winding* and modes with negative m are called *co-winding*.

Although the restriction to positive frequencies and wavenumbers appears more intuitive, it constrains the investigation of certain spatio-temporal mode configurations that may occur in reality. It is therefore more general to let α_r take both signs. In that case, co-winding modes correspond to $\alpha_r m < 0$ and counter-winding modes to $\alpha_r m > 0$. Hence, a co-rotating co-winding mode corresponds to positive m and ω_r and negative α_r . These modes exist especially in swirling jets and they can only be expressed by negative wavenumbers. In fact, for the presentation of certain diagrams, it is convenient to let also ω_r take both signs with negative values being derived from equation (2.4). This implies that co-rotating modes refer to $\omega_r m > 0$ and counter-rotating modes to $\omega_r m < 0$. In figure 2.2 the six non-axisymmetric mode variants are summarized in a schematic drawing. It may serve as a visual aid that comes in handy during the discussion of the stability analysis presented in chapter 5.

2.4 Linear Stability Analysis

Computing spatially growing disturbances in shear layers by means of linear stability analysis has a long history. Michalke (1965) calculated the spatial stability characteristics for the hyperbolic-tangent velocity profile according to inviscid theory. Spatial growth rate and amplitude distribution agreed well with measurements conducted by Freymuth (1966), but they failed in some detail when the flow was divergent. As refinement, several attempts have been made to account for non-parallel effects (Cohen et al. 1994; Crighton & Gaster 1976; Gaster 1974; Gaster et al. 1985; Plaschko 1979). Gaster et al. (1985) applied the inviscid linear stability analysis to the periodically forced turbulent and slightly divergent mixing layer. The computed normalized phase and velocity amplitudes agreed with experimental data but the amplification rates in the direction of streaming were strongly overpredicted. The robustness of the stability analysis was demonstrated by Weisbrot & Wygnanski (1988), whose computed eigenmodes correctly predicted the measured phase and amplitude distributions of the excited waves, although the latter were forced at high amplitudes clearly exceeding the linear regime. It is important to note that for high Reynolds numbers, the stability analysis is based on the time-averaged turbulent flow which is not a stationary solution of the Navier–Stokes equation. It is argued that this infringement of the linear stability theory is possible 'knowing that the random changes in the mean velocity occur on a time scale that is short in comparison with the period associated with the large coherent structures' (Weisbrot & Wygnanski 1988).

For the linear stability analysis conducted in this work quasi-parallel flow is assumed. Hence, the streamwise development of a traveling wave is derived by successively solving the local parallel flow problem. Therefore, the Orr–Sommerfeld eigenvalue problem must be solved for fictitious parallel flows at each streamwise location. The global shape of an instability mode is then constructed from the local solutions by applying a multiple-scale approximation (Ho & Huerre 1984; Huerre & Monkewitz 1990).

2.4.1 Eigenvalue Problem of the Parallel Flow

To analyze the linear stability at a given axial location of the mean flow, velocity and pressure disturbances $(v_x^c, v_r^c, v_\theta^c, p^c)$ are superposed onto the corresponding mean velocity profile. These perturbations are periodic in time and are decomposed in normal modes, yielding

$$(v_x^c, v_r^c, v_\theta^c, p^c) = \Re \left\{ [H, iF, G, P] e^{i(\alpha x + m\theta - \omega t)} \right\}, \quad (2.6)$$

where H, F, G and P are the complex eigenfunctions. Upon substituting the modal decomposition (2.6) into the Navier–Stokes equations, linearized about the mean flow $\mathbf{V}(x, r, \theta)$, we obtain the linear system of ordinary differential equations for continuity

$$F' + \frac{F}{r} + \frac{mG}{r} + \alpha H = 0, \quad (2.7a)$$

for the x -momentum

$$\frac{H''}{\text{Re}} + \frac{H'}{r\text{Re}} + \left[i\omega - \frac{imV_\theta}{r} - i\alpha V_x - m^2 r^2 \text{Re} \right] H - iV'_x F - i\alpha P = \frac{\alpha^2 H}{\text{Re}} \quad (2.7b)$$

for the r -momentum

$$\frac{iF''}{\text{Re}} + \frac{iF'}{r\text{Re}} - \left[\omega - \frac{mV_\theta}{r} - \alpha V_x + \frac{i(m^2 + 1)}{r^2 \text{Re}} \right] F - 2 \left[\frac{im}{r^2 \text{Re}} - \frac{V_\theta}{r} \right] G - P' = \frac{i\alpha^2 F}{\text{Re}} \quad (2.7c)$$

and for the θ -momentum

$$\frac{G''}{\text{Re}} + \frac{G'}{r\text{Re}} + \left[i\omega - \frac{imV_\theta}{r} - i\alpha V_x - \frac{m^2 + 1}{r^2 \text{Re}} \right] G - \left[iV'_\theta + \frac{2m}{r^2 \text{Re}} + \frac{iV_\theta}{r} \right] F - \frac{imP}{r} = \frac{\alpha^2 G}{\text{Re}} \quad (2.7d)$$

where the primes denote d/dr . For the free jet, the boundary conditions in the farfield are (Khorrami et al. 1989)

$$F(\infty) = G(\infty) = H(\infty) = P(\infty) = 0 \quad (2.8)$$

and in the limit along the centerline ($r = 0$) impose

$$F(0) = G(0) = H(0) = P(0) = 0 \quad \text{if} \quad |m| > 1 \quad (2.9a)$$

$$\left. \begin{array}{l} H(0) = P(0) = 0 \\ F(0) + mG(0) = 0 \\ 2F'(0) + mG'(0) = 0 \end{array} \right\} \quad \text{if} \quad |m| = 1 \quad (2.9b)$$

$$\left. \begin{array}{l} F(0) = G(0) = 0 \\ H(0) \quad \text{and} \quad P(0) \quad \text{finite} \end{array} \right\} \quad \text{if} \quad m = 0 \quad (2.9c)$$

For a given mean velocity profile, the system of equations (2.7–2.9) describes an eigenvalue problem. A non-zero solution of (F, G, H, P) exists if and only if the complex pair (α, ω) satisfies the dispersion relation $\mathcal{D}(\alpha, \omega, m, \Gamma, \text{Re}) = 0$. The symbol Γ represents all control parameters describing the mean velocity profiles.

2.4.2 Temporal, Spatial, and Spatio-temporal Analysis

The above introduced eigenvalue problem can be solved for a complex ω and a given real α , for a complex α and a given real ω , or for a complex α and a complex ω .

The first approach is called *temporal analysis*, yielding temporally growing ($\omega_i > 0$) or decaying ($\omega_i < 0$) modes. It is most appropriate for the analysis of bounded flows that have no free stream velocity such as the Taylor–Couette flow.

The second approach is called *spatial analysis*, yielding spatially growing ($-\alpha_i > 0$) or decaying ($-\alpha_i < 0$) modes. It is applicable to open shear flows that are convectively unstable (noise amplifiers, see Michalke 1965). In weakly non-parallel flows, the spatial analysis describes the streamwise growth and decay of flow perturbations initiated at a certain axial location, e.g. $x = 0$. Within the framework of the multiple-scale analysis, the global disturbance velocity field is given by

$$\mathbf{v}^c(\mathbf{x}, t) = \Re \left\{ A_0(x) [H(x, r), iF(x, r), G(x, r)] \exp \left[i \left(\int_0^x \alpha(\xi) d\xi + m\theta - \omega_r t \right) \right] \right\}. \quad (2.10)$$

It is assumed that the (small) length scale of the instability is separated from the (large) length scale that characterizes the streamwise non-uniformity of the mean flow (Huerre & Monkewitz 1990). This implies a slow streamwise variation of the term $A_0[H, iF, G]$ with x and a fast streamwise variation of the wavenumber α with ξ .

Crighton & Gaster (1976) have developed a first order correction for weakly non-parallel flows that enables to derive a slowly varying amplitude scaling $A_0(x)$ from a ordinary differential equation employing the eigenfunction and its adjoint. Accounting for the streamwise and radial varying term $A_0[H, iF, G]$ implies that the growth rate and phase velocity of a traveling wave depends on the streamwise and radial coordinate and on the velocity component. Hence, α_i and $c_{ph} = \omega_r/\alpha_r$ must be considered as rough estimates of these two quantities. This is confirmed by experimental observations of streamwise traveling waves in the mixing layer Gaster et al. (1985).

However, for the sake of simplicity, we omit the weakly non-parallel correction and assume A_0 to be uniform throughout this work. This quasi-parallel approach is justified by the following reasons. The swirling jet flows considered here are highly non-parallel due to strongly enhanced jet spreading and vortex breakdown. Under these conditions, the local analysis exceeds its strict limits of validity and so does the weakly non-parallel correction scheme. The resulting inaccuracies in the prediction of the fast variable α is much more crucial than the inaccuracies in the prediction of the slowly varying A_0 . The present argumentation is in line with a previous study on the instabilities in the wake of a cylinder conducted by Juniper et al. (2011).

Within the framework of quasi-parallel stability analysis, a disturbance at frequency ω_r and azimuthal wavenumber m that travels downstream is amplified in flow regions where $-\alpha_i > 0$ and damped in regions where $-\alpha_i < 0$. Assuming $A_0 = 1$, the amplitude distribution of the axial velocity component of the traveling wave corresponds to the modulus of the eigenfunction $H(x, r)$ computed at each streamwise location and weighted by the amplitude ratio $g(x) = \exp[-\int_0^x \alpha_i(\xi) d\xi]$, yielding

$$|\hat{v}_x(x, r)| = |H(x, r)| \exp \left[- \int_0^x \alpha_i(\xi) d\xi \right], \quad (2.11)$$

where the eigenfunction H depends parametrically on x . In order to assemble the eigenfunctions computed for different x , a consistent normalization is required, which introduces an ambiguity to the present analysis. Here, a uniform total kinetic energy $K = \int_0^\infty |[H, iF, G]|^2 r dr$ is used. Note that the normalization with other quantities such as the Euclidean norm or the radially integrated amplitude did not noticeable effect the results.

The streamwise phase velocity for the parallel flow is given by $c_{\text{ph}} = \omega_r / \alpha_r$. This corresponds approximately to the phase velocity of the disturbance traveling in the center of the shear layer (Gaster et al. 1985). Nonetheless, an exact prediction of the phase velocity is impossible within the quasi-parallel approach.

The third approach, where the eigenvalue problem is solved for complex α and complex ω is called *spatio-temporal analysis*. It is applicable to flows that undergo self-excited oscillations at a discrete tone, as for instance wakes (Monkewitz 1988; Provansal et al. 1987), hot jets (Monkewitz et al. 1990), or cold swirling jets undergoing vortex breakdown (Gallaire et al. 2006; Liang & Maxworthy 2005). The intrinsic oscillations of these so-called *globally unstable* modes are strongly connected to a spatial domain where the flow is absolutely unstable (Chomaz et al. 1988; Chomaz et al. 1991). In that region, disturbances are promoted that grow in time in upstream and downstream direction, ultimately contaminating the entire flow (flow oscillators). In contrast, in convectively unstable regions, modes grow solely in downstream direction and are swept away from their source (flow amplifiers). In order to distinguish between absolute and convective instability, the *absolute frequency* ω_0 must be derived (Briggs, R. 1964; Huerre & Monkewitz 1990). This implies tracking for saddle points in the complex α -plane by minimizing $d\omega/d\alpha$. The complex frequency at the saddle point $\omega_0 = \omega_{0,r} + i\omega_{0,i}$ is then associated with the absolute frequency and the streamwise distribution of $\omega_0(x)$ can be considered as a global dispersion relation. A key feature of globally unstable flows is the existence of a wavemaker from which the global oscillations arise. In case of a linear global mode, this wavemaker is located at a saddle point in the complex x -plane (Chomaz et al. 1991). The complex frequency of the global mode ω_s is selected at the wavemaker location, yielding

$$\omega_s = \omega_0(X_s) \quad \text{with} \quad \frac{d\omega_0}{dX_s}(X_s) = 0. \quad (2.12)$$

Hence, if the imaginary part of the global frequency ω_s is larger than zero, the flow is considered as linearly globally unstable. In case of a nonlinear global mode, the wavemaker is located at the convective absolute transition point (Pier & Huerre 2001).

2.4.3 Numerical Method

Khorrani et al. (1989) demonstrated that the eigenvalue problem can be efficiently solved by using a Chebyshev spectral collocation method. Following this study, the system of ordinary differential equations (2.7) is solved numerically by discretizing the three velocity components and the three momentum equations at the Chebyshev collocation points. The continuity equation is enforced at the mid grid points. This approach has been successively applied by Khorrani (1991) to the temporal problem and recently to the spatial problem by Parras & Fernandez-Feria (2007). For a detailed description of the numerical procedure, the reader is referred to Khorrani et al. (1989), and thus, only a brief summary is given here.

The boundary conditions (2.8) are enforced at a large but finite radius $r_{\text{max}} \gg 1$ in consistency with the work of Olendraru & Sellier (2002) and Parras & Fernandez-Feria (2007). A coordinate transformation is necessary to map the Chebyshev collocation points, in the interval $-1 \leq \xi \leq 1$, onto the physical domain of the problem, in the range $0 \leq$

$r \leq r_{\max}$. Here, the two-parameter transformation proposed by Malik et al. (1985) is used, which reads

$$\frac{r}{r_c} = \frac{1 + \xi}{1 - \xi + 2r_c/r_{\max}}. \quad (2.13)$$

Since the Chebyshev collocation points are known to be distributed in the vicinity of $r = 0$ and r_{\max} , the parameter r_c is necessary to redistribute the collocation points. It allows half of the points to be distributed in the region $0 \leq r \leq r_c$. Finally, the eigenvalue problem (2.7) for the case of spatial stability (given real ω , complex eigenvalue α) is linearized by introducing a generalized eigenvector $\mathbf{X} = [F, G, H, \alpha F, \alpha G, \alpha H, P]^T$. Discretizing the system of ordinary differential equations (2.7) in terms of the variable ξ and enforcing the boundary conditions (2.8–2.9), we may write the generalized eigenvalue problem as

$$\mathbf{D}\mathbf{X} = \alpha\mathbf{E}\mathbf{X}. \quad (2.14)$$

Taking Z as the number of Chebyshev points, both \mathbf{D} and \mathbf{E} are square matrices with dimensions of $7Z$. Note that the last 14 rows of matrix \mathbf{D} contain the boundary conditions. The eigenvalue problem (2.14) is solved using a standard EIG routine embedded in the software environment MATLABTM. Spurious eigenmodes, caused by the discretization, are discarded by two independent criteria: first, all eigenmodes are discarded that do not diminish at $r \rightarrow \infty$, that is to say that only those eigenvalues are considered that satisfying

$$\frac{\sum_{i=1}^{Z/10} |F(r_i)|^2}{\sum_{i=1}^Z |F(r_i)|^2} < \epsilon_1, \quad (2.15)$$

with r_i being the radial points and ϵ_1 a given tolerance. Second, spurious eigenvalues are filtered out by comparing the computed spectra \mathcal{S}_Z and $\mathcal{S}_{Z'}$ for $Z' > Z$. The location of the spurious modes in the complex α -plane is very sensitive to the number of Chebyshev points Z , in contrast to the few physical eigenvalues of the problem. Thus, the eigenvalues α are considered as spurious if $\min|\alpha - \alpha'| > \epsilon_2$.

The accuracy of the calculations is first checked by comparing the computed eigenvalues with those calculated by Khorrami et al. (1989) and Parras & Fernandez-Feria (2007). The computed eigenvalues agree for all shown digits which is not surprising as these authors use exactly the same numerical method. A comparison of the computations with the results presented by Gallaire & Chomaz (2003) is more challenging as their results are retrieved by direct numerical simulations of the linear impulse response. Unfortunately, Gallaire & Chomaz do not explicitly present computed eigenvalues of their spatio-temporal analysis but only display the complex frequency ω of the temporal problem. Hence, for the sake of comparison, the temporal modes are computed using the same base flow as used by Gallaire & Chomaz. Figure 2.3 clearly shows that for $m = 1$ both numerical methods arrive at the same solutions. The correctness of the computed eigenvalues makes provides enough confidence to apply the computations to the present flow configuration. In comparison to the base flow used by Gallaire & Chomaz and Parras & Fernandez-Feria, our mean flow is more complex as it consists of two axial and two azimuthal shear layers. Thus, the problem is more demanding and the number of collocation points has to be increased. To satisfy the

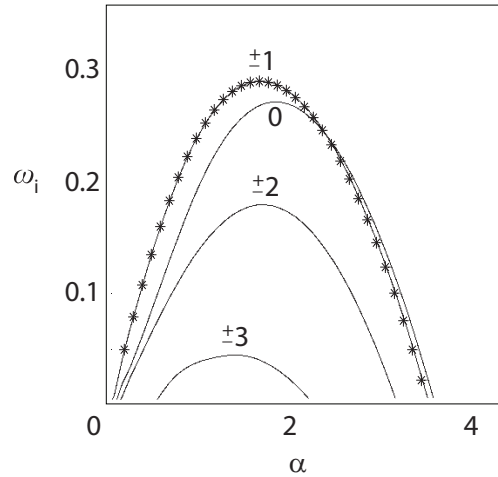


Figure 2.3: Temporal stability analysis of a non-swirling jet. The growth rate ω_i is plotted over the axial wavenumber α . The corresponding azimuthal wavenumbers m are shown close to the corresponding curves. The solid lines represent computations reprinted from Gallaire & Chomaz (2003). Symbols represent the computations at $m \pm 1$ using a Chebyshev collocation method ($Z = 180$, $a = 3$, $r_{\max} = 100$, $\epsilon_1 = 10^{-11}$, $\epsilon_2 = 10^{-3}$).

filter criterion (2.15) and to successfully discard the spurious eigenvalues, the number of Chebyshev points is increased to $Z = 300$. A convergence study optimizes the parameters a and r_{\max} of the transformation (2.13) yielding $a = 3$ and $r_{\max} = 100$ for all computations presented here. It was observed that the calculated eigenvalues are relatively insensitive to the radial distribution of the collocation points.

A further challenging aspect of the computation of spatial instability is the sorting of the eigenvalues and eigenfunctions with respect to the corresponding modes. Spatial branches have to be identified and tracked in the complex wavenumber plane while a parameter of the dispersion relation is changed. A well-designed sorting routine is of great importance to accurately follow the spatial branches into the region of negative growth $\alpha_i > 0$. In this region, many modes coexist and several spatial branches intersect. A routine is developed which sorts the eigenvalues and eigenfunctions of the dispersion relations \mathcal{D} and \mathcal{D}' by incorporating two criteria: first, eigenvalues are sorted by minimizing the distance $|\alpha - \alpha'|$; second, the normalized eigenvectors \mathbf{X} are sorted by minimizing $|1 - \langle \mathbf{X}\mathbf{X}' \rangle|$. The efficiency of the sorting routine is validated by visually checking the spatial branches.

For the study of the moderately swirling jet (chapter 5), the numerical scheme is further simplified by implementing the MATLABTM routine EIGS which solves an eigenvalue problem and returns only one eigenvalue that is closest to a given estimate. The eigenvalue problem is first solved for one combination of the parameters (ω_r, m, Γ) by using the standard MATLABTM routine EIG, which returns numerous eigenvalues including the spurious ones. The physically meaningful solutions are then sorted out, a posteriori, by using two independent criteria mentioned earlier. Starting from this solution, the eigenvalue problem is solved for a new set of parameter $(\omega_r, m, \Gamma, \text{Re}_t)$ using the EIGS routine. The required estimate is thereby derived from cubic extrapolation of the already obtained solutions while going in small increments through the m - ω_r - Γ -parameter space. Particular attention must be paid when several modes exist for one parameter setting since the EIGS routine may

switch from one mode to the other. All results are cross-checked by using the standard EIG routine.

For the spatio-temporal analysis, the absolute frequency ω_0 is tracked while traversing through the flow field in streamwise direction, using a method introduced by Rees (2009). It is based on a truncated Taylor series expansion that is expected to converge in the vicinity of a saddle point. The required starting values of ω_0 are derived iteratively from cubic extrapolation. The routine is started at an axial location where ω_0 is derived visually from global pictures computed at two closely spaced axial locations (see Suslov (2006) for details on global pictures and required eigenvalue sorting routines). Details of the procedure are given in the work of Rukes (2010). The location of the wavemaker X_s and the associated global complex frequency ω_s are derived from equation (2.12) by analytic continuation of $\omega_0(X)$ into the complex X plane. Therefore, $\omega_0(x)$ is fitted to a Padé polynomial.

2.4.4 Modeling Small-scale Turbulence

To apply linear stability analysis to a turbulent mean flow, it is assumed that the turbulent fluctuations are at a much smaller time and length scale than the coherent structures that arise due to hydrodynamic instability. An interaction between these coherent structures, the mean flow, and turbulent fluctuations is neglected. Notwithstanding, it is assumed that fine-scale turbulence provides additional mixing and behaves like an added eddy viscosity. The instabilities in free shear flows are typically inviscid, and hence, the additional eddy viscosity due to fine-scale turbulence has primarily a stabilizing effect (e.g., see Liu 1971; Marasli et al. 1991). This fictitious viscosity ν_t that adds to the kinematic viscosity ν is integrated into the stability analysis by writing the dispersion \mathcal{D} with the turbulent Reynolds number

$$\text{Re}_t = \frac{V\delta_x}{\nu + \nu_t}. \quad (2.16)$$

The eddy viscosity is derived from the well-known Boussinesq's approximation, yielding

$$-\overline{v'_x v'_r} = \nu_t \left[\frac{\partial V_x}{\partial r} + \frac{\partial V_r}{\partial x} \right]. \quad (2.17)$$

As stated by Townsend (1956), this simple eddy viscosity model is only valid within the turbulent flow and must therefore be weighted by an intermittency factor γ that is derived from the PIV snapshots using the following approach: First, the instantaneous azimuthal vorticity is calculated from each PIV snapshot. Second, the noise from the obtained vorticity field is removed by setting values below 5 % to zero. The resulting vorticity distributions provide a reasonably well description of the instantaneous boundary between rotational and irrotational flow. Third, the number of events of irrotational flow N_{pot} are derived for each measurement location. The intermittency function is then defined as $\gamma = N_{\text{pot}}/N$, where N is the total number of PIV snapshots. The eddy viscosity weighted by the intermittency function is assumed to be constant in radial direction but may vary in axial direction.

2.5 Proper Orthogonal Decomposition

This section provides a brief introduction to the principal concept of the proper orthogonal decomposition (POD). In this work, POD is used to extract the dominant coherent structures that are naturally prevalent in the globally unstable swirling jet.

We consider the fluctuation snapshots of a velocity field

$$\mathbf{v}'(\mathbf{x}, t_k) = \mathbf{v}(\mathbf{x}, t_k) - \mathbf{V}(\mathbf{x}),$$

where \mathbf{x} is a point in a spatial domain $\Omega \subset \mathbb{R}^3$, and t_k , $k = 1, \dots, N$, are the sampling instants. The goal is to find a least-order expansion of the snapshots

$$\mathbf{v}'(\mathbf{x}, t_k) = \sum_{p=1}^I a_p(t_k) \Phi_p(\mathbf{x}) + \mathbf{v}_{res}(\mathbf{x}, t_k), \quad (2.18)$$

which minimizes the residual \mathbf{v}_{res} in a sense specified below. The snapshots are considered as elements of the Hilbert space of square integrable vector fields $\mathcal{L}_2(\Omega)$. This Hilbert space is equipped with the inner product in Ω between two vector fields \mathbf{v} and \mathbf{w} defined by

$$(\mathbf{v}, \mathbf{w})_\Omega := \int_\Omega \mathbf{v} \cdot \mathbf{w} \, d\mathbf{x}, \quad (2.19)$$

and the related norm $\|\mathbf{v}\|_\Omega$ reads

$$\|\mathbf{v}\|_\Omega := \sqrt{(\mathbf{v}, \mathbf{v})_\Omega}. \quad (2.20)$$

The velocity fields are provided by PIV snapshots taken at N uncorrelated points at the times t_k , $k = 1, \dots, N$. In addition to the inner product in space, we define the ensemble average of a quantity ζ as

$$\bar{\zeta} := \frac{1}{N} \sum_{k=1}^N \zeta(t_k). \quad (2.21)$$

The quantity ζ may be a scalar, a vector or any other tensor. The norm and ensemble average allows one to formulate an optimal property of the Galerkin expansion (2.18). We require that the spatial modes are chosen such that the time-averaged \mathcal{L}_2 error is minimal for the number of modes $I = 1, \dots, N$:

$$\chi_2(\Phi_1, \dots, \Phi_I) := \overline{\|\mathbf{v}_{res}\|^2} = \min. \quad (2.22)$$

Note that the minimized residual $\mathbf{v}_{res} \equiv 0$ for $I = N$. This optimality property is fulfilled by the snapshot POD modes introduced by [Sirovich \(1987\)](#). The corresponding algorithm is based on the $N \times N$ autocorrelation matrix $\mathbf{R} = (R_{kl})$ defined by

$$R_{kl} := \frac{1}{N} (\mathbf{v}'(\mathbf{x}, t_k), \mathbf{v}'(\mathbf{x}, t_l))_\Omega \quad (2.23)$$

quantifying the relation between the snapshots. The correlation matrix is symmetric and positive semi-definite, i.e. the eigenvalue problem

$$\mathbf{R}\mathbf{a}_p = \lambda_p\mathbf{a}_p \quad (2.24)$$

has real and non-negative eigenvalues $\lambda_p \geq 0$. Without loss of generality, we assume the eigenvalues to be sorted by magnitude:

$$\lambda_1 \geq \lambda_2 \geq \dots \geq \lambda_N = 0.$$

Note that $\lambda_N = 0$ since N linearly independent snapshots cannot span the whole N -dimensional space. Two points, for instance, define a one-dimensional line. The corresponding eigenvectors $\mathbf{a}_p := [a_p(t_1), \dots, a_p(t_N)]^t$, called temporal modes, are orthogonal by construction. For reasons of convenience, we require

$$\overline{a_p a_q} = \frac{1}{N} \sum_{k=1}^N a_p(t_k) a_q(t_k) = \lambda_p \delta_{pq}. \quad (2.25)$$

Now, the spatial POD modes can be calculated as a linear combination of the fluctuation snapshots

$$\Phi_p(\mathbf{x}) = \frac{1}{N\lambda_p} \sum_{k=1}^N a_p(t_k) \mathbf{v}'(\mathbf{x}, t_k). \quad (2.26)$$

These spatial POD modes are orthonormal by construction:

$$(\Phi_p, \Phi_q)_\Omega = \delta_{pq}. \quad (2.27)$$

The eigenvalues λ_p represent twice the amount of the fluctuating kinetic energy contained in each POD mode, $K_p := \overline{(\mathbf{v}', \Phi_p)_\Omega^2} / 2 = \lambda_p / 2$. The total fluctuation energy is defined as the sum of the modal contributions owing to orthonormality (2.27):

$$K := \frac{1}{2} \overline{\|\mathbf{v}'\|_\Omega^2} = \sum_{p=1}^N K_p = \frac{1}{2} \sum_{p=1}^N \lambda_p. \quad (2.28)$$

K is generally referred to as turbulent kinetic energy (TKE). Snapshot POD extracts the most energetic structures representing them as linear combinations of the snapshots and imposes orthogonality in spatial and temporal modes. Snapshot POD is the time-discrete variant of a general continuous formulation (Holmes et al. 1998). In turbulent flows, the large-scale structures usually contain a major portion of the TKE, so the POD modes with high energy content can hence be expected to span the basis for the dominant coherent structures.

Chapter 3

Experimental Arrangements and Measurement Techniques

3.1 The Swirling Jet Water Facility

The water facility belongs to the laboratory of Prof. I. Wygnanski at the University of Arizona. A schematic view of the experimental apparatus is shown in figure 3.1. The facility consists of a horizontal swirling jet discharging into a large transparent water tank that has a 1000 mm by 1000 mm cross section and measures 1300 mm in length. A 762 mm long plexiglass cylinder with an inner diameter of 254 mm serves as a settling chamber and houses the apparatus generating the swirl. Similar to the method used by Billant et al. (1998), the swirl is generated by passing the water through a rotating cylinder, placed in the interior of the settling chamber. The jet axial velocity is generated by a pump and the flow is set into a state of solid body rotation by inserting a 559 mm long honeycomb into the inner rotating cylinder. The swirling flow is then guided through a converging nozzle attached to the outer cylinder and mounted onto the tank. A serrated ring glued to the interior surface of the contraction trips the flow, thus preventing transitional effects associated with a change of Reynolds number. The nozzle diameter is $D = 52.4$ mm. Effects of confinement are minimized by the relatively large size of the tank and the large diameter of the scooping nozzle. Consequently, the measured recirculation currents are found to be negligible. The water surface is covered by a floating foam in order to minimize the vertical temperature gradients resulting from evaporation. Additional information about this facility are given in the work of Richard (2003), Oberleithner (2006), and Seele (2008).

3.2 The Swirling Jet Air Facility

The air facility belongs to the laboratory of Prof. C. O. Paschereit at the TU Berlin. A turbulent swirling jet is generated using an apparatus that resembles the one built by Chigier & Chervinsky (1965). The schematic arrangement of the facility is shown in figure 3.2. The primary axial stream of air passes through a deep honeycomb prior to entering a swirler through which a secondary air stream is introduced through four tangential slots, each 80 mm long. The flow is then guided through a 600 mm long tube, before entering

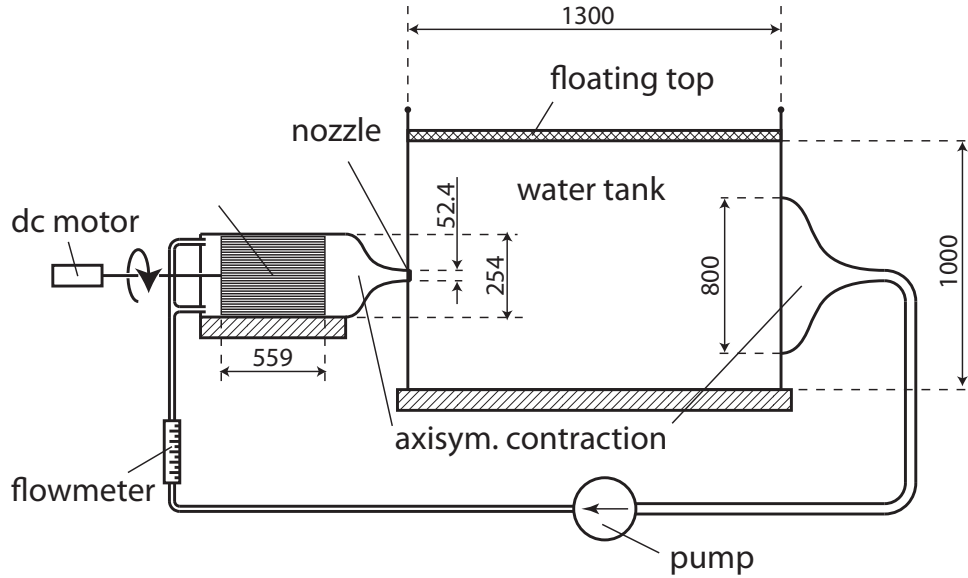


Figure 3.1: Sketch of the swirling jet water facility (all lengths are expressed in mm)

the contraction forming the nozzle. A perforated plate is mounted in the tube to minimize possible inhomogeneities resulting from the tangential inlets in the swirl chamber. The swirl levels generated by the facility depend on the ratio of mass flows coming through the two inlets: a non-swirling jet is generated when no air enters tangentially through the swirler and the maximum swirl level is attained when the axial inflow is zero. Two frequency-controlled blowers provide the necessary airflow. The volume flow of each blower was measured using calibrated orifices connected to BARATRON gauges. The blowers are feed-back controlled to provide a constant volume flux. The nozzle diameter is $D = 51$ mm.

Particular attention was paid to the design of the excitation device located at the nozzle lip where the thin shear layer between the jet and the quiescent surrounding fluid is unstable to all azimuthal modes (Cohen & Wygnanski 1987; Gallaire et al. 2004). Acoustic excitation is applied using an array of eight loudspeakers equally spaced along the azimuth (figure 3.2). Such an array provides radial fluctuations that trigger the inviscid shear layer instabilities. An acoustic wave-guide from each actuator terminates in a rectangular duct leading to a narrow slot that does not interfere with the jet flow when the speakers are inactive. The loudspeakers are driven by a set of digital-to-analog converters under program control. The actuators are adjusted to equal amplitudes under no-flow conditions using a microphone located at the centerline in the exit plane of the nozzle. The azimuthal disturbances can be controlled by varying the phase difference between the actuators. With an array of eight actuators the highest azimuthal mode numbers that can be excited are $m = \pm 4$. A similar excitation device was successfully used by Long & Petersen (1992) to study instabilities in non-swirling jets and by Panda & McLaughlin (1994) for swirling jets. For the measurements of the impulse response, a pulse is generated by using only one of the eight loudspeakers. A delta-pulse in time and space is generated by running the speaker with a saw-tooth signal with a sharp rising edge and a linearly decaying falling edge. The peak velocities of the zero-mass-flux jets created by the actuators are measured at the slots using a hot-wire probe. This characteristic velocity scales linearly with the speaker input

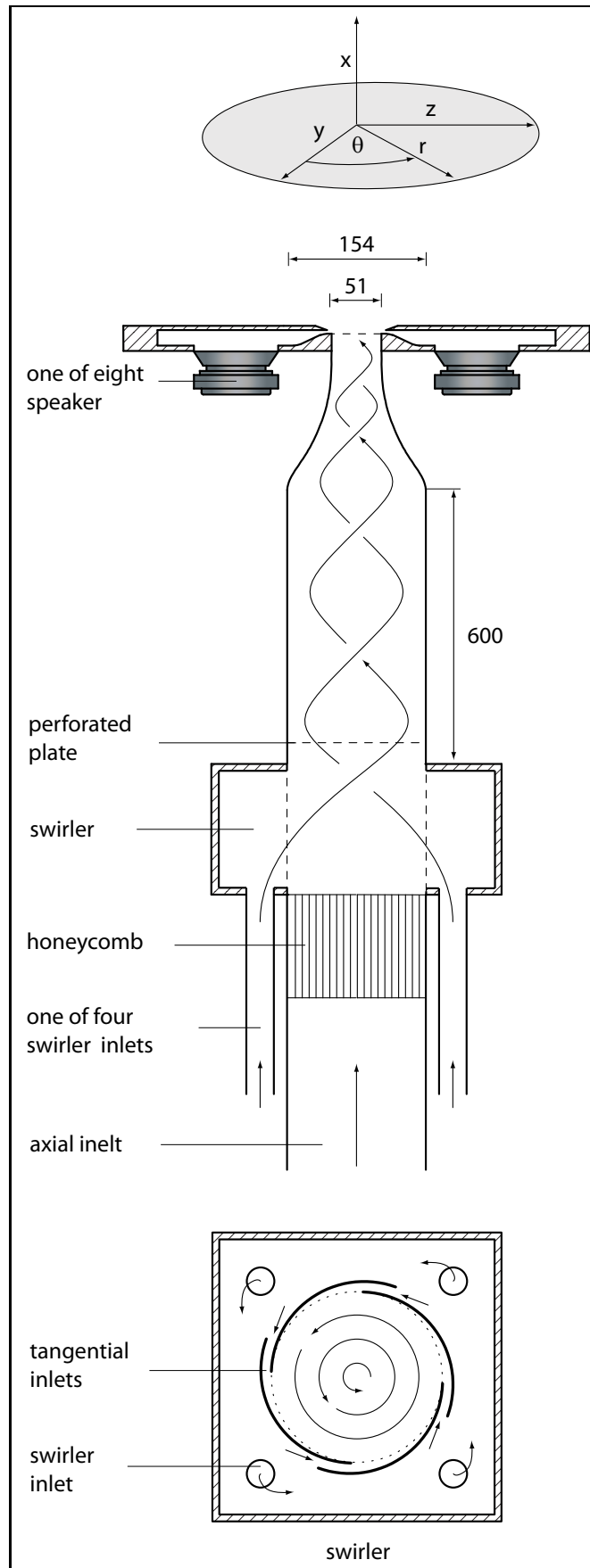


Figure 3.2: Sketch of the swirling jet air facility (all lengths are expressed in mm)

voltage A_{spk} . Details about the design of the actuators and their calibration are given in appendix B.

3.3 Stereo-PIV Measurements

Stereoscopic particle image velocitometry (Stereo-PIV) was used to measure the flow field. It consists of velocity measurements of particles going through a laser sheet generated by a double-pulsed Nd:Yag laser at 532 nm. Two CCD cameras were positioned at a 45° angle in order to measure all three velocity components in a 2D plane. The cameras observed the light sheet in a Scheimpflug configuration, each inclined at 45° to the light sheet plane. For calibration, the cameras were focused on a target that was placed in the measurement domain and aligned with the laser light-sheet. Datum marks were automatically mapped on the picture of the target by the PIV evaluation software to define the physical length scale of the images. A multigrid evaluation strategy was used (64x64, 32x32 interrogation size at 50 % overlap) including window deformation, Whittaker peak fitting, and B-Spline reconstruction. Errors due to misalignment of the laser sheet were minimized by the corrected mapping functions. Therefore, the datum marks for the initial calibration were back-projected onto the actual light sheet plane via linear triangulation using the pinhole model.

3.3.1 Measurements in Water

The system consisted of two X-STREAM VISION CCD cameras with a resolution of 1024×1020 pixels, a 40 mJ flash lamp pumped Nd:YAG laser, an articulated arm, standard light sheet forming optics, a synchronization and timing unit to control the laser and camera timing, and a commercial PIV evaluation software (INTELLIGENT LASER APPLICATIONS GmbH). To minimize optical distortion and to avoid total reflexion at the air–water interface, the water tank was equipped with water-filled prisms on both sides. The light sheet entered from the bottom into the tank.

The pump operated continuously to mix the flow and to provide a constant temperature in the entire tank. 20 minutes before acquiring data, the tank was stirred manually to obtain homogeneous seeding. Data were taken in the x - r -plane (streamwise plane) for $0.3 < x/D < 3$ and $r/D \leq 1.1$ and in the r - θ -plane (crosswise plane) at $x/D = 1.1$ for $r/D \leq 1.1$. Each ensemble of PIV snapshots consists of 400 events captured at approximately 3 Hz. The oscillation frequencies of the dominant coherent structures in water at the considered Reynolds number were orders of magnitude below the acquisition frequency and, hence, the measurement can be considered as time-resolved.

3.3.2 Measurements in Air

The first measurement campaign at the air facility was conducted with a double-pulsed Nd:Yag laser at 532 nm and 25 mJ in 5 ns burst. Two CCD cameras with a resolution of 1.3 million pixels were used. The cameras and the laser were mounted onto a single traversing system. Data were taken in the crossflow plane as well as in the axial plane. Each ensemble of PIV snapshots consists of 800 events captured at approximately 3 Hz. The results of that measurement campaign are presented in chapter 6.

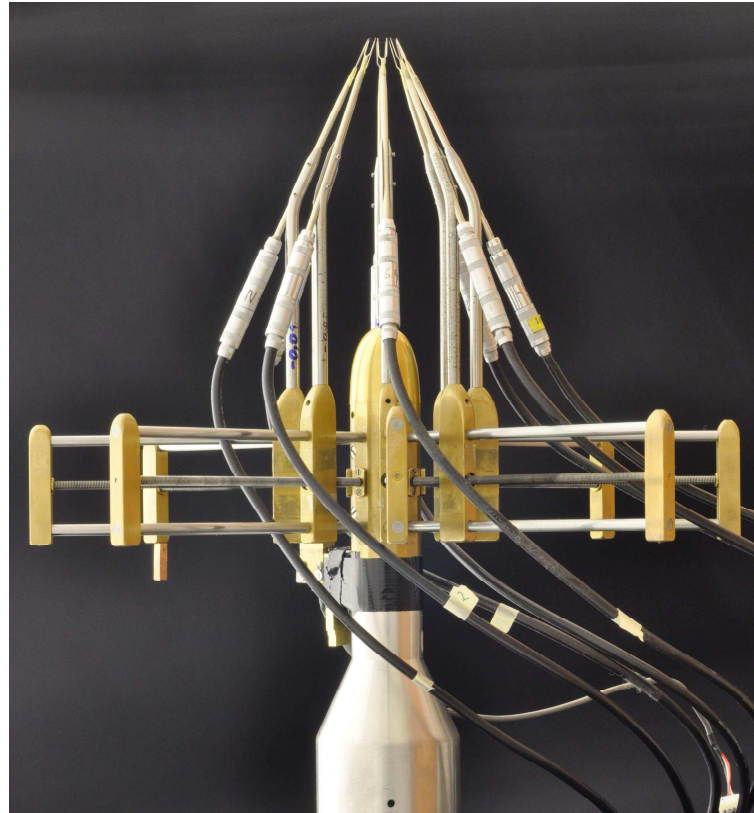


Figure 3.3: Hot-wire traversing system

During the PhD work, a new PIV system was purchased. It consists of a double pulsed Nd:Yag laser at 532 nm and 160 mJ and two CCD cameras with a resolution of 2048×2048 pixels. The PIV data presented in the chapters 5 and 7 were acquired using the new system. Both cameras were positioned at a 45° angle in back-scattering mode in order to measure all three velocity components in the x - r -plane. Each ensemble of PIV snapshots consists of 900 events captured at approximately 6 Hz. The camera view angle allows to obtain data even inside the nozzle which is necessary to have reliable data at $x/D = 0$.

3.4 Hot-wire Measurements in the Moderately Swirling Jet

In order to capture the downstream traveling instability waves in the moderately swirling jet, time-resolved volumetric measurements were conducted using eight hot-wire probes simultaneously (chapter 5). A unique traversing mechanism was used that allows to simultaneously move all hot-wires in radial and axial direction (figure 3.3). The hot-wire anemometers, which were built locally, were used in conjunction with a A.A.LAB SYSTEM LTD anemometer system. The hot-wires, made of tungsten, were 5 μm in diameter. They were kept at a constant overheat ratio of 1.6 and had a maximum frequency response of 50 kHz. An analog low-pass filter with a cut-off frequency of 6.2 kHz was used to condition the measured signals prior to the AD-converter. All channels were sampled simultaneously at 20 kHz, giving a maximum frequency response (Nyquist frequency) of 10 kHz.

In order to retain the phase information of the forced experiments, the excitation signal was recorded together with the signal from the hot-wire anemometer. In case of sinusoidal forcing, the typical length of a velocity record used for averaging was equivalent to 1500 periods of the excitation frequency. In case of pulsed experiments, the record length is equivalent to 600 pulses which are generated at 10 Hz.

The probes were distributed circumferentially around the jet center, with the wires being parallel to the tangential velocity. This enabled to measuring the axial velocity with a high spatial accuracy in radial direction. The hot-wires were calibrated in the exit plane of the jet at no-swirl conditions against a standard Pitot tube at seven different velocities. Particular attention was paid to the radial adjustment of the hot-wire probes. This was done in no-swirl conditions by placing each of the eight hot-wires at the center of the shear layer, where the mean velocity is reduced to one-half of the centerline value. After completing the fine alignment of the probes, all wires were traversed simultaneously in the radial and axial direction. Details to the experimental procedure are given in the work of Kuhn (2010).

3.4.1 Coherent Velocity Extraction of the Excited Flow

The time resolved axial velocity component $v_x(\mathbf{x}, t)$ of the jet being excited at sinusoidal perturbations derived from hot-wire measurements, is decomposed into the three parts of the triple decomposition, yielding

$$v_x(\mathbf{x}, t) = V_x(\mathbf{x}) + v_x^c(\mathbf{x}, t) + v_x^s(\mathbf{x}, t). \quad (3.1)$$

The coherent velocity which is periodic in t and θ is decomposed into a Fourier series with coefficients

$$\hat{v}_x(x, r, m, n) = \frac{1}{2\pi T} \int_0^{2\pi} \int_0^T v_x^c(x, r, \theta, t) e^{i(m\theta - 2\pi nt/T)} d\phi dt. \quad (3.2)$$

The coefficients \hat{v}_x are complex, and m and n correspond to the azimuthal wavenumber and the time harmonic, respectively. Throughout this investigation, we neglect higher harmonics of the excited waves and set $n = 1$. The amplitude of the forced mode at a given axial location x is then derived by integrating the radial amplitude distribution across the axial shear layer (Delbende et al. 1998), yielding

$$A_m(x) = \left(\int_{R_{.05}}^{R_{.95}} |\hat{v}_x|^2 r dr \right)^{1/2}. \quad (3.3)$$

The radial phase distribution of the forced mode is

$$\varphi_m(x, r) = \arg(\hat{v}_x). \quad (3.4)$$

3.4.2 Ensemble Average of the Pulsed Experiments

The pulsed experiments were conducted in order to measure the impulse response in the shear layer of the moderately swirling jet (chapter 5). The pulse was generated by a single speaker at the nozzle exit. Its downstream development was captured via hot-wire measurements. In order to reduce noise caused by turbulent fluctuations, the pulsed experiments were repeated 600 times and were ensemble-averaged. A detailed description of this method is

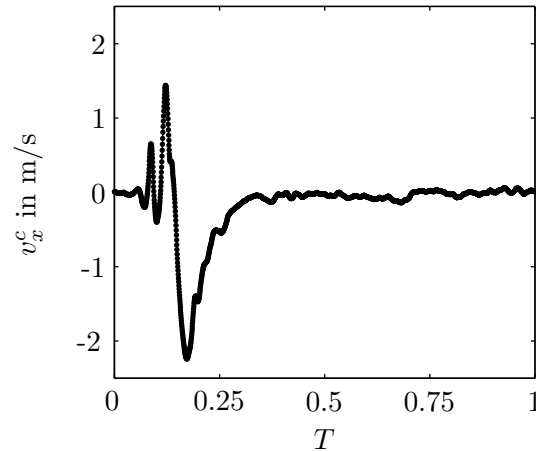


Figure 3.4: Hot-wire signal of a traveling wave packet in the swirling jet ($x/D = 0.27$; $r/D = 0.47$; $\theta = \pi/4$)

given in [Gaster & Grant \(1975\)](#). The method was further finalized to reduce the ambiguity in the mean quantities due to jitter in the arrival time and location. These irregularities, which are induced by random turbulent motion of the base flow, may blur the actual shape of the wave packet. Therefore, the signal of each individual recorded wave packet, which is a function of θ and t , was cross-correlating with the ensemble-averaged signal. The correlation peak provides an estimate of the t - and θ -displacement of each pulse in respect to the mean values. The displacement was then compensated for each pulse and the ensemble average was redone. This procedure was repeated iteratively until convergence was achieved. For a detailed description of this method, the reader is referred to [Zhou et al. \(1996\)](#) and references therein. An example of the resulting phase-averaged signal of a wave packet passing a hot-wire is shown [figure 3.4](#).

Chapter 4

The Onset of Vortex Breakdown and Global Instability

The investigation described in this section is aimed to provide quantitative insights into the onset of vortex breakdown and the bifurcation to a global spiral mode. Several flow features that accompany vortex breakdown are combined to one consistent picture, starting from a weakly swirling jet and ending with a strongly swirling jet. The different flow states that evolve at incrementally increasing swirl are characterized by means of time-resolved stereo PIV measurements in conjunction with post-processing tools, including Fourier analysis and proper orthogonal decomposition. The experiment presented in this section is properly scaled by the swirl number based on the axial momentum flux when omitting the commonly used boundary layer approximations. Vortex breakdown occurs first intermittently, accompanied by strong axial oscillations. By further increasing the swirl, vortex breakdown stabilizes and a region of reversed flow appears in the mean flow. This region grows linearly with increasing swirl until the flow undergoes a supercritical Hopf bifurcation to a global single-helical mode and vortex breakdown becomes spiral shaped. The appearance of an internal stagnation point is accompanied by a supercritical-to-subcritical transition of the inflow profiles, in accordance to Benjamin's inviscid theory (Benjamin 1962). This critical swirl number is found to be smaller than the one for the supercritical Hopf bifurcation. The observed mean flow sequence compares well with the transient formation of spiral vortex breakdown in laminar swirling jets as reported by Bruecker & Althaus (1995), Liang & Maxworthy (2005), and Ruith et al. (2003).

4.1 Literature Review

Free and confined strongly swirling jets are of great interest due to their unique feature, commonly known as vortex breakdown. This phenomenon occurs when the ratio of the azimuthal to axial momentum exceeds a certain threshold, while both quantities have to be of the same order of magnitude. Breakdown in swirling jets is characterized by a transition of a jet-like axial velocity profile to a wake-like profile with a local minimum on the axis.

This leads to a stagnation point to be followed by a highly turbulent region of reverse flow farther downstream. It can play a crucial role – from desired to detrimental – in a variety of technical applications. For example, vortex breakdown stabilizes the flame of a gas turbine combustor and enhances mixing, thus leading to a reduction of NO_x emissions (Huang & Yang 2009). On the other hand, bursting of leading-edge vortices adversely affects the lift distribution on delta wings resulting in poor flight performance. Understanding the cause of the vortex breakdown is therefore of great importance in order to develop appropriate control strategies. Furthermore, the transition of the flow from jet-like to wake-like that generates coexisting inner and outer shear layers and the concomitant axial and azimuthal shear makes this flow complex and highly three-dimensional, and thus, poses a formidable challenge to fundamental studies. A detailed introduction to the fundamental physics of vortex breakdown is given, for example, by Hall (1972), Leibovich (1978, 1984), Escudier & Keller (1985), and Lucca-Negro & O’Doherty (2001).

Several types of vortex breakdown have experimentally been observed. Lambourne & Bryer (1962) were the first to describe the axisymmetric and spiral type of vortex breakdown. Swirling jet experiments in pipes conducted by Sarpkaya (1971) and Faler & Leibovich (1978) identified three different types of vortex breakdown, namely the single-helical, the double-helical, and the bubble-shaped vortex breakdown. Billant et al. (1998), investigating a swirling jet at a low Reynolds number, observed an additional conical-shaped breakdown type.

Several theories have been proposed to explain the vortex breakdown phenomenon. They can be roughly divided into three categories: The first associates vortex breakdown with a critical state related to wave phenomena. The basic ideas were developed by Benjamin (1962) for a steady inviscid axisymmetric vortex. The abruptness of vortex breakdown is described by a downstream transition from a supercritical to a subcritical flow, analog to a hydraulic jump. The supercritical flow supports only downstream traveling waves, whereas the subcritical flow supports both downstream and upstream traveling waves. The second concept considers vortex breakdown that is analogous to a boundary layer separation (Hall 1972) and the third idea suggests that vortex breakdown is a consequence of hydrodynamic instability (Lessen et al. 1974; Ludwig 1961).

However, experiments conducted by Escudier & Keller (1985) and Liang & Maxworthy (2005) and direct numerical simulations conducted by Ruith et al. (2003) indicate a clear separation of flow criticality and flow instability. It was proposed that the criticality of the flow determines the basic, wake-like character of the flow and that instability waves are a superimposed fine detail. Recent quantitative investigations could significantly contribute to the understanding of the dynamics accompanying the onset of vortex breakdown. Time-resolved measurements conducted by Liang & Maxworthy (2005) indicate that a recirculation bubble with nearly axisymmetric shape accompanies the first appearance of a stagnation point. It was further noticed that in the wake of this dividing streamline a single-helical vortex arises near the jet center that amplifies until it imposes its frequency onto the entire nearfield. The authors suggest this to be a self-excited/globally unstable mode, supposedly arising from a region of local absolute instability in the lee (downstream) of vortex breakdown. Forced experiments using vortex generators mounted on a rotating nozzle support the absolute/convective nature of the dominating instabilities. Gallaire et al. (2006) performed a linear stability analysis based on numerical simulations of a swirling

jet at $Re = 200$ that were conducted by [Ruith et al. \(2003\)](#). They found a convective to absolute instability transition in the lee of the recirculation-bubble with a single-helical mode being most unstable. Thus, it is likely that the precessing of the vortex core and the appearance of strong oscillations that have been observed in experiments and simulations ([Duwig & Fuchs 2007](#); [Liang & Maxworthy 2005](#); [Martinelli et al. 2007](#); [Ruith et al. 2003](#)) can be attributed to a self-excited global mode initiated by flow instabilities in the region of vortex breakdown.

4.2 Objective and Approach

The investigation presented in this chapter provides an overview of the different flow states at increasing swirl that ultimately leads to the formation of a spiral vortex breakdown. The experiments were conducted with the swirling jet water facility of the University of Arizona. Details to the experimental setup and procedure are given in section 3.1.

This study is closely related to the experimental work of [Liang & Maxworthy \(2005\)](#) who study a laminar swirling jet with particular interest on the onset of global instability. Due to the absence of a contraction, their facility generates a swirling jet that differs considerably from the one presented here. A more similar – but also laminar – flow configuration was investigated experimentally by [Billant et al. \(1998\)](#) and [Loiseleux & Chomaz \(2003\)](#) and theoretically by [Gallaire & Chomaz \(2003\)](#). All authors provide valuable insight into the instabilities dominating laminar swirling jets with particular interest in the formation of a global mode. The present experiments supplement their work by investigating vortex breakdown in a turbulent base flow at precisely controlled conditions.

The flow is investigated at a swirl intensity that is successively increased at very small increments. At each swirl configuration, PIV measurements are conducted to reveal the onset of vortex breakdown, the bifurcation to a globally unstable flow, and the formation of a spiral vortex breakdown. Since the flow is turbulent, a quantitative description of the fluctuating flow field is only possible by employing statistical means as time- or phase-averaging and proper orthogonal decomposition (POD). The PIV measurements were partially carried out by Roman Seele during his Master thesis work that he conducted at the University of Arizona ([Seele 2008](#)). His contribution to this work shall be greatly acknowledged here.

The description of the investigation is organized as follows. First, an overview of the flow configurations considered throughout this chapter is given in section 4.3. A discussion of the used swirl number definition is presented in section 4.4. The onset of vortex breakdown and its associated flow field is quantitatively described in section 4.5 and its relation to the flow criticality is discussed in section 4.6. In section 4.7 the dominant coherent structures in the shear layers are quantified for various swirl numbers. Thereby, particular attention is paid to swirl numbers beyond the onset of breakdown where self-excited oscillations dominate the flow dynamics. In section 4.8 the main observations are summarized and conclusions are drawn. The reader is also referred to the appendices [A.1](#) and [A.2](#), which provide additional information about the mean and fluctuating flow field.

4.3 The Mean Flow Configuration

All PIV measurements presented throughout this chapter are conducted at a Reynolds number of

$$\text{Re}_D = \frac{VD}{\nu} = 3300, \quad (4.1)$$

based on the nozzle diameter and the bulk velocity. The latter is defined as the time-averaged axial velocity in the potential core of the non-swirling jet. It is derived from PIV measurements with a non-rotating honeycomb.

To give an overview of the investigated flow configurations, streamlines are computed from the axial and transverse mean velocity components in the x - r -plane and shown in figure 4.1. The displayed swirl configurations cover the different flow regimes that are observed while successively increasing the rotation rate of the honeycomb. The corresponding swirl numbers are given in the caption of figure 4.1 and are defined in the next section.

At a rotation rate of $\Omega = 1.5 \text{ min}^{-1}$, the streamlines in the core of the jet are approximately parallel ($r/D < 0.5$ at $x/D < 3$). Entrainment of the steady ambient fluid is indicated by the nearly vertical streamlines outside the jet (e.g. $r/D > 0.7$ at $x/D = 0.5$). At $\Omega = 4.0 \text{ min}^{-1}$, the streamlines indicate a strong widening of the jet downstream of $x/D = 0.7$. It will be shown later that this flow configuration exhibits reversed flow on the jet axis at some instances in time that is not detectable from the time-averaged flow. Therefore, it is still considered as a pre-breakdown state. At $\Omega = 4.2 \text{ min}^{-1}$, two stagnation points are visible with a region of reversed flow in between them. Its approximate axial extent is $1.3 < x/D < 1.6$ with its maximum diameter being $0.3D$. This region appears to be similar to the recirculation bubble that can often be observed in swirling pipe flows (Escudier & Keller 1985; Faler & Leibovich 1978; Leibovich 1978). However, in the present case the streamlines do not converge towards the jet axis and contours of the azimuthal vorticity do not suggest a closed recirculation bubble (shown later).

To emphasize this difference, the phrase 'region' instead of 'bubble' is used throughout this investigation. A further increase of the revolution speed to $\Omega = 4.4 \text{ min}^{-1}$ causes a drastic change of location and size of the recirculation region. It moves upstream and grows in size, having an axial extent of $0.7 < x/D < 1.6$ and a maximum diameter of $0.7D$. When the amount of swirl is increased to $\Omega = 5.4 \text{ min}^{-1}$, the recirculation region moves closer to the nozzle, but its size remains approximately the same. At the highest rotation rate, the recirculation region has moved close to the nozzle and its size has decreased. This behavior is attributed to the influence of the nozzle walls on the development of the jet near the orifice. For very high swirl, the recirculation region is literally "swallowed" by the nozzle. The streamlines indicate that this also reduces the spreading rate of the jet. These confinement effects can already be observed at $\Omega = 5.4 \text{ min}^{-1}$ but in a less pronounced way.

One may, therefore, qualitatively divide the presented data into three regimes, the first describing the *pre-breakdown state* with $\Omega < 4.2 \text{ min}^{-1}$, the second characterizing the *breakdown state* with $4.2 \text{ min}^{-1} \leq \Omega < 5.4 \text{ min}^{-1}$, and the third describing the *confined breakdown state* being influenced by the nozzle orifice with $\Omega \geq 5.4 \text{ min}^{-1}$.

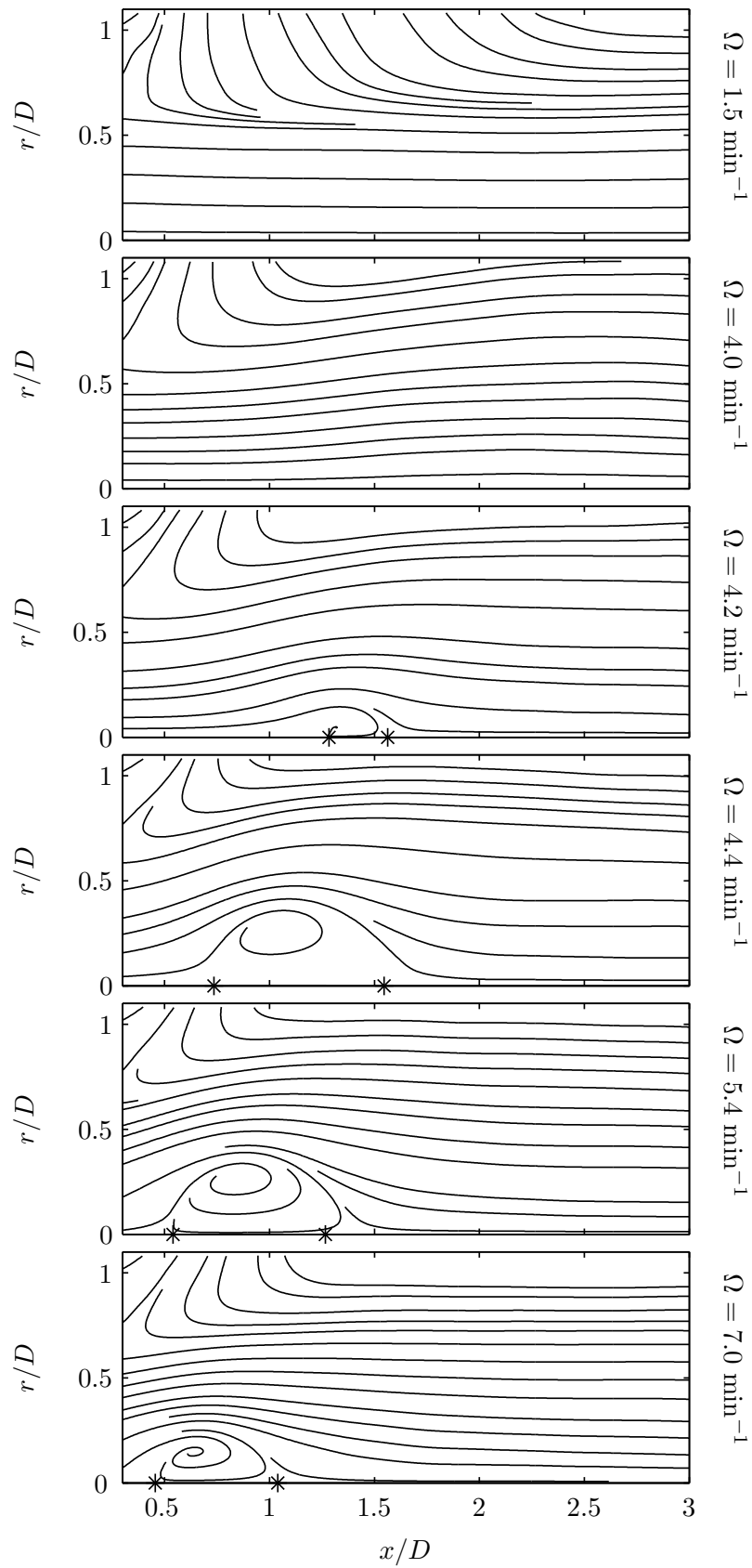


Figure 4.1: Streamlines in the $x-r$ -plane for different rotation rates of the honeycomb Ω . From top to bottom, the corresponding swirl numbers are $S = (0.38, 1.01, 1.07, 1.12, 1.37, 1.78)$. Black stars mark stagnation points on the jet axis.

4.4 Momentum Balance and Swirl Number Discussion

In this section an attempt is made to define a swirl number that consistently scales the flow for all configurations considered. Several swirl number definitions exist in the literature, each being applicable to a certain flow regime but none being universal. Their definitions are typically based on either velocity or momentum ratios. The former are conveniently derived from single point measurements, but they strongly depend on the axial location at which they are derived. It seems more appropriate to use the swirl number definition that is based on the ratio of axial flux of azimuthal momentum \dot{G}_θ to axial flux of axial momentum \dot{G}_x , yielding

$$S = \frac{\dot{G}_\theta}{D/2\dot{G}_x}, \quad (4.2)$$

as this quantity is conserved in axial direction. The calculation of the axial momentum flux based on the full equations of motion demands very accurate data at decent spatial resolution. Simplifications that include boundary layer approximations and the negligence of the turbulent stresses are typically introduced. These stipulations are valid for non-swirling and moderately swirling jets and for the farfield of strongly swirling jets (Chigier & Chervinsky 1965, 1967; Pratte & Keffer 1972; Semaan et al. 2009). However, the nearfield of strongly swirling jets is highly divergent and the validity of boundary layer approximations is questionable. The swirl number is therefore suggested to be based on the full equations of motion. According to Rajaratnam (1976), the equations for the axial flux of axial and angular momentum of an inviscid, incompressible and axisymmetric swirling jet can then be written as

$$\dot{G}_\theta = 2\pi\rho \int_0^\infty \left(\underbrace{V_x V_\theta}_I + \underbrace{\overline{v'_x v'_\theta}}_II \right) r^2 dr \quad (4.3)$$

$$\dot{G}_x = 2\pi\rho \int_0^\infty \left[\left(\underbrace{V_x^2 - \frac{V_\theta^2}{2}}_III + \underbrace{\overline{v_x'^2} - \frac{\overline{v_r'^2} + \overline{v_\theta'^2}}{2}}_IV \right) r + \left(\underbrace{V_x \frac{\partial V_r}{\partial x} + V_r \frac{\partial V_r}{\partial r}}_V + \underbrace{\frac{\partial \overline{v'_x v'_r}}{\partial x}}_VI \right) \frac{r^2}{2} \right] dr. \quad (4.4)$$

The expressions are grouped to six terms marked by Roman numerals. (Chigier & Beer 1964), who introduced the most simplified swirl number definition, assume that $\overline{v_x'^2} \approx \overline{v_r'^2} \approx \overline{v_\theta'^2}$, resulting in term IV to vanish. They further neglect the terms containing the radial velocity component (term V) and turbulent shear stresses (terms II and VI) and arrive at the most commonly used definition for the axial flux of momenta

$$\dot{G}_\theta = 2\pi\rho \int_0^\infty V_x V_\theta r^2 dr. \quad (4.5)$$

$$\dot{G}_x = 2\pi\rho \int_0^\infty \left(V_x^2 - \frac{V_\theta^2}{2} \right) r dr. \quad (4.6)$$

The validity of these stipulations is investigated in detail for $\Omega = 4.4 \text{ min}^{-1}$ (figure 4.2). The streamwise distribution of \dot{G}_x and \dot{G}_θ are derived from equations (4.3-4.4) for each term marked by a Roman numeral (figure 4.2a-b). The comparison reveals that the terms II, IV, and V contribute significantly to the axial momentum flux within the region of

vortex breakdown and should therefore not be neglected. In particular \dot{G}_x based on term V reaches considerable high magnitude, which is attributed to the considerably high radial component due to the jet divergence (see also appendix A.1). The turbulent shear stress $\overline{v'_x v'_\theta}$, represented by term II, increases around the upstream end of the recirculation zone and approximately balances the decaying term I upstream of $x/D = 1$. However, the turbulent shear stress $\overline{v'_x v'_\theta}$ and corresponding term VI is nearly zero within the measurement domain. Hence, all terms except for VI contribute to the momentum balance and need to be considered within the region of vortex breakdown. The swirl number based on these terms (I, II, III, IV, and V) remains approximately constant within $0.3 < x/D = 1.1$ (figure 4.2c). Further downstream, the determination of the swirl number becomes erroneous because the jet exceeds the measurement domain. The simplified swirl number based on the terms I and III varies significantly in streamwise direction within $0.3 < x/D = 1.1$, revealing the invalidity of the boundary approximations. It is likely that the two swirl numbers are equal at the nozzle exit where the flow is parallel and the boundary approximations hold (confer with Toh et al. (2010)).

Hence, for the present investigation the swirl number is used that is based on the terms I, II, III, IV, and V averaged within $0.3 < x/D < 1.1$ as the characteristic swirl number. From here on, this quantity will be referred to as S . Figure 4.3 displays how S is related to the rotation rate of the honeycomb, revealing an approximate linear increase of S for $\Omega \leq 4.8 \text{ min}^{-1}$. For the confined breakdown state ($\Omega \geq 5.4 \text{ min}^{-1}$) the values decrease and increase again. This somewhat implausible behavior for the two highest swirl configurations is caused by the confinement of the flow. The calculations of the axial momentum is erroneous as pressure forces induced by the nozzle walls are not incorporated. The swirl number that represents the present experiment best is, therefore, derived from a linear fit of S neglecting these two highest values (see dashed line in figure 4.3). The fitted values are expressed by $S = \Omega 0.25 \text{ min}$ and will be used throughout this investigation.

To conclude, one may state that the calculation of the swirl number based on momentum conservation is very delicate within the region of vortex breakdown. The terms containing the radial velocity component and its gradients as well as the turbulent normal and shear stresses, particularly $\overline{v'_x v'_\theta}$, need to be taken into account. The conservation of axial momentum flux within the entire measurement domain can be seen as a challenging benchmark to validate the consistency and quality of the acquired data. However, it should be noted that the invalidity of the boundary approximations for the strongly swirling jet could probably overcome by using spherical coordinates.

4.5 Onset of Vortex Breakdown

This section contains a quantitative investigation of the mean and instantaneous flow field at swirl numbers around the onset of vortex breakdown. Thereby, vortex breakdown is strictly associated with a stagnation point on the jet axis. Thus, breakdown can be tagged from the time-averaged or from the instantaneous flow field. The latter is evaluated by statistical methods and its results are linked to the observed mean flow pattern.

Considering the mean flow at swirl numbers below breakdown, flow stagnation is observed to be foreshadowed by the formation of a local minimum of the axial velocity on the jet axis. Hence, vortex breakdown (in the mean flow) occurs when the minimum local axial

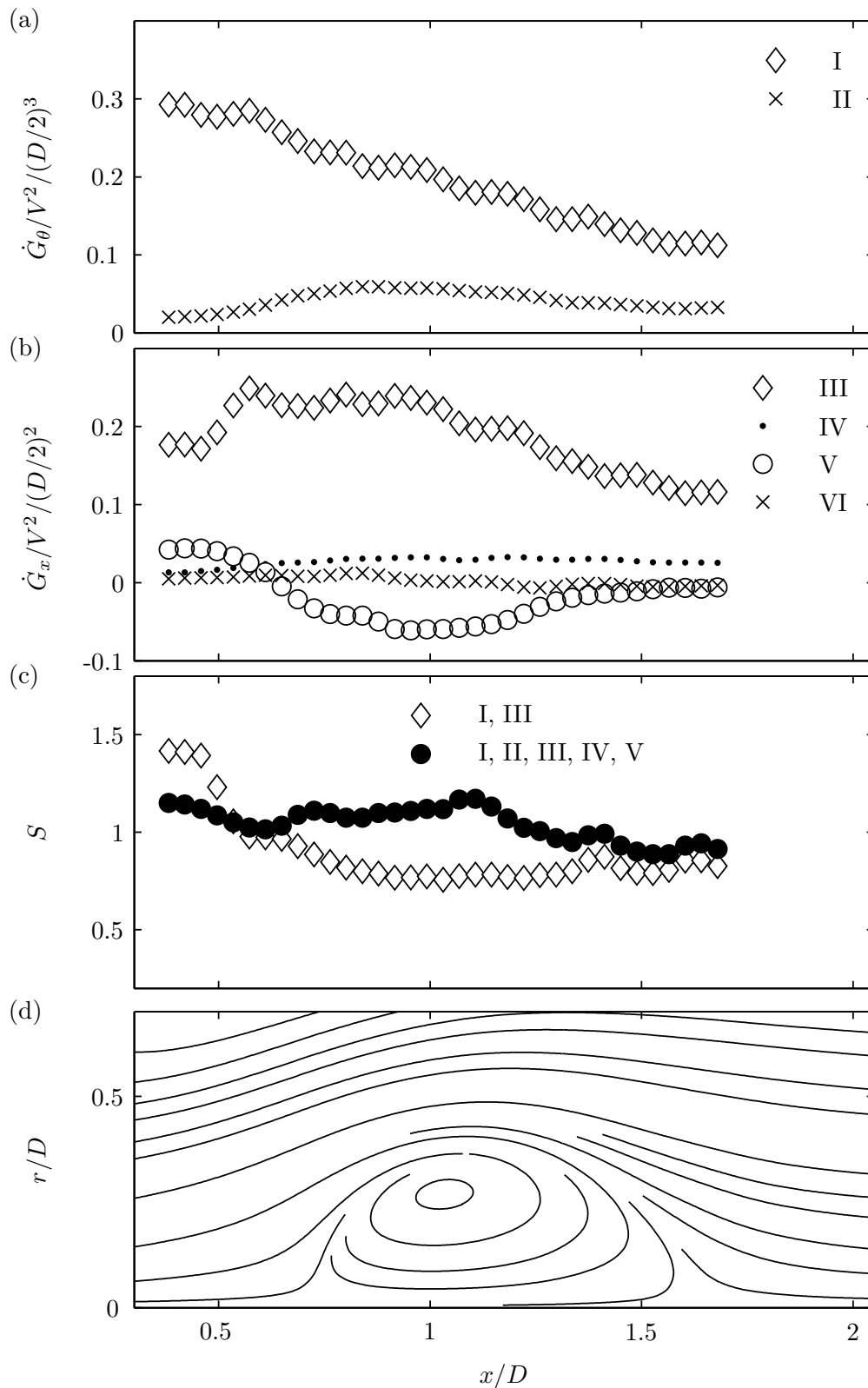


Figure 4.2: Streamwise distribution of axial flux of azimuthal (a) and axial (b) momentum and the swirl number (c). The Roman letters refer to the terms of equations (4.3-4.4) that are used to calculate the respective quantities. The streamlines visualize the corresponding flow configuration ($\Omega = 4.4 \text{ min}^{-1}$, $S = 1.12$).

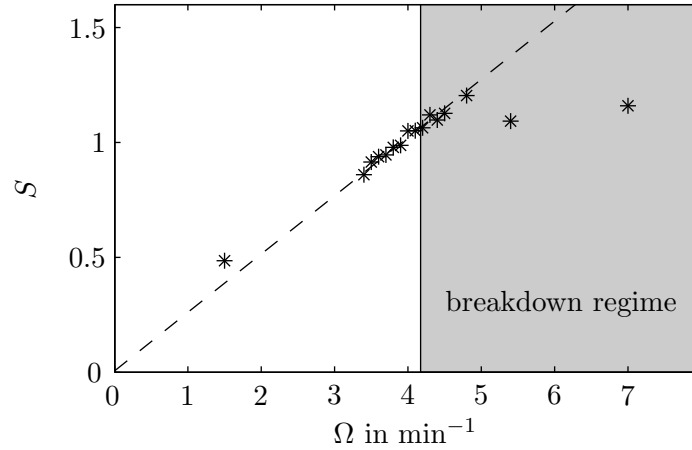


Figure 4.3: Development of the swirl number S with rotation rate Ω of the honeycomb; black stars refer to measurements averaged within $0.3 \leq x/D \leq 1.1$. Dashed line represents linear fit expressed by $S = \Omega \cdot 0.25 \text{min}$

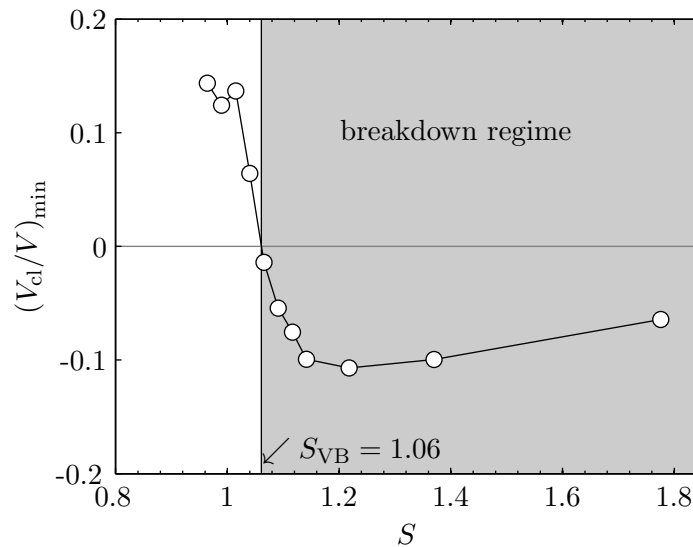


Figure 4.4: Decay of axial velocity at a local minimum on the jet axis with increasing swirl; for $S \geq S_{VB}$ a stagnation point exists on the jet axis.

velocity is equal to or smaller than zero. This quantity is plotted versus the swirl number in figure 4.4. The root of the curve defines the lowest swirl number $S_{VB} = 1.06$ at which vortex breakdown occurs. It separates the pre-breakdown regime from the breakdown regime. For $S < 0.96$ no minimum is found as the axial velocity decreases monotonically in axial direction. For swirl numbers near S_{VB} , the minimum decreases approximately linearly with increasing swirl number ($0.99 \geq S \geq 1.16$). For higher swirl, the minimum levels off at approximately $(V_{cl}/V)_{min} = -0.1$ and gently increases for $S \geq 1.37$.

The axial location of that minimum is drawn in figure 4.5 (black stars). For swirl numbers below S_{VB} the local minimum figure at $x/D \approx 2.24$. Exceeding S_{VB} causes the minimum to jump abruptly upstream to $x/D = 1.42$. In the breakdown regime, the minimum successively propagates upstream with increasing swirl indicating an upstream movement of the recirculation region that is slowed down at the proximity to the nozzle exit. The location of the upstream stagnation point follows the same trend (white circles

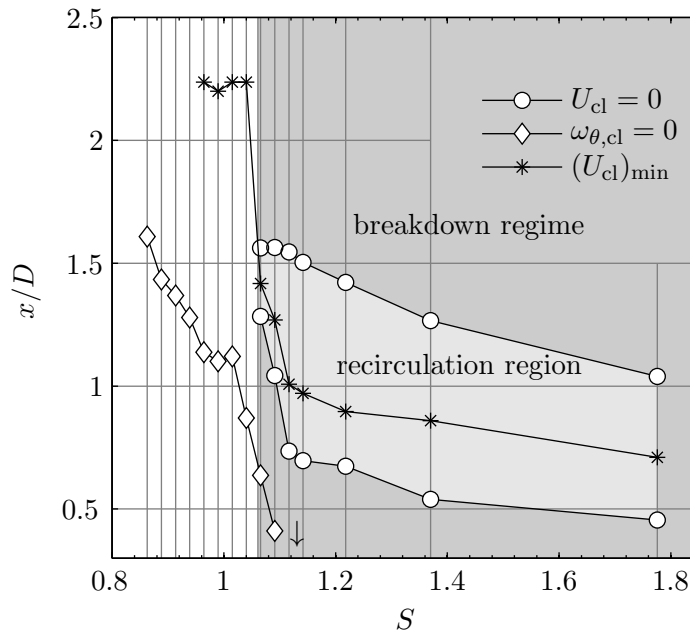


Figure 4.5: Axial locations of the local minimum of axial velocity, the stagnation points, and the root of azimuthal vorticity along the jet centerline with increasing swirl.

in figure 4.5). Its distance from the nozzle exit decreases even more rapidly with increasing swirl for $S_{VB} < S \leq 1.11$ than the local minimum does. The downstream stagnation point only moves marginally in that range of swirl, which results in a rapid growth of the recirculation region with increasing swirl. It reaches its maximum axial extent at $S \approx 1.11$. For higher swirl, it is shifted further upstream and shrinks for $S \geq 1.37$ due to confinement effects.

Another characteristic of vortex breakdown is the existence of a change of sign in the azimuthal vorticity ω_θ near the jet axis (e.g., see Akilli et al. 2003; Brown & Lopez 1990; Gallaire et al. 2004). In principal, this change of sign is caused by a transition of the axial velocity profile from jet-like to wake-like. Certainly, this criterion is weaker than the criterion of a stagnation point, but it is nevertheless a useful indicator for the precursor to vortex breakdown. Contours of the axial and azimuthal vorticity component are displayed in figure 4.6 for increased swirl numbers. For moderate swirl, azimuthal vorticity is concentrated in the outer part of the jet. For $S \geq 0.86$ a pocket of negative azimuthal vorticity appears in the jet core that increases in size and intensity while moving upstream with increased swirl. Its leading edge comes closer to the nozzle exit and presumably reaches it at $S > 1.12$. The present experiment does not provide information about the downstream end of the negative ω_θ pocket. It may end due to turbulent diffusion, although the $\omega_\theta = 0$ curve seems to be open toward the downstream end of the measurement domain.

The point where the azimuthal vorticity changes its sign near the jet axis is included in figure 4.5 and is marked by white diamonds. It is detectable for swirl numbers $S \geq 0.86$, which is far below the onset of vortex breakdown. Except for a small plateau near $S = 1$, the point of vorticity transition moves continuously upstream with increasing swirl. Around S_{VB} a linear relation of this movement is evident. For values beyond $S = 1.09$ the point of ω_θ reversal has moved out of the measurement domain and possibly into the nozzle (indicated by the black arrow).

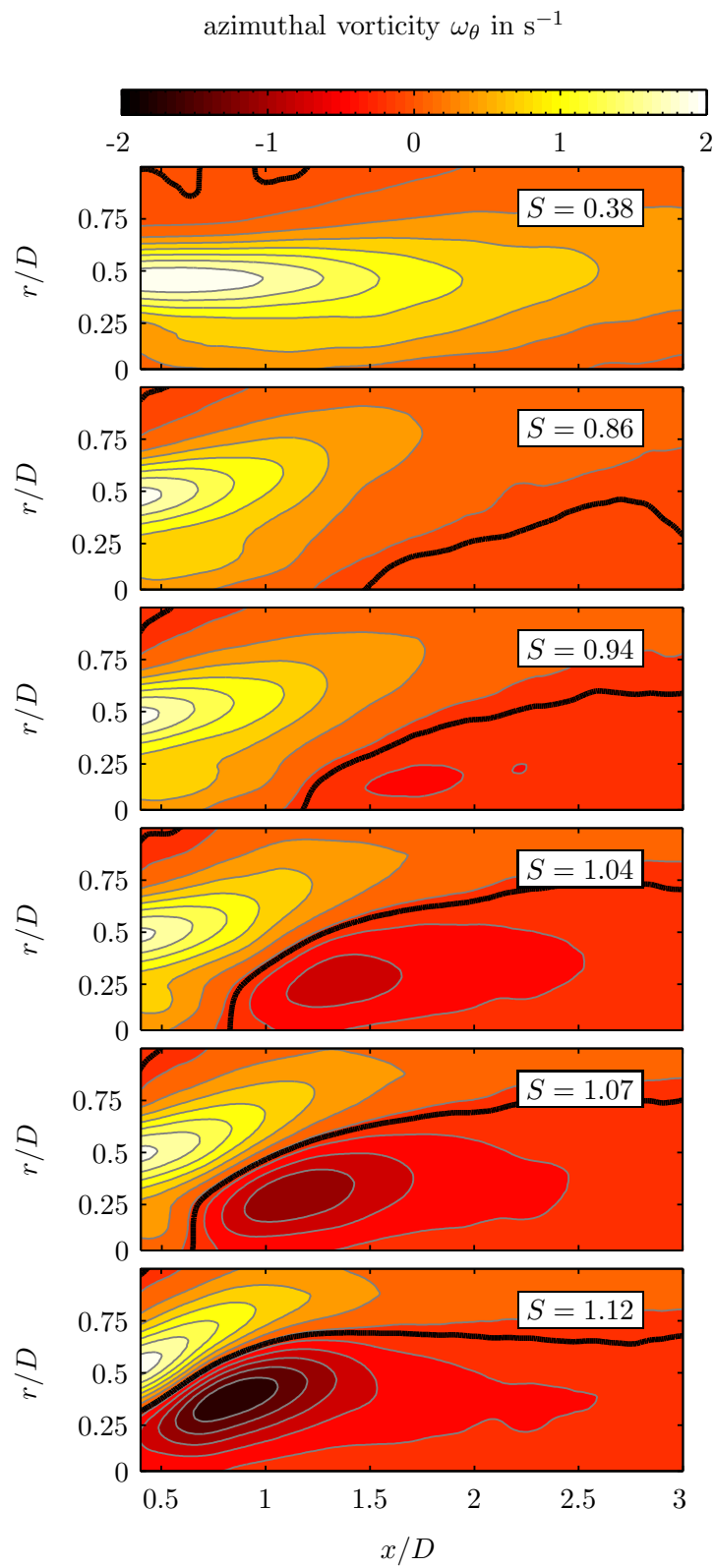


Figure 4.6: Azimuthal vorticity contours at increasing swirl; the black thick line marks $\omega_\theta = 0$

The smooth upstream progression of the position where the azimuthal vorticity component changes its sign indicates that there must be a mechanism for vortex breakdown that develops progressively with increasing swirl at swirl numbers that are considerably lower than S_{VB} . On the other hand, the rapid decrease in the distance where the axial velocity component has its minimum and the rapid decrease in the value of this minimum magnitude when S_{VB} is exceeded suggests an abrupt appearance of vortex breakdown.

In order to clarify this contradiction, the onset of vortex breakdown is determined from the instantaneous velocity field. The analysis of the time-resolved velocity field demands for additional statistical quantities that are defined as following: The probability P of a random continuous variable $v(t)$ to take a value in the interval $[v_1, v_2]$ is commonly defined as

$$P[v_1 \leq v \leq v_2] = \int_{v_1}^{v_2} \text{PDF}[v]dv,$$

with $\text{PDF}[v]$ being the probability density function of $v(t)$. The PDF is non-negative everywhere, and the probability of $v(t)$ to take an arbitrary value can be lower than one, yielding

$$1 \geq \int_{-\infty}^{\infty} \text{PDF}[v]dv.$$

By considering the instantaneous axial velocity component $v_x(\mathbf{x}, t, S)$, which depends parametrically on S , as the random variable, the corresponding probability density function $\text{PDF}[v_x](\mathbf{x}, S)$ becomes parametrically dependent on the position vector \mathbf{x} and the swirl number. However, for axisymmetric jets, vortex breakdown occurs (in the mean) centered to the jet axis and hence, it seems sufficient to consider the instantaneous axial velocity on the jet centerline $v_{cl}(x, t, S)$, which makes $\text{PDF}[v_{cl}](x, S)$ parametrically dependent on the streamwise coordinate x and the swirl number S .

The results of the statistical analysis of the emergence of vortex breakdown are summarized in figure 4.7. The first diagram (figure 4.7a) shows the probability of reversed flow

$$P_{RF}(x, S) = \int_{-\infty}^0 \text{PDF}[v_{cl}](x, S)dv_{cl}. \quad (4.7)$$

This quantity provides information about the size and location of an intermittently appearing recirculation region that might not be detectable from the mean flow. The diagram on the left hand side of figure 4.7b shows contours of $\text{PDF}[x_{st}](S)$, the probability density function of the streamwise location of the most upstream stagnation point $x_{st}(t, S)$. The associated zero-crossing of v_{cl} is thereby estimated from each PIV snapshot by cubic interpolation. The diagram reveals the probability of vortex breakdown to occur at a specific axial location for a given swirl number. The probability of vortex breakdown to occur at any point inside the measurement domain is obtained from the integral

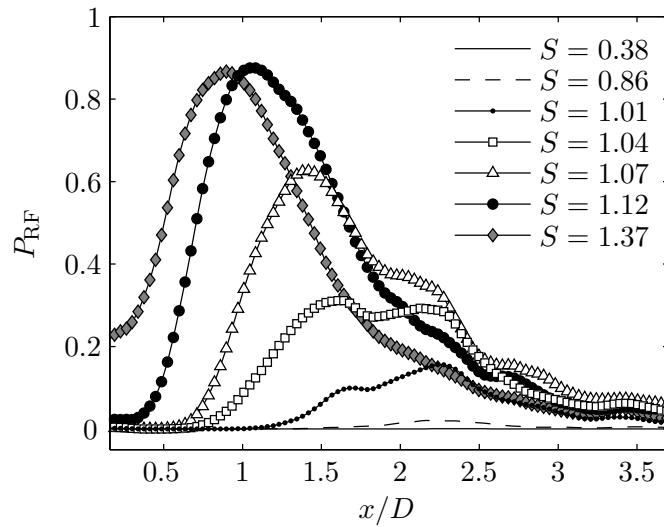
$$P_{VB}(S) = \int_{0.3D}^{3.5D} \text{PDF}[x_{st}](S)dx. \quad (4.8)$$

It is displayed on the right hand side of figure 4.7b. P_{VB} ranges from 0 to 1, representing 0 to 400 snapshots that exhibit flow stagnation, respectively. The gray area in the background of the diagrams shown in figure 4.7b indicate the swirl number regime where an internal stagnation point exists in the mean flow. Figure 4.7c displays the power spectral density PSD of

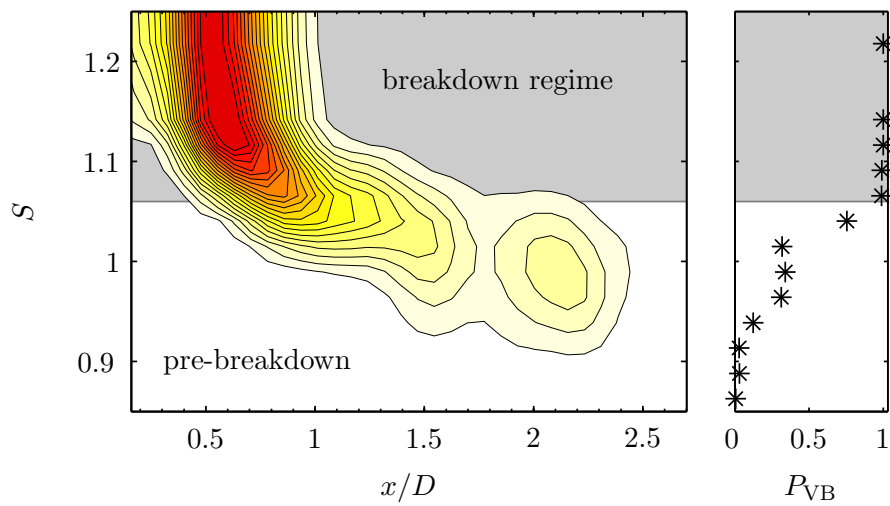
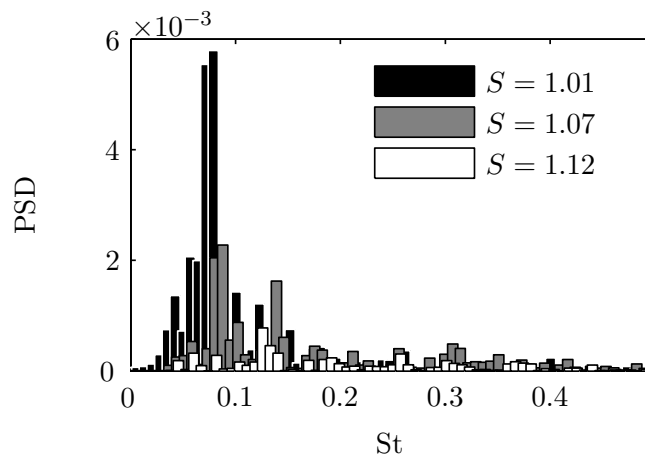
the upstream stagnation point as a function of the dimensionless frequency $St = fD/V$ for three selected swirl numbers. This quantity, defined as $\text{PSD}(f) = |\text{FFT}[x_{\text{st}}(t)/D]|^2$, provides information about the streamwise oscillation frequency and amplitude of the vortex breakdown location.

Figure 4.7a shows that for $S = 0.38$ the instantaneous flow exhibits no reversed flow. For $S = 0.86$ a few events of back-flow are detectable, with a maximum probability of 0.023 at $x/D \approx 2.3$. Intensifying the swirl to $S = 1.01$ increases this probability to 0.15 with the maximum still located at $x/D \approx 2.3$. In addition, a second maximum appears, which is located at $x/D = 1.68$. For the same swirl number, the contours of $\text{PDF}[x_{\text{st}}]$ exhibit two peaks located at $x/D \approx 1.5$ and $x/D \approx 2.1$ (figure 4.7b). This is a strong indication for an oscillating vortex breakdown location. A further increase of swirl to $S = 1.04$ increases the upstream maximum of P_{RF} and displaces it in upstream direction. The upstream maximum of $\text{PDF}[x_{\text{st}}]$ is correspondingly displacement upstream. This indicates that the stagnation point oscillates between a fixed downstream location of $x/D \approx 2.1$ and an upstream location which moves upstream with increasing swirl. When S_{VB} is exceeded, the upstream peak of $\text{PDF}[x_{\text{st}}]$ increases rapidly while the downstream peak disappears. For $S > 1.1$, the streamwise fluctuations of the stagnation point are strongly reduced, indicated by a narrow $\text{PDF}[x_{\text{st}}]$. Moreover, the probability of vortex breakdown P_{VB} asymptotes one, which corresponds to the permanent occurrence of vortex breakdown. The unsteadiness of vortex breakdown in the pre-breakdown flow regime is confirmed by the PSD shown in figure 4.7c. The strongest oscillations of the stagnation point are detected at $S = 1.1$, where $\text{PDF}[x_{\text{st}}]$ is very broad and exhibits two distinct but nearly equally valued maxima. The dominant frequency is $St \approx 0.08$, which is significantly lower than the frequencies associated with hydrodynamic instability waves (typically $St > 0.3$ (Loiseleux & Chomaz 2003)). This is in qualitative agreement with experimental observations on vortex breakdown over a delta wing conducted by Gursul & Yang (1995).

Combining the statistical observations (figure 4.7) with the time-averaged flow features (figures 4.4-4.6), one may draw the following conclusions: For $S = 0.86$ vortex breakdown occurs very rarely but at approximately the same axial location, thus resulting in a local axial velocity deficit on the jet axis and the associated negative ω_θ . For higher swirl numbers, which are still below S_{VB} , the occurrence of vortex breakdown becomes more frequent and it is accompanied by strong oscillations of the stagnation point. Thereby, it oscillates between the point where breakdown initially emerged ($x/D \approx 2.1$) and an axial location that moves upstream with increasing swirl. This explains the continuous growth of the pocket of concentrated azimuthal vorticity and its upstream movement in the pre-breakdown regime (figures 4.5 and 4.6) and also clarifies the discontinuous movement of the local minimum of axial velocity (figure 4.5). This minimum occurs first at $x/D \approx 2.24$ which corresponds to the intermittent emergence of reversed flow. The vortex breakdown stabilizes once S_{VB} is exceeded, as indicated by the decaying oscillations in the PSD, and the minimum is discontinuously displaced to $x/D \approx 1.42$. Furthermore, S_{VB} coincides with the swirl number beyond which vortex breakdown occurs permanently ($P_{\text{VB}} \approx 1$). Below that value, a stagnation point appears intermittently within the measurement domain. Thus vortex breakdown, like transition to turbulence, occurs intermittently over a certain range of swirl numbers.



(a) probability of reversed flow versus axial distance

(b) left: probability density function of x_{st} (contour lines: 0.1 to 2 at 0.1 increments); right: probability of vortex breakdown(c) power spectral density of x_{st} **Figure 4.7:** Statistic evaluation of onset of vortex breakdown. All quantities are derived on the jet axis.

These findings are qualitatively consistent with previous observations. Billant et al. (1998) and Liang & Maxworthy (2005) report the occurrence of an unstable recirculation region at $x/D \approx 4$, which grows and propagates upstream with increasing swirl. Their experiments were conducted at a much lower initial turbulence level (the flow in the nozzle was not tripped) and may, therefore, be contaminated by transition to turbulence. Liang & Maxworthy observed high amplitude oscillations of vortex breakdown and concluded that time-averaged flow measurements are not representative in this specific flow regime. However, a comparison of the mean flow field in the pre-breakdown regime as displayed in figure 4.1 with the time dependent measurements conducted by Bruecker & Althaus (1995) shows clear similarities. Hence, the time average of the intermittent flow field reveals the same flow features that can be observed during the temporal formation of vortex breakdown. One may pose the question of whether the time-averaged flow at swirl numbers close to S_{VB} approximates the time sequence of the laminar flow undergoing a controlled vortex breakdown as observed by Bruecker & Althaus (1995).

4.6 Vortex Core Criticality

An attempt is made to relate the onset of vortex breakdown, observed in the present experiment, to the inviscid model developed by Benjamin (1962). His derivations are based on the assumption that the sudden occurrence of vortex breakdown is similar to the appearance of a hydraulic jump. The existence of a critical state is suggested that separates a subcritical from a supercritical flow state. A supercritical flow supports only downstream traveling waves while a subcritical flow supports upstream and downstream traveling waves. Experimental and numerical investigations confirm that vortex breakdown represents a transition from supercritical to subcritical flow (e.g. Escudier & Keller (1985); Ruith et al. (2003); Sarpkaya (1971)).

Following the derivations of Benjamin (1962) and using notations similar to Ruith et al. (2003) the criticality of the base flow can be predicted by the criticality condition

$$\frac{d^2\phi_c}{dr^2} - \frac{1}{r} \frac{d\phi_c}{dr} + \left[\frac{1}{r^3 V_x^2} \frac{d(rV_\theta)^2}{dr} - \frac{r}{V_x} \frac{d}{dr} \left(\frac{1}{r} \frac{dV_x}{dr} \right) \right] \phi_c = 0 \quad (4.9)$$

that delivers the *test function* ϕ_c except for an arbitrary constant multiplier. The boundary conditions are $\phi_c(r=0) = 0$ and $d\phi_c(r=0)/dr = 1$. For pipe flows, Benjamin shows that a necessary and sufficient condition for a subcritical state is that ϕ_c has to vanish at least once within the pipe radius. Following Mager (1972) and Ruith et al. (2003) who apply Benjamin's analysis to radially unbounded flows, ϕ_c has to diminish within the characteristic core radius for subcritical flow. Ruith et al. emphasize the importance of ϕ_c within the core radius in determining the criticality of the flow, arguing that the ability of rotating flows to support traveling waves depends on the magnitude of axial vorticity (Escudier & Keller 1985; Ruith et al. 2003).

The present flow is not parallel, particularly in the vicinity of vortex breakdown. Nonetheless, Benjamin's analysis is applied, which is strictly speaking only valid for columnar flows. Ruith et al. demonstrate that the analysis may successfully predict the location of vortex breakdown of a laminar flow retrieved from direct numerical simulation. Their approach is extended by investigating the applicability of the analysis to time-averaged

turbulent flow. Hence, the criticality condition (4.9) is applied to the measured velocity profiles at different axial locations. The flow at a certain axial location is considered subcritical if the test function ϕ_c diminishes within the core radius.

The critical radius r_{crit} at which $\phi_c = 0$ is shown on the left-hand side of figure 4.8 as a black solid line together with contours of measured axial vorticity ω_x . The radial extent of the vortex core r_{core} is defined as the contour line on which $\omega_x = 0$ and is marked as a red thick line. The right-hand column shows the projected streamlines together with contours of ω_θ .

For $S = 0.38$ the flow does not exhibit deceleration and the profiles remain supercritical everywhere. Upon increasing the swirl to $S = 1.01$, vortex breakdown occurs intermittently and negative azimuthal vorticity is generated in the jet core. The critical radius does not exceed the core radius, and thus the profiles are supercritical everywhere. At $S = 1.04$, the largest swirl number available that is still lower than S_{VB} , the profiles become subcritical at $1.3 < x/D < 2.2$. This region agrees well with the area where vortex breakdown appears intermittently (figure 4.7a-b). It is interesting that the locations of the two local minima of r_{crit} agree with the maxima of $PDF[x_{st}]$ (figure 4.7b). In spite of the somewhat loose definition of r_{core} the latter agreement provides an explanation for the oscillating vortex breakdown in the pre-breakdown range: For $S = 1.04$ there are two separated subcritical regions causing vortex breakdown to oscillate between them.

For swirl numbers higher than $S_{VB} = 1.06$, vortex breakdown stabilizes and two stagnation points exist on the jet axis (see black stars in figure 4.8). The flow becomes subcritical upstream of the first stagnation point and returns to supercriticality downstream of the second stagnation point. Hence, the region of reversed flow is entirely trapped within the subcritical region.

According to the columnar assumption of Benjamin's model, the criticality of the inflow profile should suffice for predicting vortex breakdown. Due to measurement limitations, the criticality of the inflow profile can only be assessed by extrapolating r_{crit} and r_{core} to $x/D = 0$. It turns out that the inflow profiles undergo a supercritical-to-subcritical transition when S_{VB} is exceeded, yielding a surprisingly good agreement with Benjamin's inviscid theory. This differs from the findings of Ruith et al. (2003), who successfully predict breakdown from the local criticality, but fail to predict breakdown solely from the inflow profiles. They attribute the discrepancy to the influence of viscosity due to very low Reynolds numbers. The high initial turbulence level in the present experiment eliminates the significance of viscous effects (see appendix A.2 for a detailed discussion of the turbulent quantities).

Concluding, the recirculation region that appears for $S > S_{VB}$ is explained by the criticality character of the inflow profiles and hence this swirl number can be attributed to the critical swirl number for vortex breakdown. Furthermore, the location of vortex breakdown and its intermittent occurrence for $S < S_{VB}$ is well predicted by the local criticality character of the time-averaged velocity profiles. The good applicability of Benjamin's model suggests that the mechanism that drives breakdown is inviscid for the present experiment.

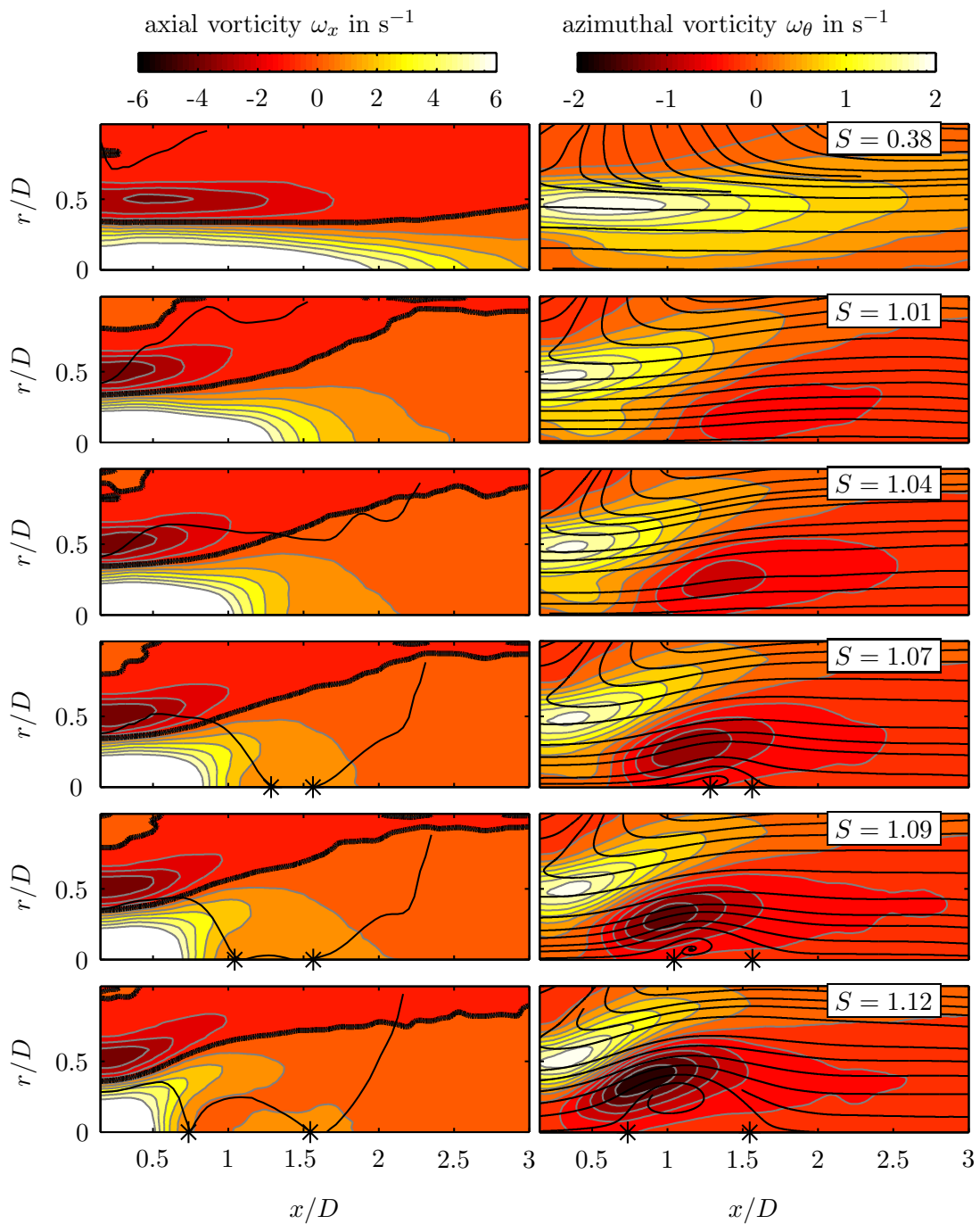


Figure 4.8: Left-hand column: Criticality of the vortex core according to Benjamin (1962); flow is subcritical when test function ϕ_c of equation (4.9) vanishes inside the vortex core, i.e. r_{crit} (black solid line) is smaller than core radius r_{core} (red line). Inflow profiles undergo supercritical-to-subcritical transition for $S > 1.04$ in correspondence with the appearance of an internal recirculation region (black stars mark stagnation points). The local criticality characteristic successfully predicts intermittent breakdown ($S = 1.04$) and stationary breakdown ($S \geq 1.07$).

4.7 Coherent Structures

Numerous theoretical and experimental investigations have shown the importance of helical instabilities in swirling jets (e.g., see Gallaire & Chomaz 2003; Liang & Maxworthy 2004; Loiseleux & Chomaz 2003; Panda & McLaughlin 1994; Ruith et al. 2003). The breaking of rotational symmetry and the corresponding appearance of spiral-shaped vortices are attributed to instabilities generated by axial and azimuthal shear. Experimental investigations of laminar swirling jets reveal that the azimuthal mode number and axial phase velocity of the dominant instabilities strongly depend on the amount of swirl and the relative location of the axial and azimuthal shear layers (Liang & Maxworthy 2004; Loiseleux & Chomaz 2003). Despite the different experimental setups and consequently different base flow configurations, there is a consensus when considering laminar swirling jets: At weak swirl, instabilities with azimuthal wavenumbers $m = 0$ and $m = \pm 1$ are equally dominant in agreement with non-swirling jets. At moderate swirl, non-axisymmetric instabilities become dominant while their overall amplification is reduced. At strong swirl beyond breakdown, single-helical large-scale oscillations are observed that are caused by a supercritical Hopf bifurcation to a self-excited global mode (Gallaire et al. 2006; Liang & Maxworthy 2005; Ruith et al. 2003). For an introduction to the concept of global stability, the reader is referred to the review articles of Huerre & Monkewitz (1990) and Chomaz (2005).

In this section, the azimuthal modes that are detected from crosswise measurements are briefly described, followed by a detailed discussion of the self-excited oscillations that arise at very strong swirl. Furthermore, links are established between the vortex breakdown unsteadiness and the appearance of the global mode.

4.7.1 Local Examination of Azimuthal Waves

In order to obtain information about azimuthal waves, PIV-measurements are conducted along the r - θ -plane at the axial location $x/D = 1.1$. The sequences of PIV snapshots are Fourier decomposed in time and in space providing the spectral distribution of spatial modes. Thus, the time resolved three-component PIV snapshots, depicted as $\mathbf{v}(x, r, \theta, t)$, are decomposed into complex Fourier coefficients $\hat{\mathbf{v}}$ yielding

$$\hat{\mathbf{v}}(x, r, m, f) = \frac{1}{2\pi T} \int_0^T \int_0^{2\pi} \mathbf{v}(x, r, \theta, t) e^{i(m\theta - 2\pi ft)} d\theta dt. \quad (4.10)$$

Note that $m > 0$ modes rotate with the mean flow and are referred to as co-rotating while $m < 0$ modes are counter-rotating. The PIV snapshots are recorded for $N = 400$ samples at a rate of 2.25 Hz yielding a maximum resolvable frequency of 1.125 Hz. In order to reduce noise, the spectra are averaged with the drawback of doubling the maximum resolvable frequency to $\Delta f = 2f_s/N = 0.0056$ Hz. The power spectral density contained in a single azimuthal mode is defined as the square of the modulus, yielding $\text{PSD} = |\hat{\mathbf{v}}|^2$. Figure 4.9 displays the PSD of $-3 \leq m \leq 3$ modes. The spectra are taken at the radial position of the highest energy content. It is interesting to note that these locations coincide approximately with the center of the shear layer of the jet-like axial velocity profile (figure 4.9a-b) and with the center of the *inner* shear layer of the wake-like axial velocity profile (figure 4.9c-d). The overall picture is presented in figure 4.10. It shows the distribution of the total energy \tilde{K}_{tot}

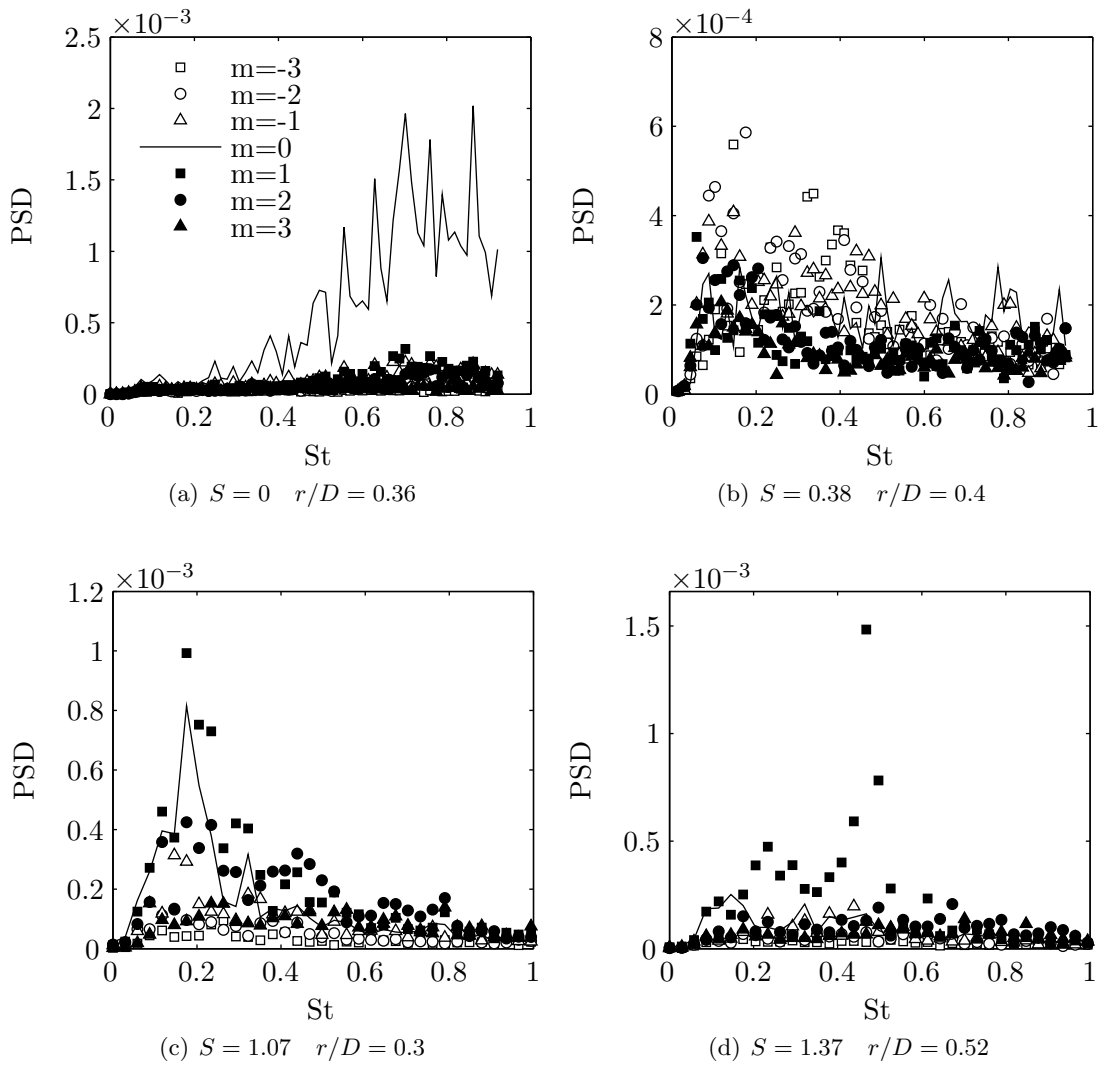


Figure 4.9: PSD of azimuthal modes derived at $x/D = 1.1$ at the radial location of highest energy contents

among the azimuthal modes ranging from $m = -5$ to $m = 5$. The total energy corresponds to the accumulated energy of all considered frequencies and radial positions.

In absence of swirl, mode $m = 0$ is clearly dominant for $0.6 < St < 1$ and all other modes are weak (figures 4.9a and 4.10). By increasing the swirl to $S = 0.38$, the energy of mode $m = 0$ is strongly reduced. Figure 4.9b shows that the counter-rotating modes ($m < 0$), marked by open symbols, become more energetic than the axisymmetric and co-rotating ones and they peak at lower oscillation frequencies ($0.1 < St < 0.4$). These results can be compared to the linear stability analysis conducted by Gallaire & Chomaz (2003). Their analysis is based on the velocity profiles measured by Billant et al. (1998), which agree reasonably well with the present flow (see appendix A.1 for detailed comparison). They predict mode $m = 0$ and $m = \pm 1$ to be most unstable for $S = 0$ with a somewhat higher amplification rate of mode $m = \pm 1$. However, it is usually $m = 0$ which dominates in laboratory jets because random disturbances generated upstream of the settling chamber become axisymmetric at the nozzle exit, due to the high area ratio of contractions used in

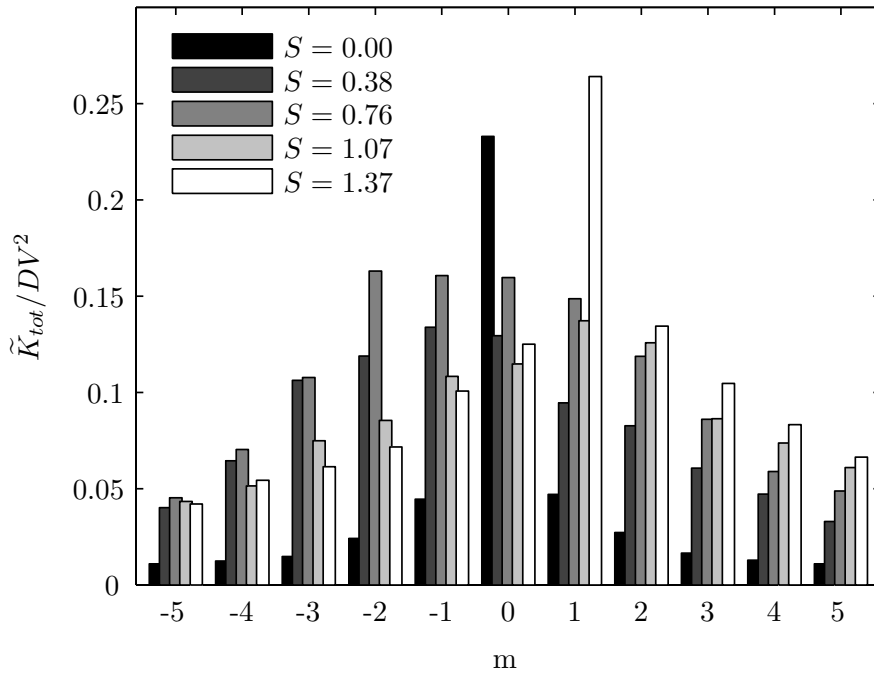


Figure 4.10: Total energy distributed among azimuthal modes at $x/D = 1.1$.

those jet facilities (Cohen & Wygnanski 1987; Long & Petersen 1992). For moderate swirl, Gallaire & Chomaz (2003) predict mode $m = -1$ to be most unstable, followed by mode $m = -2$ and $m = -3$. This agrees well with the present results, revealing mode $m = -1$ to be dominant, followed by $m = 0$, $m = -2$, and $m = -3$ for $S = 0.38$ (figure 4.10). The relative significance of the axisymmetric mode is likely to be caused by the random noise created by the facility upstream of the contraction, in the same way as for the non-swirling jet. The modal distribution reported by Liang & Maxworthy (2005) differs from the present results as they found only azimuthal waves that co-rotate with the base flow ($m > 0$). Due to the absence of a contraction, the mean flow in their experiment differs substantially from the one investigated by Billant et al. (1998); Gallaire & Chomaz (2003); Loiseleux & Chomaz (2003) and the time-averaged flow presented here. The reduction of the dominant frequency with increasing swirl (figure 4.9a-b) disagrees with the observations of Loiseleux & Chomaz (2003), who found the local Strouhal number to decrease only slightly with increasing swirl. Presumably, the high initial turbulence level in the present experiment enhances the shear layer growth, thus reducing the dominant frequencies more rapidly with increasing distance from the nozzle. A detailed investigation of the instability at moderate swirl is given in chapter 5.

At the swirl number $S = 1.07$, breakdown occurs and a recirculation region is generated. Spectra taken at the center of the inner shear layer show considerably higher energy for $m = 1$ and $m = 0$ mode at $St \approx 0.2$ (figure 4.9c). This is representative for the flow regime associated with unsteady vortex breakdown. The axial fluctuation of the recirculation region generates $m = 0$ fluctuations while a meandering of the recirculation region in the direction of the basic flow rotation causes $m = 1$ fluctuations. This modal distribution is typical for the inner jet region only. In the outer shear layer, $m = 1$ and $m = 2$ modes dominate as indicated by the total energy distribution (figure 4.10). At very strong swirl,

where vortex breakdown has stabilized, a clear peak of mode $m = 1$ arises that indicates the existence of a dominant coherent structure (figure 4.9d). Its total energy exceeds mode $m = 0$ for the non-swirling jets (figure 4.10).

4.7.2 The Onset of the Global Mode

The emergence of large-scale oscillations for swirl numbers exceeding breakdown has been observed by many researchers. It may be characterized by a precessing vortex core (PVC) that is a well known flow feature arising in swirl-stabilized combustors (Syred 2006). Recent theoretical and experimental investigations on laminar swirling jets show that this precession can be interpreted as a globally unstable single-helical mode (Gallaire et al. 2006; Liang & Maxworthy 2005; Ruith et al. 2003).

The introduction to the main idea of this concept shall be recapitulated here: According to local parallel linear stability theory, the velocity profile at a specific axial location is said to be absolutely unstable, if a localized disturbance spreads in upstream and downstream direction, ultimately contaminating the entire parallel flow (Huerre & Monkewitz 1990). If, by contrast, disturbances are swept away from the source, the velocity profile is said to be convectively unstable. Examples for convectively unstable flows are non-swirling jets (Cohen & Wygnanski 1987) and mixing layers (Gaster et al. 1985) and examples for absolutely unstable flows are the cylinder wake (Yang & Zebib 1989) and hot jets (Monkewitz 1988). The two latter examples are subjected to intrinsic large-scale (global) oscillations that arise at a critical control parameter. These flow configurations are globally unstable and are typically treated by employing a global stability analysis with a two-dimensional perturbation ansatz (e.g., see Sipp & Lebedev 2007). Weakly nonlinear theory allows to connect the local and global stability. Accordingly, only shear flows are globally unstable that exhibit a sufficiently large region of absolute instability (Chomaz 1992; Chomaz et al. 1988; Chomaz et al. 1991). The large-scale oscillations that are distinct for global modes are synchronized to one frequency by a so-called wavemaker that is located near the region of absolute instability. For swirling jets, this region is usually associated with reversed flow on the jet axis.

The transient experiments conducted by Liang & Maxworthy (2005) show that in conjunction with vortex breakdown, a global mode arises from the jet center that grows rapidly in time, reaches the outer shear layer, and ultimately imposes its frequency onto the entire flow. Hence, it is likely that the global mode $m = 1$ observed in experiments originates from a pocket of absolutely unstable flow that exists near the jet axis due to vortex breakdown. This scenario is supported by the stability analysis of a simulated laminar swirling jet (Gallaire et al. 2006) and by the spatio-temporal stability analysis presented in chapter 7. Once the global mode has saturated at its limit-cycle oscillation it can be characterized by a convectively unstable mode $m = 1$ that amplifies in the outer shear layer at a frequency that is imposed by the wavemaker located on the jet centerline. This flow state is also often referred to non-axisymmetric or spiral vortex breakdown (e.g., see Billant et al. 1998; Bruecker & Althaus 1995; Liang & Maxworthy 2005; Ruith et al. 2003).

A characteristic of global modes is a single (global) oscillation frequency within a spatial domain (Monkewitz et al. 1990; Provansal et al. 1987), and indeed, the high amplitude

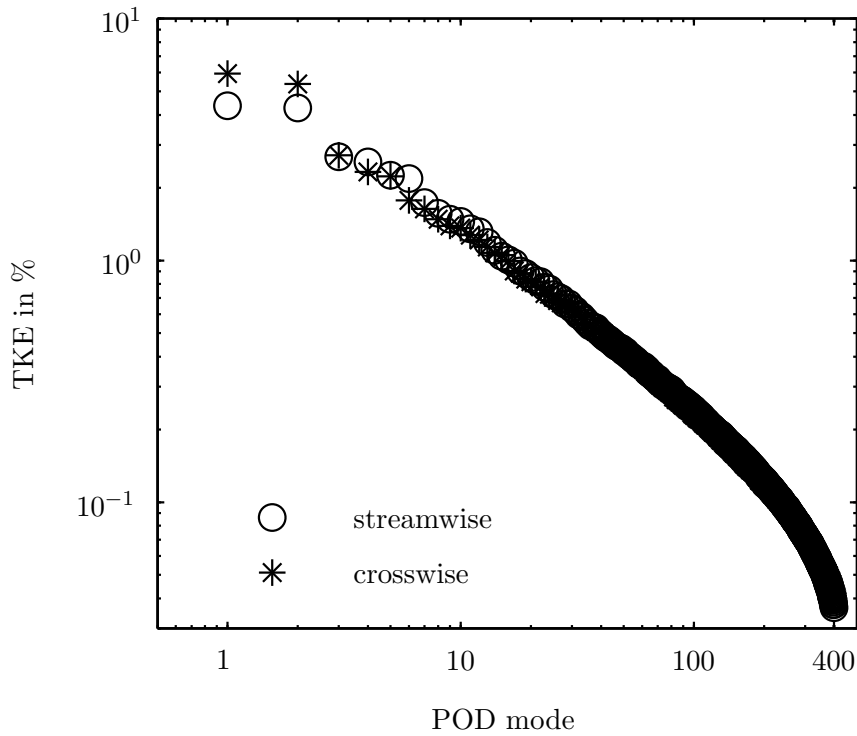


Figure 4.11: Turbulent kinetic energy captured in the POD modes ($S = 1.37$)

oscillation frequency shown in figure 4.9 is detected at several positions in the flow (not shown).

In case of a dominant global frequency, the phase-averaged flow field can be accurately derived by means of proper orthogonal decomposition (POD). The reader is referred to chapter 6.5 for a detailed description of the phase-averaging procedure. A brief introduction to the POD applied in the present investigation is given section 2.5. For a comprehensive survey on POD, the reader is referred to (Berkooz et al. 1993; Holmes et al. 1998; Lumley 1967). For the phase-averaging procedure, the PIV snapshots are decomposed into spatial POD modes $\Phi_i(\mathbf{x})$ and temporal POD modes $a_i(t)$ with $i = 1, 2, \dots, N$. The eigenvalues λ_i represent twice the turbulent kinetic energy contained in the corresponding POD mode.

The energy distribution of the POD modes of the highly swirling jet at limit cycle oscillations is shown in figure 4.11. The hollow circles correspond to POD modes derived from streamwise measurements while the star symbols correspond to modes derived from crosswise measurements at $x/D = 1.2$. The two leading POD modes contain approximately equal energy and span the convecting vortex pattern that corresponds to the global oscillatory motion. The energy content of the streamwise modes is somewhat smaller since the streamwise domain also covers regions where the oscillations are weak (see section 6.5.1 for details).

To validate whether the first two POD modes represent the global mode, one may compare the corresponding temporal POD modes a_1 and a_2 with the Fourier coefficients derived from equation (4.10). The normalized PSD of mode $m = 1$ is displayed in figure 4.12a and compared to the normalized PSD of a_1 and a_2 of the crosswise and streamwise POD modes respectively (figure. 4.12b-c). Evidently, the first two POD modes correspond to the same

oscillating structure and they accurately represent the dynamics of mode $m = 1$. The spectra of the first two streamwise temporal POD modes do not perfectly agree with each other and they also show a broader peak compared to the spectrum of mode $m = 1$. This is again attributed to the fact that the streamwise domain contains regions of weak oscillations subjected to more jitter and noise. Nonetheless, the characteristic frequency is well captured, which implies that the periodically fluctuating global mode is represented by the first two POD modes in both measurement planes. It is a straight forward procedure to assign a phase angle φ_j of mode $m = 1$ to each PIV snapshot indexed by j using $\tilde{a}_j e^{i\varphi_j} = a_1(t_j) + ia_2(t_j)$. Hence, it is possible to define a flow phase via the POD and consequently obtain phase-averaged quantities of the dominant oscillatory mode.

The structure of the global mode along the streamwise and crosswise plane of the measurement is shown in figure 4.13 for $S = 1.37$. The first row corresponds to the mean flow, the second row to the coherent flow, and the third row shows the sum of both. The projected streamlines emphasize the eddy-like structures. The coherent structures associated with the global mode are best visualized by the coherent component (figure 4.13c-d). Traveling waves are created in the outer shear layer that lead to a roll-up of a helical vortex that is wrapped around the recirculation region. Vorticity on the jet axis upstream of the recirculation region indicates the precession of the vortex core. The shape of the global mode agrees well with the one found at higher Reynolds numbers at a similar configuration (see chapter 6 and 7). The structure on the jet centerline is identified as the wavemaker that excites instabilities in the convectively unstable outer shear layer. Adding the time-averaged flow to the coherent flow yields the phase-averaged flow field shown here at an arbitrary phase (figure 4.13e-f). The streamwise plane indicates the waviness of the synchronized inner and outer shear layer. The crosswise plane shows an eccentric vortex – the precessing vortex core (PVC).

Generally, the amplitude of a global mode is governed by the forced Landau equation (Huerre & Monkewitz 1990; Landau & Lifshitz 1987). Near critical conditions and in the absence of forcing, the limit cycle amplitudes should increase proportionally to the deviation from a control parameter, yielding

$$A_{\text{sat}} \propto \sqrt{S - S_{\text{crit}}} \quad , \quad (4.11)$$

where S_{crit} is the critical control parameter for a constant Reynolds number and $S \geq S_{\text{crit}}$. In the present experiment, A_{sat} is derived from the PSD of the leading two temporal POD modes a_1 and a_2 (figure 4.12b-c). This is preferable to the PSD of the Fourier modes (figure 4.12a) since the POD modes capture the oscillation amplitude of the entire spatial domain yielding a more representative global value. Both, the saturation amplitude derived from streamwise or crosswise data are found to be proportional to $\sqrt{S - S_{\text{crit}}}$ (figure 4.14). The linear dependence suggests that the oscillation is of the supercritical Hopf bifurcation type. As mentioned earlier, the amplitudes differ between streamwise and crosswise POD modes due to the different measurement domains. Note that the streamwise POD modes also capture the weak oscillations for $S = 1.12$ that are not detectable by the crosswise measurement located at $x/D = 1.1$. A linear fit of the streamwise and crosswise saturation amplitudes yields a critical swirl number $S_{\text{crit}} = 1.1$, which is clearly higher than the critical swirl number $S_{\text{VB}} = 1.06$ for vortex breakdown. This disagrees with the observations of

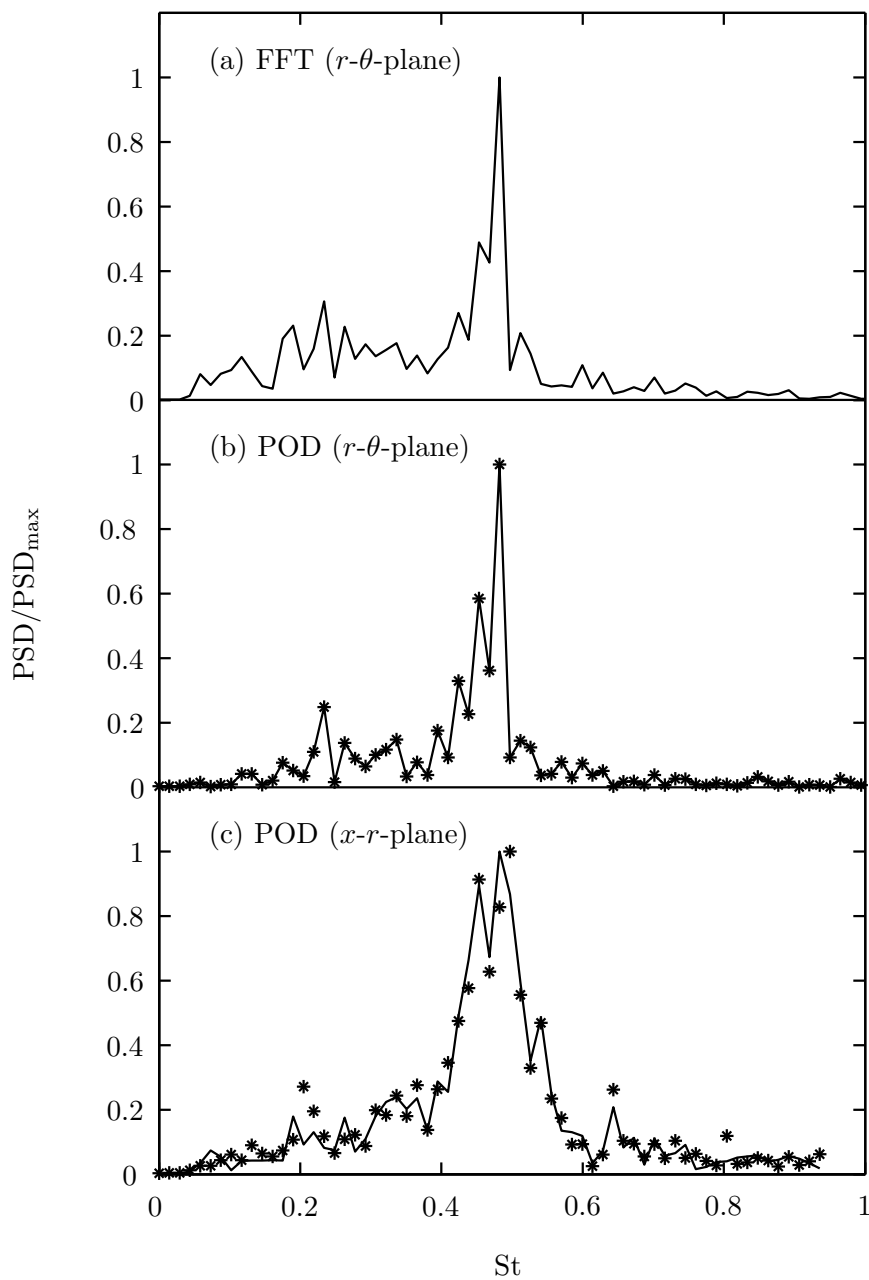


Figure 4.12: (a) PSD of mode $m = 1$ derived via spatial Fourier analysis of the r - θ -plane at $x/D = 1.1$ according to equation (4.10). (b) PSD of temporal POD mode a_1 (symbol) and a_2 (line) derived from the r - θ -plane at $x/D = 1.1$. (c) PSD of temporal POD mode a_1 (symbol) and a_2 (line) derived from x - r -plane.

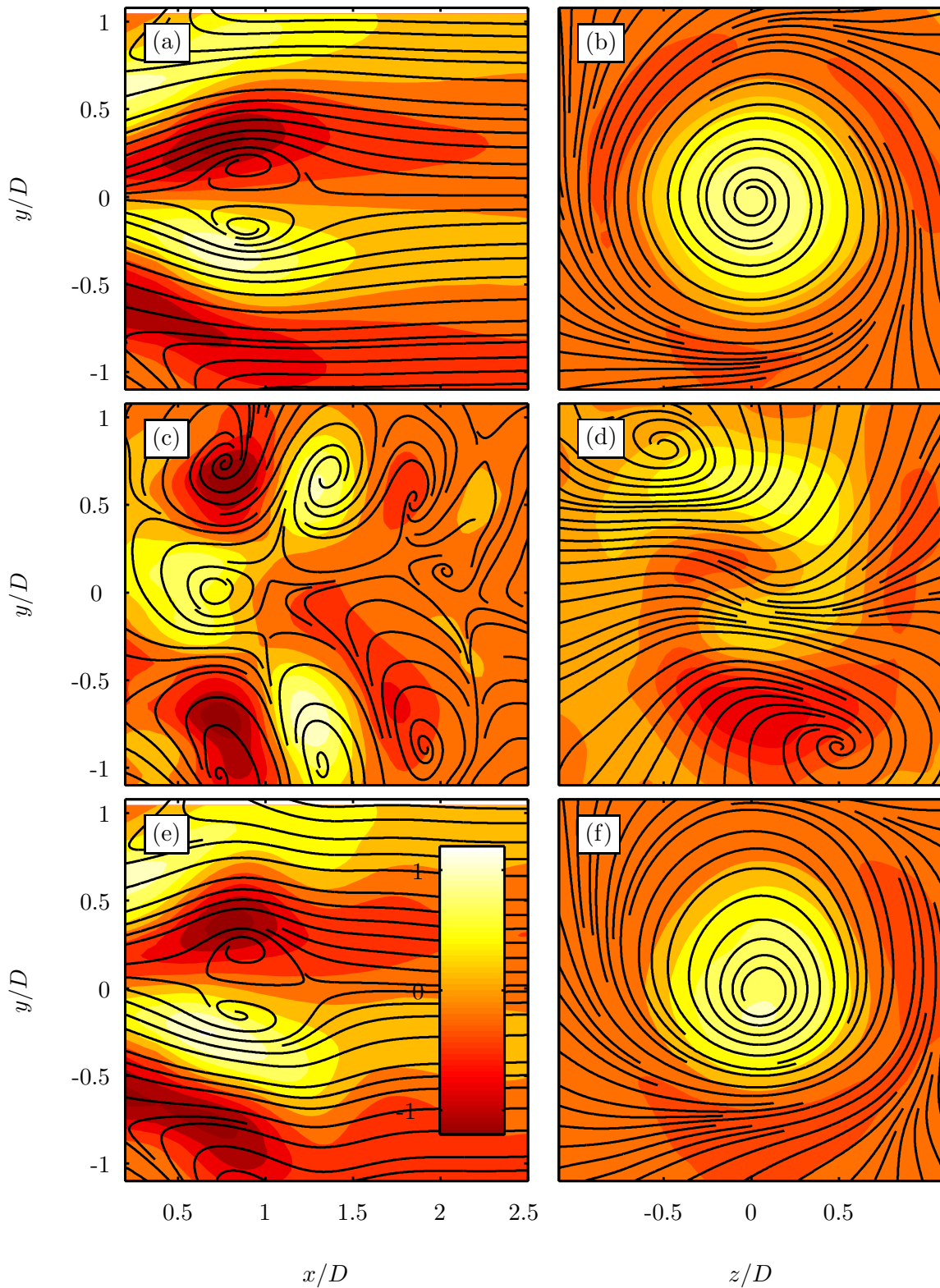


Figure 4.13: Portrait of co-rotating counter-winding global instability mode $m = 1$; projected streamlines and through-plane vorticity component ω_z in the streamwise and crosswise ($x/D = 1.1$) measurement plane; (a-b) time-averaged flow; (c-d) coherent flow (times 5 for equal color scale); (e-f) time-averaged plus coherent flow; coherent flow is displayed at an arbitrary phase; ($S = 1.37$)

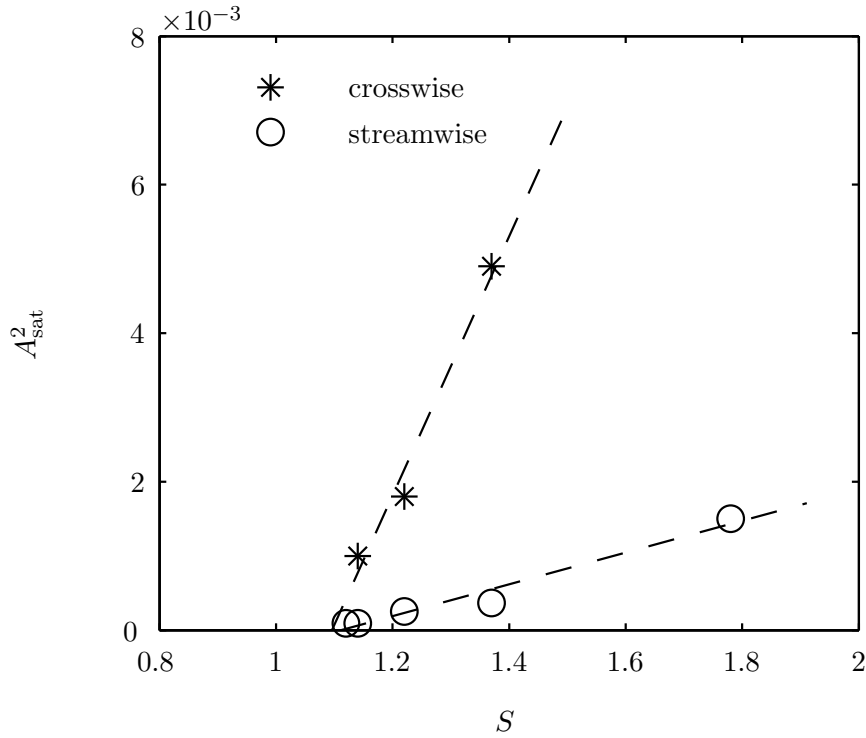


Figure 4.14: Square of limit cycle amplitudes of global oscillation derived from temporal POD modes of the crosswise (white circles) and streamwise (black stars) plane of measurement. Linear extrapolation predicts $S_{\text{crit}} = 1.1$ to be the critical swirl number where the flow undergoes a supercritical Hopf bifurcation

Liang & Maxworthy (2005), who suggest that both swirl numbers coincide. In fact, they found S_{crit} to be below S_{VB} but argued that due to noise, the former is underestimated.

The present findings support the sequence leading to the global mode $m = 1$ that is described at the beginning of this section: Axisymmetric vortex breakdown is established and persists permanently at swirl numbers below a critical bifurcation parameter S_{crit} . Exceeding that, the region of reversed flow that generally promotes absolute instability, reaches a sufficient size to set up a feedback mechanism that leads to a global mode and vortex breakdown becomes non-axisymmetric. It is interesting to note that the critical swirl number S_{crit} coincides with the swirl number for which the linear growth of the recirculation region stagnates (see figure 4.5). Any further increase in swirl only leads to an upstream movement of that region. Furthermore, the critical swirl number coincides with the swirl number at which the axial fluctuations of the stagnation point reach their minimum value (figure 4.7b). Apparently, the onset of the self-excited oscillations dampen the low frequency breakdown oscillations and interact with the mean flow in such a way that any further growth of the recirculation zone is inhibited.

4.8 Summary and Discussion

This chapter describes the experimental investigation of the nearfield of an unconfined swirling jet by means of time-resolved stereoscopic PIV. Experiments were conducted in

water at $Re = 3300$. The flow is fully turbulent at the nozzle exit due to a serrated tip-ring mounted upstream of the nozzle. The amount of swirl was adjusted carefully near the onset of vortex breakdown in order to map the different flow states ultimately leading to its non-axisymmetric state. The investigation provides a quantitative characterization of the mean and the instantaneous flow field with an emphasis on the vortex breakdown dynamics and the associated coherent structures.

The attempt is made to scale the experiments conducted for a wide range of swirl levels by using one universal swirl number definition. It is found that the commonly used swirl number – the axial flux ratio of axial to azimuthal momentum – is inaccurate for strong swirl due to the invalidity of the underlying boundary layer approximations. A detailed investigation of the individual terms of the equations of motion show that the turbulent stresses and radial velocity component contribute significantly to the momentum conservation in regions of strong jet divergence. Taking this into account, the swirl number is conserved in the axial direction and increases linearly with the rotation rate of the swirl-generating honeycomb. However, for very strong swirl, vortex breakdown moves into the nozzle and the presented swirl number definition is still inaccurate, presumably due to the negligence of pressure forces induced by the nozzle walls. For these cases the swirl number is derived from a linear extrapolation.

The various flow states observed for increasing swirl intensity and the corresponding dominant vortical structures are characterized by three different methods. First, the occurrence of vortex breakdown, associated with a stagnation point on the jet axis, is tagged from the mean flow and from each individual PIV snapshot. Second, Benjamin's (Benjamin 1962) criticality concept is applied to the mean flow and the axial positions of supercritical–subcritical transition are derived. Third, azimuthal instability modes are detected via Fourier decomposition of PIV measurements taken along the crosswise plane. In case of large-scale intrinsic oscillations, PIV snapshots, taken along the streamwise plane, are phase-averaged a posteriori by employing POD.

Figure 4.15 provides an schematic overview of the major findings. Starting with the non-swirling jet, the axisymmetric mode $m = 0$ is found to be dominant near the nozzle. By increasing the swirl, the symmetry breaks and counter-rotating modes with $m < 0$ are destabilized. For $0.86 < S < 1.06$ vortex breakdown appears intermittently and oscillates in axial direction at low frequencies ($St < 0.1$), but it remains undetectable from the mean flow. At $S = 1.04$ two nearly separated subcritical regions exist that match the axial locations of these oscillations. Thus, the unsteady vortex breakdown is well predicted from the local criticality of the mean flow that does not exhibit vortex breakdown at that swirl intensity. This supplements the findings of Ruith et al. (2003), who successfully apply the local criticality concept to localize steady vortex breakdown in a laminar jet. By further increasing swirl, the occurrence of vortex breakdown increases progressively until it appears in the mean flow at $S_{VB} = 1.06$. At that swirl number, the inflow profiles transition from supercritical to subcritical, in agreement with the theoretical prediction of Benjamin (1962). The good applicability of Benjamin's model suggests that the mechanism that drives breakdown is inviscid for the present experiment. For swirl numbers above S_{VB} , a recirculation region appears that grows continuously with increasing swirl until its size stagnates at $S \approx 1.11$. At that flow configuration, the low frequency axial oscillations of

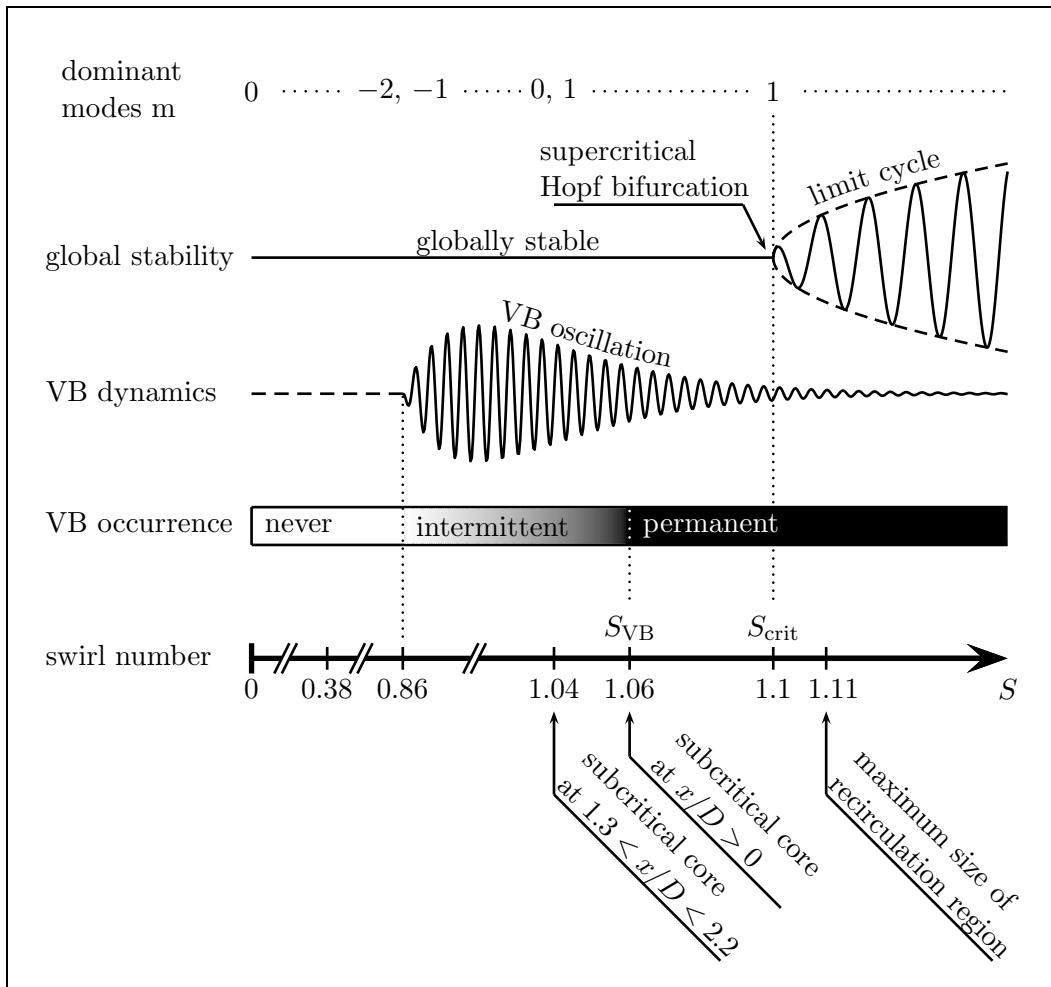


Figure 4.15: Conceptual drawing summarizing the experimental results.

vortex breakdown have completely decayed whereas strong helical waves at higher frequencies ($St > 0.44$) are found. Experiments indicate that the flow undergoes a supercritical Hopf bifurcation to a global mode $m = 1$ at $S_{crit} = 1.1$. The selection of mode $m = 1$ is in agreement with previous numerical, theoretical, and experimental investigations and is well documented in recent literature (Gallaire et al. 2006; Liang & Maxworthy 2005; Ruith et al. 2003). However, the observation that $S_{VB} < S_{crit}$ is new and stands in contrast to the experiments of Liang & Maxworthy (2005) who found $S_{VB} > S_{crit}$. They report that their S_{crit} is likely to be underestimated due to unwanted external forcing from their facility.

In conclusion, the following scenario can be derived from the presented experiment: The turbulent swirling jet undergoes intermittent and heavily oscillating vortex breakdown at swirl numbers far below $S_{VB} = 1.06$ that is initiated by two small and spatially separated regions of subcritical flow. By increasing the swirl to S_{VB} , the inflow profiles undergo a supercritical-to-subcritical transition and axisymmetric vortex breakdown occurs permanently. A further increase in swirl causes the recirculation zone to grow linearly until the promoted pocket of absolutely unstable flow is sufficiently large for the mode $m = 1$ to become globally unstable. At $S_{crit} = 1.1$, a feedback mechanism sets in that stimulates the vortex core to precess in the direction of the mean flow rotation and vortex breakdown becomes non-axisymmetric. A further increase in swirl enhances the global oscillations

and associated nonlinear mean flow interactions which inhibits a further increase of the recirculation zone.

The presently observed time-averaged turbulent flow states that describe the formation of vortex breakdown with increasing swirl, compare well with the transient flow states of a laminar jet undergoing vortex breakdown that were observed by [Bruecker & Althaus \(1995\)](#). Hence, the present investigation provides representable and repeatable measurements of the stepwise formation of spiral vortex breakdown in a turbulent base flow.

Chapter 5

Instabilities in the Moderately Swirling Jet

This chapter focuses on the streamwise growth of coherent structures in jets at swirl intensities below the onset of vortex breakdown. All flow configurations considered are globally stable. The main question addressed in this investigation is, how swirl effects the evolution of convectively unstable modes. The problem is approached theoretically by conducting a quasi-parallel spatial linear stability analysis employing the mean flow. The impact of small-scale turbulence on the stability is incorporated using an eddy viscosity model derived from the measured Reynolds stresses. The major theoretical results presented throughout this part are compared to hot-wire measurements of the single-mode actuated and pulsed actuated flow, showing good agreement. The swirling jet at the nozzle is receptive to a shear instability and a centrifugal instability mode. The previous is primarily generated by the radial stratification of axial velocity (axial shear) and is much stronger than the latter that is generated by the radial stratification of azimuthal velocity (azimuthal shear). With increasing downstream distance, the centrifugal instability stabilizes much more rapidly than the shear instability. Swirl affects the streamwise phase velocity of helical (oblique) traveling waves, which is explained by simple kinematic considerations. The non-zero azimuthal group velocity is thereby the key driver. The swirling jet selects a co-winding $m = 2$ mode as the preferred mode in the nearfield and a co-winding $m = 1$ mode further downstream. The swirling jet is unstable to streamwise modes with zero axial wavenumber and steady modes with zero frequency. The latter may reach significant high amplitudes, which explains the breaking of rotation symmetry in the mean flow that is often observed in swirling jet experiments. Comments to swirl-enhanced jet spreading are given at the end of this part and connections to the presently found stability characteristic are made.

5.1 Background and Scope

The investigation described in this chapter focuses on axisymmetric unconfined turbulent jets at swirl intensities below the onset of vortex breakdown, which are referred to as moderately swirling jets. Due to the ability of swirl to enhance turbulent production and shear layer spreading, these flows are commonly used in industrial applications where efficient turbulent mixing is required. The great importance of swirling flows for the combustion industry is reflected by the large number of related publications (see review articles of Gutmark et al. 1995; Huang & Yang 2009; Knowles & Saddington 2006; McManus K. et al. 1993; Syred 2006, and references therein).

During the last two decades, various ideas have come up to explain the enhanced mixing in swirling flows. There is a common consensus that the vortical structures in swirled shear layers, which differ to those found in non-swirling jets, must be the driving force for the enhanced turbulent production and entrainment rate. However, the characteristics and the sources of the flow structures that reside in swirled shear layers are still unclear. It is known that with the addition of swirl, the flow promotes shear instabilities and centrifugal instabilities, but their ability to enhance jet spreading is still a controversial issue. Linear stability analysis based on swirling jet models reveal that centrifugal instabilities become successively destabilized with increasing swirl (Gallaire & Chomaz 2003; Loiseleux et al. 2000; Lu & Lele 1999; Martin & Meiburg 1996, 1998; Müller & Kleiser 2008). Several investigators suggest these instabilities, which promote disturbances at smaller scales than shear instabilities, to be the cause for the enhanced jet spreading (Cutler et al. 1995; Mehta et al. 1991; Panda & McLaughlin 1994; Wu et al. 2006). This stands in contrast to the experimental observation of Naughton et al. (1997), who found swirl-enhanced mixing for a centrifugally stable profile, which is confirmed by the numerical studies of Hu et al. (2001*a,b*). These authors conclude that centrifugal instability is not a necessary condition for enhanced jet spreading. In fact, their direct numerical simulations indicate that the growth of swirled shear layers is augmented by a nonlinear interaction of primary vortex ring and the columnar vortex that leads to a rapid breakdown of large flow structures into smaller scales.

The three-dimensional nature of the vortical structures in swirling jets was demonstrated by several experimental investigations. Panda & McLaughlin (1994) successfully excited axisymmetric and non-axisymmetric modes in the shear layer of a turbulent swirling jet, revealing a lower receptivity for axisymmetric modes in comparison to the non-swirling jet. Billant et al. (1998) and Loiseleux & Chomaz (2003) investigated the dynamics in the nearfield of a natural laminar jet for various swirl intensities. They found large-scale co-winding double- and triple-helical structures in the pre-breakdown state that were perfectly steady for the experiments conducted by Billant et al. (1998), whereas Loiseleux & Chomaz (2003) observed them to rotate at very low frequencies in direction of the base flow rotation. A spatio-temporal stability analysis conducted by Gallaire & Chomaz (2003) for a mean flow measured by Billant et al. (1998) at approximately half a diameter downstream of the nozzle lip revealed an absolute-convective instability transition of the double-helical mode when exceeding a certain amount of swirl. The authors suggest this mode to be a self-excited globally unstable mode with its wavemaker located at the nozzle lip.

The temporal analysis of Gallaire & Chomaz (2003) confirm that swirl destabilizes modes of high negative azimuthal wavenumbers due to the centrifugal instability in good agreement with the analysis of Leibovich & Stewartson (1983). However, the mode selection predicted by their temporal analysis disagrees with the experimental observations of Billant et al. (1998) and Loiseleux et al. (2000), which they explain with the above mentioned onset of global instability. The authors admit that their arguments remain vague as the analysis is based on a single measurement location, which does not reflect the streamwise varying base flow and associated stability. The mode selection in the swirling jet experiments conducted by Liang & Maxworthy (2005) differs significantly from the previously reported one. For various swirl intensities, all detected helical modes are co-rotating counter-winding and are aligned with the local helical vortex lines of the mean flow. The investigators argue that the relative location and thickness of the axial and azimuthal shear layers have a great influence on the streamwise evolution of the dominant modes. Hence, a comparison of their results to stability analysis based on simplified velocity models, as attempted by the authors, remains only qualitative.

In consideration of the complexity of swirling jet instabilities and their sensitivity to base flow variations, a linear stability analysis is conducted employing the entire nearfield of an unconfined spatially evolving swirling jet derived from time-averaged flow measurements. The theoretical results are compared to measurements of the externally excited flow. The author is aware that there exists no universal swirling jet configuration and that the one investigated presently represents only one of several possibilities. Nonetheless, a detailed description of the stability of this particular flow in conjunction with a quantitative experimental validation will enhance the fundamental understanding of the dynamics in swirling jets, in order to properly interpret other experimental findings and to develop flow control methods for mixing enhancement.

Experiments are conducted at the swirling air jet facility at the TU Berlin. The experimental setup is described in section 3.2 and details of the conducted hot-wire measurements and data treatment are given in section 3.4. The investigation is organized as follows. The flow configurations discussed throughout this chapter are described in section 5.2, ranging from zero swirl to strong swirl below onset of vortex breakdown. A detailed investigation of the linear stability of the swirling jet at the nozzle is presented in section 5.3, followed by the examination of the streamwise evolution of instability in section 5.4. The results of the experimental investigation of the single-mode and pulsed actuated flow are described in section 5.5 and 5.6, respectively. The major findings are summarized and discussed in section 5.7.

5.2 The Mean Flow Configuration

A swirling air jet was generated using the facility described in section 3.2. The mean flow in the x - r -plane was derived from the Stereo-PIV measurements for different swirl intensities at $Re_D = DV/\nu = 20000$.

5.2.1 Analytic Representation of the Mean Flow

The experimental data is approximated by profiles given by the following analytic expressions:

$$V_x = \frac{V_{cl}}{1 + (\exp [(r/R_{.5})^2 \log(2)] - 1)^{N_x}}, \quad (5.1a)$$

$$V_r = 0, \quad (5.1b)$$

$$V_\theta = \Omega_{cl} r \exp [-(r/R_\theta)^{N_\theta}/N_\theta]. \quad (5.1c)$$

A slightly modified version of the expression for the axial velocity component V_x was introduced by Monkewitz & Sohn (1988). Later, Gallaire & Chomaz (2003) used this profile to approximate the measurements conducted by Billant et al. (1998). V_{cl} represents the centerline axial velocity and $R_{.5}$ the jet radius, defined as the radial distance where $V_x = 0.5V_{cl}$. The dimensionless parameter N_x is related to the radial gradient of the axial velocity profile and is inversely proportional to the axial shear layer thickness. The model for the azimuthal velocity component V_θ was first introduced by Carton & McWilliams (1989) and more recently used by Gallaire & Chomaz (2003). Ω_{cl} represents the rotation rate on the jet axis and R_θ the radial location of the maximum azimuthal velocity. The dimensionless parameter N_θ is inversely proportional to the azimuthal shear layer thickness. The parameters N_x and N_θ are determined from a least squares fit of the expressions (5.1a) and (5.1c) to the axial and azimuthal mean velocity, respectively.

The contraction upstream of the nozzle generates an overshoot of the axial velocity profile in agreement with previous studies (Billant et al. 1998; Panda & McLaughlin 1994; Semaan et al. 2009). To account for this hump in the axial velocity profile, Gallaire & Chomaz (2003) introduced an additional term to (5.1a), yielding the more complex expression

$$V_x = \frac{V_{cl}}{1 + (\exp [(r/R_{.5})^2 \log(2)] - 1)^{N_x}} + V_{os} \exp[-(r/r_c)^2], \quad (5.2)$$

where V_{os} represent the strength of the overshoot and r_c its radial extent. According to Gallaire & Chomaz (2003), the axial overshoot has minor effect on the instability of the base flow. Preliminary computations conducted for both models confirm the insignificance of the overshoot for the present flow. Hence, the stability analysis presented throughout this study is based on the mean flow approximated by the simpler and far more generic model (5.1a).

5.2.2 The Velocity Distribution at the Nozzle

The back-scattering configuration of the PIV measurements enables to access the flow quantities at the nozzle exit. The corresponding axial and azimuthal mean velocity profiles are shown in figure 5.1. Measurements are conducted at four different swirl configurations ranging from zero swirl, labeled by S_1 , to strong swirl, labeled by S_4 . The solid lines correspond to the simple model (5.1) and the dashed lines correspond to model (5.2) that compensates for the axial overshoot. The model parameters are given in table 5.1. Despite the formation of an overshoot, the swirl does not significantly alter the axial velocity profile, which is in agreement with measurements of laminar swirling jets (Billant et al. 1998). The axial shear layer thickness increases slightly with increasing swirl, indicated by a decrease of

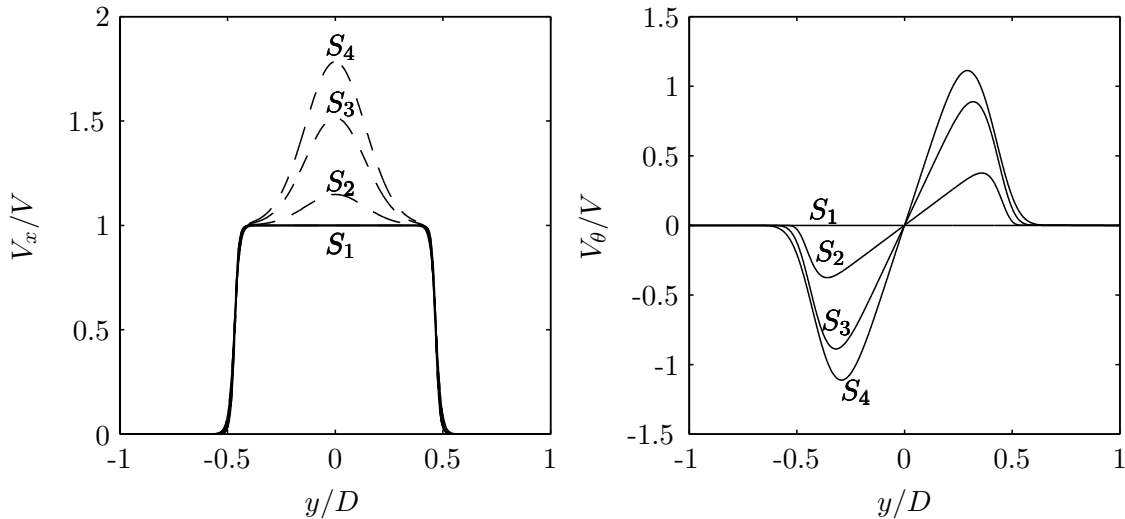


Figure 5.1: Mean velocity profiles at the nozzle for different swirl intensities. The solid lines correspond to the simple model (5.1) and the dashed lines correspond to model (5.2) that compensates for the axial overshoot. The model parameters are given in table 5.1.

	S_1	S_2	S_3	S_4
V_{cl}/V	1	1	1	1
$\Omega_{cl}R_{.5}/V_{cl}$	0	0.54	1.54	2.23
$R_{.5}/D$	0.47	0.47	0.47	0.47
R_θ/D	—	0.36	0.32	0.29
N_x	17.78	16.74	14.61	12.75
N_θ	—	10.37	6.14	4.45
r_c	—	0.42	0.42	0.42
V_{os}/V	—	0.15	0.52	0.78

Table 5.1: Parameters of the mean flow approximation (5.1) determined by a least order fit to the measured velocity profiles at at $x/D = 0$.

N_x . The azimuthal velocity profile is certainly effected by an increase in swirl. The rotation rate near the jet axis, expressed as the dimensionless ratio $\Omega_{cl}R_{.5}/V_{cl}$, is gained up to 2.23 with increasing swirl. Moreover, the radial position of the maximum azimuthal velocity R_θ moves towards the jet center and the azimuthal shear layer thickens considerable, indicated by an decrease of N_θ . The latter is not observed in the laminar swirling jet experiments conducted by Billant et al. (1998); Loiseleux & Chomaz (2003), where N_θ and R_θ remain constant with increasing swirl.

5.2.3 Quantification of Swirl at the Nozzle Exit

Several swirl number definitions exist in the literature, each being applicable to a certain flow regime, but none being universal. For the sake of comparison, the most common definitions of swirl numbers are derived at the nozzle exit and listed in table 5.2 together with

definition	references	S_1	S_2	S_3	S_4
$\frac{2 \int_0^\infty V_x V_\theta r^2 dr}{D \int_0^\infty (V_x^2 - V_\theta^2/2) r dr}$	Chigier & Chervinsky (1965); Lu & Lele (1999); Müller & Kleiser (2008); Panda & McLaughlin (1994)	0	0.19	0.46	0.6
$\frac{\sqrt{\int_0^\infty V_\theta^2/r dr}}{V_{cl}}$	Billant et al. (1998)	0	0.28	0.55	0.62
$\frac{2V_{\theta, \max}}{V_{x, \max}}$	Escudier & Keller (1985)	0	0.66	1.17	1.25
$\frac{2V_\theta(r=D/4)}{V_{cl}}$	Billant et al. (1998); Loiseleux & Chomaz (2003)	0	0.5	1.04	1.19
$\frac{\Omega_{cl} D/2}{V}$	Liang & Maxworthy (2005)	0	0.58	1.64	2.38
$\left(\frac{\Omega_{cl} R_\theta}{V}\right)^{-1}$	Billant et al. (1998); Spall et al. (1987)	∞	2.41	0.96	0.72
$\arctan\left(\frac{V_\theta}{V_x}\right)_{\max}$	Sarpkaya (1971)	0	20.52	40.64	46.01

Table 5.2: Values for different swirl number definitions at $x = 0$

the corresponding references. Throughout this investigation, the four flow configurations considered will be simply referred to as S_1 , S_2 , S_3 , and S_4 . A comparison with the listed literature reveals that the highest swirl number S_4 is still below the critical level where vortex breakdown occurs.

5.2.4 Streamwise Distribution of Mean Velocities and Turbulent Stresses

The figures 5.2 and 5.3 depict the mean flow distribution along the streamwise plane of measurement derived from PIV measurements for the non-swirling and swirling jet, respectively, together with the velocity profiles approximated by the simplified model (5.1). The agreement between the fit and the actually measured values is excellent for the non-swirling jet. For swirl configuration S_3 , the analytic approximation of the axial velocity component is also good, despite a slight underestimated shear layer thickness near the nozzle exit. The swirl profiles are represented reasonably well by the model, however, upstream of $x/D = 1$ the inflection point inside the vortex core region is not reproduced.

The contour surfaces shown in the figures 5.2 and 5.3 indicate regions of high turbulent production. they represent the normalized turbulent shear stress component $\overline{v'_x v'_r}$ for the non-swirling jet, and $\overline{v'_x v'_r}$ and $\overline{v'_r v'_\theta}$ for the swirling jet. Without swirl, $\overline{v'_r v'_\theta}$ is orders of magnitude smaller than for the swirling case and is therefore covered in noise (not shown). The contours reveal the radial maximum is located approximately at the highest radial gradient of V_θ , indicating that $\overline{v'_r v'_\theta}$ is primarily generated by the azimuthal shear. The turbulent shear stress component $\overline{v'_x v'_r}$ is also enhanced by the addition of swirl, which presumably results in an enhanced downstream growth of the axial shear layer and a shortening of the potential core region. Furthermore, the turbulent shear stresses confirm that the axial overshoot near the nozzle, which creates an additional inflection point in the axial velocity

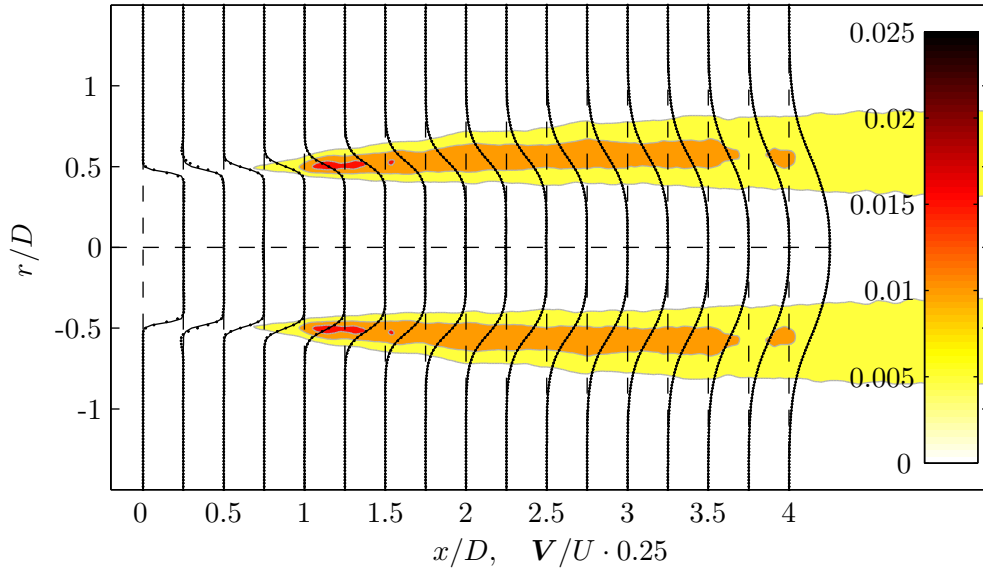


Figure 5.2: Non-swirling jet configuration S_1 : Profiles of the axial velocity are shown together with contours of the turbulent shear stress $\overline{v'_x v'_r}/V^2$. Black dots refer to measurements and black solid lines refer to the analytic approximation (5.1a).

profile, does not contribute significantly to the turbulent production, and hence, instabilities growing in the inner shear layer seem to be negligible. Similarly, the aforementioned inflection point of the azimuthal profile near the jet center upstream of $x/D = 1$ does not generate turbulent shear stress and it is not expected to promote dominant instabilities. The poor approximation of this feature is therefore considered to be insignificant. Note that PIV measurements are only conducted for the unforced flow where the coherent velocity cannot be extracted. Hence, the turbulent shear stresses discussed here are derived from the fluctuating velocity field that comprises stochastic and coherent motion.

5.2.5 Parametrization of the Divergent Mean Flow

The evolution of the mean flow with downstream distance is characterized by the streamwise distribution of the model parameters. The parameters that scale the axial velocity profiles are shown in figures 5.4a, 5.4c, and 5.4e and those corresponding to the azimuthal velocity profile are shown in figures 5.4b, 5.4d, and 5.4f. The figures 5.4g display the streamwise development of the momentum thickness δ_x . It is used as the characteristic length scale throughout this chapter and represents a measure for the axial shear layer thickness, defined as

$$\delta_x = \int_{R_{.05}}^{R_{.95}} \frac{V_x}{V_{cl}} \left(1 - \frac{V_x}{V_{cl}}\right) dr. \quad (5.3)$$

Figure 5.4a indicates the axial extent of the potential core, the region where V_{cl} is equal to the bulk velocity V . For the non-swirling jet (S_1), the potential core exceeds the measurement domain. By increasing the swirl, the potential core region is significantly shortened due to the increased growth of axial shear layer thickness. For S_3 , V_{cl} declines for $x/D > 2$, whereas Loiseleux & Chomaz (2003) measures a potential core length of

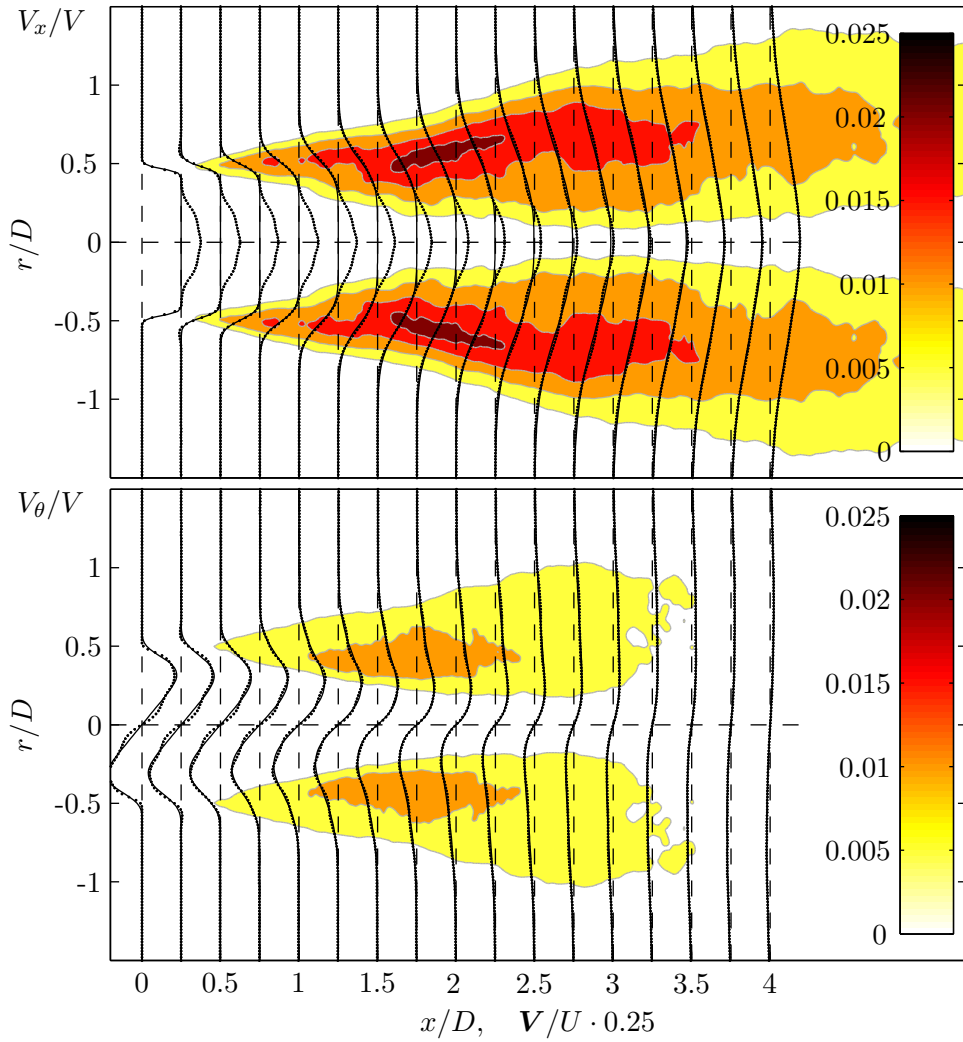


Figure 5.3: Swirling jet configuration S_3 : Profiles of the axial velocity are shown. Black dots refer to measurements and black solid lines refer to the analytic approximation (5.1). Symbols refer to experimental data. Contours represent turbulent shear stresses $\overline{v'_x v'_r}/V^2$ (top) and $\overline{v'_r v'_\theta}/V^2$ (bottom)

$x/D \approx 3.8$ at comparable swirl intensity. Hence, the presently found streamwise extent of the potential core is much smaller than for laminar swirling jets.

It is interesting to note that the swirl parameter (inverse Rossby number) shown in figure 5.4b remains perfectly constant within the potential core, despite the downstream decay of the maximum swirl velocity $V_{\theta, \max}$. It is the only local swirl number of the definitions listed in table 5.2 that remains constant within the potential core. All other numbers show a dependence on the axial distance already close to the nozzle exit, which makes a quantitative comparison to the investigations of Billant et al. (1998); Gallaire & Chomaz (2003); Loiseleux et al. (1998) very difficult. It is further worth noting that downstream of the potential core, the Rossby number decays at the same rate independent of the swirl intensity and it ultimately collapses to one curve that asymptotes zero.

The quantities shown in figure 5.4c, 5.4e, and 5.4f indicate the enhanced jet spreading with increasing swirl. The non-monotonic development of R_θ is somewhat unexpected

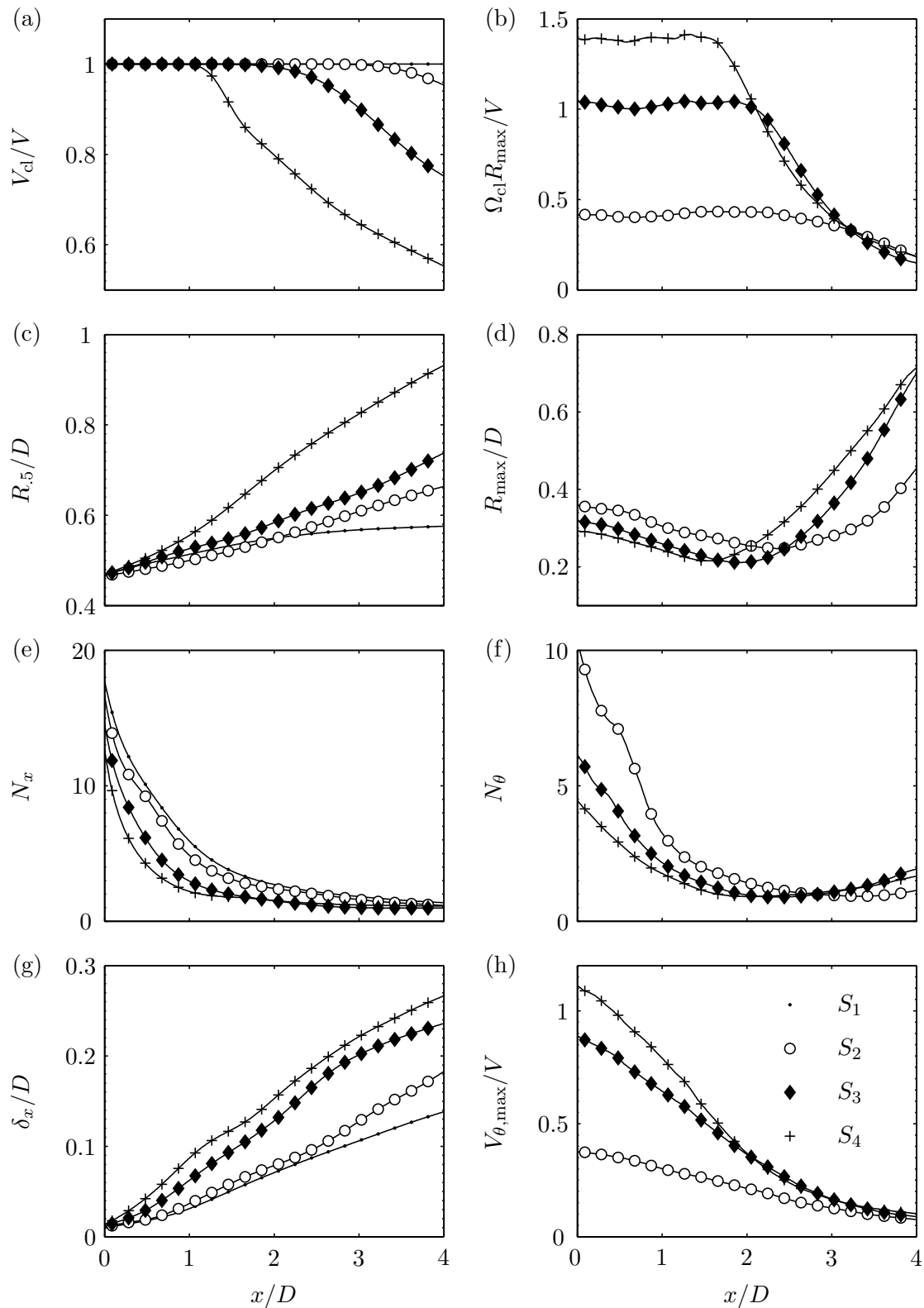


Figure 5.4: (a-f) Streamwise development of mean flow parameters of (5.1); Streamwise development of axial momentum thickness (g) and maximum swirl velocity (h).

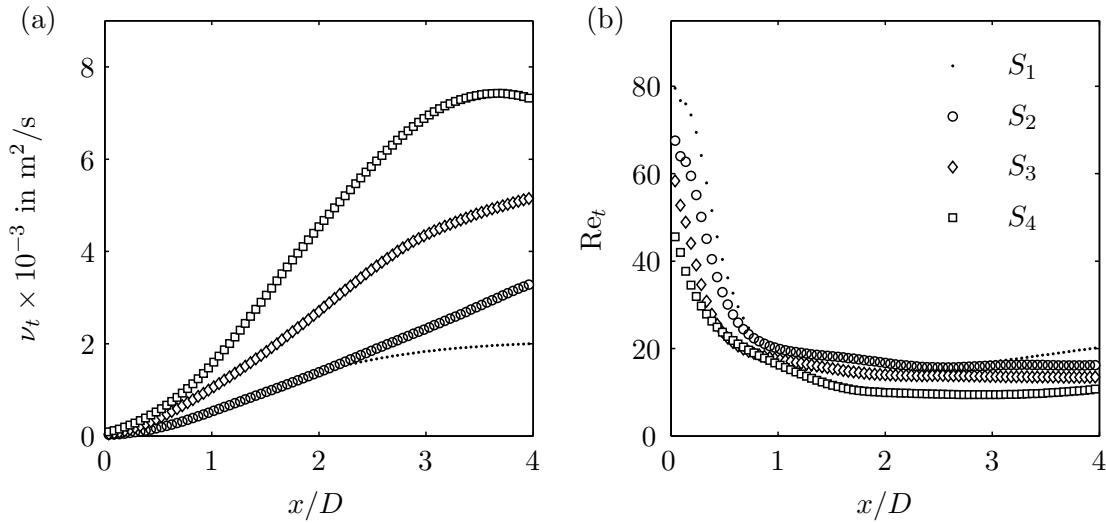


Figure 5.5: Spatial development of eddy viscosity (a) and turbulent Reynolds number (b) for the swirl configurations considered.

(figure 5.4d). Within the potential core, the downstream growth of the azimuthal shear layer leads to a displacement of the maximum of the swirl component to the jet center, while the constant swirl parameter (figure 5.4b) implies that Ω_{cl} must increase correspondingly. Downstream of the potential core, the maximum of V_θ moves outwards and the azimuthal shear layer thickness decreases, indicated by an increasing shape parameter N_θ . The maximum azimuthal velocity $V_{\theta,\max}$ decelerates drastically within the potential core and collapses for all swirl configurations at $x/D > 3.5$ in a similar manner as the inverse Rossby number. Apparently, the growth of the azimuthal shear layer is coupled to the growth of axial shear layer in the potential core region, which leads to a constriction of the vortex core. Further downstream, the axial shear layer merges on the jet axis, the vortex core spreads radially, and the inverse Rossby number decays.

5.2.6 Streamwise Distribution of the Eddy Viscosity

Figure 5.5a displays the streamwise distribution of the weighted eddy viscosity ν_t averaged in radial direction. A detailed description of how this quantity is derived from the PIV data is given in section 2.4.4. For all swirl configurations, the turbulent viscosity is nearly equal at the nozzle exit and grows rapidly with downstream distance. The growth is enhanced with increasing swirl in consistency with the enhanced shear layer growth discussed in section 5.2.5. Without swirl, ν_t asymptotes to a constant level of approximately 0.002 at $x/D > 3$ (Figure 5.5b). The turbulent Reynolds number decays rapidly upstream of $x/D = 1$ and then asymptotes at similar constant values within the range $10 < \text{Re}_t < 20$. The growth of eddy viscosity appears to be balanced by the growth of momentum thickness.

5.3 Stability at the Nozzle Exit

From a preliminary spatio-temporal analysis of the considered configurations, the existence of absolute instability for $|m| \leq 3$ can be excluded. This implies the flow is globally stable

and the signaling problem is valid. Hence, the spatially traveling disturbance waves are best modeled by the spatial stability analysis (Huerre & Monkewitz 1990). The Orr–Sommerfeld type eigenvalue problem is, therefore, solved for complex eigenvalues α and given real ω . Within the quasi-parallel approximation, $-\alpha_i$ refers to the streamwise (spatial) growth rate and α_r to the streamwise wavenumber. The flow is considered as spatially unstable when a disturbance grows with x , i.e. when α_i is negative. The mean flow is made dimensionless by using δ_x as the characteristic length scale and V as the characteristic velocity scale. The eigenvalues α and the frequencies ω that are presented throughout this investigation are always normalized with respect to δ_x and V , which vary significantly in axial direction.

A linear stability analysis is applied to the mean flow at the nozzle exit ($x/D = 0$) for different swirl intensities. As described in section 5.2.2, the mean flow at the nozzle exit is characterized by a top-hat axial velocity profile that is nearly independent of the swirl. The azimuthal velocity profile of the swirling jet is characterized by a linear region near the jet center (solid body rotation) and an outward decaying region (azimuthal shear layer). Both depend strongly on the amount of swirl. Hence, the stability of the flow at the nozzle exit is solely altered by the varying swirl component. For the following discussion, the reader is encouraged to use the schematic representation displayed in figure 2.2 in order to distinguish between the different mode alignments.

5.3.1 Shear Instability

Figure 5.6 provides an overview of the influence of swirl on the dominant instability. This rather unusual plotting style appears several times throughout this chapter and is therefore described in more detail at this point. The filled contours represent the dimensionless spatial growth rate $-\alpha_i\delta_x$ computed for various frequencies ω_r and azimuthal wavenumbers m . All contour plots shown within one figure have always the same contour levels. Regions of negative growth rate ($-\alpha_i\delta_x < 0$) are blanked. The labeled contour lines refer to the dimensionless axial wavenumbers $\alpha_r\delta_x$ and are also only displayed for unstable modes ($-\alpha_i\delta_x > 0$). For better visibility, the contour lines of $\alpha_r\delta_x$ are black, while the lines separating the filled contours of $-\alpha_i\delta_x$ are light-gray. For most cases, we allow the frequency and axial wavenumber to have positive and negative values. This implies redundant information for $\alpha_i\delta_x$ contours shown in the ω_r - m -plane, as modes at negative frequencies have the same growth rate and streamwise wavenumber with the latter having an opposite sign (see transformation (2.4)). Recall that the label S_1 refers to the non-swirling jet, while S_2 , S_3 and S_4 refer to swirling jets at increasing swirl intensity. A detailed description of the considered mean flow configurations are given in chapter 5.2, while the corresponding swirl numbers are listed in table 5.2.

The stability analysis applied at the nozzle reveals two unstable eigenvalues, each corresponding to a different instability mode. In this section we focus on the mode with higher amplification rate, while the additional, less unstable, mode is described in the subsequent section. At the nozzle exit, the non-swirling jet (figure 5.6a) is most unstable to axisymmetric disturbances in agreement with previous investigations (e.g., see Cohen & Wygnanski 1987; Crighton & Gaster 1976; Gallaire & Chomaz 2003). In the absence of swirl, co-rotating and counter-rotating modes are equally unstable. The growth rate decays continuously with increasing azimuthal wavenumber, yielding a cutoff at $|m| = 18$. The streamwise wavenumber of maximum amplification is approximately $\alpha_r\delta_x = 0.2$ and

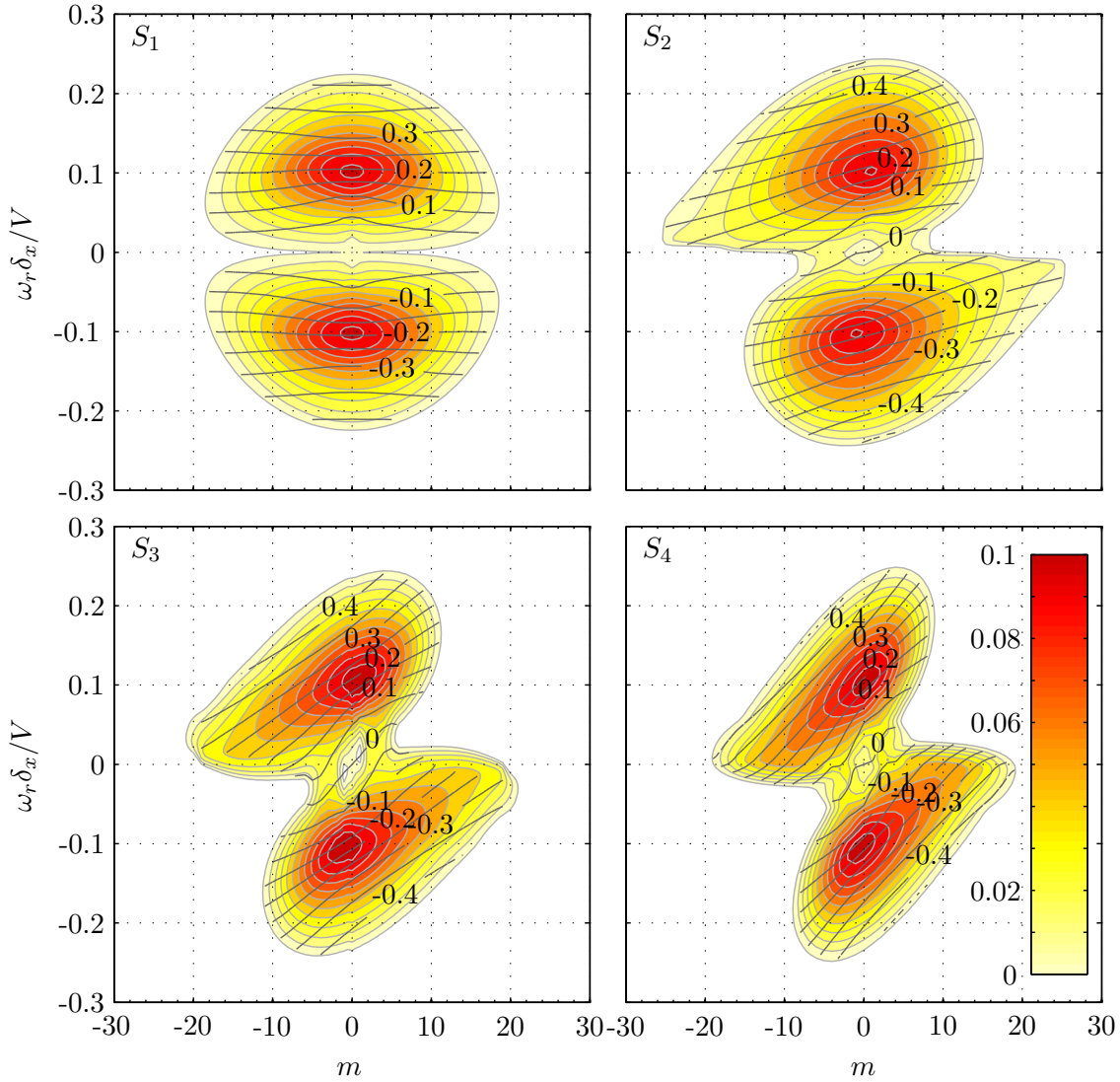


Figure 5.6: Instability of the shear mode at the nozzle exit ($x/D = 0$) for the non-swirling jet (S_1) and the swirling jets (S_2 - S_4). Filled contours refer to the spatial growth rate $-\alpha_i \delta_x$. Dark-gray labeled contour lines refer to the streamwise wavelength $-\alpha_r \delta_x$. Stable modes $-\alpha_i \delta_x < 0$ are blanked. Quantities are derived theoretically for varying azimuthal wavenumbers m and frequencies ω_r .

remains constant for varying m . The overall maximum amplification and corresponding frequency agrees well with the values reported by Cohen & Wygnanski (1987). This brings credibility to the measured mean flow on which the analysis is based.

By imposing swirl onto the flow (confer with S_2 - S_4 in figure 5.6), the symmetry breaks. Counter-rotating modes at low frequencies are destabilized, whereas co-rotating modes at high frequencies become less unstable. By increasing swirl, the filled contours cross the $\omega_r = 0$ line, indicating the steady modes are unstable, in contrast to the non-swirling jet. However, the maximum growth rates and associated streamwise wavenumbers are nearly unaffected by the swirl component. This indicates that this instability is driven by the axial shear layer similar to the Kelvin–Helmholtz instability of the non-swirling baseline case. Throughout the remaining part of this thesis, we will, therefore, refer to this instability as

the *shear instability mode* in differentiation to the *centrifugal instability mode* that is also found in the present flow configuration.

The contours in figure 5.6 reveal that the growth rates of the shear mode is not significantly affected by the swirl and solely depends on the axial velocity profile. However, there is yet a considerable influence of the swirl component on the selected frequencies and azimuthal wavenumbers that are most amplified. This is discussed in detail by considering profiles of the streamwise growth rate α_i , the streamwise wavenumber α_r , and the streamwise phase velocity $c_{\text{ph}} = \omega_r/\alpha_r$ for the non-swirling (S_1) and strongly swirling jet (S_3) presented in figure 5.7. To avoid redundancy, m takes only positive values, with α of negative m and positive ω_r being transformed to positive m and negative ω_r . Hence, the four variants of possible mode alignments refer conveniently to the four quadrants of the α_r - ω_r -diagram (see labels in figure 5.7a). Note that figure 5.7a and c depict only those quantities that refer to unstable modes with $-\alpha_r > 0$.

For the non-swirling baseline case (figure 5.7a, left), unstable modes are in the first and third quadrant, depicting this flow to be unstable to co-rotating counter-winding and counter-rotating co-winding modes. The wavenumbers increase approximately linearly with ω_r and do not change considerably with m . Moreover, the non-swirling jet is stable to streamwise modes ($\alpha_r = 0$) and steady modes ($\omega_r = 0$).

For the swirling jet configuration S_3 , the streamwise wavenumbers and growth rates of the axisymmetric modes ($m = 0$) are very similar to the non-swirling jet. These modes are unaffected by the addition of swirl, as they are purely driven by the axial shear layer. The non-axisymmetric modes ($m \neq 0$) are affected by the azimuthal shear. With swirl, the streamwise wavenumber depends on the azimuthal mode number, yielding decreasing α_r for increasing m (figure 5.7a, right). This relation implies that, within a certain frequency and wavenumber band, unstable non-axisymmetric modes exist in the fourth quadrant, which renders swirling jets to be receptive to steady modes, to co-rotating co-winding modes, and to streamwise modes. The non-winding (streamwise) modes are purely driven by azimuthal shear in contrast to the axisymmetric mode that is purely driven by the axial shear. The spatial growth rate displayed in figure 5.7b for the S_1 and S_3 configuration replicates the results shown in figure 5.6a and c. These diagrams emphasize that the swirling and non-swirling jet is unstable to the same finite frequency band. Hence, the axial shear layer acts as a band-pass filter with the band being determined by the shape of the axial velocity profile. The selected wavenumbers, however, are altered by the addition of swirl (figure 5.7a).

The streamwise phase velocity c_{ph} for the non-swirling jet shows typical features of the Kelvin–Helmholtz instability (figure 5.7c, left). For frequencies near neutral amplification, c_{ph}/V asymptotes 0.55, which implies that waves propagate in downstream direction at approximately half the bulk velocity. Moreover, in the absence of swirl, waves are weakly dispersive ($\partial c_{\text{ph}}/\partial \omega_r \approx 0$) for a wide range of frequencies. According to Cohen & Wygnanski (1987), non-dispersive waves in shear layers that travel downstream with equal phase velocity interact nonlinearly, provided that specific resonance conditions are satisfied. The weak dispersiveness of non-swirling jets allows for nonlinear interactions between a downstream traveling wave at neutral amplification and its subharmonic (Paschereit et al. 1995). This is associated with the process of vortex merging that is the key driver for the streamwise growth of the shear layer in the near-field of axisymmetric non-swirling jets (Gutmark

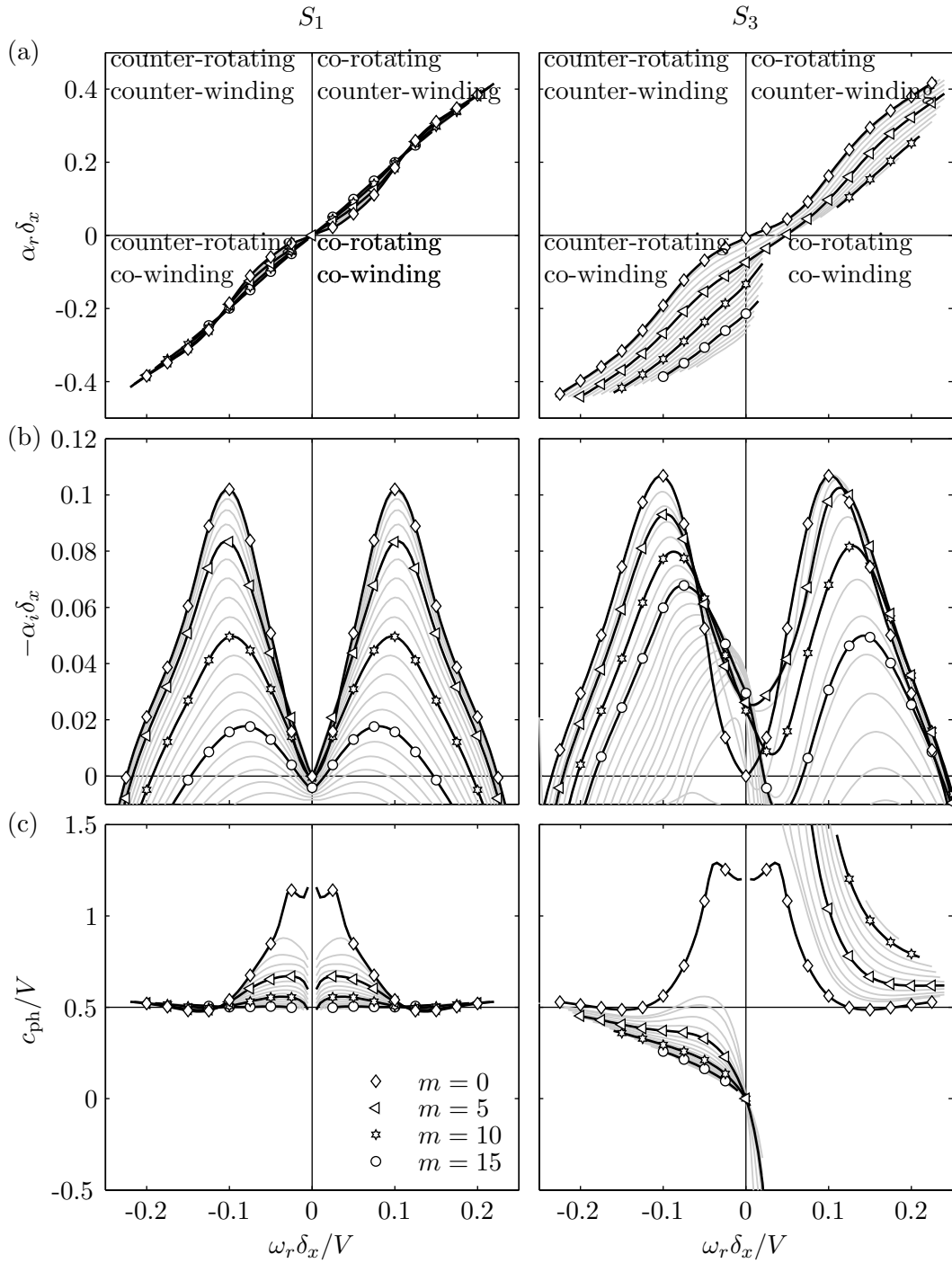


Figure 5.7: The streamwise wavenumber α_r (a), the spatial growth rate $-\alpha_i$ (b), and the axial phase velocity $c_{ph} = \omega_r / \alpha_r$ (c) versus the frequency ω_r of the shear mode; only unstable modes are shown. Quantities are derived from linear stability analysis of the mean flow at $(x/D = 0)$ for the non-swirling jet (S_1) and the swirling jet (S_3).

et al. 1995; Ho & Gutmark 1987). Moreover, the constancy of c_{ph} for varying m enables nonlinear interactions between waves at different azimuthal mode numbers, which may lead to a drastic distortion of the mean flow (Long & Petersen 1992).

These mechanisms are not as rigorously applied to swirling jets. As shown on the right side of figure 5.7c, only the modes with $m < 2$ may resonate with their subharmonics. For higher azimuthal modes, the phase velocity at the neutral frequency differs significantly from that at the subharmonic. Moreover, the dependency of c_{ph} on m inhibits an interaction between two azimuthal modes at the same frequency. A subharmonic resonance between two different azimuthal modes is principally possible. For instance, the $m = 1$ mode at $\omega_r = 0.2$ could resonate with the subharmonic $\omega_r = 0.1$ of the $m = 0$ mode. However, at these frequencies, the phase velocity of the two modes depend differently on $\omega_r \delta_x / V$ and, thus, on x . This implies that the resonance conditions for two modes are only fulfilled at a single streamwise location and it is, thus, very unlikely to find a mode pair that interacts within a sufficiently large streamwise domain. Nonetheless, the axisymmetric mode should be the best candidate for a subharmonic resonance as its streamwise phase velocity is not effected by the swirl.

The dependence of c_{ph} and α_r on m is directly related to the swirl component. In a swirling jet, a disturbance initiated at the nozzle lip is convected in axial *and* azimuthal direction. Hence, the group velocity of a traveling wave has a non-zero axial and azimuthal component. This allows to define a group rotation rate $\Omega_{\text{gr}} = (\partial\omega_r/\partial m)_{\alpha_r=\text{const.}}$ in addition to the commonly known axial group velocity $c_{\text{gr}} = (\partial\omega_r/\partial\alpha_r)_{m=\text{const.}}$. Ω_{gr} represents the slope of the $\alpha_r \delta_x$ contour lines shown in figure 5.6. Accordingly, it increases successively with increasing swirl for all unstable modes. A positive group rotation rate implies that the streamwise wavenumber must decrease with increasing azimuthal wavenumber at constant ω_r . Moreover, the non-zero Ω_{gr} is related to the appearance of unstable streamwise modes ($\alpha_r = 0$) for the swirling jet. For these modes, the phase rotation rate $\Omega_{\text{ph}} = \omega_r/m$ is equal to the group rotation rate Ω_{gr} . For the non-swirling jet, a disturbance travels only in axial direction ($\Omega_{\text{gr}} \approx 0$) and the group velocity is solely given by c_{gr} that is, assuming non-dispersiveness, equal to c_{ph} . The non-zero Ω_{gr} for swirling jets is supported by the experimental investigation of the impulse response that will be discussed in section 5.6.

The radial amplitude distribution of the most unstable modes, given by their eigenfunctions, are shown in figure 5.8 for the non-swirling (S_1) and swirling jet (S_3). The eigenvector $X = (H, iF, G, P)$ is normalized with respect to the Euclidean norm $\|X\| = \sqrt{(X, X)}$. The radial coordinate is normalized using the jet half width $R_{.5}$ and the momentum thickness δ_x . Hence, the zero coordinate corresponds to the center of the axial shear layer. The eigenfunctions are not significantly altered by the swirl. All velocity components peak approximately at the center of the axial shear layer ($r = R_{.5}$), indicating the importance of the axial shear layer for this type of instability. It is interesting to note that the azimuthal component of the axisymmetric mode $m = 0$ is not zero for the swirling flow in contrast to the non-swirling flow.

Summarizing this section, the most unstable modes at the nozzle exit are driven by a shear instability, with the overall maximum spatial growth rate determined by the shape of the axial velocity profile. The selection of the most amplified axial wavenumbers α_r^{max} depends only weakly on S and m , as shown in figure 5.6 and, more explicitly, on the left side of figure 5.9. However, the corresponding frequencies ω_r^{max} depend strongly on S and

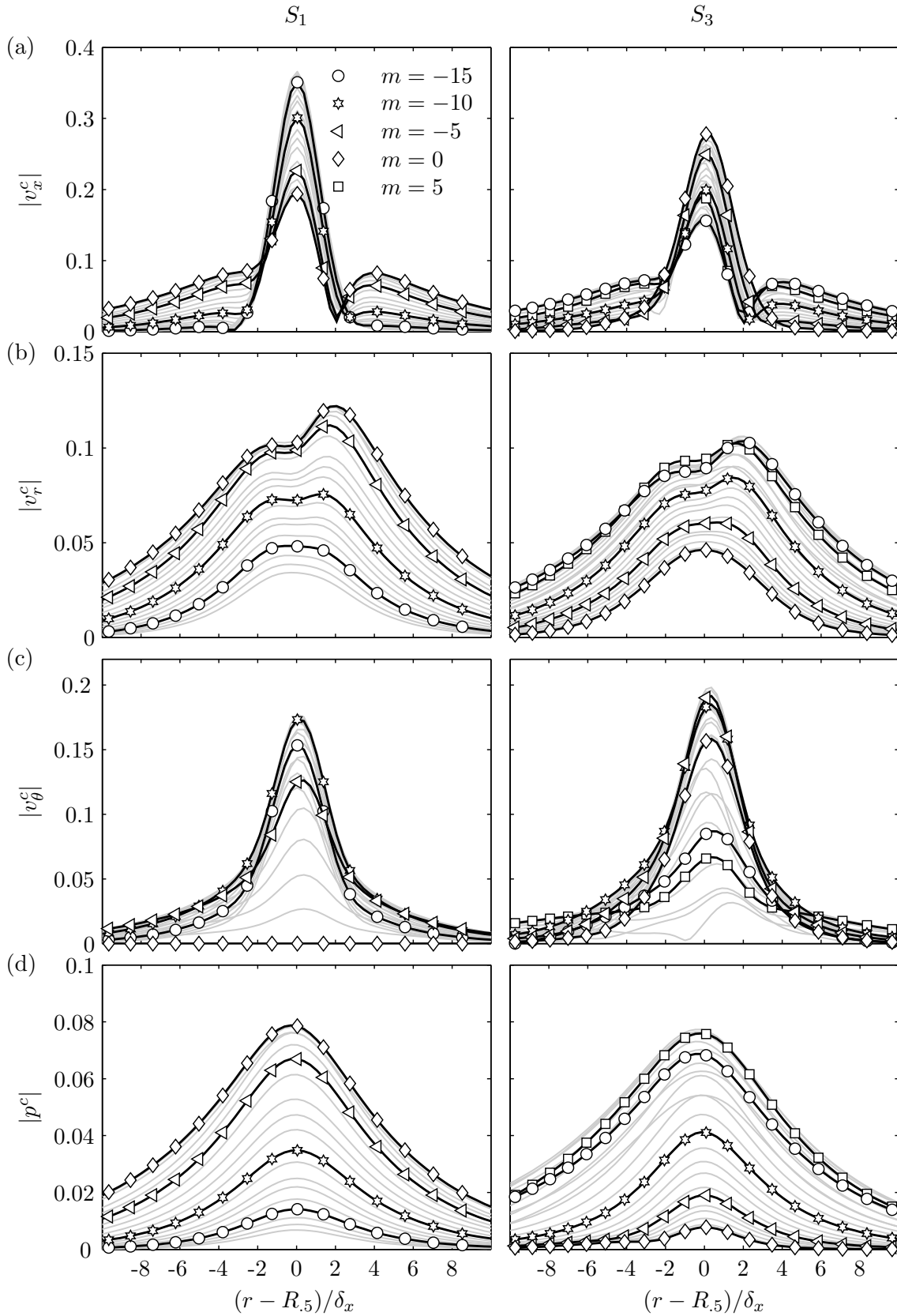


Figure 5.8: Amplitude distribution of the shear mode at the nozzle exit ($x/D = 0$) for the non-swirling jet S_1 (left column) and the swirling jet S_3 (right column) calculated for frequencies at maximum spatial amplification ω_r^{\max} . Rows refer to the axial (a), radial (b), and azimuthal (c) velocity component and the coherent pressure (d).

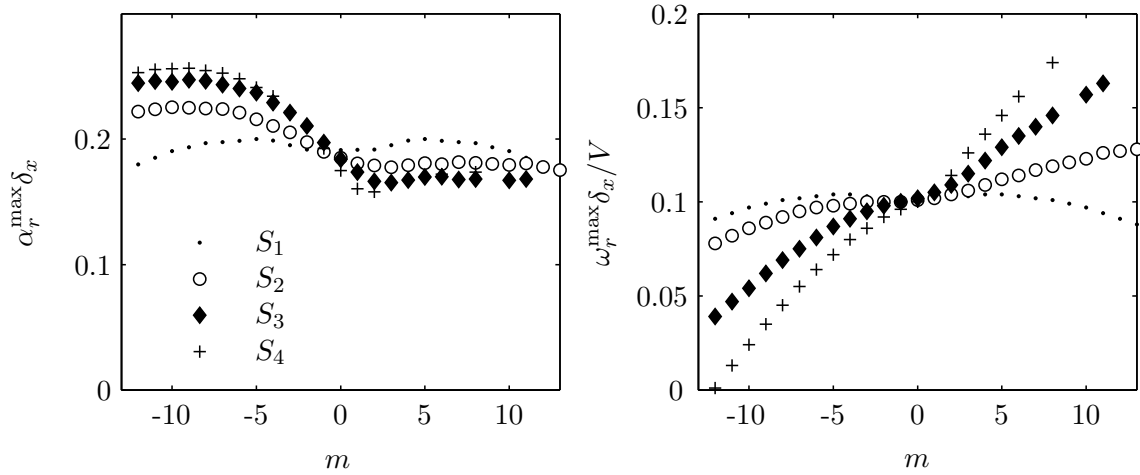


Figure 5.9: Axial wavenumber α_r^{\max} (left) and frequency ω_r^{\max} (right) at maximum growth rate $-\alpha_i$ for different azimuthal wavenumbers and swirl intensities at the nozzle exit ($x/D = 0$)

m due to the non-zero azimuthal group rotation rate Ω_{gr} caused by the swirling motion of the mean flow. This dependency is a kinematic effect, as stated by Martin & Meiburg (1994), and can be illustrated by considering inclined waves on a infinite long cylinder as a model for instability waves traveling along a swirling jet. Consider first waves fixed to the rotating cylinder. For a given wavenumber (here α_r^{\max}), the axial phase velocity depends on the rotation rate of the cylinder (here Ω_{gr} or S) and the inclination of the waves (m/α_r^{\max}), yielding $c_{\text{ph}} \propto \Omega_{\text{gr}} m / \alpha_r^{\max}$. Now, consider a non-rotating cylinder that moves in axial direction at constant velocity (here $V/2$). The phase velocity is then given by $c_{\text{ph}} = V/2$, independent of the inclination. Superimposing these two cases results in the relation $c_{\text{ph}} \propto V/2 + \Omega_{\text{gr}} m / \alpha_r^{\max}$ and with $c_{\text{ph}} = \omega_r / \alpha_r^{\max}$ we get the proportionality $\omega_r \propto V/2 \alpha_r^{\max} + \Omega_{\text{gr}} m$, which describes the influence of swirl on ω_r and m of the most unstable wavenumber α_r^{\max} .

5.3.2 Centrifugal Instability

The radial stratification of angular momentum can lead to centrifugal instability in swirling jets. Rayleigh's well known inviscid criterion provides a necessary and sufficient condition for axisymmetric disturbances to be centrifugally unstable. For steady ambient fluid and the circulation Γ being positive, the stratification of angular momentum is unstable if Γ decays monotonically in radial direction, yielding

$$d\Gamma/dr < 0.$$

In the present investigation, the azimuthal shear layer is indeed centrifugally unstable as shown in figure 5.10. The flow at the nozzle exit should, ideally, reveal a dimensionless circulation that is parabolic in radial direction with a sharp peak at $r = D/2$ with value unity that drops thereafter to zero (solid body rotation). In practice, however, a boundary layer generated by the nozzle wall causes a smooth drop of the azimuthal velocity component in radial direction. The radial extent of this initial azimuthal shear layer, which is $R_{\text{max}} <$

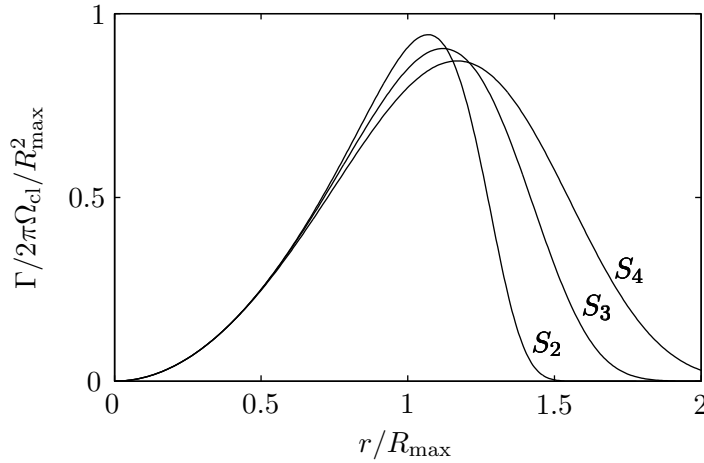


Figure 5.10: Radial stratification of angular momentum Γ

$r < D/2$, depends on the swirl intensity. Hence, Γ is nearly parabolic for $r < R_{\max}$ and drops off smoothly in outward direction for $r > R_{\max}$.

In contrast to the shear mode, a centrifugal mode is expected to primarily depend on the azimuthal profile, and indeed, a detailed inspection of the dispersion relation reveals a second unstable mode that exists only for the swirling jets. The corresponding contours of $-\alpha_i \delta_x$ in the ω_r - m -plane are shown in figure 5.11 for different swirl intensities. Its overall maximum growth rate increases with increasing swirl, but it gains no more than a third of the maximum growth rate of the shear mode for the swirl intensities considered. For the weakly swirling jet S_2 , centrifugal modes with $m = -7$ and $\omega_r \delta_x / V \approx 0.3$ are most unstable. For stronger swirl (S_3 and S_4), modes with $m = -2$ and $\omega_r \delta_x / V \approx 0.5$ are most amplified. The cutoff azimuthal wavenumber for S_3 is $m = 28$ for negative ω_r and $m = 4$ for positive ω_r , revealing a strong tendency of this instability to counter-rotating modes. The streamwise wavenumber α_r , indicated as black contour lines in figure 5.17, is much larger in regions of maximum amplification in comparison to the shear instability. The centrifugally unstable azimuthal shear layer selects short axial and azimuthal wavelengths at high frequencies, a typical characteristic of centrifugal instability.

Figure 5.12 displays profiles of streamwise growth rate, axial wavenumber, and axial phase velocity of the centrifugal instability modes. The magnitude of α_r increases linearly with increasing frequency, yielding an axial group velocity $c_{gr} \approx 1$. The axial wavenumber decays with increasing m similar to the shear instability. However, neither co-rotating co-winding nor counter-rotating counter-winding modes are unstable. Moreover, this type of instability does not promote steady or streamwise modes. The axisymmetric mode ($m = 0$) is unique, as its axial phase velocity is equal unity for all unstable frequencies (figure 5.12c), revealing that the centrifugal instability promotes non-dispersive axisymmetric waves that travel in downstream direction with the same speed as the bulk velocity. All non-axisymmetric modes asymptote $c_{ph} = V$ for higher ω_r , but they remain dispersive within their unstable frequency band.

As mentioned earlier, the shear modes of the non-swirling jet are non-dispersive for higher frequencies with $c_{gr} \approx c_{ph} \approx 0.5V$ (figure 5.7c) meaning that the individual waves and the entire wave packet travel in axial direction with approximately half the jet velocity. This is consistent with the amplitudes of the shear modes that peak at $R_{.5}$ (see figure 5.8),

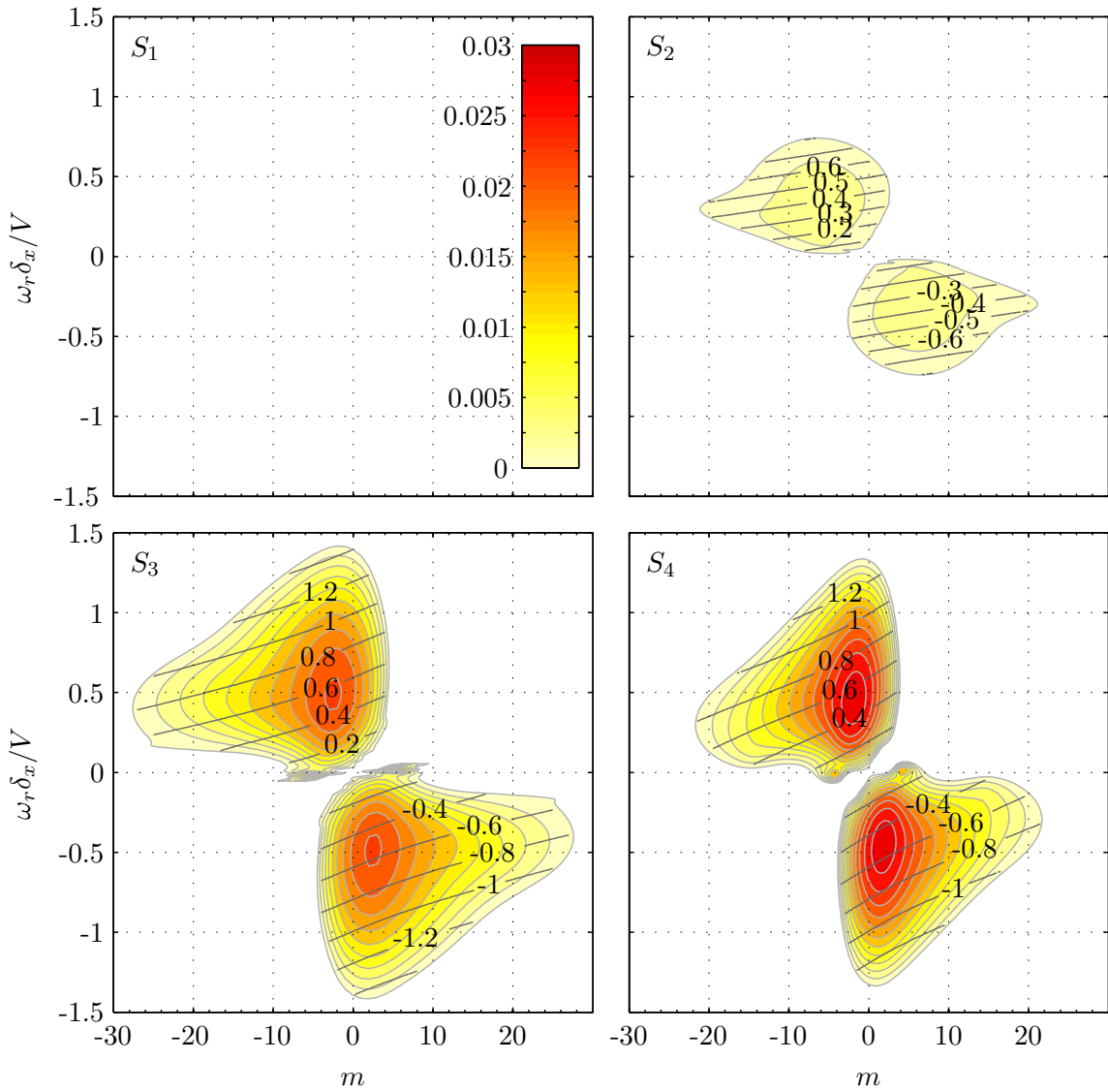


Figure 5.11: Instability of centrifugal mode at $x/D = 0$ for the non-swirling jet (S_1) and the swirling jets (S_2 - S_4). Same plot style as in figure 5.6.

the radial location where $V_x = 0.5V$. In contrast, the amplitudes of the centrifugal modes do not peak at $R_{.5}$ as they are generated in the azimuthal shear layer with its center located at the vortex core radius R_v . This length scale is derived from the mean flow model parameters using $R_v = R_{\max}(1/N_\theta)^{-1/N_\theta}$, with N_θ being the shape parameter of the azimuthal shear layer (see section 5.2 for details). It corresponds to the center of the azimuthal shear layer (Gallaire & Chomaz 2003). Eigenfunctions of the centrifugal instability reveal that the magnitude of v_r^c , v_x^c , and v_θ^c of the most energetic modes ($3 < m < 6$) are indeed located around R_v (figure 5.13). The modes at higher negative azimuthal wavenumbers ($m < -10$) are less unstable and their peaks are shifted towards the jet centerline. The vortex core radius R_v is located closer to the jet axis than the center of the axial shear layer ($R_v/R_{.5} = 0.91$). Hence, the centrifugal modes are located inside the potential core and are convected downstream with the bulk velocity V . This explains the axial group velocity of $c_{\text{gr}} \approx V$.

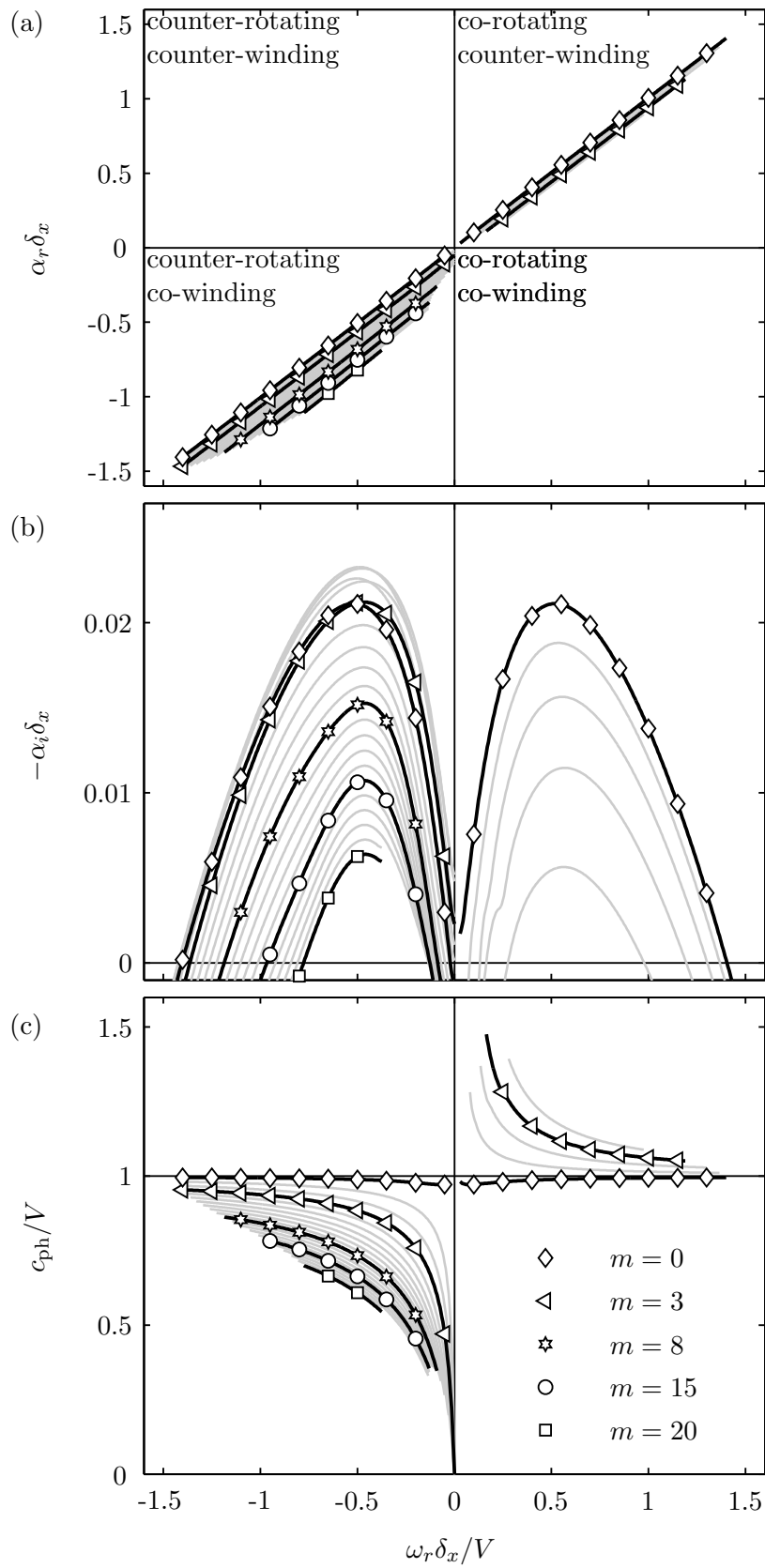


Figure 5.12: The streamwise wavenumber α_r (a), the spatial growth rate $-\alpha_i$ (b), and the axial phase velocity $c_{ph} = \omega_r / \alpha_r$ (c) versus the frequency ω_r of the centrifugal mode; only unstable modes are shown. Quantities are derived from linear stability analysis of the mean flow at $(x/D = 0)$ for the swirling jet (S_3).

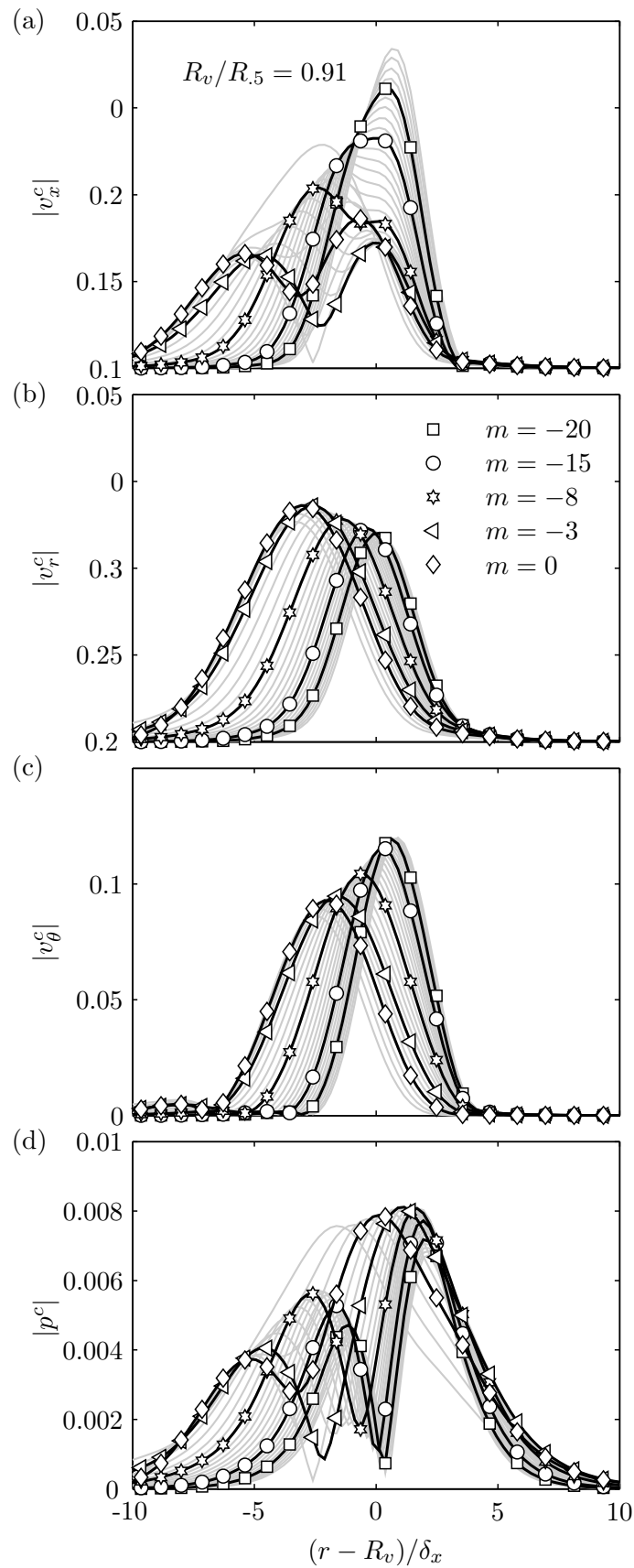


Figure 5.13: Amplitude distribution of the centrifugal mode at the nozzle exit ($x/D = 0$) for the swirling jet S_3 calculated for frequencies at maximum spatial amplification ω_r^{\max} . Rows refer to the axial (a), radial (b), and azimuthal (c) velocity component and the coherent pressure (d).

In conclusion, a second, less unstable, mode is found that is of centrifugal type. It promotes primarily counter-rotating co-winding modes at short axial and azimuthal wavelengths at much higher frequencies than the shear instability. The overall maximum spatial growth rate increases with increasing swirl. Waves are most energetic in the azimuthal shear layer that is mainly located inside the potential core region. This causes the modes to travel downstream with the bulk velocity.

5.4 Streamwise Evolution of Instability

The stability analysis of the mean velocity profiles at the nozzle exit reveal the coexistence of a shear instability and a centrifugal instability, with the previous being more unstable. Both instabilities promote modes at a wide range of m , ω_r , and α_r . As a next step, the downstream development of these instabilities is investigated. Due to the divergence of the jet, the mean flow and corresponding stability characteristics change significantly in streamwise direction, which implies that certain modes stabilize with downstream distance and die away, while other modes are continuously amplified. To obtain the overall growth of the instability modes, it is necessary to perform the stability analysis at various streamwise locations following the quasi-parallel approach introduced in section 2.4. It is understood that the quasi-parallel assumption is responsible for an increase in amplification rates of the linear modes and may not accurately predict second order, nonlinear interactions among modes that may resonate with one another to dominate the large structure observed. The complex analysis of such interactions is mostly beyond the scope of this thesis. In line with the previous section, we will first consider the shear instability followed by a discussion of the centrifugal instability.

5.4.1 Shear Instability

The Kelvin–Helmholtz instability in axisymmetric non-swirling jets have been investigated by numerous researchers. It will be considered as a benchmark to validate the present numerical results and the mean flow on which the analysis is based on. At the nozzle exit, where the shear layer is thin, the non-swirling jet is known to be unstable to various axial and azimuthal wavenumbers and frequencies (e.g., see [Cohen & Wygnanski 1987](#)). With increasing distance from the nozzle, the number of unstable azimuthal modes decreases successively. At the end of the potential core, only the bending modes with $m = \pm 1$ remain unstable.

The present investigation shows very similar results. Figure 5.14 displays the contours of spatial growth rate in the ω_r - x -plane for $0 \leq m \leq 3$. Recall that in the absence of swirl, co-rotating counter-winding modes have equal growth rates and wavenumbers as the counter-rotating co-winding modes and hence, we can restrict their presentation, as for instance in figure 5.14, to positive m and ω_r without loss of generality. The axisymmetric mode, which is most unstable at the nozzle exit, becomes stable at $x/D \approx 3$. All non-axisymmetric modes except for $m = \pm 1$ stabilize in downstream direction with their neutral point located closer to the nozzle for higher $|m|$. The frequency and wavelength of the most unstable mode remains approximately constant with x , indicating the appropriate choice of the velocity and length scale.

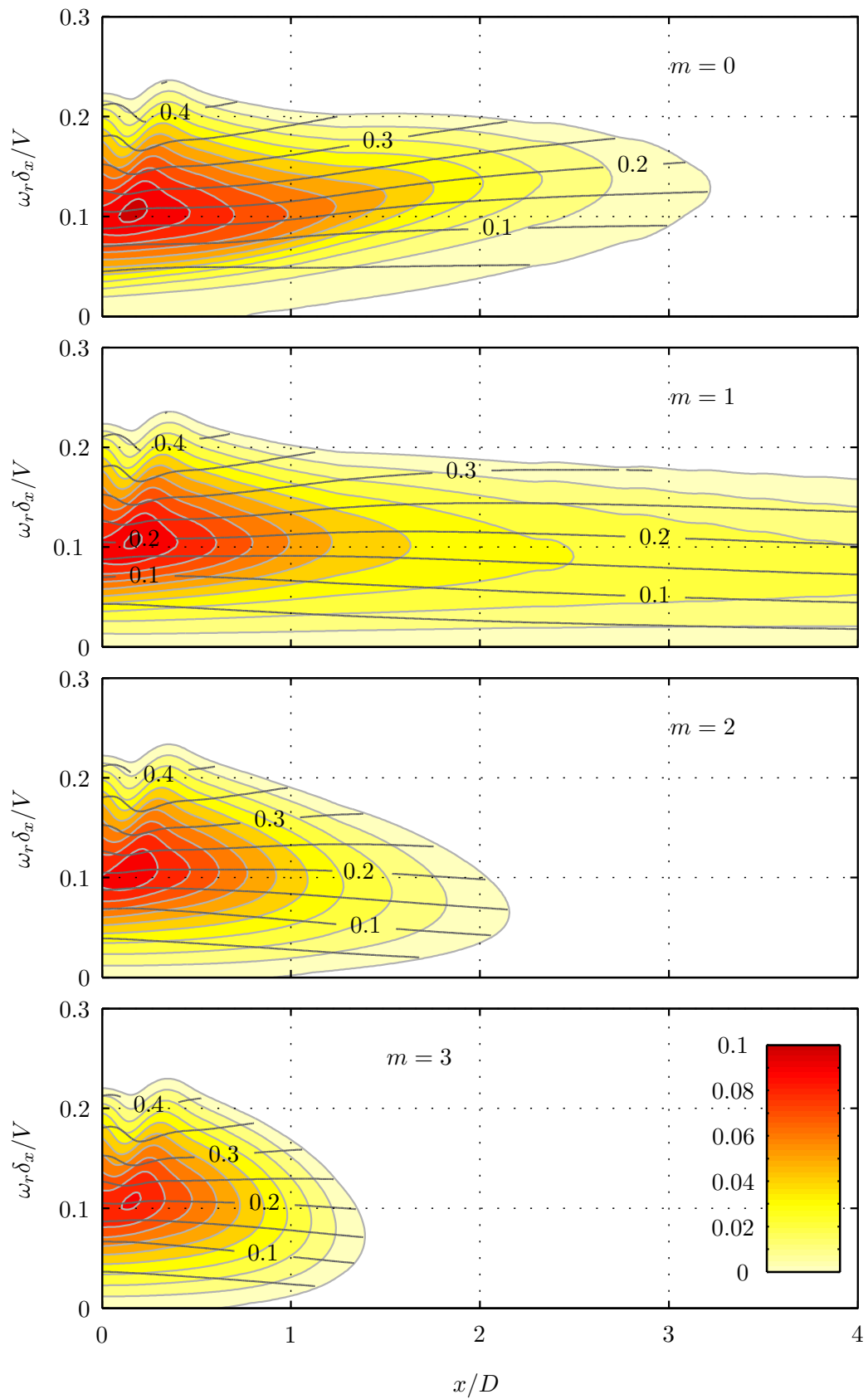


Figure 5.14: Streamwise evolution of spatial growth rate of the shear mode for the non-swirling jet S_1 for the azimuthal wavenumbers $m = (0, 1, 2, 3)$ (from top to bottom). Same plot style as in figure 5.6.

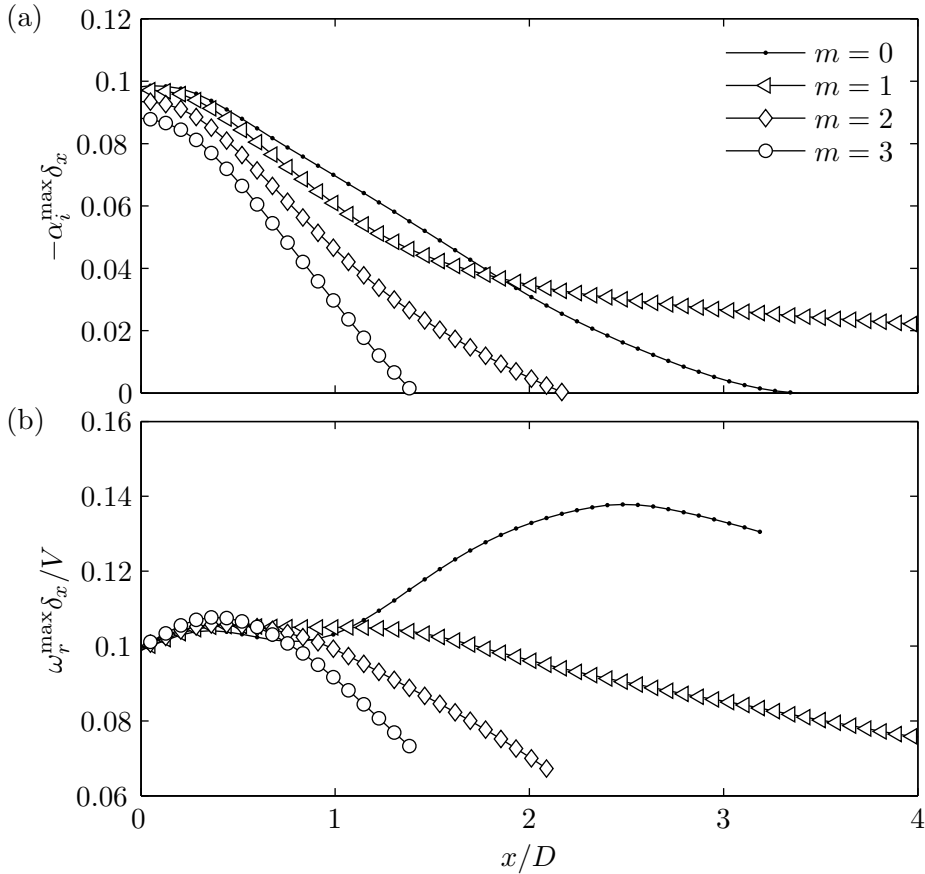


Figure 5.15: Streamwise development of the maximum growth rate $-\alpha_i^{\max} \delta_x$ (a) and corresponding frequency ω_r^{\max} (b) of the shear modes with $m = (0, 1, 2, 3)$ for the non-swirling jet S_1 .

The maximum growth rates α_i^{\max} and the corresponding frequencies ω_r^{\max} are shown explicitly in figure 5.15. It can be directly compared to the results from the inviscid analysis conducted by Cohen & Wygnanski (1987). Close to the nozzle exit, the agreement is good. However, the viscous analysis presented here predicts a faster downstream decay of $-\alpha_i^{\max}$. In the present analysis, the axisymmetric modes ($m = 0$) become neutrally stable at $x/D \approx 3.3$, while the inviscid analysis of Cohen & Wygnanski (1987) predicts $x/D \approx 4.5$. Perhaps more importantly, the maximum growth rate of the bending modes with $m = \pm 1$ presented here asymptotes to 0.22, which is less than half of the value derived by Cohen & Wygnanski (1987).

The discrepancy between the viscous and the inviscid analysis is due to the eddy viscosity model used in the present investigation. Near the nozzle exit, the turbulent viscosity ν_t is very small and it has only a marginal effect on the growth of instability. With larger distance from the nozzle, the turbulent fluctuations increase, resulting in a rapid increase of ν_t . This fictitious viscosity drastically dampens the growth rate of the instability modes. Consequently, the inviscid analysis overestimates the growth rate that is observed in experiments, as shown by Cohen & Wygnanski (1987), while the present approach yields a theoretical prediction that agrees favorably with the experimental results (see section 5.5).

The streamwise distribution of α_i of the swirling jet configurations S_2 and S_3 is shown in figure 5.16 for $0 \leq m \leq 3$. By introducing swirl to the flow, the symmetry breaks and

co-rotating modes undergo different amplification cycles than counter-rotating modes and hence, contours of $-\alpha_i \delta_x$ must be derived for positive and negative frequencies, separately.

During the ensuing discussion of the divergent swirling, it is more meaningful to classify the instability modes by their sense of winding than by their direction of rotation. In this spirit, the contour line $\alpha_r = 0$ in figure 5.16 that refers to streamwise modes is emphasized as it separates the regime of co-winding modes from the regime of counter-winding modes. It is located in a ‘valley’ between regimes of high amplification and thus, the streamwise modes are always less unstable than the most unstable winding modes. This contour line must not necessarily coincide with $\omega_r = 0$, as it is the case for the non-swirling jet (confer with figure 5.14). As can be seen, for instance, in figure 5.16c, co-rotating streamwise modes, depicted by the $\alpha_r = 0$ contour line, are unstable in the swirling jet S_2 and S_3 . The rotation rate of these modes is related to the base flow rotation and thus, their frequencies must be larger than zero and increase with swirl.

The analysis of the streamwise evolving flow reveals a different mode selection than one would expect from the analysis of the mean flow at the nozzle exit. The streamwise decay of the growth rates of the co-winding modes, corresponding to regions of $\alpha_r < 0$ in the figures 5.16b-d, is reduced with increasing swirl. In contrast, the streamwise decay of the growth rates of the counter-winding modes ($\alpha_r > 0$ in figures 5.16b-d) and the axisymmetric modes (figure 5.16a) is enhanced with increasing swirl although these modes are most unstable at the nozzle exit (confer with figure 5.6). Hence, the modes that are most amplified at the nozzle ext, which are presently the counter-winding modes, are not necessarily the modes which undergo the strongest overall amplification.

For the swirling jets S_2 and S_3 , the streamwise wavenumbers of the most amplified modes are approximately constant in axial direction at $\alpha_r \delta_x \approx 0.2$, independently of the azimuthal wave number (figure 5.16). This agrees with the non-swirling jet (figure 5.14). However, the most amplified frequencies are not constant in axial direction unlike the non-swirling jet. For the modes with $m > 1$ (figure 5.16c-d), the frequency at maximum amplification increases in downstream direction. This results in a destabilization of co-winding steady modes ($\omega_r = 0$, $\alpha_r < 0$) at streamwise wavenumbers that are similar to the most amplified ones in the non-swirling jet. At sufficient strong swirl (right column in figure 5.16), the $\alpha_r = -0.2$ contour line, depicting roughly to the most amplified modes, asymptotes the $\omega_r = 0$ line. This implies that, with increasing downstream distance from the nozzle, the rotation rate of the most amplified co-winding counter-rotating modes decrease continuously until they stand still ($\omega_r = 0$).

The ability to promote steady modes at considerable high amplification rates is a unique feature of swirling jets. The tendency of the co-winding modes to lower rotation rates (frequencies) appears plausible when considering the proportionality $\omega_r \propto V/2\alpha_r^{\max} + \Omega_{\text{gr}}m$, derived in section 5.3.1. It implies that with increasing swirl (increasing Ω_{gr}), the frequency ω_r of the most unstable counter-rotating co-winding mode ($m > 0$, $\omega_r < 0$, $\alpha_r^{\max} < 0$) must increase in order to maintain constant wavenumber. In the same train of thought, steady modes become most unstable when $V/2\alpha_r^{\max} = -\Omega_{\text{gr}}m$, which seems to be fulfilled at certain axial locations for $m > 1$.

Furthermore, figure 5.16 reveals that all modes become successively more stable with increasing downstream distance from the nozzle, except for the co-winding modes with

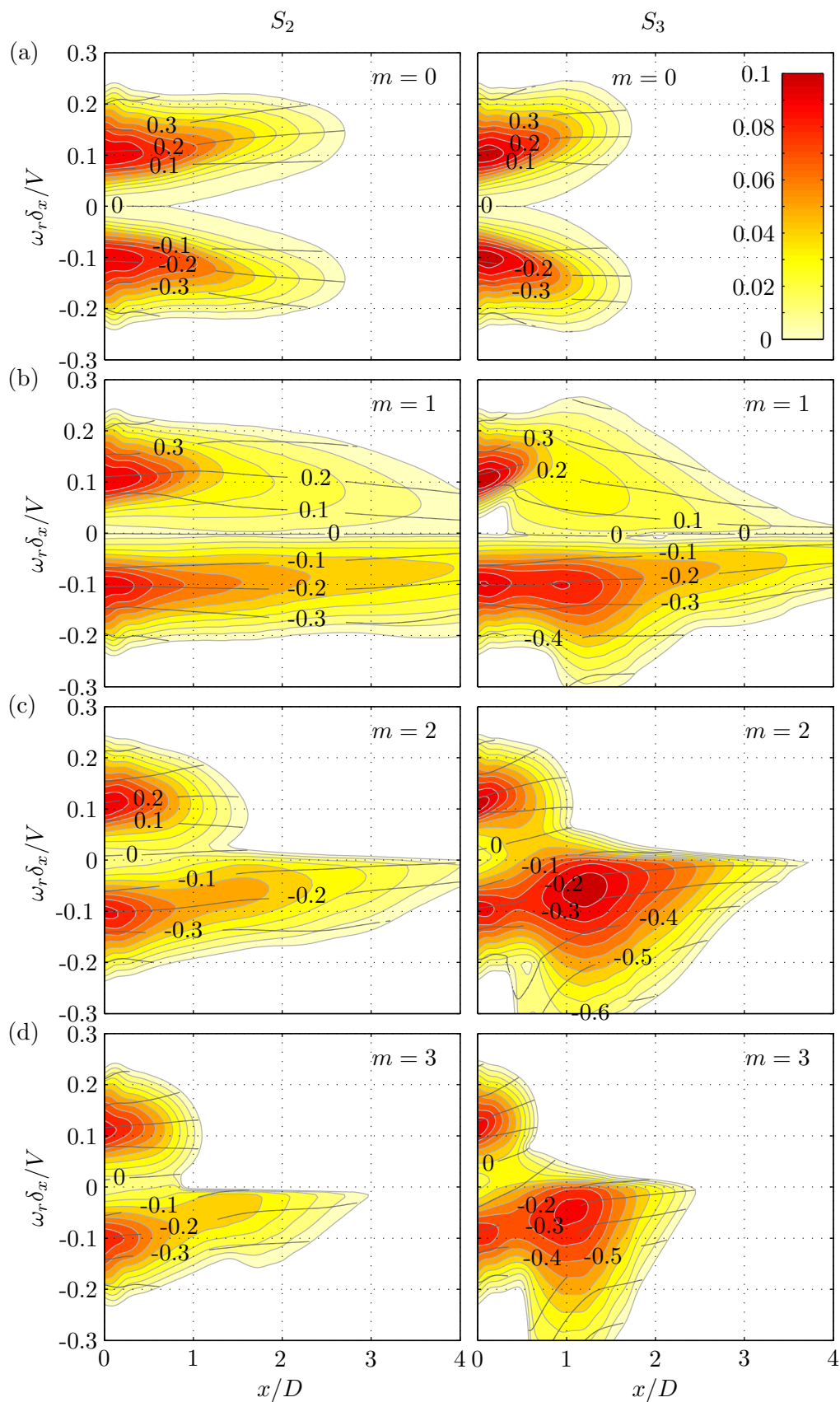


Figure 5.16: Streamwise evolution of spatial growth rate $-\alpha_i$ of the shear mode at azimuthal wavenumbers $m = (0, 1, 2, 3)$ for the swirling jets S_2 (left column) and S_3 (right column). Same plot style as in figure 5.6.

$m = 1$. Computations based on a larger domain could reveal that these modes remain the only unstable ones within $0 < x/D < 8$ (not shown). Interestingly, their spatial growth rate asymptote to the same value for all swirling jets considered, which is twice as high as for the non-swirling jet. It appears that the swirl-induced destabilization of the co-winding modes and the stabilization of counter-winding modes is maintained for a wide streamwise distance, although the swirl component decays very rapidly in downstream direction (see figure 5.4). The collapse of the growth rates downstream the potential core is presumably linked to the formation of an universal swirl velocity profile, as indicated by the collapse of the Rosby number, N_θ , and $V_{\theta,\max}$ (see figure 5.4).

Hence, the swirling jet selects a counter-rotating co-winding $m = 1$ mode to be the remaining unstable mode at sufficient downstream distance. This mode is expected to dominate the farfield dynamics. The nearfield is dominated by various co-winding modes with the azimuthal wave number $m = 2$ to be most amplified. The frequencies of the most amplified modes decay in downstream direction due to the rotational motion of the mean flow, which results in a significant destabilization of steady modes.

5.4.2 Centrifugal Instability

The downstream development of the centrifugal instability is shown in figure 5.17 for S_3 . The analysis at the nozzle exit has revealed that the centrifugal instability promotes modes at high negative and low positive azimuthal wave numbers (figure 5.11). In order to track their downstream development, the analysis is conducted at various streamwise locations for positive ω_r and azimuthal mode numbers $m = (-10, -5, -2, -1, 0, 1, 2)$. The results are shown in figure 5.17. Accordingly, the modes driven by the centrifugal instability decay with downstream direction at a much faster rate than the shear mode, and they all become neutrally stable upstream of $x/D = 1$. The rapid downstream decay of the growth rate is presumably caused by the decreasing radial gradient of angular momentum Γ due to the continuous decay of the maximum azimuthal velocity $V_{\theta,\max}$ that goes in hand with a thickening of the azimuthal shear layer (see model parameters in figure 5.4 in section 5.2). Hence, the centrifugal instabilities are restricted to a small spatial region near the nozzle lip and, therefore, are not expected to have significant influence on the streamwise evolution of large-scale flow structures.

5.5 Single-mode Actuation

In a first experiment, the jet at different swirl intensities was forced at the azimuthal mode $m = 1$. The disturbance field of the excited wave was measured with hot-wires and compared to the theoretical predictions discussed in the previous sections. Good agreement will bring credibility to the stipulations that are made for the presented stability analysis. These assumptions are summarized here again:

- The instabilities of the mean turbulent flow represent the coherent structures.
- Small-scale turbulence is well modeled by the eddy viscosity.
- The axial overshoot is negligible.
- The quasi-parallel approximation is sufficiently accurate.

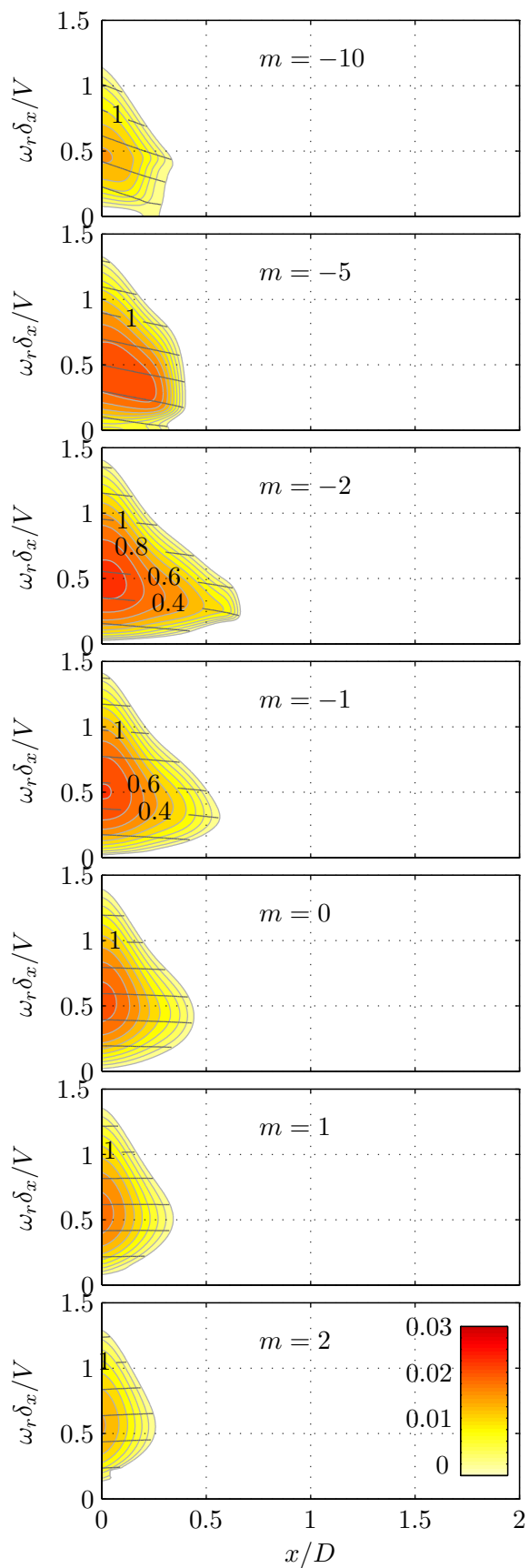


Figure 5.17: Streamwise evolution of spatial growth rate $-\alpha_i$ of the centrifugal mode at azimuthal wavenumbers $m = (-10, -5, -2, -1, 0, 1, 2)$ for the swirling jet S_3 . Same plot style as in figure 5.6.

In the second experiment, the swirling jet configuration S_3 was forced at different azimuthal wavenumbers $-2 \leq m \leq 2$ at a frequency of 100 Hz. This experiment is aimed to validate the dependency of the phase velocity on the azimuthal mode number for the swirling jet.

5.5.1 Streamwise Growth of the Co-rotating Single-helical Mode

Hot-wire measurements were conducted at several axial and radial positions within the range $0 < x/D < 1.2$ and $0 < r/D < 0.8$. The single-helical $m = 1$ mode was actuated at the frequencies 150 Hz, 100 Hz, and 80 Hz for the swirl numbers S_1 , S_3 , and S_4 , respectively. This corresponds to dimensionless frequencies ranging from $\omega_r \delta_x / V \approx 0.07$ at the nozzle lip to $\omega_r \delta_x / V \approx 0.4$ at $x/D = 1.2$. The frequencies were selected as such that the actuated modes go through their entire amplification cycle within the measurement domain. The frequencies do not correspond to the maximum overall amplification.

The choice of the actuation amplitude is not trivial as it has to be large enough to overcome the random turbulent noise in the shear layers. On the other hand, it must be sufficiently low to provide linear amplification. Moreover, forcing the flow at too high amplitudes would alter the mean flow substantially and thereby falsify the theoretical predictions that are based on the non-forced flow. The most appropriate amplitude for each flow configuration was derived through a preliminary parameter study. Therefore, the flow was forced at various amplitudes and a trade-off between good signal-to-noise level and a clear linear response was found.

As outlined in section 3.4.1, the flow excited at a single mode is decomposed into a mean, a coherent, and a turbulent part. The coherent part is derived from phase-averaged hot-wire measurements and is Fourier decomposed in time and azimuthal direction. The obtained amplitude distribution of the axial component $|\hat{v}_x|$ can be compared to the stability eigenfunctions. Figure 5.18 shows the amplitude of the co-rotating counter-winding traveling $m = 1$ mode at selected axial locations. The black lines refer to the theoretical predictions derived from spatial linear stability analysis. Symbols are derived from phase-locked measurements. The amplitudes are normalized with respect to the area below the graph. Good agreement between theory and experiments are found in the unstable region of the forced instability, which is approximately upstream of $x/D = 0.75$.

The radially integrated amplitude measure $A_m(x)$ is derived using equation (3.3). Figure 5.19 shows the streamwise amplitude distribution of the modes actuated at $m = 1$. The amplitudes are shown in a logarithmic scale and are normalized by their initial value at $x/D = 0$. Hence, the graphs represent an amplitude ratio of the radially integrated axial velocity component. For all cases, the excited waves saturate at similar axial locations. The waves in the non-swirling jet undergo an overall amplification that is an order of magnitude higher than for the swirling jet.

The spatial growth rate of the axial velocity component can be derived from the slope of the amplitude ratio displayed in figure 5.19. The black stars in figure 5.20 show its streamwise development for the swirling jet (left) and non-swirling jet (right) normalized by the local momentum thickness δ_x . For the non-swirling jet, neutral amplification of the excited mode is reached at approximately $x/D = 0.75$. For the swirling jet, the excited mode is neutrally stable at approximately $x/D = 0.5$.

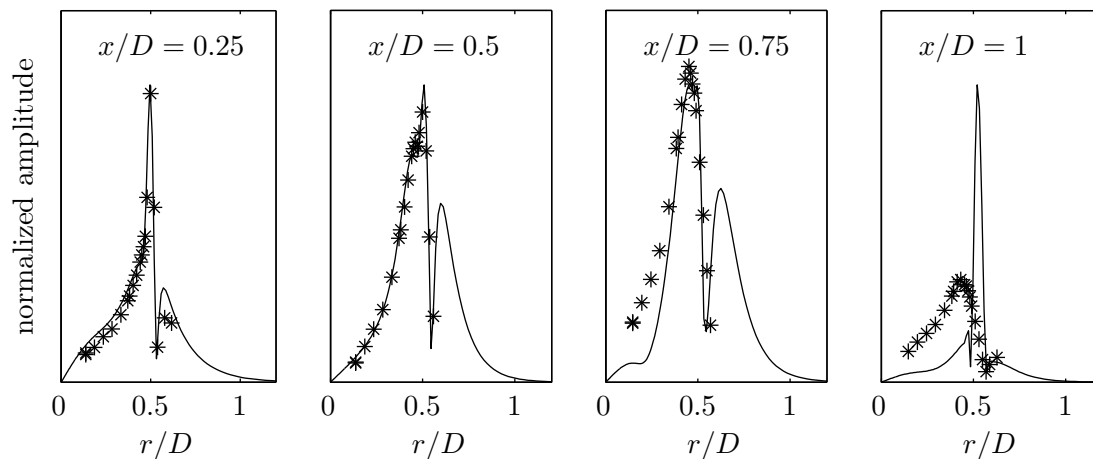


Figure 5.18: Radial amplitude distribution of the axial velocity component of the $m = 1$ mode for the swirling jet configuration S_3 ; markers correspond to measurements and lines represent viscous linear theory

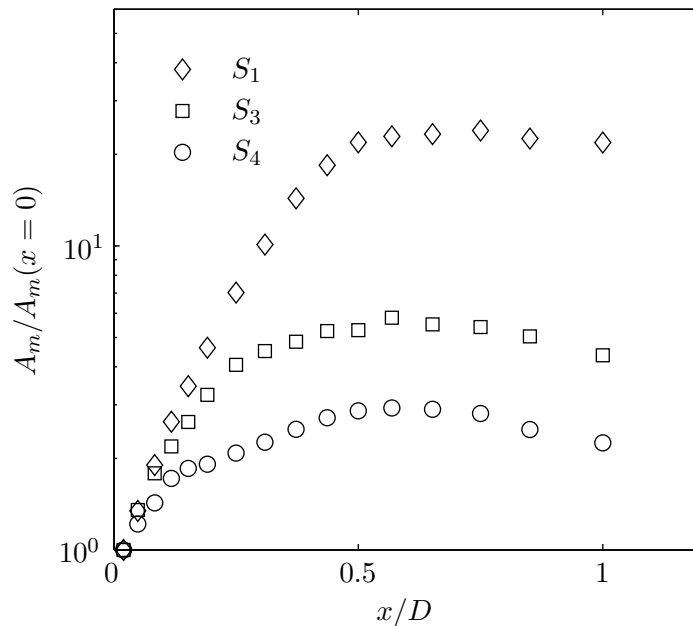


Figure 5.19: Streamwise amplitude distribution of actuated co-winding $m = 1$ mode for various swirl configurations. Actuation frequencies are 150 Hz, 100 Hz, and 80 Hz for the swirl numbers S_1 , S_3 , and S_4 , respectively, to obtain neutral amplification at similar axial locations.

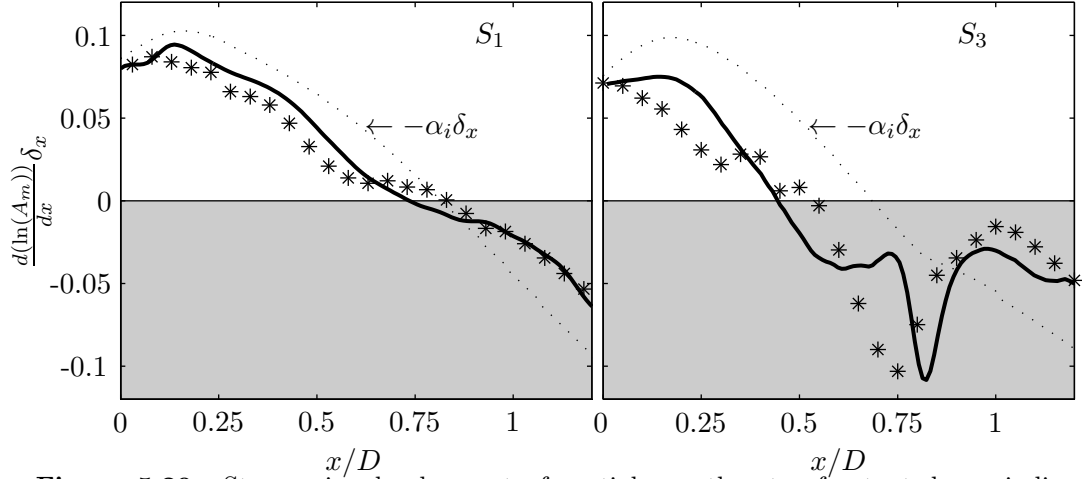


Figure 5.20: Streamwise development of spatial growth rate of actuated co-winding $m = 1$ mode for the non-swirling jet S_1 (left) and the swirling jet S_3 (right); the black stars refer to measurements; the black thick line refers to the theoretical prediction using equation (5.5) that incorporates the shear layer spreading; the black dots represent the theoretical predicted eigenvalue $\alpha_i \delta_x$ that does not corroborate shear layer spreading.

The growth rate of the axial velocity component can also be derived from the stability analysis. As outlined in section 2.4, the amplitude distribution of the axial velocity component of the downstream traveling wave is approximated by

$$|\hat{v}_x(x, r)| = |H(x, r)| \exp \left[- \int_0^x \alpha_i(\xi) d\xi \right], \quad (5.4)$$

where H is the eigenfunction of the axial velocity component, which depends parametrically on x . In line with the experimental approach, the integrated amplitude of the axial velocity component is then derived from

$$A_m(x) = \left(\int_{R_{0.5}}^{R_{0.95}} |\hat{v}_x|^2 r dr \right)^{1/2}. \quad (5.5)$$

The actual growth rate of the theoretically derived $A_m(x)$ is shown as a black thick line in figure 5.20. The streamwise development of the growth rate $-\alpha_i \delta_x$ that corresponds to a parallel flow is displayed in the same figure.

At the nozzle lip, the growth rate of A_m is well represented by $-\alpha_i \delta_x$. Further downstream, the growth rate of the parallel flow overestimates the actual growth rate of A_m . This is more pronounced for the swirling jet. The non-uniformity of the flow implies different growth rates for different velocity components, and hence, $-\alpha_i \delta_x$ does not represent the growth rate of the axial velocity component. However, the growth rates of the axial velocity component derived from the equations (5.4-5.5) agree well with the experimental data. This indicates that the negligence of the amplitude scaling A_0 of the weakly non-parallel correction does not significantly affect the accuracy of the predicted amplitudes.

One may conclude that the local quasi-parallel analysis approximates the streamwise growth of a single-mode excited wave at a sufficient measure of accuracy. The growth rate $-\alpha_i \delta_x$ of the parallel flow provides an approximate measure of the growth of instability, but

for an accurate comparison with experiments the streamwise varying eigenfunction must be considered.

The theoretical results presented in figure 5.20 correspond to the shear instability. The growth rates of the centrifugal instability do not match the experimental results at all (not shown), which indicates that centrifugally unstable modes are not excited by the applied actuation.

5.5.2 Streamwise Phase Velocity in the Swirling Jet

One important finding of the stability analysis of the swirling jet is the dependence of the axial phase velocity and wavelength on the azimuthal wavenumber. This is validated experimentally by actuating the swirling jet S_3 at various azimuthal wavenumbers. The corresponding phase distribution $\varphi_m(x, r)$ is derived from the phase-locked hot-wire measurements using equation 3.4. The phase velocity for a given m is derived by

$$c_{\text{ph}}(x, r) = \frac{2\pi f_{\text{act}}}{\partial\varphi_m(x, r)/\partial x}. \quad (5.6)$$

It is a function of the axial and radial coordinate. Figure 5.21 shows the phase distribution of the co-rotating counter-winding traveling waves $m = 1$ at selected axial locations. The agreement between measurement and theoretical prediction is reasonably well in the region of amplification $x/D < 0.7$.

The phase cannot be integrated across the shear layer, as it is done for the amplitude distribution. Hence, the streamwise development of the phase velocity of an excited wave must be considered for each radial location separately. However, it is here assumed, that the phase velocity in the center of the shear layer $r = R_{.5}$ represents approximately the average phase velocity of the entire forced coherent structure. This approximation is supported by measurements in the forced mixing layer (Gaster et al. 1985).

Figure 5.22 shows the measured phase delay of modes actuated at $-2 \leq m \leq 2$ derived at the center of the axial shear layer $R_{.5}$ for the swirling jet S_3 . All modes are excited at the same frequency. Accordingly, for lower m the phase increases more rapidly with downstream distance. At $x/D = 0.7$, the $m = -2$ mode has gone through more than one period while the $m = 2$ mode has gone only through somewhat more than half a period.

The phase velocity of the excited modes is derived from the slope of the phase delay shown in figure 5.22. Results are displayed in figure 5.23. The maximum c_{ph} is found at the nozzle for all modes considered. c_{ph} decreases rapidly with downstream distance to a local minimum that is followed by a slight increase in the region of neutral amplification $x/D \approx 0.7$. As already indicated by the phase delay, modes at lower m have lower axial phase velocities than modes with higher m . This confirms the trend predicted by the stability analysis. As discussed in section 5.3, the mean flow rotation results in a dependency of the streamwise phase velocity on the azimuthal wavenumber. The analysis confirms that co-rotating waves at higher m travel at a higher streamwise phase velocity.

A quantitative comparison between the measured phase velocity distribution $c_{\text{ph}}(x, r)$ with the results from the stability analysis is impossible within the present approach. The phase of the eigenfunctions computed at different streamwise locations cannot be aligned with streamwise distance in a consistent way. A quantitative comparison of the phase

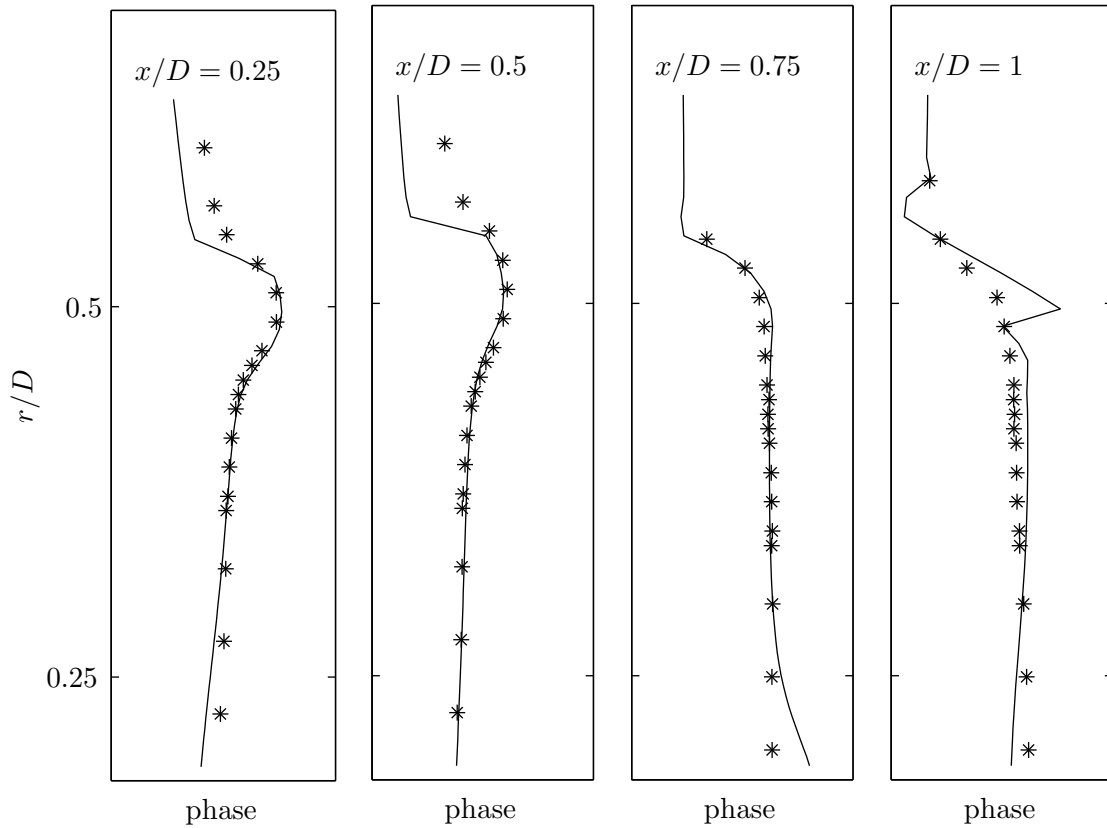


Figure 5.21: Phase distribution of mode $m = 1$ for the swirling jet at $S=0.4$, markers correspond to measurements, lines represent viscous linear theory

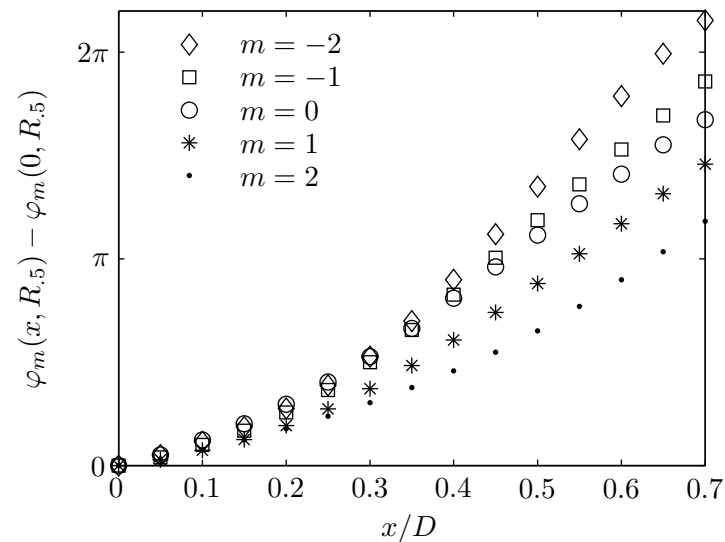


Figure 5.22: Streamwise evolution of the phase delay $\varphi_m(x, R_5) - \varphi_m(0, R_5)$ for modes excited at various azimuthal wavenumbers m for the swirling jet S_3 . Values are taken in the center of the axial shear layer R_5 .

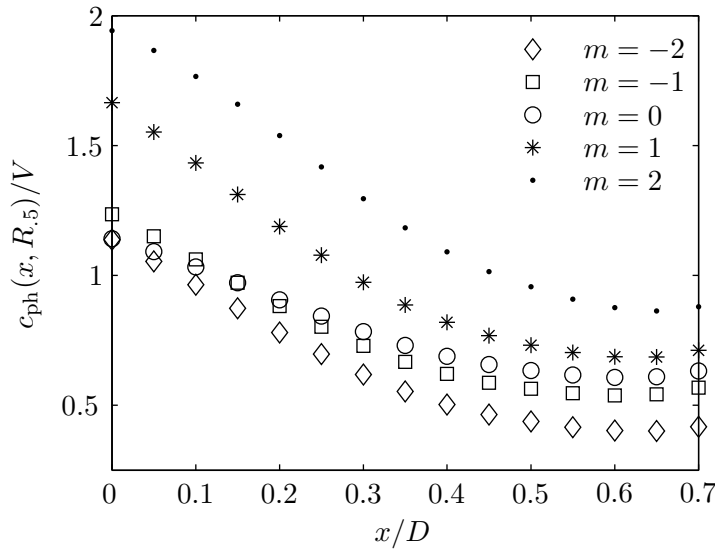


Figure 5.23: Streamwise evolution of the phase velocity c_{ph} for modes excited at various azimuthal wavenumbers for the swirling jet S_3 . Values are taken in the center of the axial shear layer $R_{.5}$.

velocity, would require to solve a second differential equation describing the streamwise development of the eigenfunctions. Nonetheless, the experiments confirm the theoretical prediction, revealing that, for swirling jets, the axial phase velocity depends on the azimuthal wave number m .

5.6 Impulse Response

In the second experimental approach the response of the shear layer to a single pulse is investigated experimentally. A time- and space-discrete disturbance is created at the nozzle lip using one of the eight loudspeakers that are mounted circumferentially around the nozzle lip. The downstream development of the excited wave packet is captured via ensemble-averaged hot-wire measurements. Details of the data acquisition and treatment are given in section 3.4.2. In contrast to the single-mode actuation discussed in the previous section, the delta pulse excites an infinite number of modes, which are either amplified or damped, depending on the stability of the mean flow. At sufficient distance from the nozzle, all stable modes should have died out and the wave packet is expected to consist solely of unstable modes. The modal content of the wave packet is compared to the results from the stability analysis for various streamwise locations. The aim of this experiment is to validate the mode selection predicted from the local stability analysis.

The downstream evolution of a traveling wave packet is modeled accurately by linear stability analysis provided that the unstable modes do not interact with each other. In order to force all modes at equal amplitude, the initial disturbance should ideally be a delta function in time and space. However, in the present experiment, the pulse is generated by one loudspeaker driven at a saw-tooth signal, which generates a pulsed jet with an azimuthal extent of $\Delta\theta = \pi/4$ and an axial extent of $x/D = 0.02$. This differs significantly from a delta function in space. Forcing artifacts are introduced that influence the development of the wave packet between the nozzle lip and the next downstream measurement position

($x/D = 0.25$). Further downstream, the influence on the particular forcing characteristic becomes insignificant and the wave packet evolution is in line with the linear prediction, as will be shown later.

In the following, the development of the wave packet envelope will be described first, revealing the shape, the location and the velocity of the wave packet. Thereafter, the modal content of the wave packet is discussed and compared to the spatial stability analysis. Results are shown for the non-swirling jet S_1 and the swirling jet S_3 .

5.6.1 Trajectory of the Wave Packet Envelope

In general, the Fourier coefficients of a signal v_j sampled at $j = 1 \dots N$ time points is given by

$$\hat{v}_n = \frac{1}{N/2} \sum_{j=0}^N v(t_j) \exp\left(-i \frac{\pi n j}{N/2}\right) \quad (5.7)$$

and the envelope of the signal is given by

$$v^e(t_j) = \left| \sum_{n=0}^{N/2} \hat{v}_n \exp\left(i \frac{\pi n j}{N/2}\right) \right|. \quad (5.8)$$

The measured signal of the wave packet is represented by the coherent axial velocity component $v_x^c(\mathbf{x}, t)$. The experimental arrangement allows for a very good temporal resolution, a reasonably good spatial resolution in radial direction, and, due to the specific ensemble averaging procedure, a good spatial resolution in azimuthal direction. The resolution in axial direction is poor, as data are acquired only for the streamwise locations $x/D = (0.02, 0.25, 0.6, 1, 1.5, 2, 2.5, 3)$. Hence, the signal of the wave packet is Fourier decomposed in r -, θ -, and t -direction for each streamwise position, separately, and the corresponding envelope $v_x^e(\mathbf{x}, t)$ is derived from the inverse 3-dimensional Fourier transformation, in accordance with equation (5.8). In consistency with the single-mode investigation, the radial dependence of the envelope is omitted by integrating the envelope across the axial shear layer, yielding the following expression for the envelope amplitude

$$A^e(x, \theta, t) = \left(\int_{R.05}^{R.95} (v_x^e)^2 r dr \right)^{1/2}. \quad (5.9)$$

Figure 5.24 shows the trajectory of the wave packet envelope in a 3D-plot for the non-swirling jet S_1 and the swirling jet S_3 . 2D-contours are displayed for each streamwise measurement location, showing the envelope amplitude distribution along the θ - t -plane. The time is made dimensionless using the half bulk velocity $V/2$, which is approximately the streamwise convection velocity of the disturbance. At each axial location, A^e is normalized by its maximum value A_{\max}^e within the corresponding θ - t -plane. This normalization facilitates to compare the wave packet envelope between different crosswise measurement planes. Contour surfaces with $A^e/A_{\max}^e < 0.5$ are blanked and the lowest contour line $A^e/A_{\max}^e = 0.5$ is selected arbitrarily as the characteristic outer bound of the wave packet. The corresponding coordinates of the leading and trailing edge of the wave packet are projected on the axis planes (see dotted lines at $x/D = 1.5$). They are marked by white-filled black circles in the x - t -axis-plane and by gray-filled black circles in the x - θ -axis-plane. The

center of the wave packet is associated with $A^e/A_{\max}^e = 1$. Its coordinate is marked on the axis planes by big black dots. The streamwise development of A_{\max}^e are shown in the small images placed near the bottom-right corner of the figures 5.24a and b.

To get familiar with this rather complex plotting style the non-swirling jet is discussed first (figure 5.24a). The pulse is initiated at the nozzle exit at $t = 0$ and $-\pi/8 \leq \theta \leq \pi/8$. This creates a wave packet that peaks at $\theta = 0$, with an azimuthal extend of $\Delta\theta\pi/4$ (see marker in the θ - x -axis-plane at $x/D = 0.02$). The leading edge arrives at the first measurement position ($x/D = 0.02$) only shortly after $t = 0$ followed by the maximum and the trailing edge (see marker in the x - t -axis-plane at $x/D = 0.02$). While traveling to the next downstream measurement point ($x/D = 0.25$) the wave packet spreads significantly in azimuthal direction and in time and A_{\max}^e decays slightly. The significant deformation of the wave packet near the nozzle is presumably caused by the imperfect forcing. However, with further downstream distance, amplification sets in and the wave packet maximum grows continuously up to a downstream distance of $x/D = 2.5$ (see small image in figure 5.24a). Within this region of amplification, the envelope maintains its shape remarkably well despite the streamwise variation of the mean flow. This confirms the weak dispersiveness of the shear layer of the non-swirling jet as predicted from the stability analysis. The wave packet maximum is found to propagate in axial direction at a velocity of approximately $0.7V$ near the nozzle ($0 < x/D < 0.6$) and at $0.54V$ for $x/D > 0.6$. The lower value, which corresponds to the amplifying region, compares well with the phase-velocity derived from the linear theory of $0.5V$ (confer with figure 5.7c).

Figure 5.24b shows the trajectory of the wave packet for the swirling jet S_3 . The envelope at $x/D = 0.02$ is very similar to the non-swirling jet, showing equal shape and maximum amplitude A_{\max}^e . The abrupt spreading of the pulse upstream of $x/D < 0.25$ is also observed for the swirling jet, although the widening of the envelope in time direction is less pronounced compared to the non-swirling jet. The streamwise evolution of A_{\max}^e does not indicate a region near the nozzle lip where the wave packet decays. In fact, the wave packet is amplified already at the nozzle exit and gains amplitude up to a streamwise distance of $x/D = 2.5$. For the swirling jet, the irregularities introduced by the imperfect forcing seem less significant than for the non-swirling jet and linear amplification set in at a shorter distance to the nozzle lip. It is further interesting to note that the wave packet in the swirling jet gains higher amplitudes than in the non-swirling jet although the maximum growth rates of the modes are higher for the non-swirling jet.

The wave packet in the swirled shear layer propagates in axial direction *and* in the direction of the base flow rotation, as indicated by the coordinates of A_{\max}^e projected on the θ - x -axis plane (figure 5.24b). The azimuthal propagation velocity, expressed as an azimuthal rotation rate Ω^e , is $2\pi\Omega^e D/V \approx 1.1$ within the region $0 < x/D = 1.5$, which coincides roughly with the potential core region and the region of constant Rossby number (see figure 5.4a-b). With further downstream distance, Ω^e decays rapidly, yielding $2\pi\Omega^e D/V \approx 0.1$ at $x/D = 3$. It is interesting to note that the theoretically derived azimuthal phase velocity ω_r/m of the streamwise modes ($\alpha_r = 0$) with $m = 2$ and $m = 3$ agree quite well with the rotation rate of the wave packet envelope. This is consistent with the kinematic relation $\omega_r \propto V/2\alpha_r^{\max} + \Omega_{\text{gr}}m$ derived in section 5.3, if one interprets Ω^e as the group rotation rate Ω_{gr} . The streamwise propagation velocity of the envelope is very similar to the non-swirling jet, ranging from $0.7V$ near the nozzle to $0.5V$ further

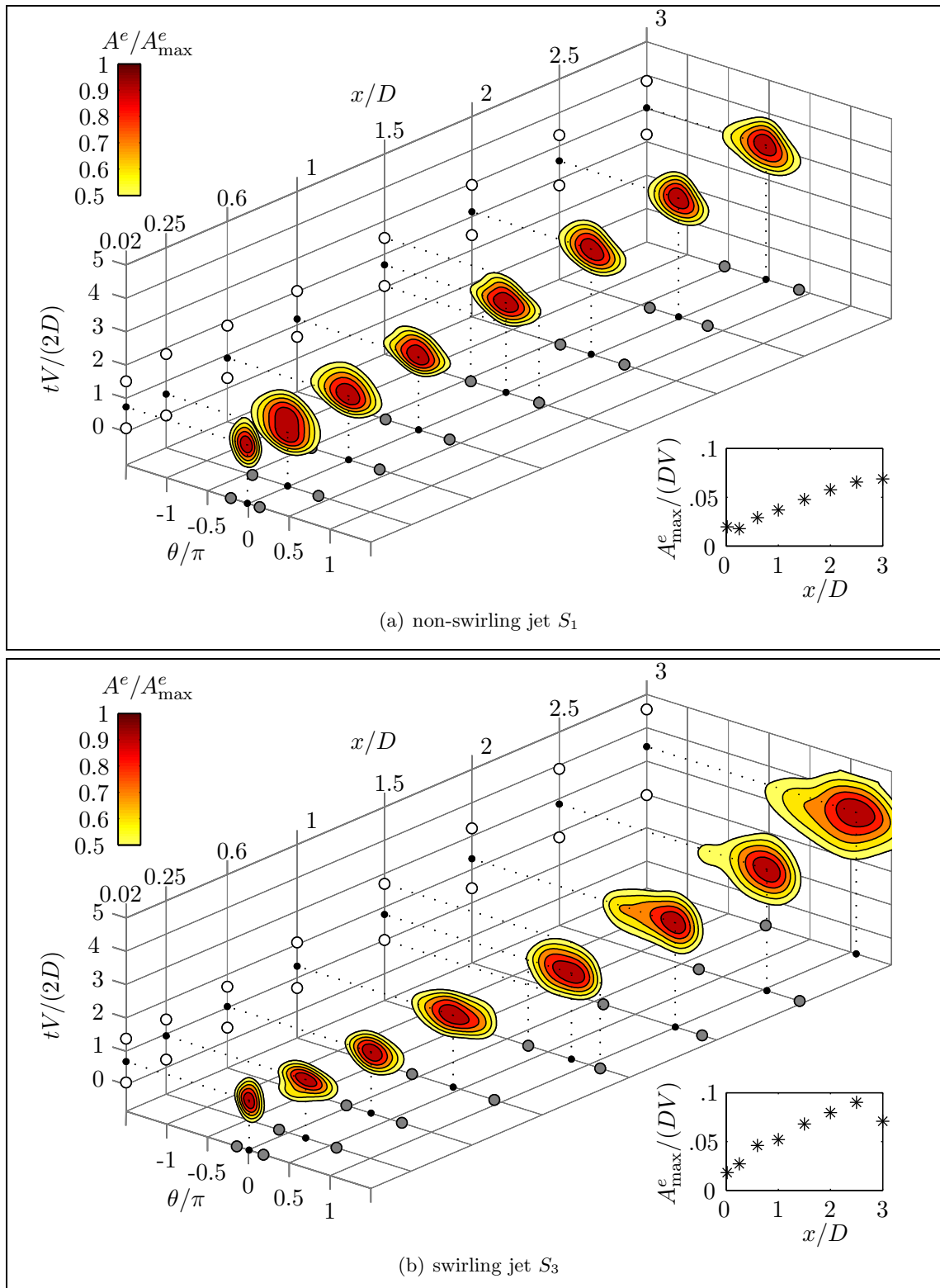


Figure 5.24: Trajectory of the wave packet envelope for the swirling and non-swirling jet. The pulse is initiated at $\theta = 0$, $t = 0$ and $x/D = 0$. Contours show the envelope amplitude distribution A^e at each r - θ -plane of measurement normalized by the corresponding maximum A_{\max}^e . Big black dots refer to the maximum of the envelope projected onto the θ - x - and t - x -plane. White-filled black circles refer to the leading and trailing edge of the wave packet in time direction. Gray-filled black circles refer to the leading and trailing edge of the wave packet in θ direction.

downstream ($x/D > 0.6$). This seems plausible, as the stability analysis predicts modes with low azimuthal wavenumbers, which are dominant further downstream, to have a similar axial phase velocity as for the non-swirling jet.

However, a prediction of the wave packet propagation speed based on the phase velocities of the individual modes remains cumbersome for the swirling jet due to the dispersiveness of the shear layers. The latter is indicated by a strong deformation of the wave packet envelope during its downstream propagation. In the region of strong amplitude gain ($0.6 \leq x/D \leq 2.5$), the envelope loses its symmetry and its maximum is shifted closer to the leading azimuthal bound, revealing a steep front and a smooth tail of the disturbance envelope in θ -direction. It is assumed that this pattern results from the superposition of modes with different azimuthal wavenumbers traveling at different streamwise phase velocities, as predicted by the linear theory. Contrarily, the wave packet is not deformed significantly in t -direction while traveling downstream. The most unstable modes have small azimuthal wavenumbers ($m < 3$) and small inclination angles α_r/m and thus, different phase velocities result in strong amplitude variations in θ -direction but only weak variations in t -direction.

5.6.2 Modal Decomposition of the Wave Packet

Within the framework of linear stability analysis, the wave packet created by a short pulse consists initially of an infinite number of modes and frequencies that are either linearly stable or unstable. While the wave packet travels downstream, stable modes decay and unstable modes grow at a rate that is given by the local dispersion relation $\mathcal{D}(\alpha, \omega_r, m, \Gamma, \text{Re}_t)$. Hence, in a non-parallel flow, the dominant modes in the traveling wave packet successively replace each other in accordance to the stability of the downstream varying base flow.

The theoretical investigation in section 5.4 reveals that for the non-swirling jet, the axisymmetric modes are most unstable at the nozzle lip and are replaced by the bending modes with $m = \pm 1$ for $x/D > 2$, which remain the only unstable modes downstream of $x/D = 3.3$. For the swirling jet, the mode selection is more complex as positive and negative modes have different growth rates. Close to the nozzle, the axisymmetric and co-winding modes are more unstable than the counter-winding modes, but they stabilize more rapidly with downstream distance and the counter-winding modes become dominant with $m = 2$ to be most unstable within a large streamwise region. The counter-winding mode with $m = 1$ remains unstable throughout the entire measurement domain.

Consistent with the single-mode analysis, the amplitude distribution of a instability mode excited at $x = 0$ is derived from equation 2.11 and the radially integrated amplitude is given by the expression

$$A_m(x, \omega_r) = \left(\int_{R_{.05}}^{R_{.95}} |\hat{v}_x|^2 r dr \right)^{1/2}. \quad (5.10)$$

Contrarily to the single-mode amplitude distribution (5.5), the modal amplitude distribution of the wave packet $A_m(x, \omega_r)$ depends now parametrically on m and is a function of x and ω_r . It is computed for the entire measurement domain for modes with $|m| \leq 5$ and $\omega_r \leq 0.3$. Results are displayed as contours in the m - ω_r -plane at the axial locations where the hot-wire measurements are conducted (figure 5.25).

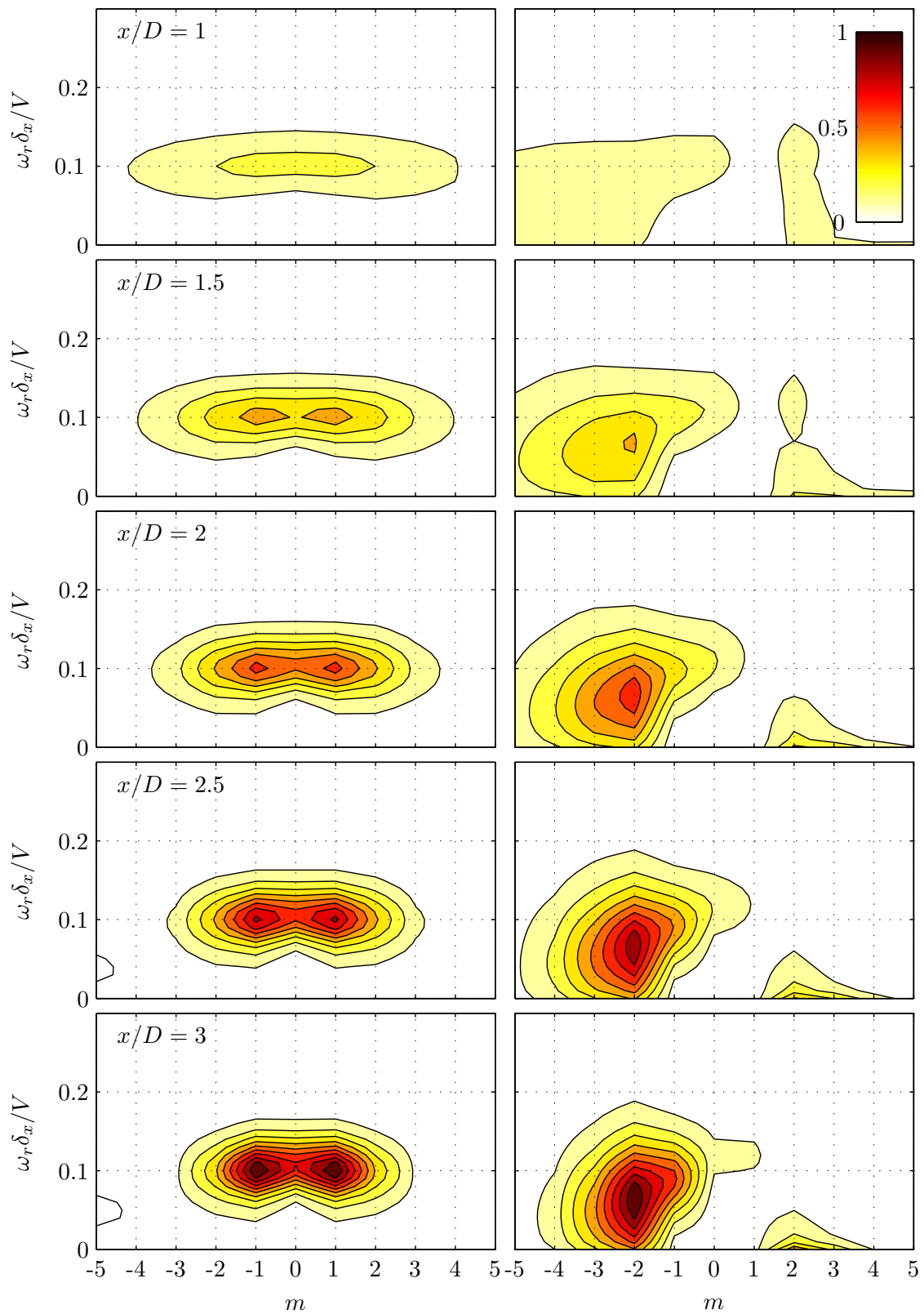


Figure 5.25: Modal amplitude distribution derived from linear stability analysis; left column refers to the non-swirling jet S_1 and right column to the swirling jet S_3 , contours refer to amplitude A normalized by its overall maximum.

The theoretical predictions are compared to the modal content of the measured wave packet. Therefore, the measured coherent axial velocity of the wave packet $v_x^c(x, r, \theta, t)$ is transformed into Fourier space, yielding the coefficients $\hat{v}_x^c(x, r, m, \omega_r)$. The modal amplitude distribution is then derived from equation (5.10). Results are shown in figure 5.26 for the swirling and non-swirling jet. It can be directly compared to the theoretical prediction shown in figure 5.25.

For the non-swirling jet, the agreement between measurements and theoretical prediction is reasonably well downstream of $x/D = 1$. The measurements confirm that the wave packet in the non-swirling shear layer is first dominated by axisymmetric waves at frequencies around $\omega_r \delta_x / V = 0.1$ (see second frame in left column). Further downstream, the bending $m = \pm 1$ modes become most dominant. The normalized frequency of highest amplitude remains constant with downstream distance, confirming that the most amplified wavelengths in the packet scales with the local length scale δ_x . The mismatch between theoretical prediction and experiment at $x/D \leq 1$ is probably attributed to the imperfect forcing and to spatially decaying modes at low frequencies that are excited at the nozzle.

For the swirling jet, the mode selection is in line with the theoretical prediction. Note that the sense of winding of the helical waves cannot be derived from the measurements and the modes can only be classified in co-rotating and counter-rotating modes, which corresponds in the figures 5.25 and 5.26 to $m > 0$ and $m < 0$, respectively. This implies a special caution in interpreting these figures, since for the swirling jet, modes with the same sense of winding may have negative or positive m . This is the case for the co-winding double-helical mode that is most amplified within the measurement domain. Its maximum amplitude is located at a frequency of $\omega_r \delta_x / V \approx 0.06$ at $m = -2$, yielding that the most amplified mode is the co-winding counter-rotating double helical mode. In agreement with the theoretical prediction, the dimensionless frequency of the most unstable mode is reduced with the addition of swirl. The experiments further show that this co-winding double-helical mode can be counter-rotating ($\omega_r > 0, m = -2$), steady ($\omega_r = 0, m = \pm 2$), or co-rotating ($\omega_r > 0, m = 2$). Hence, the existence of steady modes at considerable high amplitude are confirmed by the present experiments. Moreover, the measurements conducted downstream of $x/D = 2$ indicate the amplification of the single-helical counter-rotating mode in good agreement with the theoretical prediction.

5.6.3 Morphology of the Wave Packet

The shape of the wave packet for given x and r is displayed in figure 5.27 for the non-swirling and swirling jet. The visualizations are based on hot-wire measurements conducted in the center of the axial shear layer at the downstream end of the measurement domain. The shear layer of the non-swirling jet is dominated by equally unstable co-rotating and counter-rotating single-helical modes that create a wave packet with a v-shaped front that propagates downstream with its open end pointed in upstream direction. The morphology of the disturbance traveling in the swirling jet can be described as a wave packet with two wave crests that move in negative θ -direction with increasing t . This corresponds to the dominant counter-rotating double-helical mode. One wave crest is somewhat higher than the other indicating the appearance of the single-helical mode. The passage time of a wave crest is much longer for S_3 than for S_1 which corresponds to lower frequencies and, assuming similar convection velocities, to larger streamwise wavelengths.

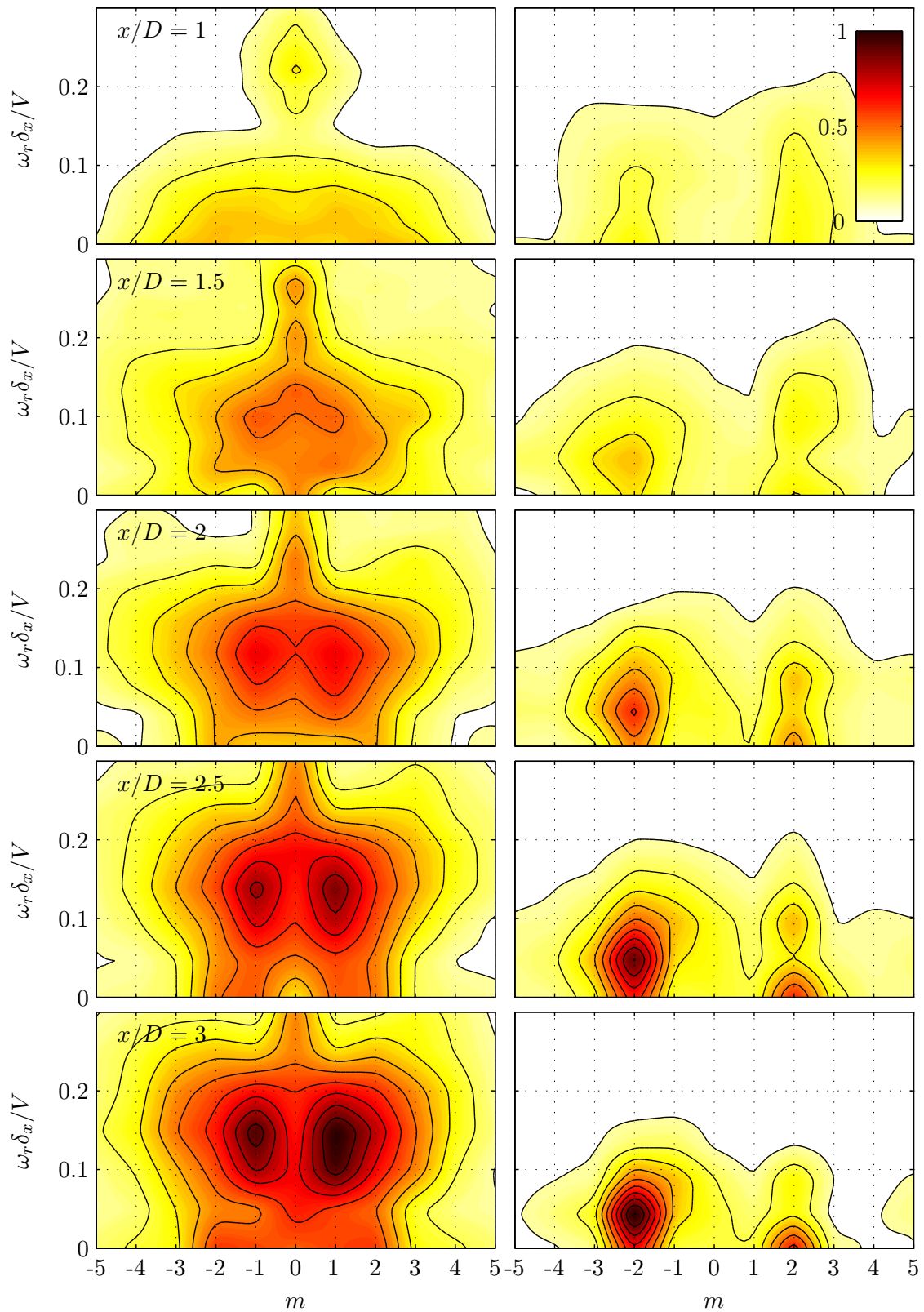


Figure 5.26: Modal amplitude distribution derived from hot-wire measurements; left column refers to the non-swirling jet S_1 and right column to the swirling jet S_3 , contours refer to amplitude A normalized by its overall maximum.

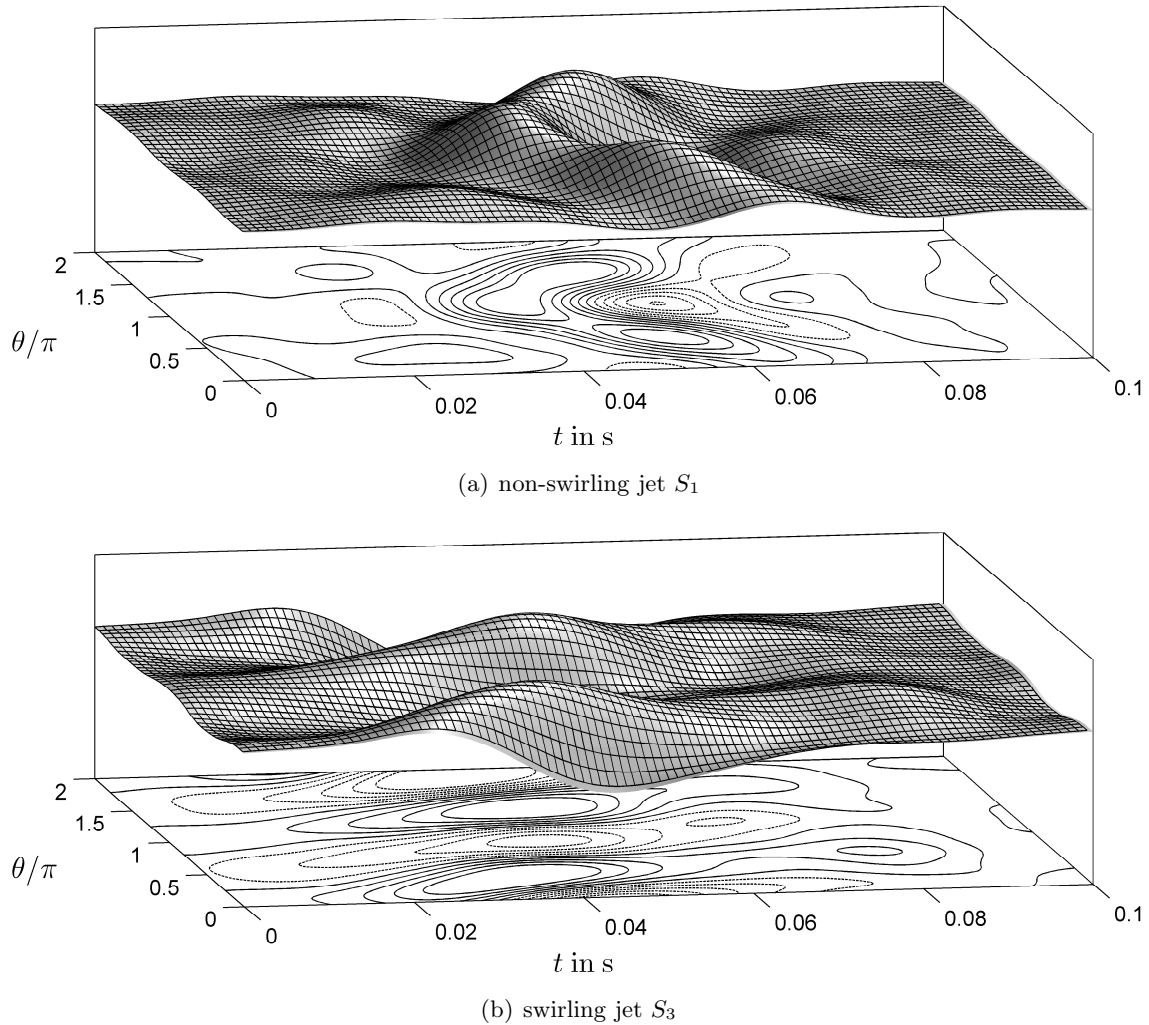


Figure 5.27: 3D-wireframe visualization of the traveling wave packet based on v_x^c measured in the center of the shear layer $r = R_{.5}$ at $x/D = 3$. Dashed contour lines refer to negative v_x^c .

5.7 Summary and Discussion

5.7.1 The Purpose of the Present Investigation

The nearfield of a turbulent axisymmetric unconfined swirling and non-swirling jet is investigated for a Reynolds number of $Re_D = 20000$. The swirl intensity is below that for the onset of vortex breakdown. This work focuses on the formation of vortical structures in the streamwise growing shear layer between the swirling jet and the quiescent surrounding fluid. The spatially growing disturbance waves therein are modeled theoretically by means of quasi-parallel linear stability analysis based on the measured mean flow and experimentally by acoustically forced experiments.

Within the last two decades, the stability of swirling jets has been investigated extensively. However, most studies were restricted to parallel flows using generic model-based velocity profiles that do not reflect the experimental findings. Although these model-based studies are useful to study the effects of certain parameters on the stability, their relevance

to real flows is often difficult to assess. In the present work we depart from model-based studies and apply stability analysis to the measured swirling jet flow. This allows for a quantitative comparison of the empirically derived vortical structures with the theoretical results. The theoretical approach implicitly accounts for nonlinear effects induced by Reynolds stresses that alter the mean flow and, more importantly, for the strong divergence of the swirling jet. The major question addressed in this investigation is: What are the dominant coherent structures that evolve in turbulent swirling jets and what instability mechanism is responsible for their spatial growth.

5.7.2 The Main Observations

Stability analysis is carried out at the nozzle lip, where the swirling jet differs only by its swirl component from the non-swirling jet. The swirling jet is found to promote a shear instability and a less unstable centrifugal instability, represented by two solutions of the dispersion relation. The characteristics of these disturbance modes are similar to those found in swirled shear layers (Cooper & Peake 2002; Lu & Lele 1999; Müller & Kleiser 2008). However, in the present flow, only the growth rates of the centrifugal modes increase with increasing swirl while the growth rates of the shear modes remain constant. Note that it seems to be not always possible to strictly distinguish between centrifugal and shear instabilities. Gallaire & Chomaz (2003) applied linear stability analysis to a jet with a thicker axial shear layer than the present one, revealing only one perturbation mode that is a clear Kelvin–Helmholtz instability for no-swirl, while it comprises characteristics of a centrifugal instability for strong swirl. Nonetheless, for the present study, the two types of instabilities occur always as two individual wavenumber branches and are considered as two modes driven by two different mechanisms. This allows the instabilities to be phenomenologically separated into centrifugal modes that exist only for the swirling jet and shear modes that are primarily driven by the strong shear of the axial velocity profile. The centrifugal instability promotes chiefly co-winding modes at high frequency and wavenumbers, whereas the shear layer instability promotes co-winding and counter-winding modes at the same frequency and wavenumber band as the Kelvin–Helmholtz instability of the non-swirling jet.

The centrifugal instability is weak even near the nozzle where it is somewhat relevant. All centrifugal modes are stable within a distance of half a nozzle diameter due to the rapid growth of the azimuthal shear layer. The rapid downstream decay of the centrifugal instability confirms the weakly non-parallel stability analysis of Cooper & Peake (2002), who investigated the stability of a swirled shear layer that spreads radially due to viscosity. However, they found the shear mode to be significantly amplified by the addition of swirl, which contradicts the present findings. In sharp contrast, the growth rate of the shear mode is presently found to scale inversely with the axial shear layer thickness and, thus, it decreases with increasing swirl due to enhanced shear layer spreading. These correlations are confirmed by the present experiments and support the qualitative considerations of Panda & McLaughlin (1994).

Moreover, the swirl component is found to alter the frequencies selected by the most unstable non-axisymmetric modes. As noticed by Martin & Meiburg (1994), this is a pure kinematic effect of the mean flow rotation. As explained in more detail in the present work, the rotational motion implies a non-zero azimuthal group velocity that results in the

dependence of streamwise wavelength and phase velocity on the azimuthal wavenumber. In other words, the inclination of the helical waves for a given frequency are altered with increasing swirl due to an azimuthal propagation velocity of disturbances in the swirled shear layer. This further implies that the shear layers of the swirling jets are dispersive. The wave crests of modes at different frequencies or azimuthal wavenumbers travel at a different streamwise velocities, which is not the case for the non-swirling jets. This inhibits the subharmonic resonance to occur in contrast to the non-swirling jets (Paschereit et al. 1995), which explains the absence of vortex pairing in the swirled shear layer as observed by Panda & McLaughlin (1994). Moreover, the dispersiveness hinders controlled intermodal interactions, which may occur at certain conditions in non-swirling jets (Long & Petersen 1992). These findings are consistent with the presented experimental results. Phase-locked measurements of the single-mode actuated flow clearly reveal the dependence of the streamwise phase velocity on the azimuthal wavenumber, whereas ensemble-averaged measurements of the pulsed flow confirm the enhanced dispersiveness of the shear layers with increasing swirl.

In the spirit of non-swirling jet studies, the question is targeted, whether or not a swirling jet selects a preferred mode. As reexamined in this work, the non-swirling jet is unstable to a large wavenumber and frequency band at the nozzle exit with the axisymmetric mode being most unstable. However, with increasing downstream distance all modes successively stabilize except for the $m = \pm 1$ modes that remain unstable. They are usually considered as the preferred modes (e.g., see Cohen & Wagnanski 1987; Petersen & Samet 1988) of non-swirling jets. Consistently, the present experiments reveal that a pulse initiated at the nozzle lip creates a wave packet that consists solely of the preferred modes at sufficient downstream distance from the nozzle.

The mode selection in swirling jets is more complex as symmetry breaks and co-rotating modes undergo different amplification than counter-rotating modes. Experimental and numerical results consistently show that the co-winding double-helical mode gains maximum amplitude in the potential core region and is, therefore, considered as the preferred mode of the swirling jet nearfield. However, downstream of the potential core, this mode stabilizes and the co-winding single-helical mode remains the only unstable mode and is expected to dominate the farfield dynamics. The present mode selection is in line with model-based studies that indicate that swirl tends to destabilize co-winding modes ($\alpha_r m < 0$) and to stabilize counter-winding modes ($\alpha_r m > 0$). Note that the dominance of the axisymmetric mode observed in swirling and non-swirling jet experiments (e.g., see Ho & Gutmark 1987; Liang & Maxworthy 2005; Loiseleux & Chomaz 2003) is usually attributed to an accidental axisymmetric forcing caused by the facility upstream of the contraction and must not be mistaken with the preferred mode (Cohen & Wagnanski 1987).

Moreover, swirl is found to destabilize two rather exotic types of shear modes, namely the streamwise modes with $\alpha_r = 0$ and the steady modes with $\omega = 0$. The first is purely driven by azimuthal shear revealing relatively small grow rates due to the thick azimuthal shear. The steady modes, however, are driven by the axial shear and azimuthal shear, which allows for significant spatial growth. In fact, the modes $m = -2$ and $m = -3$ reveal significant amplification rates at frequencies around zero. The measurements of the traveling wave consistently confirm the existence of steady and weakly rotating double-helical modes.

Steady and nearly steady co-winding spiral modes with $m = 2$ or $m = 3$ have been observed in experimental arrangements similar to the present one (Billant et al. 1998; Loiseleux & Chomaz 2003; Oberleithner et al. 2007). Gallaire & Chomaz (2003) assign the weakly rotating $m = 2$ mode observed by Loiseleux & Chomaz (2003) to a self-excited mode that arises from a convective/absolute transition point near the nozzle exit. In other words, they associate the preferred mode with a globally unstable mode with its wavemaker located near the nozzle exit. Their argumentation remains vague as their spatio-temporal analysis is based on one axial measurement location neglecting the divergence of the mean flow. Recall that a spatio-temporal analysis preliminarily applied to the present flow configuration could not reveal any region of absolutely unstable flow. It is, therefore, suggested that the appearance of double or triple-helical structures, as reported by (Billant et al. 1998), Loiseleux & Chomaz (2003), and Oberleithner et al. (2007) correspond to convectively unstable steady or nearly steady modes. Their spatial phase may be tagged by a small irregularity of the experimental arrangement, which leads to a breaking of rotational symmetry of the mean flow. Moreover, for very high swirl below breakdown, Loiseleux & Chomaz (2003) observe a counter-rotating $m = 1$ mode at high rotation rates (frequencies). This mode presumably corresponds to the presently found preferred mode $m = 1$ of the farfield that also counter-rotates at much higher frequencies than mode $m = 2$.

5.7.3 Final Remarks

The present work describes the formation of three-dimensional disturbance modes in turbulent swirling and non-swirling jets. The major theoretical findings derived from linear stability analysis are supported by an experimental investigation. At the nozzle exit, the swirling jet differs only by its swirl component from the non-swirling jet, revealing a weak influence of the swirl component on the stability. The different initial swirl strengths, however, cause a significantly different downstream development of the mean flow which effects the selected modes and their growth rates. Therefore, it appears that the stability analysis of a spatially evolving flow derived from measurements leads to significantly different results than studies based on fictitious velocity models. The present linear stability analysis is based on the mean flow, which intrinsically corroborates nonlinear interactions between the spatially growing waves and the mean flow. The results can be especially used to predict the dynamics, shape, and receptivity of large-scale flow structures that reside in the mean flow, which is of immense importance for effective flow control applications. The present theoretical approach is incapable of explaining with sufficient certainty the cause for the swirl-enhanced jet spreading that leads to the presently observed reduction of the shear layer receptivity. However, the present results may support or cancel out one or the other of the recent arguments. The present investigation confirms that vortex merging, the nonlinear mechanism that leads to a successive shear layer spreading in the potential core region of a non-swirling jet (Gutmark et al. 1995; Ho & Gutmark 1987), is inactive in swirling jets due to the swirl-enhanced dispersiveness of the shear layer. Moreover, the idea of a significant swirl-induced destabilization of centrifugal and/or shear modes that would intensify the growth of coherent structures and enhance the entrainment rates (e.g., see Cooper & Peake 2002; Cutler et al. 1995; Lu & Lele 1999; Mehta et al. 1991; Panda & McLaughlin 1994; Wu et al. 1992) is not supported by the present work. The strong increase of jet spreading is unlikely to be attributed to the rather small change in the base

flow stability found at the nozzle exit. It is more likely that complex nonlinear effects are the driving force. Recent investigations indicate that these nonlinearities might be triggered by an interaction of the centrifugal and the shear modes (Martin & Meiburg 1994, 1996) or by the coexistence of axial and azimuthal shear which causes a modification of the involved turbulent structures (Hu et al. 2001*a,b*; Martin & Meiburg 1998; Naughton et al. 1997; Örlü & Alfredsson 2008).

Chapter 6

Coherent Structures in the Strongly Swirling Jet

In this chapter the large-scale coherent structures are investigated that arise in a turbulent swirling jet undergoing vortex breakdown. Experiments suggest the existence of a self-excited global mode having a single dominant frequency. This oscillatory mode is characterized by a co-rotating counter-winding helical structure that is located at the periphery of the recirculation zone. It arises from a precessing vortex core that is located further upstream. The resulting time-periodic 3D velocity field is derived theoretically by means of spatial stability analysis employing the mean flow data from experiments. The 3D oscillatory flow is constructed from uncorrelated 2D snapshots of PIV data, using the proper orthogonal decomposition (POD), a phase-averaging technique and an azimuthal symmetry associated with helical structures. Stability-derived modes and empirically derived modes correspond remarkably well, yielding prototypical coherent structures that dominate the investigated flow region. The proposed method of constructing 3D time-periodic velocity fields from uncorrelated 2D data is explained in detail. It is applicable to a large class of turbulent shear flows. The employed phase-averaging technique is also used in chapters 4 and 7 of this thesis.

6.1 Motivation, and Approach

The present investigation deals with coherent structures of a strongly swirling jet undergoing vortex breakdown. As shown in chapter 4, this flow configuration is subjected to self-excited flow oscillations. The corresponding 3D time-periodic coherent structures are predicted by linear stability theory and are constructed from 2D PIV data via a proposed identification method.

In principle, self-excited oscillations are known to arise from a region of absolutely unstable flow. They can be described by an unstable global mode (Chomaz 2005) or by local spatio-temporal stability analysis with complex frequency and wavenumber (Huerre & Monkewitz 1990; Monkewitz et al. 1993; Pier & Huerre 2001). However, for the underlying flow configuration a simple local spatial stability analysis is employed to approximate the

velocity of the global mode. This simplification serves the main purpose of this study, which is to enhance the understanding of turbulent coherent structures in highly turbulent swirling flows. It is in line with similar studies (Juniper et al. 2011).

As described in chapter 4, strong oscillations at the global frequency are found upstream of vortex breakdown, revealing a precession of the vortex core that acts as the global wavemaker. In the outer shear layer, downstream traveling instabilities are detected that are internally forced by the wavemaker and are synchronized to its frequency. These waves serve as amplifiers to external forcing, which suggests that the signaling problem is valid for the outer flow region. Assuming that the outer shear layer responds to internal forcing in the same way as to external forcing, the large-scale fluctuations downstream of the wavemaker may be approximated by convectively unstable modes that oscillate at the global frequency. Hence, the spatial analysis presented here is conducted with an unknown complex streamwise wavenumber and the known real global frequency.

This approach can also be justified within the generalized mean field model proposed by Noack et al. (2003). Accordingly, the mean flow at limit cycle oscillation is globally marginally stable. This was validated for the cylinder wake by Barkley (2006). This implies that the absolute frequency from the local analysis should be real at the wavemaker location. Hence, it is justified to model the coherent structures of the global mode from a spatial analysis with real frequency and unknown complex streamwise wavenumber.

For this study, the swirling jet air facility at the TU Berlin is used. The experimental setup is described in section 3.2 and details on the PIV measurements are given in section 3.3.

The outline of this chapter is as follows. A brief introduction to empirical mode construction is given next. Then, the main features that characterize the strongly swirling jet undergoing vortex breakdown are summarized in section 6.3. This flow is dominated by strong oscillations resulting from a self-excited global mode. A POD-based method to extract the three-dimensional coherent velocity of this mode from uncorrelated PIV snapshots is explained in section 6.5. In section 6.6, the global mode shape is derived from a local spatial stability analysis. The results of both methods are compared in section 6.7. and a three-dimensional reconstruction of the global mode is presented. It is based on stability analysis and on PIV data providing a portrait of the dominant coherent structures. The main observations are summarized in section 6.8.

6.2 A Brief Survey on Empirical Mode Construction

Large-scale coherent structures in many turbulent shear flows are visually similar to predominant instability modes persisting over a wide range of Reynolds numbers (e.g., see Van Dyke 1975). This similarity applies to flows whose mean velocity profiles are inviscidly unstable and whose shape of these profiles does not materially change during the transition from laminar to turbulent flow. This observation suggests that stability considerations can be applied to the mean turbulent flow field, although there is no theoretical basis for this step. However, weakly nonlinear stability approaches explicitly assume that instability modes and most energetic (POD) modes are the same, at least near the onset of a supercritical Hopf bifurcation (Noack et al. 2003; Stuart 1958).

Stability theory approximates the flow as a given mean flow and a superposition of space- and time-dependent modes. In similar spirit, turbulent coherent structures can be conceptualized as an expansion of modes. A corresponding least-order representation of a flow snapshot ensemble is obtained by the POD. This approach minimizes a time-averaged residual of the POD expansion for a given number of modes, and it is equipped with further useful analytical properties (Holmes et al. 1998; Lumley 1967). Historically, Lumley (1967) introduced POD as a least-biased definition of coherent structures following up on the analytical approach by Townsend (1956) and the well-known Karhunen–Loève decomposition from the 1940s.

Meanwhile, many other empirical expansions of flow snapshots have been proposed serving dynamical systems or control theory goals. For instance, the dynamic mode decomposition (DMD) extracts modes from snapshots that are more related to stability eigenmodes (Rowley et al. 2009; Schmid 2010). Furthermore, the balanced POD serves as economic expansion for linear input-output relationships (Rowley 2005). The present study is restricted to the classical POD since it targets an optimal kinematical representation of the flow.

6.3 Description of the Flow Configuration

This investigation focuses on the nearfield of a turbulent jet at a very high rate of swirl. The basic features of this flow will be described in the following section in order to explain the motivation for investigating the evolution of the coherent structures.

6.3.1 Characteristic Numbers

The Reynolds number and the swirl number are the two independent dimensionless numbers that characterize the global behavior of the flow. The previous is based on the nozzle diameter D and on the axial plug flow velocity V , which is derived from the mean mass flow rate. Throughout this chapter, the Reynolds number is set to $\text{Re}_D = 20000$. The swirl number S is the commonly used parameter that quantifies the amount of swirl (Chigier & Chervinsky 1965; Panda & McLaughlin 1994). It is defined as the ratio between the axial flux of angular momentum \dot{G}_θ and the axial flux of axial momentum \dot{G}_x . According to the conservation of momentum, the swirl number is conserved in the axial direction (Rajaratnam 1976). It is set to $S = 1.22$ throughout this chapter.

6.4 Mean Flow Properties

Figure 6.1 illustrates the streamwise distribution of the time averaged flow. Due to the occurrence of vortex breakdown, the maximum axial velocity is displaced from the jet center. The axial velocity profiles have a local velocity minimum in the inner region of the jet. Thus, a wake with a region of reversed flow on and near the jet axis is resembled with a recirculation bubble that is bound by upstream and downstream stagnation points. This reversed flow region is similar to one created by an obstacle placed on the jet center. Hence, the flow emanating the nozzle is a swirling ring-jet with inner and an outer axial and azimuthal shear layers.

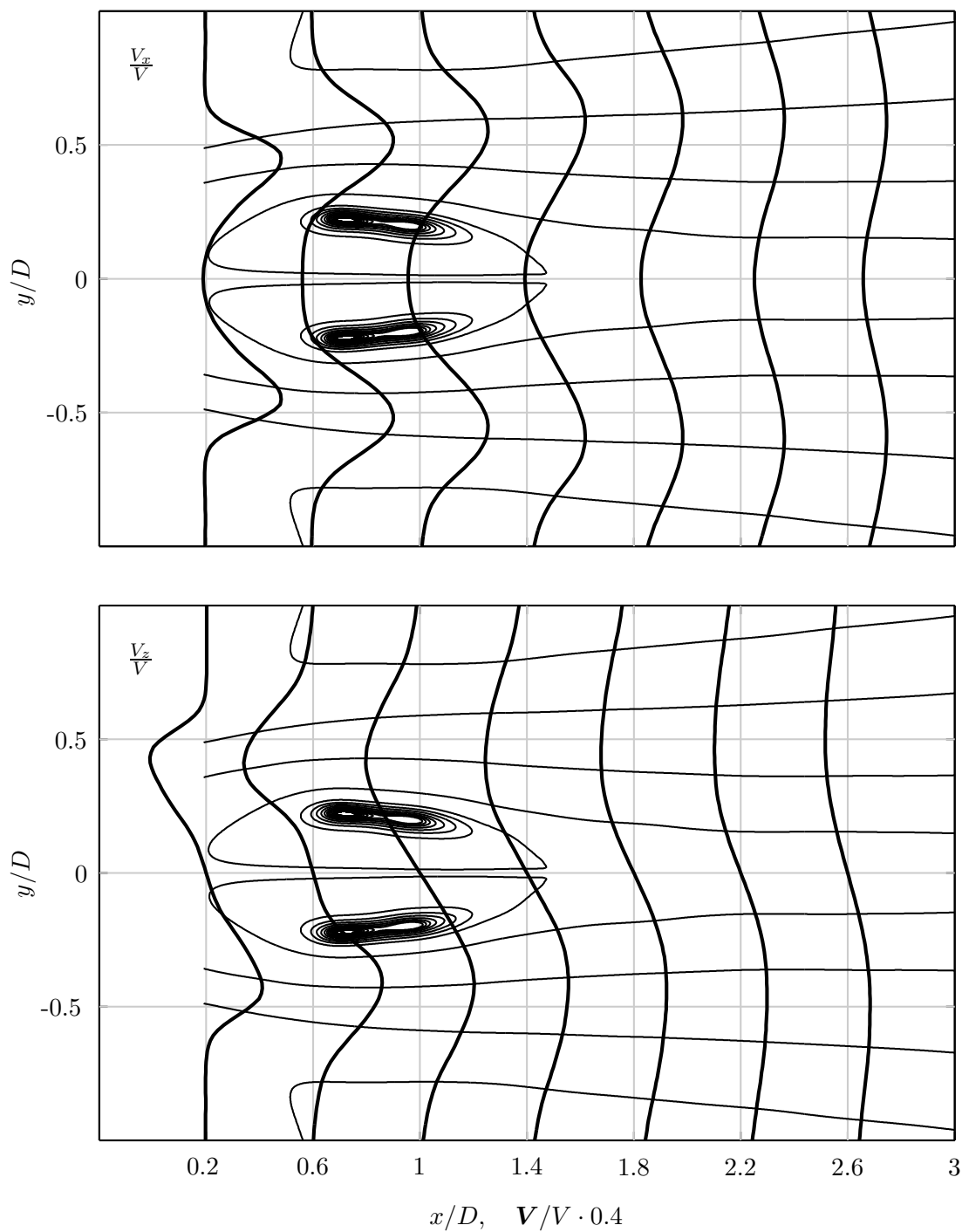


Figure 6.1: Profiles of the mean axial and plane-normal velocity at various axial locations; velocities are normalized by bulk-velocity V ; Streamlines indicate the location of the recirculation bubble ($Re_D = 20000$; $S = 1.22$);

The streamlines shown in figure 6.1 illustrate how the flow is guided around the recirculation zone causing a rapid increase of the jet diameter. Downstream the recirculation zone, at approximately $x/D > 1.4$, the inner shear layers begin to merge and the axial velocity on the jet center increases gradually with increasing downstream distance. The azimuthal velocity profiles may be divided into a vortex core, the region between the jet center and the maximum azimuthal velocity and into the outer azimuthal shear layer located between the maximum azimuthal velocity and the quiescent surrounding fluid. The axial velocity profile has two inflection points and thus, in terms of inviscid hydrodynamic stability they possess as many plane instability modes. Since the flow is axisymmetric these could combine with azimuthal modes. The convex streamlines over the frontal part of the recirculation bubble coupled with the decelerating outer flow provide the necessary conditions for centrifugal instability, as do the concave streamlines in the lee of the bubble coupling with the inner shear layer.

6.4.1 Analytic Representation of the Mean Flow

The incompressible mean flow of the unconfined swirling jet is expressed by an axial velocity V_x and a circumferential velocity V_θ . The radial velocity is neglected. The characteristic velocity scale $V_{\max} = V_{x,\max}$ is defined as the maximum axial velocity at a certain axial location, and the characteristic length scale $R_{\max} = r_{x,\max}$ is represented by the radial distance of the maximum velocity. The ‘Monkewitz profile’ approximates the axial component if we normalize all velocities by V_{\max} and all lengths by R_{\max} . In the current study, we employ a modification of this profile introduced by Michalke (1999):

$$V_x = 4BF_1 [1 - BF_2], \quad (6.1a)$$

where F_1 and F_2 are given by Monkewitz & Sohn (1988) as

$$F_j = \left[1 + (e^{r^2 b_j} - 1)^{N_j} \right]^{-1}, \quad j = 1, 2. \quad (6.1b)$$

The quantity B depends on the axial velocity on the jet centerline V_{cl}

$$B = 0.5 \left[1 + (1 - V_{cl})^{1/2} \right] \quad (6.1c)$$

$N_{1,2} \geq 1$ are the shape parameters that control the thickness of the jet shear layers. In contrast to Michalke (1999), two parameters N_1 and N_2 are used in order to approximate the inner and outer shear layer, respectively. The normalized swirl component is represented by the same equations with the simplification that $B = 1$. Therefore, the local swirl parameter $S_{loc} = V_{\theta,\max}/V_{x,\max}$ is introduced yielding:

$$V_\theta = 4F_3 [1 - F_4] S_{loc}, \quad (6.2)$$

Note that all flow parameters and fitting parameters of equations (6.1–6.2) vary in the axial direction due to the non-parallelism of the mean flow. Their quantities are displayed in table 6.2 for profiles taken at $x/D = (0.25, 0.5, 1, 1.5)$. The fitted velocity profiles are displayed in figure 6.2 together with the measured mean axial and azimuthal velocities for distances in the range $0.5 \leq x/D \leq 3$. Both velocity components are well represented

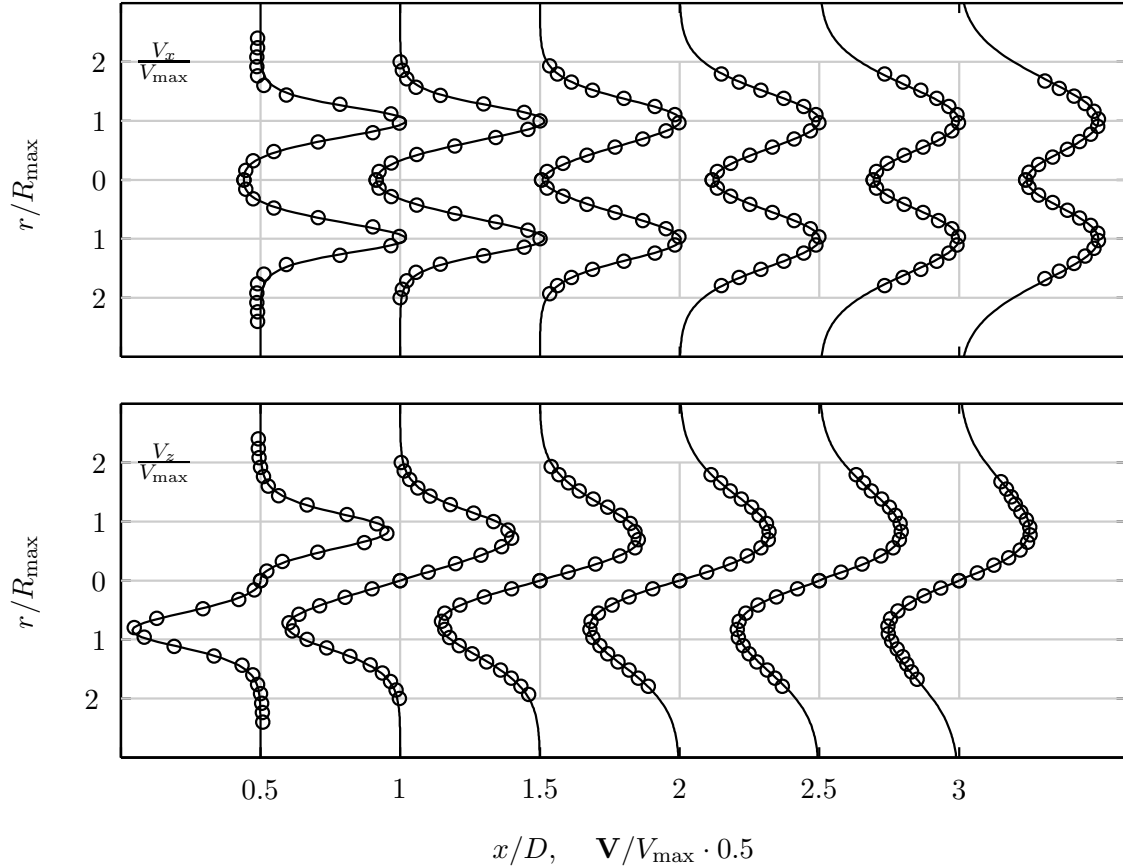


Figure 6.2: Velocity profiles of the approximated mean flow field using the shape parameters listed in table 6.2. Symbols refer to experimental data.

x/D	V_{\max}/V	S_{loc}	R_{\max}/D	B
0.25	0.87	0.91	0.45	1.01
0.50	0.76	0.90	0.50	1.03
1.00	0.63	0.81	0.56	1.04
1.50	0.51	0.71	0.58	1.00

Table 6.1: Flow parameters of mean flow approximation (6.1-6.2)

x/D	N_1	N_2	N_3	N_4	b_1	b_2	b_3	b_4
0.25	4.23	1.10	4.18	0.73	0.51	0.38	0.51	0.27
0.50	3.14	1.35	2.23	1.09	0.56	0.52	0.73	0.66
1.00	2.92	1.06	1.87	0.55	0.53	0.46	0.63	0.35
1.50	2.38	0.87	1.17	0.56	0.46	0.35	0.71	0.57

Table 6.2: Fitting parameters of mean flow approximation (6.1-6.2)

by the suggested approximation. Note that this rather complex mean flow approximation is necessary to accurately represent the two axial and azimuthal shear layers. Simpler models as introduced by Michalke (1999) and Gallaire et al. (2004) did not approximate the underlying mean flow well enough for an accurate linear stability analysis.

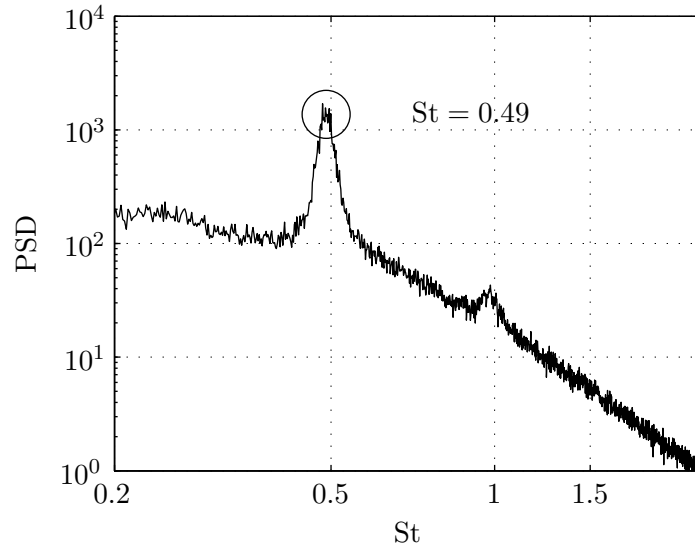


Figure 6.3: Power spectral density of hot-wire-anemometer voltage fluctuations for the unforced swirling jet at $(x/D, y/D) = (0.57, 0.38)$. The same dominant frequency is measured in the inner and outer axial shear layers.

6.4.2 Self-excited Oscillations

Former experimental investigations by [Liang & Maxworthy \(2005\)](#) and numerical simulations of [Ruith et al. \(2003\)](#) revealed that the onset of vortex breakdown is accompanied by energetic large-scale fluctuations. In the present investigation, these strong oscillations had a distinct frequency (figure 6.3). By traversing a hot-wire probe in radial and axial directions, a constant dominant frequency is observed throughout the region of interest, with highest amplitudes occurring in the inner and outer axial shear layers. As will be shown later, the spectral peak at $St = 0.49$ corresponds to the precession of the vortex core or, in terms of hydrodynamic stability, to the appearance of a strong helical instability with azimuthal wavenumber $m = 1$. This relatively sharp peak is attributed to a self-excited global mode with its origin being located on the jet centerline in the region of reversed flow ([Gallaire et al. 2006](#); [Liang & Maxworthy 2005](#); [Ruith et al. 2003](#)).

There are several experimental techniques to confirm that the flow has transitioned to a global mode via a supercritical Hopf bifurcation. According to [Huerre & Monkewitz \(1990\)](#), near critical conditions, the amplitude of the global mode A is governed by the forced Landau equation ([Landau & Lifshitz 1987](#)):

$$dA/dt = c_1 A - c_2 A^3 + g \quad (6.3)$$

where c_1 is the temporal amplification rate during the time of exponential growth and g is proportional to the external forcing amplitude. In the absence of forcing, the limit cycle amplitude should increase proportionally to the deviation from a control parameter,

$$A_{\text{sat}} \propto \sqrt{S - S_{\text{crit}}} \quad (6.4)$$

where S_{crit} is the critical control parameter for a constant Reynolds number and $S \geq S_{\text{crit}}$. The amplitude of the global mode is measured with a calibrated hot-wire placed in the

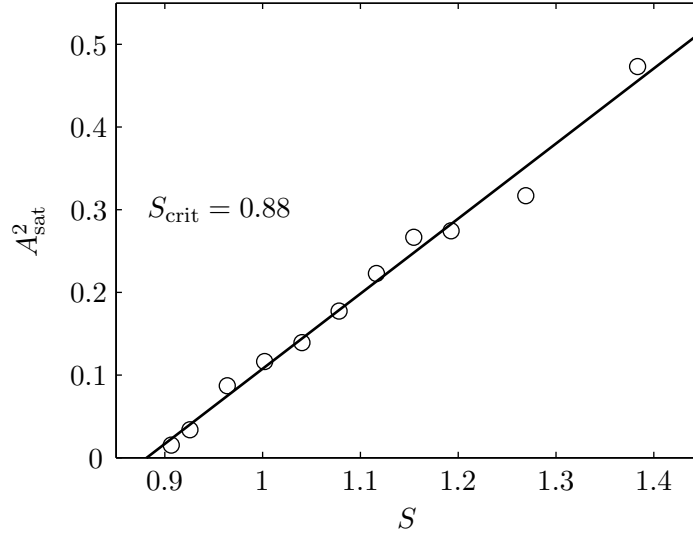


Figure 6.4: The squared saturation amplitude A_{sat}^2 of the dominant mode as a function of the increasing control parameter S . The open circles represent measurements; the straight line represents a least-squares fit to this data. This linear dependence is characteristic for a supercritical Hopf bifurcation. The zero marks the critical control parameter $S_{\text{crit}} = 0.88$. A_{sat} is measured with a single hot-wire anemometer placed at $(x/D, y/D) = (0.57, 0.38)$ in the center of the inner axial shear layer ($\text{Re}_D = 20000$).

center of the inner axial shear layer at $(x/D, y/D) = (0.57, 0.38)$. At this radial location the oscillations reach their maximum amplitude. A single-wire probe is used with the wire aligned parallel to the azimuthal velocity. The signal is Fourier transformed and the amplitude at the dominant frequency is derived. Figure 6.4 shows the growth of the global amplitude with increasing swirl while keeping the Reynolds number constant. Evidently, the saturation amplitude is proportional to $\sqrt{S - S_{\text{crit}}}$. The linear dependence suggests that the oscillation is of the supercritical Hopf bifurcation type. The critical swirl number is found to be $S_{\text{crit}} = 0.88$.

A second experimental technique that may confirm the existence of a self-excited global mode is to investigate the lock-in characteristic. According to [Provansal et al. \(1987\)](#), [Sreenivasan et al. \(1989\)](#) and [Juniper et al. \(2009\)](#), the critical forcing amplitude at which the frequency of the natural mode St_{nat} locks onto the forcing frequency St_f should linearly depend on $|\text{St}_{\text{nat}} - \text{St}_f|$. The lock-in region is defined as the forcing amplitude at which the spectral peak of the natural mode disappears and the spectrum peaks at the forcing frequency. Measurements conducted with a single hot-wire, placed on the center of the inner axial shear layer at $(x/D, y/D) = (0.57, 0.38)$, revealed that the critical lock-in amplitude is proportional to $|\text{St}_{\text{nat}} - \text{St}_f|$ (figure 6.5). This provided additional evidence for the existence of a supercritical Hopf bifurcation needed to establish a global mode.

Concluding this chapter, the base flow under investigation is a swirling ring-jet whose conical boundaries originate at the orifice due to a recirculation zone located on the jet axis. The axial and azimuthal shear layers coexist in the outer region of the jet and in the jet core. The swirl number considered presently is above the critical value at which a supercritical Hopf bifurcation takes place. Thus, the strong coherent fluctuations that are dominating the entire flow field near the nozzle are attributed to the existence of a self-excited global mode.

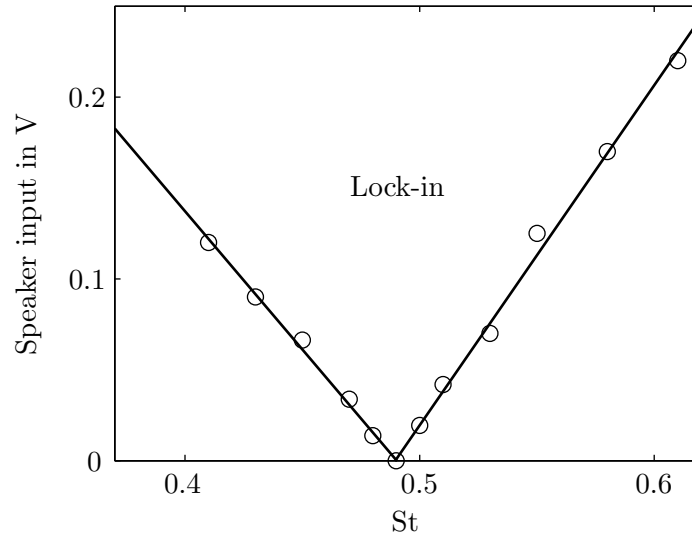


Figure 6.5: Critical loudspeaker input voltage at which the global mode locks onto the forcing frequency. The open circles mark measurement values and the solid lines represent fits to these data. The linear dependence of the threshold amplitude on $|St_{\text{nat}} - St_f|$ is another indicator of a supercritical Hopf bifurcation to a global mode. The flow is forced at the orifice at $m = 1$ which is the azimuthal wavenumber of the natural mode. The natural frequency is $St_{\text{nat}} = 0.49$ ($Re_D = 20000$; $S = 1.22$)

6.5 Empirical Construction of the Global Mode

In this section, the path is outlined leading from the POD of 2D PIV data to the construction of full 3D time-dependent velocity field. This method is applicable whenever the coherent structure is solely characterized by two POD modes that span the traveling wave pattern. This section was written in collaboration with Moritz Sieber, who worked as a research assistant for the author of this thesis. His great work is acknowledged here.

6.5.1 Spatial and Temporal POD Modes

The snapshot POD, as described above, is applied to the data taken in the crossflow and streamwise planes of measurement. Both sets of measurement consist of 800 snapshots. The observation domains have a spatial extent of $-1.1 < y/D < 1.1$ and $-1.1 < z/D < 1.1$ at $x/D = 0.57$ for the crossflow plane and $0.25 < x/D < 3$ and $-1.1 < y/D < 1.1$ at $z/D = 0$ for the streamwise plane. The eigenvalue spectrum of POD modes for both measurement planes is shown in figure 6.6.

For both cases the POD shows that the first two eigenvalues contain substantial amount of energy. In the crossflow plane the first two modes contain already 30 % of TKE while in the streamwise plane these modes contain more than 14 %. In both cases, the energy contained in the two leading modes is nearly equal suggesting that the two modes span a traveling wave.

In the crossflow plane of measurement, the first and second spatial POD modes resemble one another as do the fourth and fifth modes (figure 6.7). The first pair of modes describes an azimuthal wave represented by two modes having a $\pi/2$ phase shift. The second pair having twice the azimuthal wavenumber has a $\pi/4$ shift between them with respect to the

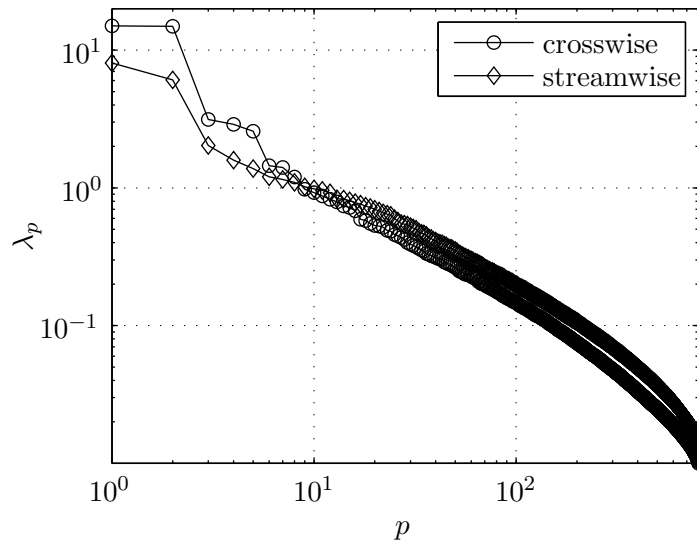


Figure 6.6: POD spectrum of the velocity modes for the crossflow and streamwise plane of measurement. TKE is expressed in per cent of the sum $K = \sum_{p=1}^N K_p$.

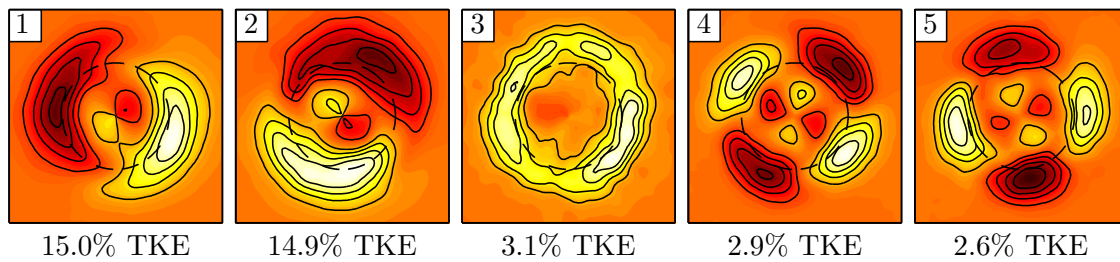


Figure 6.7: First 5 POD modes of the crossflow plane of measurement; radial velocity component is shown with contour lines $v_r/\max(v_r) = (-0.8, -0.6, -0.4, -0.2, 0.2, 0.4, 0.6, 0.8)$. The POD mode-number p is written in the top left corner and the percentage of TKE at the bottom. The dashed circle indicates the nozzle diameter.

dominant harmonics. The first pair represents a traveling azimuthal wave with wavenumber $m = 1$ and the second pair indicates a traveling azimuthal wave $m = 2$.

To elucidate the temporal behavior of the identified structures, the phase portraits of the corresponding temporal amplitudes a_p are investigated. Considering the phase portrait of a_1 and a_2 (figure 6.8), it is clearly seen that the modes describe an oscillating process. In addition, the comparison of a_1 and a_4 reveals that the second mode-pair is the second harmonics with respect to the first one, as indicated by the eight-like form of the Lissajous figure. Both mode pairs describe rotating structures that rotate with the same revolution time with azimuthal wavenumber $m = 1$ for the first and second modes and with $m = 2$ for the fourth and fifth modes. The third mode describes an axisymmetric fluctuation of the flow, which is not correlated with the identified harmonic structures (figure 6.8). This mode is related to the axial fluctuation of the location of vortex breakdown.

Figure 6.9 displays the POD modes of the streamwise cross-section. Again, the first two modes have the same azimuthal wavenumber and frequency. These similar modes are axially shifted by a quarter wavelength. They describe coherent structures that are first

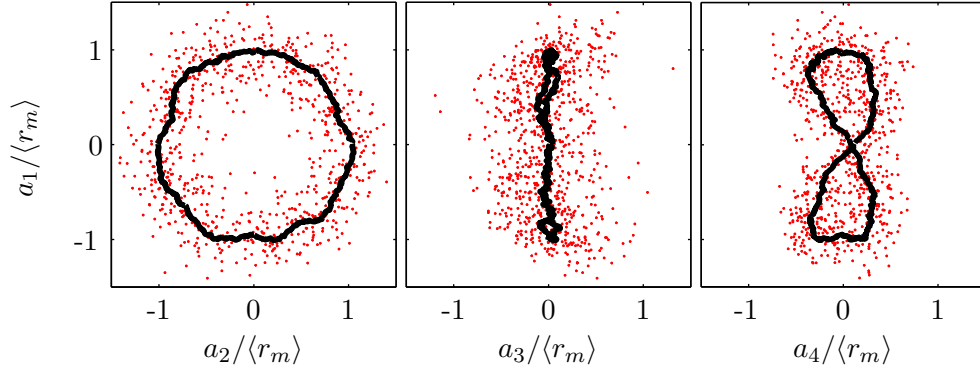


Figure 6.8: Phase portrait of the POD modal amplitudes a_p for the crossflow plane of measurement. The dots represent the experimental data. The solid line is a smoothed fit and similar to Lissajous figures. $A = \sqrt{a_1^2 + a_2^2}$ is the mean amplitude of the first two modes (see (6.5)).

growing and then decaying in the streamwise direction. The temporal representation of the first two streamwise modes corroborates an oscillating process (figure 6.10). The first two modes in both crossflow and streamwise planes of measurement describe a harmonically fluctuating structure that the spectral analysis (figure 6.3) picked up as containing one fundamental frequency. Consequently one may assume that both modes are tied to the same oscillatory structure. Linking the information from both measurements suggests that the dominant structure is a helical instability mode with azimuthal wavenumber $m = 1$ winding around the recirculation bubble. In this context, the structure at the jet center (i.e. $r/D = 0$) near the nozzle exit ($x/D < 0.5$), that is visible in the two streamwise modes, is interpreted as being the wavemaker for the global mode.

Note that the relative levels of the first mode-pair with respect to its TKE content are unequal for crosswise and streamwise observation planes. This is due to the dominant structure governing only half of the analyzed streamwise measurement domain. Hence, the energy content with respect to the entire streamwise plane is approximately half as high in comparison to the crosswise plane. Using an appropriate sub-domain for streamwise POD analysis can decrease this difference.

The third and fourth streamwise modes (figure 6.9) are coupled and represent the meandering of the recirculation bubble. The phase portrait reveals no relation to the dominant structure. Hence, the meandering is affected by other processes.

In conclusion, the periodically fluctuating global mode is represented by the first two POD modes in both measurement planes. This harmonic process is indicated by the phase portraits. It is possible to extract the phase information of the dominant coherent structure by identifying the corresponding POD modes. It is then a straight forward procedure to use the temporal amplitudes of these POD modes to obtain the phase angle φ_k for each snapshot k , yielding

$$\check{a}_k e^{i\varphi_k} = a_1(t_k) + ia_2(t_k) \quad (6.5)$$

This phase angle corresponds to the phase position of a snapshot with respect to the dominant structure, in the manner that the optimal amount of kinetic energy of each snapshot is represented by these modes. Hence, it is possible to define a flow phase via the POD. In the following this definition of phase is used to extract the coherent structures.

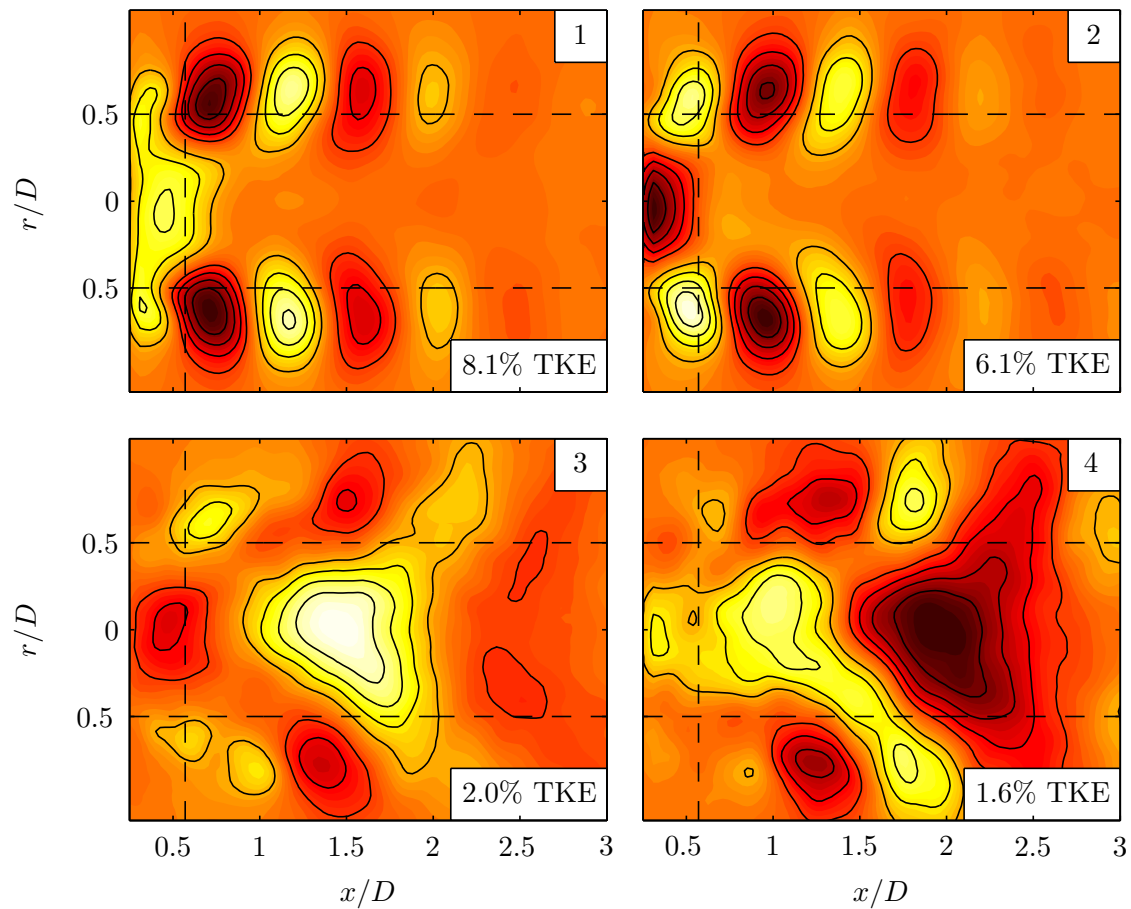


Figure 6.9: First 4 POD modes of the streamwise measurement plane; transversal velocity component is shown with contour lines $v_y/\max(v_y) = (-0.8, -0.6, -0.4, -0.2, 0.2, 0.4, 0.6, 0.8)$. The mode number is written in the top right corner and the percentage of TKE in the bottom right corner. The vertical dashed line indicates the position of crossflow plane of measurement.

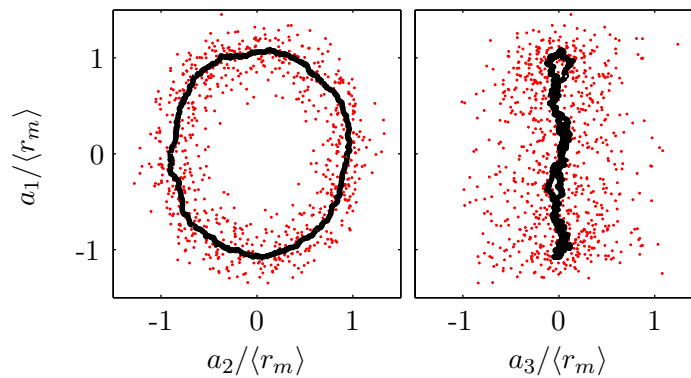


Figure 6.10: Same as figure 6.8, but with a_p of the streamwise measurement plane.

6.5.2 Linking the POD Modes to the Coherent Velocity

First, we define the coherent velocity \mathbf{v}^c . Holmes et al. (1998) recommend to identify and exploit symmetries in experimental data. This additional filter reduces the complexity of the POD and yields a better understanding of the underlying process. For an axisymmetric swirling jet, the azimuthal direction θ can be regarded as a homogeneous direction, as it is also assumed for linear stability analysis. This direction can be represented through Fourier modes with respect to the azimuthal wavenumber $m = 1$. The triple decomposition assumes the coherent component as being a phase-dependent average of a harmonic signal with temporal period T . Hence, the time can also be regarded as a homogeneous direction and can be decomposed by a Fourier representation according to the phase information φ_k of the POD (6.5). With these simplifications, the coherent velocity reads

$$\mathbf{v}^c(x, r, \theta, t) = \Re \left\{ \hat{\mathbf{v}}_{mn}(x, r) e^{i(m\theta - n\omega_r t)} \right\} \quad (6.6)$$

where m indicates the azimuthal wavenumber, n is a multiple of the fundamental frequency $\omega_r = 2\pi f$ and $\hat{\mathbf{v}}_{mn}(x, r)$ is a complex valued vector field containing the radial and axial dependence of the coherent component. The Fourier modes $\hat{\mathbf{v}}_{mn}$ are obtained through a Fourier transform of the fluctuating part of the velocity \mathbf{v}'

$$\hat{\mathbf{v}}_{mn}(x, r) = \frac{1}{2\pi T} \int_0^T \int_{-\pi}^{\pi} \mathbf{v}'(x, r, \theta, t) e^{-i(m\theta - n\omega_r t)} d\theta dt \quad (6.7)$$

As described in the previous section, the POD relates each snapshot to a phase angle of the dominant fluctuations. Thus, the Fourier modes $\hat{\mathbf{v}}_{mn}$ are obtained for a discrete time (according to φ_k) and continuous space Fourier transform:

$$\hat{\mathbf{v}}_{mn}(x, r) = \frac{1}{2\pi N} \sum_{k=1}^N \int_{-\pi}^{\pi} \mathbf{v}'(x, r, \theta, t_k) e^{-i(m\theta - n\varphi_k)} d\theta \quad (6.8)$$

This is valid only if the phase angles φ_k are equally distributed in $[0, 2\pi]$. The phase angles obtained from the POD fulfill this condition, so these angles correspond to a oscillation with uniform frequency $\varphi_k = \omega_r t_k$.

The assumed rotational symmetry is examined for the crossflow measurement plane of the vector field. If we omit the assumption of homogeneity in θ of equation (6.6), then the complex coherent component is given by

$$\hat{\mathbf{v}}_n(x, r, \theta) = \frac{1}{N} \sum_{k=1}^N \mathbf{v}'(x, r, \theta, t_k) e^{in\varphi_k} \quad (6.9)$$

This equals the definition of POD modes (2.26) provided the first two POD modes are considered in a complex representation with $\check{a}_k e^{i\varphi_k} = a_1(t_k) + ia_2(t_k)$, except that the amplitude \check{a}_k of the temporal modes is neglected. We assume the amplitude variations to be caused by turbulent noise, which is indicated by the phase portrait in figure 6.11 (see also Depardon et al. (2007)). In consequence, the spatial POD modes are similar to the coherent component, in detail $\Phi_1 + i\Phi_2 \approx \hat{\mathbf{v}}_1$ (with $\hat{\mathbf{v}}_n$ as in (6.9)).

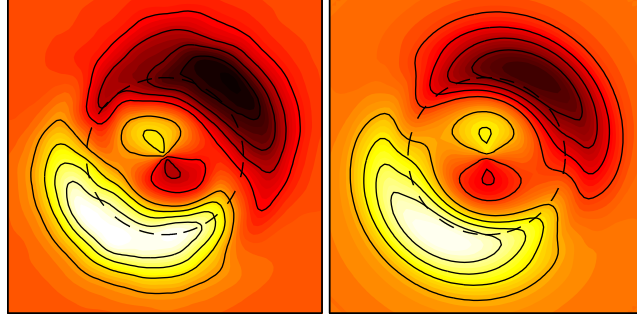


Figure 6.11: Coherent radial velocity v_r^c derived from crossflow measurement via $\mathbf{v}^c = \Re\{\hat{\mathbf{v}}_1(r, \theta)\}$ (left) is compared with the one derived from streamwise measurement via $\mathbf{v}^c = \Re\{\hat{\mathbf{v}}_{11}(r)e^{i\theta}\}$ (right). The flow is visualized by the contour lines $v_r^c/\max(v_r^c) = (-0.8, -0.6, -0.4, -0.2, 0.2, 0.4, 0.6, 0.8)$. The dashed circle indicates the nozzle diameter.

In figure 6.11, the coherent component \mathbf{v}^c in the crosswise measurement plane is compared between the simple phase-average derived from crosswise data $\mathbf{v}^c = \Re\{\hat{\mathbf{v}}_1(r, \theta)\}$ and the phase-average constructed from streamwise data assuming azimuthal symmetry $\mathbf{v}^c = \Re\{\hat{\mathbf{v}}_{11}(r)e^{i\theta}\}$. The contour plots of \mathbf{v}^c are very similar proving that the assumed symmetry is legitimate. The discrepancy between the two plots is attributed to an insufficient number of snapshots for more precise averaging.

It should be noted, that the triple decomposition, as outlined in this section, is not limited to the use of POD. The phase information of oscillatory fluctuations is often inferred in three different ways. First, if the flow is externally actuated, the phase information can be directly derived from the actuation signal. Second, it is possible to obtain the required phase information from a time resolved point measurement (e.g. hot-wire), using a bandpass filter and a Hilbert transformation. Third, it is provided by a statistical approach such as the POD described above. In the present investigation, the POD is chosen because it has some advantages with respect to the other techniques which will be shortly depicted.

Most flow oscillations do not occur at a prescribed frequency, as there is always jitter. Filtering with respect to a fixed frequency will ignore large portions of the flow affected by frequency modulation, reappearing in \mathbf{v}^s . With a locally adjusted frequency, we reduce the amount of TKE captured by \mathbf{v}^s , while \mathbf{v}^c lumps a narrow frequency band into a single frequency. In the case of a phase average, triggered by external forcing, no phase jitter is incorporated at all. If a time-resolved sensor is used, the amount of phase jitter accounted for depends on the bandwidth of the bandpass filter used. When using the POD phase, obtained according to (6.5), no fixed frequency has to be assumed, and the calculated phase is the optimal one in terms of energy representation. The optimal phase is related to the optimality of spatial POD modes, where these modes are understood as a prior guess for coherent structures providing the phase through projection on the snapshots. Furthermore, in contrast to a time-resolved point measurement, the POD approach predicts the phase angle from spatial modes and not from one single point in the flow yielding a more accurate prediction of the global phase.

6.5.3 Construction of Three-dimensional Coherent Structures

It is now straightforward to construct 3D-velocity data from the two measurement planes utilizing the identified symmetries of the coherent velocity \mathbf{v}^c discussed in the previous section. The approach for this construction is graphically outlined in figure 6.12, illustrating the main steps in this section.

- (i) Identification of a fundamental frequency by time-resolved point measurement.
- (ii) POD analysis of the PIV data in the two measurement planes, which identifies dominant structures and provides the related phase information.
- (iii) Calculation of coherent structures with phase information and identification of azimuthal symmetries through a Fourier transform.
- (iv) Construction of 3D data of the coherent structure using the identified symmetries to extrapolate data from 2D measurement plane.

In the final step, the streamwise measurement plane (r - x -plane) gives the axial and radial dependence of the coherent complex amplitude $\hat{\mathbf{v}}_{mn}(x, r)$ (6.7). As shown in the previous section, the fundamental frequency is related to the azimuthal wavenumber $m = 1$ and first harmonic $n = 1$. Combining this information in (6.6), a spatio-temporal representation of the coherent velocity is given by

$$\mathbf{v}^c(x, r, \theta, t) = \Re \left\{ \hat{\mathbf{v}}_{11}(x, r) e^{i(\theta - \omega_r t)} \right\} \quad (6.10)$$

6.6 Most Unstable Spatial Modes

Prior the discussion of the results obtained from the linear stability analysis, the simplifying assumptions are recalled here. Due to the occurrence of vortex breakdown, the underlying time-averaged flow exhibits strong gradients in the axial direction. Hence, the employed parallel-flow assumption for the normal mode decomposition (2.6) is violated due to these gradients. Various approaches have been developed to overcome this shortcoming of the linear theory, generally restricted to small deviations. Intriguingly, wavelength and radial amplitude distribution are often found to be reasonably good approximated by the eigensolution of the Orr–Sommerfeld equation solely based on a locally parallel flow.

In the scheme of linear stability analysis, the spatial amplification rate α_i is computed for the azimuthal wavenumber $m = 1$ in order to derive the coherent velocity of the single-helical instability mode that is observed in the experiment. The complex wavenumber is calculated for real frequencies in the range $0 \leq \omega_r R_{\max} / V_{\max} \leq 6$ at four different axial locations. The spatial branches are displayed in figure 6.13. Note that the frequency ω_r is normalized by the length scale R_{\max} and velocity scale V_{\max} (see section 4.1.1) whereas the Strouhal number St associated with the global oscillation frequency is based on the bulk velocity V and nozzle diameter D . The dimensionless frequency expressed by $\omega_r R_{\max} / V_{\max}$ increases in the downstream direction as the downstream increase of R_{\max} is more rapid than the decay of V_{\max} (see the open circles in figure 6.13). At the axial locations where the flow is unstable to the global frequency only one unstable spatial branch is found and the spatial amplification rate can easily be tracked in the downstream direction. Waves

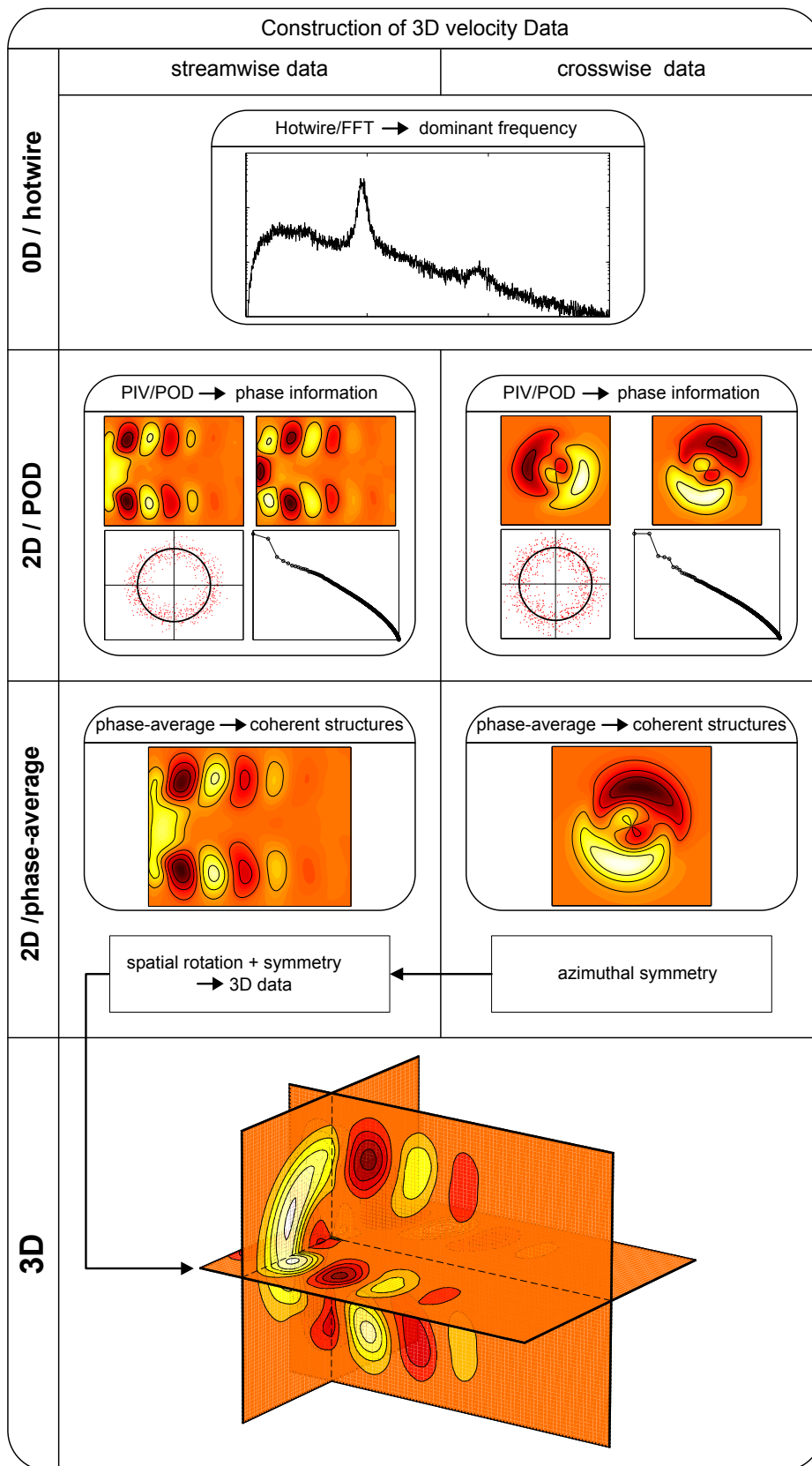


Figure 6.12: Schematic diagram of the 3D flow construction. The illustrated steps are as follows: (a) identification of the fundamental frequency; (b) POD analysis of the PIV data yielding the flow phase; (c) Identification of coherent structures and symmetries; (d) Construction of 3D data from the 2D measurements.

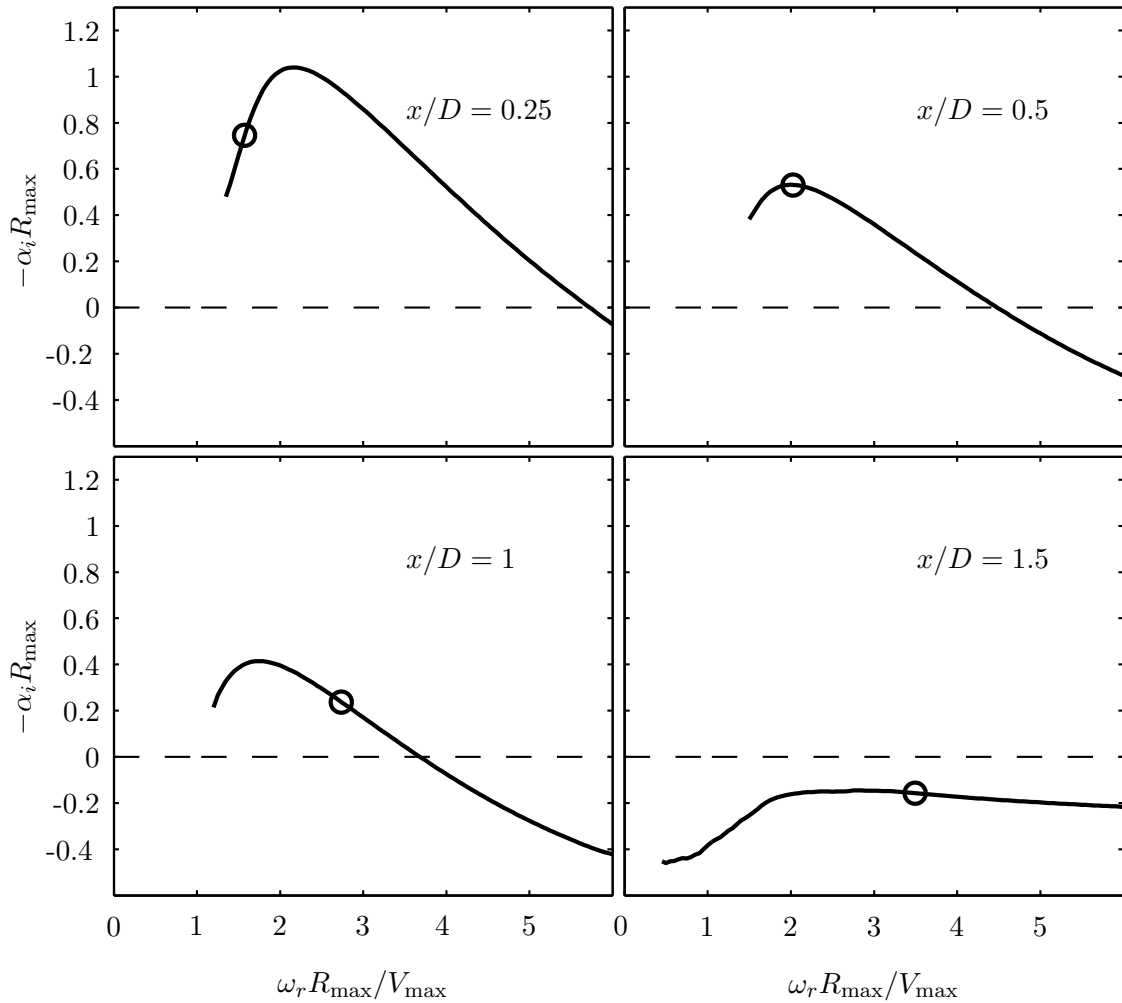


Figure 6.13: Spatial amplification rate of the mode $m = 1$ versus dimensionless real frequency at different cross-sections. The open circle marks the measured frequency of the mode $m = 1$ indicating the growth ($x/D \leq 1$) and decay ($x/D = 1.5$) of most unstable mode.

forced at the global frequency grow rapidly near the nozzle exit where the shear layer is thin relative to the nozzle radius. As the shear layer spreads in the radial direction with increasing downstream distance, the spatial amplification rate at $St = 0.49$ decreases. The corresponding spatial branch downstream of the point of neutral amplification is stable for all frequencies.

The evolution of the spatial growth rate α_i with downstream distance is investigated in detail by computing the eigenmodes for various streamwise locations at the global frequency of $St = 0.49$ (figure 6.14). Accordingly, the spatial growth rate decreases continuously with downstream distance reaching natural amplification at $x/D = 1.28$. Downstream of the neutral point, the decaying rate increases in the axial direction up to $x/D = 2$. In the decaying region several modes coexist and the spatial branch that corresponds to the most unstable mode is tracked from the unstable regime where only one mode exists by minimizing the distance between the eigenfunctions and eigenvalues (see the last paragraph of section 2.4.3 for further details). Note that in the bottom right frame of figure 6.13, only the spatial branch that corresponds to the most unstable mode is shown. The computed

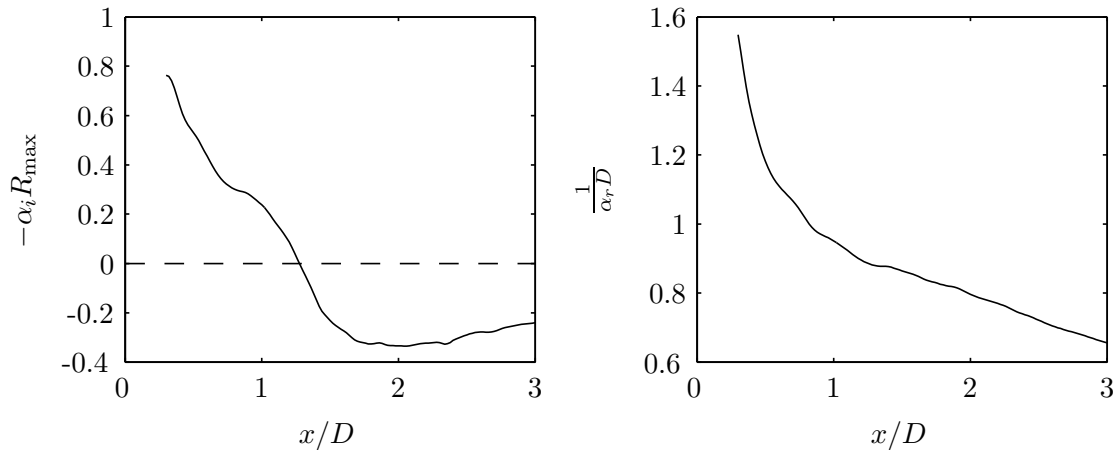


Figure 6.14: Streamwise evolution of the spatial amplification rate (left) and axial wavelength (right) of the most unstable mode $m = 1$ based on local analysis.

axial wavelength of the most amplified mode is displayed as a function of x/D in figure 6.14. The rapid decrease in wavelength in the axial direction is caused by non-parallel effects. The convectively unstable modes are amplified at constant frequency while they travel downstream. Due to the pronounced jet widening, their convection velocity, that is related to U , is rapidly decaying in the axial direction, thus causing the wavelength to decrease.

The accuracy of the stability analysis is validated by comparing the computed eigenfunctions with the actually measured phase-averaged velocities described in section 6.5. The eigenfunction of the most amplified mode is computed at $x/D = 0.57$, the axial location where crossflow measurements are conducted. Comparing the empirical mode, displayed in figure 6.11, to the stability mode, displayed in figure 6.15 (b) shows obvious similarities. Both modes agree well in the outer region of the jet where they are most energetic ($|y/D| > 0.5$). In the inner region the structures seem to be out of phase and the coherent velocity near the jet core that is evident from the measurements is not modeled by the eigenmodes. As stated previously, the present stability analysis is only valid for the outer convective unstable region of the jet. In particular, near the jet core close to the nozzle exit where coherent velocity indicates the location of the wavemaker, the present analysis should produce wrong estimations. Further downstream of the wavemaker, the agreement of the eigenmodes to the phase-averaged measurements improves even for the inner region of the jet. This is shown by constructing the streamwise shape of the global mode from the locally computed eigenfunctions and eigenvalues. The overall growth of a disturbance can be calculated by integrating the complex α along x , yielding

$$[v_x^c, v_r^c, v_\theta^c, p^c] = \Re \left\{ [H, iF, G, P] e^{i \left(\int_{x_0}^x \alpha dx + m\theta - \omega_r t \right)} \right\} \quad (6.11)$$

where α is complex and x_0 is the location of the first measured profile with $x_0/D = 0.2$. In order to consistently ensemble the local eigenmodes to a global solution, the eigenvector X is normalized using the Euclidean norm $\|X\| = \sqrt{(X, X)}$, and the phase angle is equalized

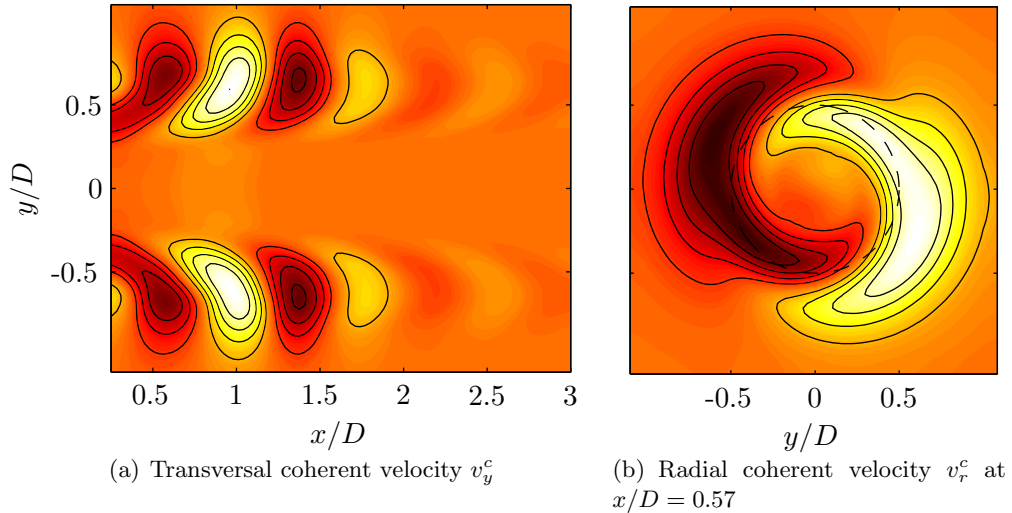


Figure 6.15: Coherent velocity of the most amplified normal mode. Eigenfunctions are shown at an arbitrary phase-angle. The contour lines represent $v_r^c / \max(v_r^c) = (-0.8, -0.6, -0.4, -0.2, 0.2, 0.6, 0.4, 0.8)$. The eigenvalue problem (2.14) is solved for the azimuthal wavenumber $m = 1$ and global frequency $St = 0.49$. The dashed circle in (b) indicates the nozzle diameter which approximately separates the inner and the outer shear layer.

at the characteristic jet radius R_{\max} . The resulting coherent velocity distribution along the stream-wise plane is shown in figure 6.15 (a).

Except for the jet core region upstream $x/D = 0.7$ where the wavemaker is located, the computations agree well with the empirical POD modes shown in figure 6.9. The axial wavelength and the radial amplitude distribution are well estimated. Even the overall amplification is well approximated with the maximum coherent amplitude at $x/D \approx 1.25$ and the decaying region further downstream.

6.7 Three-dimensional Shape of the Global Mode

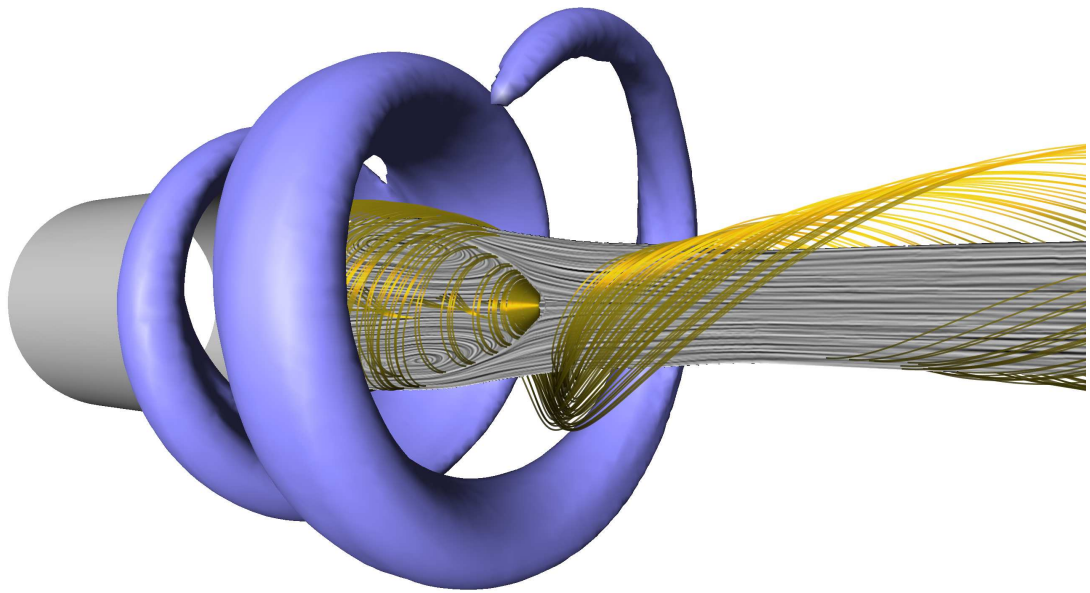
Finally, the empirically extracted mode and the mode derived from the stability model, are constructed in the entire three-dimensional domain. By adding the mean flow to the coherent velocities, the global mode renders a physically plausible shape as can be seen in figure 6.16. The blue helix represents an iso-surface having constant phase-averaged azimuthal vorticity. For the upper figure the phase-average is derived applying the empirical approach based on the POD as outlined in section 6.5, whereas for the lower figure the phase-averaged velocity is derived from the linear stability analysis based on the analytically approximated mean flow as outlined in 6.6. Both methods reveal the same structure. It represents the $m = 1$ mode that rotates in the clockwise direction with the base flow at a rotation rate corresponding to $St = 0.49$. The yellow streamlines and the gray LIC-surface (linear integral convolution Cabral & Leedom (1993); Stalling & Hege (1995)) are computed from the actually measured time-averaged flow. The streamlines are intended to visualize the direction of rotation of the mean flow and also indicate the mean boundary of the recirculation bubble. Note that the streamlines are orientated perpendicularly to

the roll-axis of the helical mode. Accordingly, the helical structure is co-rotating counter-winding. Similar results have been found in experiments by [Liang & Maxworthy \(2005\)](#) and in DNS computations conducted by [Ruith et al. \(2003\)](#). The LIC surface visualizes the flow structures inside the recirculation bubble showing a stationary ring-like vortex. This structure must be carefully interpreted because the time-averaged flow field of the inner region of the recirculation bubble differs strongly from the phase-averaged or instantaneous flow. It is observed that the entire recirculation bubble meanders around the jet center in phase with the outer coherent structure. As mentioned above, the frequency of the global mode is dictated by the wavemaker located at the jet center. This precessing of the vortex core is not visible in figure 6.16 since the level of the vorticity iso-contour is selected to most properly visualize the structures in the outer region of the jet and is therefore too high for visualizing the structures located in the interior of the jet. The 3D flow visualizations have been prepared with Amira software by Christoph Petz (Zuse-Institute, Berlin).

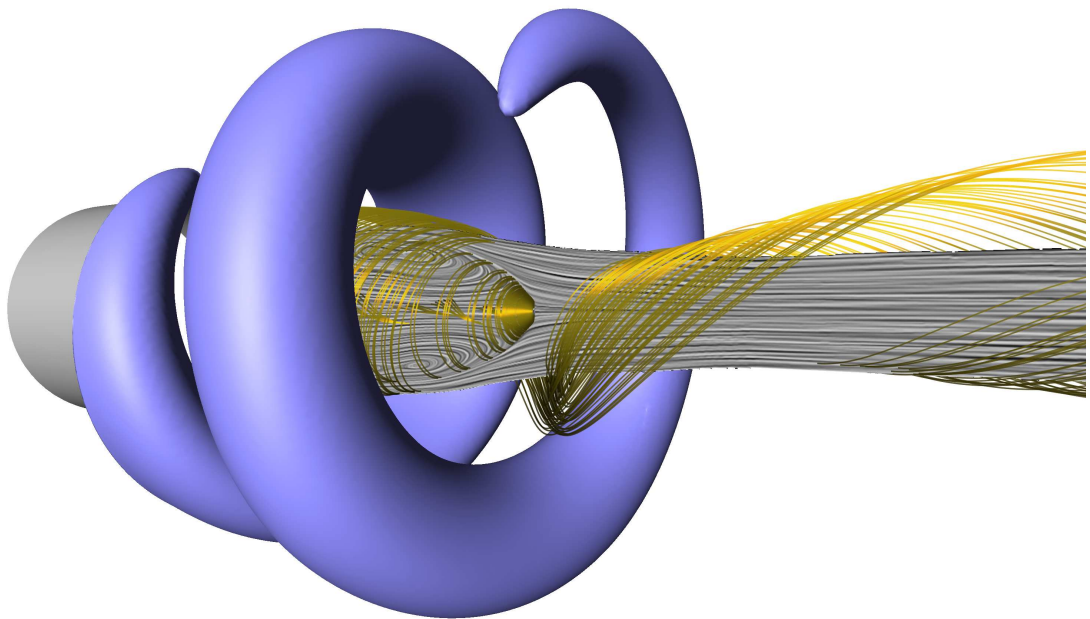
6.8 Summary and Discussion

The coherent structures of strongly swirled jets undergoing vortex breakdown are investigated. The nature of these structures is phenomenologically observed, whereupon power spectra measured by a hot-wire indicate that this flow regime exhibits pronounced harmonic oscillations. The origin of these oscillations is studied by two independent experimental techniques. First, the lock-in behavior of the forced flow is investigated and it reveals a linear relationship between the forcing frequency and the critical lock-in amplitude. Second, the limit-cycle amplitude of the dominant mode is observed to be proportional to the square root of the deviation from the swirl magnitude considered as a control parameter. Both observations corroborate quantitative relationships of a self-excited oscillatory global mode originating from a supercritical Hopf bifurcation. In other words, the results are consistent with mean-field theory. The phase-averaged velocities show the existence of a co-rotating counter-winding helical mode. Most energy of its intensity is located in the outer region of the jet. A similar structure was observed experimentally by [Liang & Maxworthy \(2005\)](#) and in numerical simulations by [Ruith et al. \(2003\)](#). Theoretical considerations of [Gallaire et al. \(2006\)](#) suggest that the self-excited global mode originates from a local region of absolute instability located in the jet center. These results are confirmed by the present observation where a strong precessing of the vortex core sets the pace of the amplified instabilities in the outer part of the jet.

The observed oscillatory helical structures are then closely examined. Starting with an experiment using 2D uncorrelated PIV snapshots in a streamwise and a cross-flow plane, the 3D time-dependent coherent structures are extracted by kinematic and dynamic considerations, exploiting the observed dominant periodicity of the flow. The kinematic velocity field reconstruction starts from the uncorrelated 2D streamwise velocity fields determined by PIV. The pronounced oscillatory nature of the fluctuations is evidenced by two leading POD modes spanning a corresponding convecting vortex pattern. These two POD modes allow one to attribute a phase to each snapshot taken. A continuous time dependence is imposed by assuming a single oscillation frequency, consistent with the experimental measurements. This assumption allows for restoration of time dependence provided that small amplitude variations of the turbulent flow such as the less-energetic higher harmonics



(a) Empirically extracted coherent structure using POD



(b) Theoretically extracted coherent structure using linear stability analysis

Figure 6.16: Three-dimensional flow field visualizing the global mode $m = 1$ that is dominating the nearfield of a strongly swirled jet ($Re_D = 20000$; $S = 1.22$). The blue iso-contour represents the constant azimuthal vorticity of phase-averaged velocities indicating the streamwise growth of a single-helical instability in the outer region of the jet. Streamlines and LIC surface are based on the time-averaged flow, visualizing the recirculation bubble and the sense of rotation of the swirling jet.

and stochastic small-scale fluctuations are negligible. A 3D flow pattern is reconstructed by exploiting an azimuthal symmetry of the observed helical coherent structures. The resulting 3D flow pattern corroborates PIV observations in crossflow planes. Thus, the spatio-temporal evolution of the full 3D helical structure is obtained from 2D uncorrelated data sets.

The velocity field of the global mode is also derived by means of a linear stability analysis employing the measured mean flow. A spatial approach is justified by previous experiments, showing that the wavemaker generating the global oscillations is located inside the jet central core upstream of the recirculation bubble imposing its frequency on the outer shear layer where instabilities are convective. Hence, for a purely spatial analysis, the precessing vortex core upstream of the vortex breakdown location is considered as a 'natural oscillator' and the convectively unstable surrounding flow field is modeled as being externally forced. The spatial approach is corroborated a posteriori by the good agreement of the stability eigenmodes, amplification rates, and wavelengths with the corresponding quantities of the measured phase-averaged flow, particularly in the periphery of the recirculation bubble. The theoretical prediction is less accurate in the interior of the jet near the wavemaker location due to the convective type of the analysis. The good agreement in the convective unstable region also gives credibility to the above-mentioned empirical reconstruction of the 3D time-periodic flow, using the same velocity field ansatz.

Finally, a three-dimensional portrait of the global mode is constructed from experimental data and from the theoretical model. Both approaches represent a co-rotating, counter-winding single-helical coherent structure that is wrapped around the recirculation zone – in a remarkable agreement. The vortex axis is perpendicular to the mean flow direction which is characteristic for the Kelvin–Helmholtz type of instability. The good agreement between instability and POD-based eigenmodes is neither self-evident nor completely unusual in free shear flows. This study reveals that the highly swirled jet has similar dynamics as, e.g. the wake flow with an absolutely unstable clock-work of vortex shedding in the recirculation zone and convectively moving structures in the far wake. Moreover, the study provides simple and effective kinematic and dynamic tools that complete the coherent-structure extraction from 2D PIV data. The proposed approach is expected to be applicable to a large class of other shear flows.

Chapter 7

Open-loop Control of the Self-excited Swirling Jet

In this investigation, harmonic actuation is applied at the nozzle lip with the aim to control the self-excited oscillations associated with the spiral vortex breakdown. A spatio-temporal analysis of the mean natural flow associates these flow oscillations to a global instability mode. The wavemaker of this mode is located upstream of a large pocket of absolutely unstable flow that is located in the vortex breakdown bubble. The limit-cycle oscillations are associated with a co-rotating counter-winding single-helical coherent structure that originates from a precessing vortex core that is most energetic in the wavemaker region. The self-excited oscillations can be synchronized to an external signal by forcing at the same azimuthal mode (global lock-in). By actuating the flow at a different azimuthal mode, it is possible to excite convectively unstable modes in the outer shear layer that gain large amplitudes with downstream distance. The resulting coherent structures enhance the streamwise growth of the outer shear layer and cause a downstream displacement and reduction of the vortex breakdown bubble. This leads to a reduction of the internal feedback mechanism and the natural global mode is suppressed. In consistency, the spatio-temporal stability analysis applied to the forced flow reveals that the pocket of absolutely unstable flow diminishes with increasing forcing amplitude.

7.1 Objectives and Approach

The investigation described in this chapter deals with open-loop control of a turbulent swirling jets undergoing vortex breakdown. This flow phenomenon is known to occur when the ratio of axial flux of azimuthal to axial flux of axial momentum exceeds a certain threshold. It is characterized by the appearance of a stagnation point on the jet centerline and the creation of an internal recirculation zone. A comprehensive investigation of the formation of vortex breakdown and the onset of global instability is given in chapter 4.

Swirling jets undergoing vortex breakdown are commonly used to improve the efficiency of swirl-stabilized combustors. In these devices, the internal recirculation zone acts as a flame holder, and the enhanced turbulent mixing leads to a reduction in NO_x emissions.

As a drawback, swirl-stabilized (in particular lean premixed) combustors are susceptible to self-excited combustion oscillations (see review article of Huang & Yang 2009). The driving mechanism of these thermo-acoustic instabilities is the dynamic coupling of heat release rate and acoustic pressure oscillations. This feedback cycle can be interrupted by controlling the flow oscillations caused by large-scale flow structures. Their occurrence in swirling jets has been extensively studied within the last decade. The most prominent structure that is consistently found in experimental and numerical investigations is a self-excited large-scale oscillation that is associated with an unstable global mode (Gallaire et al. 2006; Liang & Maxworthy 2005; Ruith et al. 2003). It is characterized by a co-rotating, counter-winding instability wave with an azimuthal wavenumber $m = 1$ that originates from a pocket of absolutely unstable flow (see section 2.4 for reviews on local/global instability concepts). This scenario is confirmed by the spatio-temporal stability analysis of Gallaire et al. (2006) based on the laminar swirling jet that was simulated numerically by Ruith et al. (2003). In chapter 6 of this thesis, the shape of this global mode is predicted by computing the most convectively unstable mode based on the measured turbulent mean flow. Its agreement with phase-averaged measurements is found to be reasonably good within the shear layers surrounding the region of reversed flow.

The applicability of the convective analysis is of great importance for efficient flow control. It implies the validity of the signaling problem, meaning that the outer shear layer acts as an amplifier to upstream perturbations. To recall, the convectively unstable nature of axisymmetric (Cohen & Wygnanski 1987; Crighton & Gaster 1976) and plane shear layers (Oster & Wygnanski 1982) have enabled efficient jet-noise and separation control by means of periodic excitation (Greenblatt & Wygnanski 2000).

In the present investigation, the feasibility of controlling this global mode with azimuthal wavenumber $m = 1$ that dominates the strongly swirling jet is investigated experimentally. Periodic excitation is applied at the nozzle lip where the outer shear layer is most receptive to external forcing (Cohen & Wygnanski 1987; Long & Petersen 1992). The flow response is assessed using stereo-PIV. A spatio-temporal stability analysis is applied to the natural and actuated mean flow states. This allows a theoretical study of the impact of forcing on the global stability of the flow.

Experiments are conducted using the swirling jet air facility at the TU Berlin (see section 3.2). Details to the PIV measurements are given in section 3.3. The outline of this chapter is as follows. The base flow configuration considered is described in section 7.2. The results of the open-loop control experiments are described in section 7.3, containing mode, amplitude, and frequency variations. Moreover, the impact of the forcing on the mean flow and its spatio-temporal stability is discussed. The main observations are summarized in section 7.6.

7.2 Description of the Unforced Flow

7.2.1 Characteristic Numbers

The global parameters that characterize the forced swirling jets are the swirl number S , Reynolds number Re_D , and the Strouhal number St , defined as

$$\text{Re}_D = \frac{DV}{\nu} \quad , \quad S = \frac{\dot{G}_\theta}{(D/2)\dot{G}_x} \quad , \quad \text{and} \quad \text{St} = \frac{fD}{V}.$$

The Reynolds number Re_D is based on the nozzle diameter D and on the bulk velocity V , which is derived from the mean mass flow rate. It is set to $\text{Re}_D = 20000$ throughout this investigation, yielding $V = 5.8$ m/s. The Strouhal number St characterizes the forcing frequency f and it is based on the nozzle diameter D and the bulk velocity V . The swirl number S is defined as the ratio between the axial flux of angular momentum \dot{G}_θ and the axial flux of axial momentum \dot{G}_x . Since the axial momentum flux must be conserved in axial direction, the swirl number S must remain constant with axial distance. However, as demonstrated in chapter 4, the commonly used expressions for the axial flux of momenta that are

$$\dot{G}_\theta = 2\pi\rho \int_0^\infty V_x V_\theta r^2 dr \quad \text{and} \quad \dot{G}_x = 2\pi\rho \int_0^\infty \left(V_x^2 - \frac{V_\theta^2}{2} \right) r dr \quad (7.1)$$

are inaccurate in the region of vortex breakdown. The underlying boundary layer approximations are invalid in the vicinity of vortex breakdown due to the strong jet divergence. Hence, it is necessary to omit these simplifications and consider additional terms of the equations of motion (Rajaratnam 1976), yielding the more complex expressions for the axial flux of azimuthal momentum

$$\dot{G}_\theta = 2\pi\rho \int_0^\infty (V_x V_\theta + \overline{v'_x v'_\theta}) r^2 dr \quad (7.2)$$

and for the axial flux of axial momentum

$$\dot{G}_x = 2\pi\rho \int_0^\infty \left(V_x^2 - \frac{V_\theta^2}{2} + \overline{(v'_x)^2} - \frac{\overline{(v'_\theta)^2} + \overline{(v'_r)^2}}{2} \right) r + \left(V_x \frac{\partial V_r}{\partial x} + V_r \frac{\partial V_x}{\partial r} \right) \frac{r^2}{2} dr. \quad (7.3)$$

Figure 7.1 depicts the swirl number based on the simplified expressions (7.1) together with the swirl number based on the expressions (7.2-7.3), both derived from the PIV measurements of the present flow configuration. It is clearly shown that upstream of $x/D = 2$, the appearance of vortex breakdown and the associated jet divergence falsifies the swirl number based on the simplified equations. Downstream of the recirculation bubble ($x/D > 2$), both quantities merge to an approximate value of $S = 1$, which remains constant throughout the remaining measurement domain.

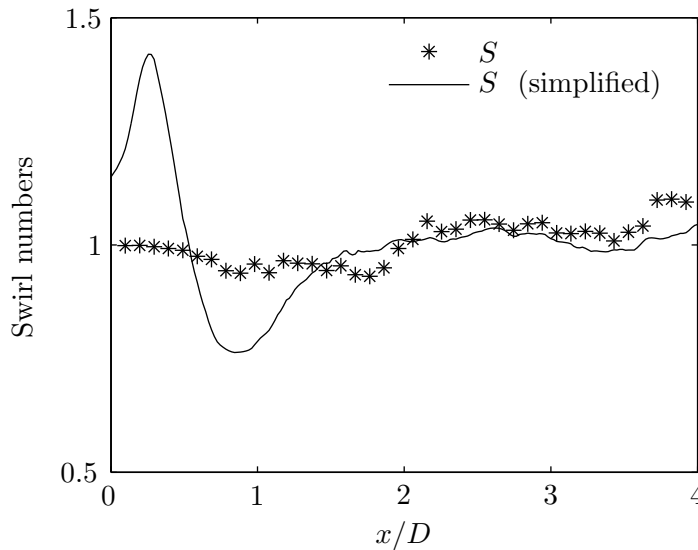


Figure 7.1: Swirl number versus axial distance. In the region of vortex breakdown ($x/D < 2$) the simplified swirl number based on (7.1) differs strongly from the one based on (7.2-7.3).

7.2.2 Flow Features

The swirling jet configuration considered is dominated by a large-scale oscillatory mode. A detailed discussion of the corresponding coherent flow structures is given in chapter 6. This mode is characterized by a helical instability wave with azimuthal wavenumber $m = 1$ rotating in the same direction as the base flow but winding in opposite direction. It is shown in chapter 6 of this thesis that this mode arises from a supercritical Hopf bifurcation with a critical swirl number of $S = 0.88$. Hence, the presently considered swirl number, $S = 1$, is supercritical and the global mode oscillates at its limit-cycle.

Figure 7.2 highlights the main features of the base flow configuration. The swirling jet at $S = 1$ undergoes vortex breakdown and flow stagnation occurs on the jet axis at $x/D \approx 0.51$ (see streamlines in figure 7.2a). A large recirculation bubble is created near the orifice and the jet emanating from the nozzle is distorted to an annular swirling jet. At the nozzle exit, the axial velocity profile is nearly top-hat shaped with strong axial shear between the jet and the quiescent surrounding fluid (see V_x -profiles in figure 7.2b). At $x/D \approx 0.3$ an inner shear layer appears and the axial velocity profiles become wake-like near the jet center.

The thick black lines in figures 7.2b and c mark the center of the axial shear layers, which coincide with the locations of maximum axial shear $\partial V_x / \partial r$. Note that the axial shear at the jet center near the nozzle exit is caused by an overshoot of the axial velocity profile (confer with most upstream velocity profile in figure 7.2b). This velocity hump is generated by the swirling jet passing the contraction upstream of the orifice (Batchelor 1967; Billant et al. 1998; Panda 1990).

The global mode is driven by a precessing vortex core (PVC) which is located upstream of the recirculation bubble. The outer shear layer, which is thin near the nozzle exit and highly receptive to external perturbations, amplifies the dynamics of the PVC emanating from the jet core. This leads to synchronized helical coherent structures that grow rapidly

Figure 7.2: Natural flow at $S = 1$ and $\text{Re}_D = 20000$: (a) 2D-streamlines and contours of coherent energy; (b) thin black lines represent the normalized axial velocity profiles V_x/V , thick black lines indicate the center of axial shear layer where $V_x/V = 0.5$, contours represent the axial shear intensity;(c) contours (video in online version) showing contours of coherent vorticity Ω_z^c , black thick lines represent the center of axial shear layer.

with downstream distance, ultimately dominating the entire nearfield dynamics. A 3D-visualization of this global mode can be found in [Petz et al. \(2011\)](#). It is reprinted in appendix C. The kinetic energy distribution of this mode is depicted in figure 7.2a. It is derived from PIV measurements that are phase-averaged with respect to the global oscillation. At the nozzle exit, energy is concentrated around the jet axis depicting the PVC. With larger downstream distance, coherent energy increases in the outer and in the inner shear layer, indicating the synchronized oscillations. At $x/D \approx 1$, where the bubble has its maximum diameter, the oscillations in the inner and outer shear layer merge and the energy peaks at the maximum of the axial velocity profile. Downstream of this axial position, the distinction between inner and outer shear layer becomes meaningless as the disturbance waves do not travel independently at each side of the annular jet. In fact, the annular jet itself oscillates at the global frequency. Contours of phase-locked through-plane vorticity of the $m = 1$ mode, depicted at an arbitrary phase angle in figure 7.2c, reveal consistent wave-like structures that arise from the jet core and move outwards around the recirculation bubble where they merge with the structures in the outer shear layer. Note that the through-plane vorticity Ω_z of the mode $m = 1$ is axisymmetric by definition and shows no discontinuity on the jet axis, while the azimuthal vorticity component that is skew-symmetric for $m = 1$ would yield a singularity on the jet axis and is, therefore, inappropriate to visualize the flow structures in the streamwise plane. Hence, the strong eddy centered at $x/D = 1.5$ and $y/D = 0.7$ corresponds to a spiral-shaped vortex that is connected to the oppositely signed eddies centered at $x/D = 1$ and $x/D = 2$ at $y/D = -0.7$.

7.3 Open-loop Control

The following section describes how the swirling jet at $S = 1$ responds to sinusoidal excitation applied at $x = 0$. The experimental facility allows to force axisymmetric and azimuthal modes. To demonstrate the effect of forcing, data taken along the crosswise plane of measurement are considered first. The first row in figure 7.3 shows contours of the mean natural flow and the mean forced flow. The second and third row in figure 7.3 show contours of the phase-locked natural and forced flow at an arbitrary phase angle. For the unforced flow the phase-average is derived with respect to the naturally prevailing global mode oscillations.

The contours shown in the first row of figure 7.3 reveal that the mean flow is nearly axisymmetric for forced and natural conditions. No deformation of the mean flow is observed for any forcing case that would indicate the interaction of two modes.

The phase-locked flow forced at $m = 1$ differs only marginally from the natural flow, showing a precessing vortex core near the jet center. By forcing $m = 1$, a lock-in to the natural helical instability is achieved. Details on the lock-in characteristic of mode $m = 1$ are given in section 6.4.2, revealing typical oscillator dynamics.

By forcing the flow at higher modes, helical waves amplify in the outer shear layer and double- and triple-spiral vortices are generated. The phase-locked jet core is deformed into an elliptical ($m = 2$) or triangular ($m = 3$) shape. By forcing $m \neq 1$, instabilities are amplified that evolve primarily in the outer shear layer.

In fact, preliminary studies have shown that an actuation of mode $m = 0$, $m = 2$, $m = 3$, or $m = 4$ have a similar affect on the vortex breakdown and on the associated global mode

$m = 1$ (Lück 2009). However, mode $m = 2$ undergoes the highest overall amplification and is, thus, considered as most efficient for active flow control. Hence, the following discussion focuses on the flow forced at $m = 2$. The forcing frequency of $St = 0.44$ used for the mode and amplitude variation studies. The frequency dependency is discussed in detail in section 7.3.2.

7.3.1 Amplitude Variation

The nature of the excited instability is of great importance for flow control applications. The question is whether the forced mode $m = 2$ is convectively or absolutely unstable. According to linear stability theory, shear flows that are convectively unstable everywhere, act as a linear amplifier to infinitesimal disturbances. This stands in contrast to absolutely unstable flows that behave as oscillators (Huerre & Monkewitz 1990).

Figure 7.4a shows the amplitude of mode $m = 2$, integrated across the shear layers, at $x/D = 0.6$ versus speaker input voltage A_{spk} . At this axial location the modes grow exponentially in downstream direction. The linear relation between forcing amplitude and mode amplitude proves the validity of the signaling problem for mode $m = 2$. Thus, the downstream exponential growth of mode $m = 2$ can be predicted by spatial linear stability analysis. This important finding enables to apply flow control at small forcing amplitudes in order to effectively control the flow further downstream.

Figure 7.4b shows the square of the saturation amplitude of the forced mode $m = 2$ versus speaker amplitude. Accordingly, the forced instabilities saturate at amplitudes that correlate linearly with the square root of the forcing amplitude, yielding

$$\left(\int |v^c|^2 r dr \right)^{1/2} \propto \sqrt{A_{\text{spk}} - A_{\text{spk},0}} \quad ,$$

with $A_{\text{spk},0} = 20.7$ mV being the critical forcing amplitude above which $m = 2$ is amplified.

The growth or decay rate of the forced instabilities are determined by the local stability of the mean flow. Without a significant change of the mean flow, the overall maximum amplitude of the mode forced at the same frequency should scale linearly with the input amplitude. Hence, the presently observed nonlinear dependence of the overall maximum amplitude on the forcing amplitude, as shown in figure 7.4b, indicates a significant manipulation of the mean flow.

Throughout the remaining chapter, the input amplitude voltage of the speaker is normalized by the critical forcing amplitude, yielding the dimensionless amplitude

$$A_{\text{spk}}^* = \frac{A_{\text{spk}}}{A_{\text{spk},0}}. \quad (7.4)$$

Thus, the input voltage $A_{\text{spk}} = [25, 50, 75, 100, 125]$ mV corresponds to the dimensionless amplitude $A_{\text{spk}}^* \approx [1.2, 2.4, 3.6, 4.8, 6]$.

Figure 7.5 shows the streamwise energy distribution of mode $m = 1$ and mode $m = 2$, for the latter being forced at various amplitudes. Recall that the amplitude of mode $m = 1$ can only be extracted from the PIV snapshots when its energy is high enough to perform a reliable phase average based on POD. For $A_{\text{spk}}^* = 0$, no forcing is applied and mode $m = 1$

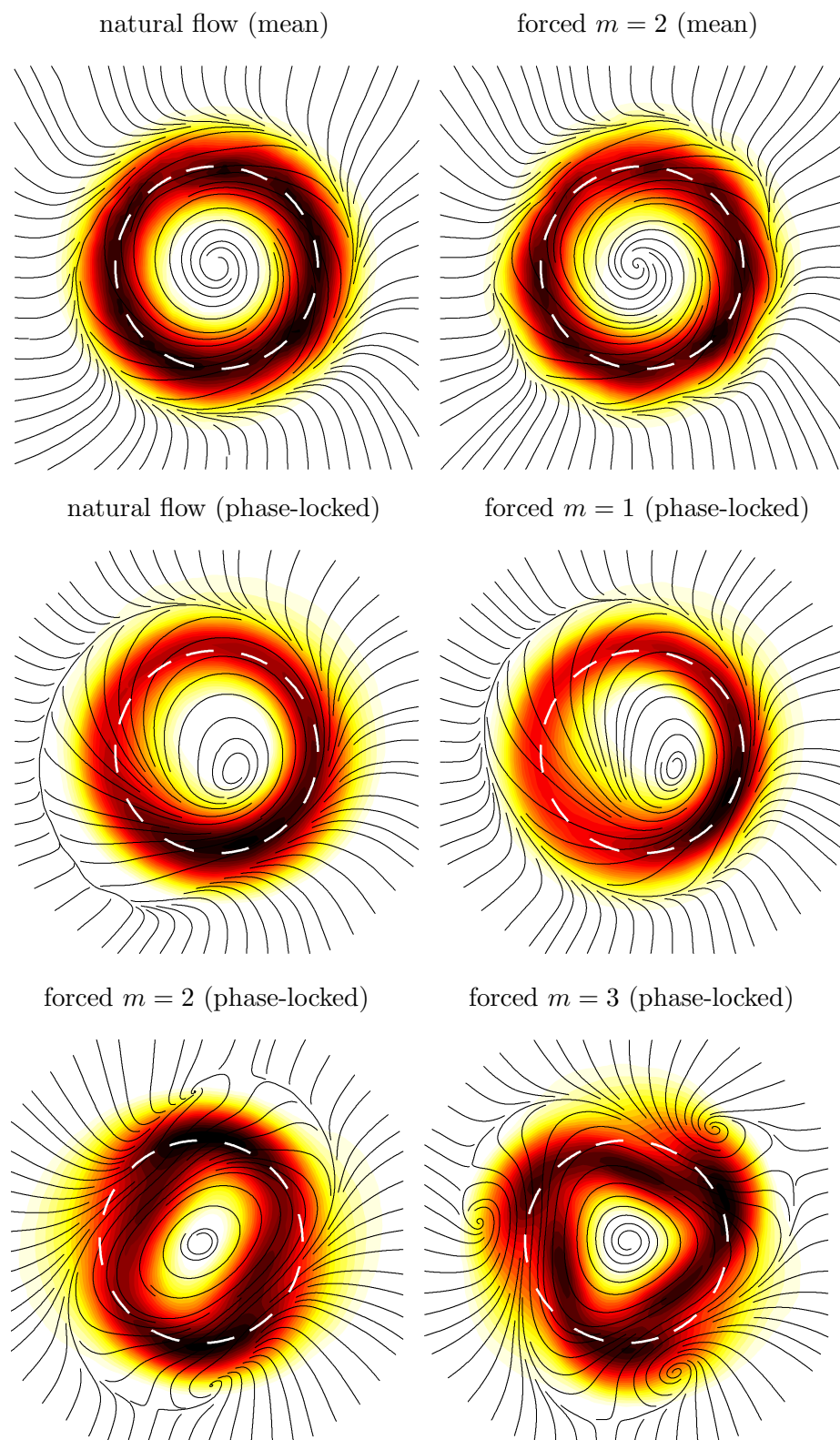


Figure 7.3: Cross-section of the jet undergoing vortex breakdown in the center of the recirculation zone ($x/D = 0.6$). Contours refer to the mean (first row) and phase-locked (second and third row) axial velocity, depicted at an arbitrary phase angle. 2D-streamlines are computed from v_y^p and v_z^p . The dashed white circle indicates the diameter of the nozzle exit. All modes rotate clockwise in the same direction as the base flow and are forced at the same frequency ($St = 0.44$).

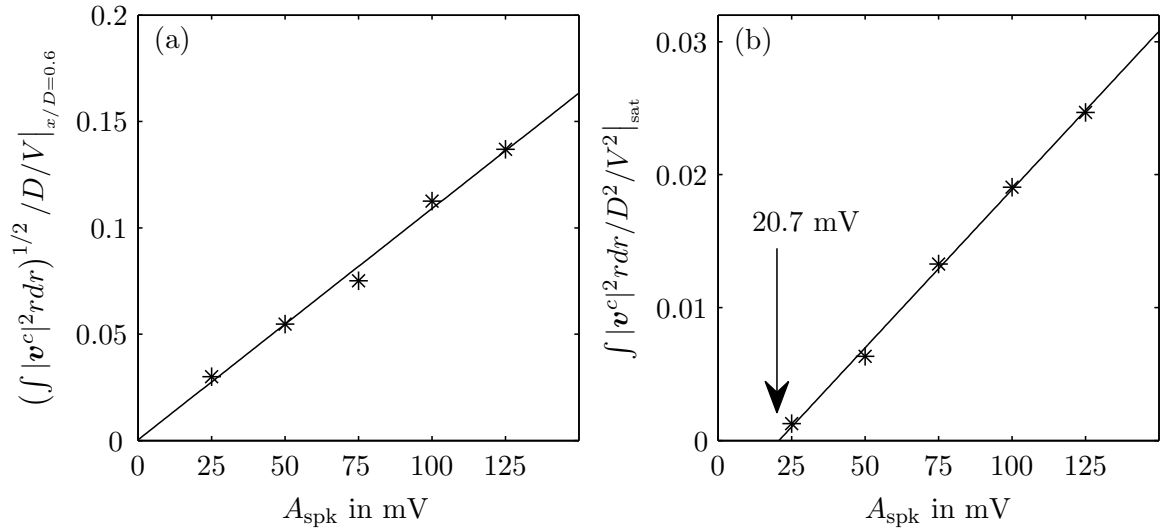


Figure 7.4: (a) Amplitude of mode $m = 2$ versus forcing amplitude. Linear fit (black line) confirms the convective nature of the excited mode. (b) Square of saturation amplitude of mode $m = 2$ versus forcing amplitude.

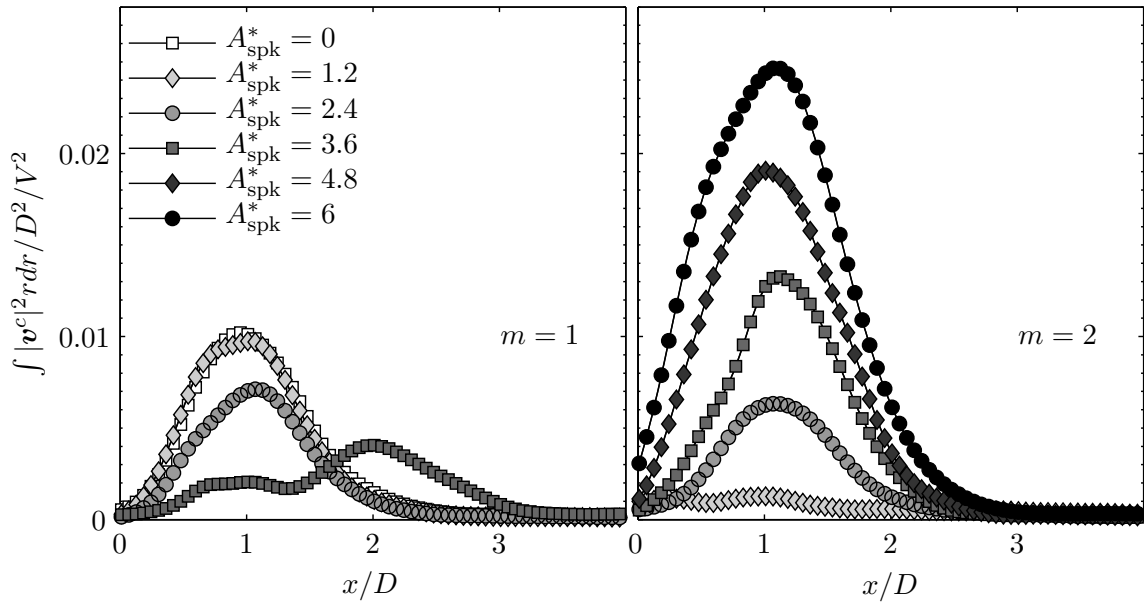


Figure 7.5: Streamwise distribution of kinetic energy of the natural mode $m = 1$ (left frame) and the forced mode $m = 2$ (right frame) forced at 40 Hz corresponding to $St = 0.44$

is dominant. Its energy saturates at $x/D \approx 1$, which coincides approximately with the maximum diameter of the recirculation bubble. Forcing mode $m = 2$ at $A_{\text{spk}}^* = 1.2$ does not influence mode $m = 1$ and there is hardly any energy for $m = 2$ detectable. However, for $A_{\text{spk}}^* > 1.2$, mode $m = 2$ undergoes significant streamwise amplification upstream of $x/D \approx 1$ and mode $m = 1$ gets successively damped. For $A_{\text{spk}}^* > 3.6$ mode $m = 1$ is too small to be accurately identified. Note that for $A_{\text{spk}}^* = 3.6$, mode $m = 1$ peaks at $x/D \approx 2$, indicating that the forcing dampens *and* displaces the global mode peak amplitude.

The mean flow correction that ultimately leads to a dampening of the global mode is characterized in section 7.4. It is interesting to note that the modes saturate at the

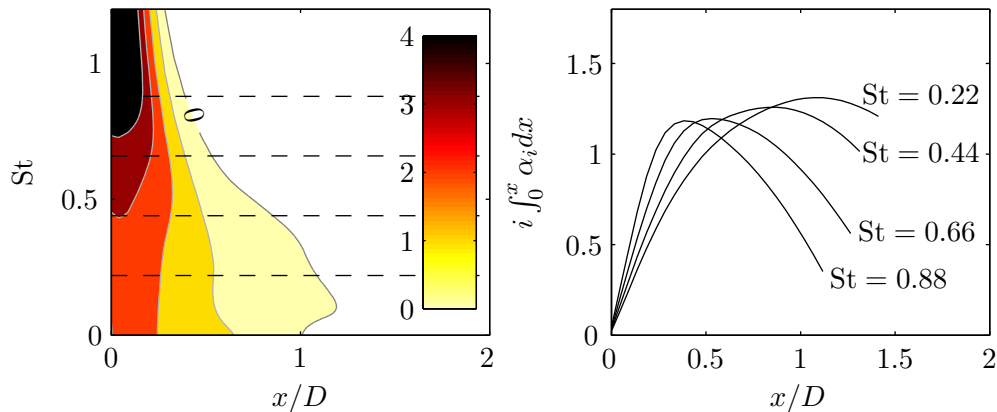


Figure 7.6: Results from spatial linear stability analysis employing the natural mean flow. Left: Contours of spatial amplification rate $-\alpha_i D$ of mode $m = 2$; dashed lines indicate the forcing frequencies of the experiments; right: overall amplification of forced mode $m = 2$.

same axial location regardless of the actuation amplitude. At this streamwise location, the inner and outer shear layers merge and one may speculate whether the nonlinear mean flow correction at this streamwise location interrupts the resonance principle of the global mode.

7.3.2 Frequency Variation

Within the framework of spatial linear stability analysis, modes forced at different frequencies undergo different amplification cycles. Figure 7.6a depicts contours of the spatial amplification rate α_i of mode $m = 2$ derived from a spatial stability analysis of the natural mean flow. Figure 7.6 (b) displays the integral $-\int_0^x \alpha_i dx$, which refers approximately to the overall amplification of mode $m = 2$ forced at a constant frequency St . As shown in chapter 5, this quantity overestimates the actually measured growth rate due to the non-uniformity of the flow. For the four frequencies considered, the computations predict the highest overall amplification for $St = 0.22$, followed by $St = 0.44$, 0.66 , and 0.88 . This disagrees with the energy distribution shown in figure 7.7. Experiments assign mode $m = 2$ forced at $St = 0.44$ to reach the highest overall amplification, causing the strongest suppression of mode $m = 1$. Forcing at $St = 0.88$ does not show any significant impact on the global mode, at all. The stability analysis based on the natural flow fails to predict the growth rates due to the significant mean flow change caused by the nonlinear interaction of the forced instability. Nevertheless, qualitatively speaking one may derive the following conclusions: Forcing at $St = 0.44$ is most effective in dampening the global mode because it goes through its complete amplification cycle before it reaches $x/D = 1$, the streamwise location where $m = 1$ is naturally most energetic. This is not the case for $St = 0.22$. In contrast, instabilities forced at $St = 0.88$ grow rapidly, saturate, and decay before they interact with the global mode. This scenario is supported by the fundamental derivations of Pier (2003). He demonstrates that flows with absolutely unstable regions are controlled by upstream harmonic forcing only when the forced mode reaches nonlinear saturation at sufficiently high amplitude upstream of the absolutely unstable region.

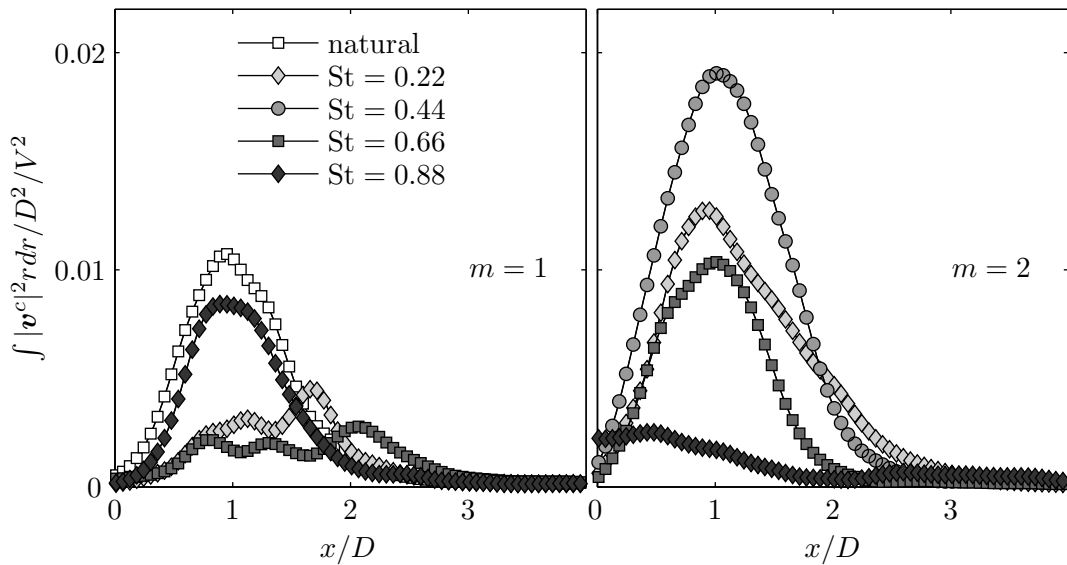


Figure 7.7: Streamwise development of coherent energy of the natural mode $m = 1$ (left frame) and the mode $m = 2$ forced at $A_{\text{spk}}^* = 4.8$ (right frame)

7.4 Impact of Forcing on the Flow Characteristics

As mentioned above, the actuated instabilities saturate nonlinearly at $x/D = 1$, thereby significantly manipulating the mean flow and its stability. The streamlines shown in figure 7.8 depict how the forcing alters the mean flow. The colored contours refer to the kinetic energy of the natural mode (shown for $y > 0$) and the kinetic energy of the actuated mode (shown for $y < 0$). The streamlines indicate how the recirculation bubble is diminished and displaced downstream with increasing forcing amplitude. The coherent energy distribution reveals a successive dampening of mode $m = 1$ with increasing forcing amplitude. Mode $m = 2$ forced at sufficiently high amplitude grows initially in the outer shear layer in contrast to the natural mode that arises from the PVC located at the jet center. The maximum coherent energy of the actuated mode is located at $x/D \approx 1$ which agrees quite well with the theoretically predicted overall amplitude (confer with figure 7.6). In that region coherent energy is transferred to the inner shear layer, the origin of the global mode, presumably leading to the nonlinear saturation depicted in figure 7.4b. Hence, the forced mode $m = 2$ originates in the outer shear layer and spreads to the inner one, whereas for the natural flow, the mode $m = 1$ originates from the jet center and spreads to the outer shear layer. It should be mentioned here that the actuated system as depicted in figure 7.8 is described by two oscillators (mode $m = 1$ and $m = 2$) with their amplitudes being nonlinearly coupled. A dynamic model based on such system has been proposed by Luchtenburg et al. (2009) and has been successfully applied to the present flow configuration. Details can be found in the work of Sieber et al. (2011) and Sieber (2012).

The instabilities excited by the external actuation may reach higher overall amplitudes than the waves forced by the PVC. This causes higher entrainment rates of the jet near the nozzle resulting in an enhanced streamwise growth of the outer shear layer. The thickness of the outer shear layer is derived from the PIV measurements by computing its momentum

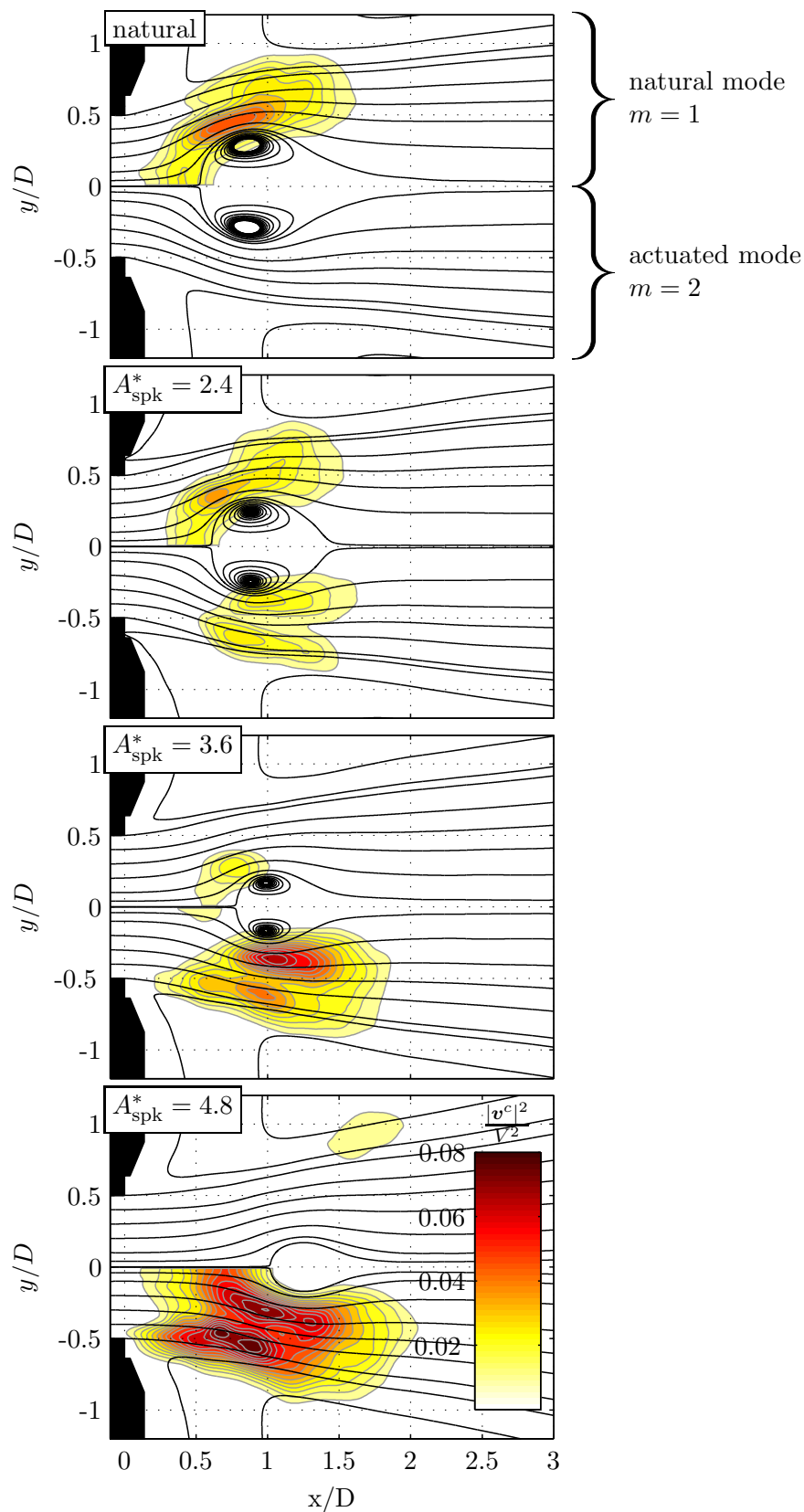


Figure 7.8: Contours of coherent energy for the natural and actuated flow and 2D-streamlines depicting the mean flow change due to forcing of mode $m = 2$ at $St = 0.44$; the contours shown for positive y refer to the natural mode and the contours shown for negative y refer to the actuated mode.

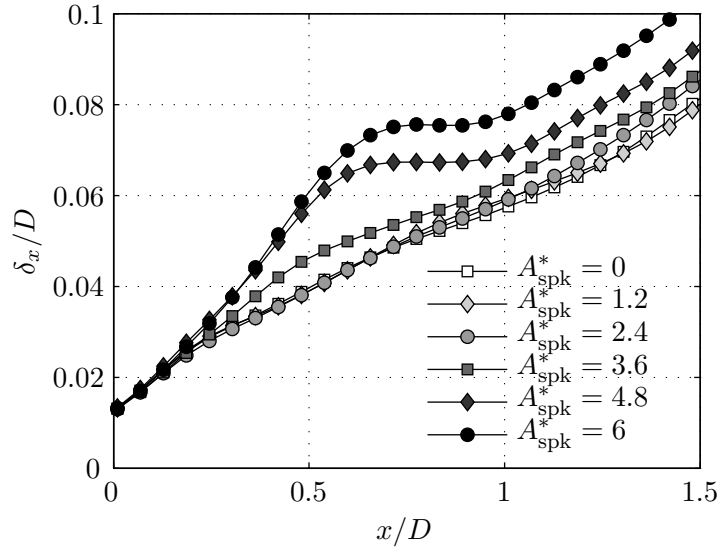


Figure 7.9: Streamwise distribution of the momentum thickness of the outer shear layer for the swirling jet forced at $m = 2$ and $St = 0.44$ at various amplitudes.

thickness

$$\delta_x = \int_{R_{\max}}^{\infty} \frac{V_x}{V_{x,\max}} \left(1 - \frac{V_x}{V_{x,\max}} \right) dr, \quad (7.5)$$

where R_{\max} refers to the radial location of the maximum axial velocity $V_{x,\max}$. Figure 7.9 depicts the streamwise development of δ_x for increasing forcing amplitudes. At the nozzle, δ_x is unaffected by the actuation, which implies that the imposed amplitudes are sufficiently small at the nozzle exit not to alter the mean flow. With increasing downstream distance, the growth of the outer shear layer is enhanced significantly for the jet forced at $A_{\text{spk}}^* \geq 3.6$ compared to the natural flow. Surprisingly, for $A_{\text{spk}}^* \leq 2.4$, a forcing amplitude at which the global mode is already somewhat damped, the outer shear layer thickness remains equal to the natural case. Hence, a thickening of the outer shear layer is not the cause for the global mode damping. It is solely a consequence of the enhanced overall amplitude of the coherent flow structures caused by sufficiently strong forcing. For the flow actuated at $A_{\text{spk}}^* \geq 3.6$, δ_x remains constant within the region $0.5 < x/D < 1$, indicating the region where the actuated waves interact with the inner shear layer. Further downstream, the forced waves cover the inner and the outer shear layers and definition (7.5) becomes meaningless.

Finally, the impact of the open-loop forcing on the location and the strength of the vortex breakdown is considered. In vortex breakdown studies it is a challenging task to define a global variable that characterizes the state of vortex breakdown. An intuitive quantity might be the size and the location of the recirculation bubble. The white-filled black circles in figure 7.10 depict the mean streamwise location of the upstream and downstream stagnation points for the natural and the forced flow. The error bars represent the corresponding RMS values of the instantaneous streamwise locations. Hence, a long error bar refers to a stagnation point that oscillates heavily in streamwise direction. For the natural flow, the upstream stagnation point is located at $x/D \approx 0.5$ with RMS value of 0.15. The corresponding downstream stagnation point is located at $x/D \approx 1.5$ and shows much higher fluctuations. The vortex breakdown bubble for the natural flow has a nearly

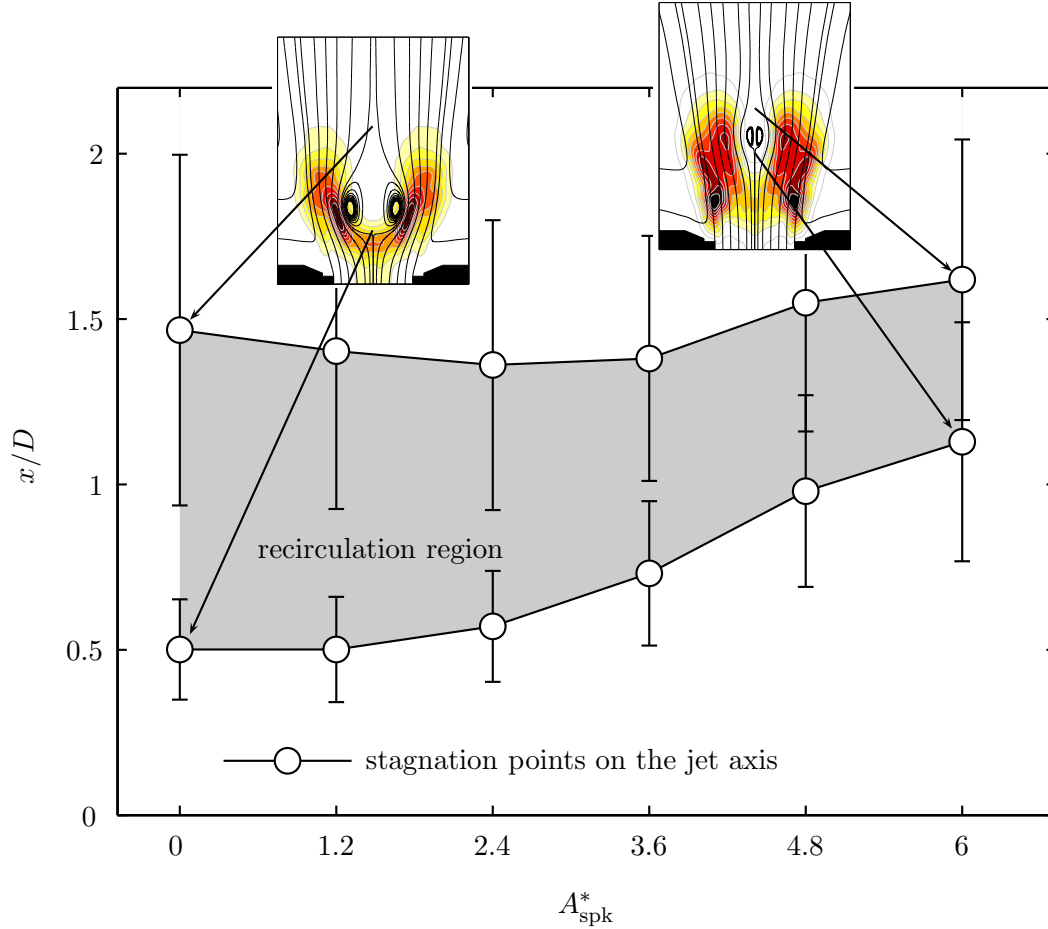


Figure 7.10: Impact of forcing mode $m = 2$ on location and size of the recirculation bubble. White-filled black circles refer to the mean streamwise locations of the upstream and the downstream stagnation point. Error bars indicate the RMS of the corresponding instantaneous streamwise locations.

steady upstream stagnation point, while its 'tail' oscillates heavily in streamwise direction. This is consistent with the observations reported in chapter 4.

Forcing mode $m = 2$ at moderate amplitudes shifts the upstream end of the recirculation bubble downstream and enhances its streamwise fluctuation. It appears that a dampening of the precessing vortex core destabilizes the vortex breakdown bubble, in agreement with the experiments discussed in chapter 4, revealing decreasing vortex breakdown oscillations with the onset of the global mode $m = 1$. Moreover, it is found that the downstream displacement of vortex breakdown correlates linearly with $\sqrt{A_{\text{spk}} - A_{\text{spk},0}}$, revealing the same nonlinearity as the saturation amplitude of the forced mode (confer with figure 7.4). This indicates a link between the downstream displacement of vortex breakdown and associated mean flow change and the interaction between the inner and the outer shear layer associated with the nonlinear saturation.

7.5 Impact of Forcing on Global Instability

A major interest in applied fluid mechanics is the prediction of the impact of external forcing on the mean flow and its dynamics. Forced instabilities that grow in shear flows can reach sufficiently high amplitudes to trigger nonlinearities that alter the mean flow and, in turn, its instability. The analysis of a flow dominated by large-scale oscillations, caused by either high amplitude forcing (convectively unstable) or self-excitation (absolutely/globally unstable), is most accurate when based on the mean flow that incorporates nonlinear effects. In contrast, an analysis of the non-forced, non-oscillating flow yields inaccurate results, as the mean flow distortion, which goes in hand with the instability, cannot be assessed from linear stability theory. Modeling the link between the coherent velocity component of a strong instability and the Reynolds stresses that alter the mean flow is still an unsolved problem of turbulence closure (Reau & Tumin 2002). The analysis based on the non-forced, non-oscillating flow (base flow) is capable to predict the linear growth of instabilities forced at low and moderate amplitudes. For heavily oscillating flows, as considered here, the analysis must be based on the actual mean flow and is used as an analytic tool rather than a predictive tool.

The main theoretical approach is in line with the spatial stability analysis conducted in the investigations described in chapter 5 and 6. However, in the present investigation, a spatio-temporal analysis is performed that involves the tracking of saddle points in the complex wavenumber plane for complex frequencies. This procedure is numerically more demanding than the spatial analysis conducted in the previous parts. The theoretical background and numerical implementation is briefly described section 2.4.

In this section, results are presented for the spatio-temporal analysis of the natural and the forced swirling jet. As mentioned in section 2.4, the analysis is capable of detecting regions of absolute instability, which correspond to a positive absolute temporal growth rate $\omega_{0,i}$. Several questions can be answered by this theoretical approach:

- Is the flow globally unstable to the $m = 1$ mode?
- Is the frequency of the precessing vortex core in agreement with the theoretically derived global frequency?
- Where is the region of absolute instability located?
- Where is the wavemaker located?
- Is the flow absolutely unstable to other modes than $m = 1$?
- How does the forcing of mode $m = 2$ alter the global stability?

These questions can be answered by considering the theoretical results depicted in figure 7.11. The black thick line represents the streamwise distribution of the absolute temporal growth rate $\omega_{0,i}$ of mode $m = 1$ for the baseline configuration (figure 7.11d). There is a region of absolutely unstable flow located inside the recirculation bubble. The global frequency ω_s and the wavemaker location X_s are derived from the streamwise distribution of ω_0 by employing the criterion (2.12). The wavemaker is located at $X_s \approx 0.4D$, indicated in figure 7.11a–d by the dashed vertical line. The global frequency is found to be $\omega_s = 52$ Hz in very good agreement with the measured PVC oscillation frequency of 51.5 Hz. Moreover, the spatio-temporal analysis conducted for modes other than $m = 1$

could not reveal any absolutely unstable flow – neither for the natural nor for the forced flow. Hence, mode $m = 1$ remains the only absolutely unstable mode for all considered flow configurations. The present analysis confirms the experimental findings described in the chapters 4 and 6, and it is line with the spatio-temporal analysis conducted by Gallaire et al. (2006) employing the base flow of a laminar swirling jet simulated by Ruith et al. (2003).

Winding up, the swirling jet undergoing vortex breakdown becomes globally unstable to mode $m = 1$. The limit cycle oscillation of this mode is characterized by a precessing vortex core and the helical roll-up of the outer shear layer. The present analysis predicts the wavemaker to be located upstream of the recirculation bubble, contrasting the results of Gallaire et al. (2006), who found the wavemaker to be located inside the bubble. The dashed vertical line in figure 7.11a–d depicts that for the present flow, the source of the global mode is located exactly where the center of the inner shear layer (thick black solid line) intersects the jet axis. This axial position coincides with the maximum coherent energy along the jet axis (7.11a), corresponding to the location of strongest dynamics of the precessing vortex core.

Figure 7.11d further depicts the absolute growth rate of mode $m = 1$ for the jet forced at $m = 2$. As mentioned in earlier, the analysis is not capable to predict the complicated nonlinearities that lead to the drastic mean field changes discussed in the previous section. However, a spatio-temporal analysis of the forced flow may shed some light on the involved mechanisms a posteriori. Forcing at $A_{\text{spk}}^* = 1.2$ does not suffice to excite instabilities, and the mean flow and corresponding $\omega_{0,i}$ remain unchanged (not shown). Forcing the flow at $A_{\text{spk}}^* = 2.4$ reduces slightly the spatial extent of the region of reversed flow (figure 7.8 and 7.10). This results in a quite significant change of $\omega_{0,i}$, leading to a reduction of the region of absolutely unstable flow. At a forcing amplitude of $A_{\text{spk}}^* = 3.6$, the mean flow is significantly altered and the flow becomes convectively unstable in the bubble, which implies that the flow must be globally stable. Hence, one may interpret the dampening of the global mode as a consequence of the mean flow change due to the excitation of convectively unstable modes. This scenario is in good agreement with the generalized mean-field model (Luchtenburg et al. 2009; Noack et al. 2003).

7.6 Summary and Discussion

Open-loop control of a turbulent swirling jet undergoing vortex breakdown was investigated. Experiments were conducted at $S = 1$ and $\text{Re}_D = 20000$. At this swirl number, the jet has undergone a supercritical Hopf bifurcation to a global mode $m = 1$. The aim of this investigation was to control the limit cycle oscillations of this global mode by means of low amplitude sinusoidal forcing at the nozzle lip.

The phase-averaged velocities of the natural flow reveal that the global oscillations originate from a precessing vortex core that is located upstream of the internal recirculation zone. Perturbations emanating from the vortex core propagate to the outer shear layer where large-scale helical coherent structures evolve. A spatio-temporal analysis based on the natural mean flow reveals that mode $m = 1$ is the only globally unstable mode with its global frequency to be equal to the measured frequency of the precessing vortex core. The analysis

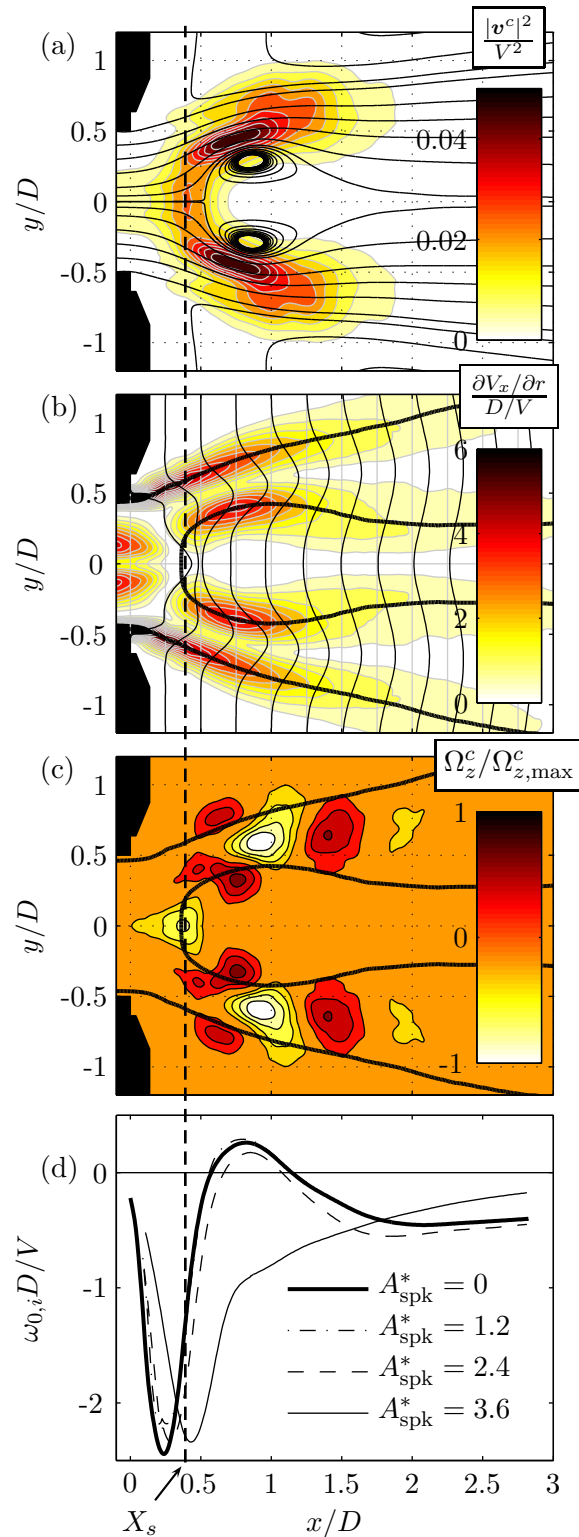


Figure 7.11: Natural flow at $S = 1$ and $Re_D = 20000$: (a) 2D-streamlines together with contours of coherent energy; (b) black thin lines refer to normalized axial velocity profiles V_x/V , black thick lines refer to center of axial shear layer $V_x/V = 0.5$, contours refer to axial shear intensity; (c) contours of coherent vorticity Ω_z^c depicted at an arbitrary phase angle, black thick lines refer to center of axial shear layer $V_x/V = 0.5$; (d) spatio-temporal analysis: absolute temporal growth rate $\omega_{0,i}$ versus x for baseline and forced configurations, regions with $\omega_0 > 0$ refer to absolute unstable flow.

predicts the wavemaker of this mode to be located upstream of the vortex breakdown bubble at the streamwise location of strongest vortex core precession ($x/D \approx 0.4$).

A manipulation of the mean flow at the wavemaker location should be most efficient to control the global mode. However, in the present experiment, external actuation was applied at the nozzle lip, which can only indirectly influence the wavemaker dynamics. Forcing mode $m = 1$ caused the global mode to lock-in to the actuation (confer with chapter 6). Forcing mode $m = 2$ excited a double-helical instability wave in the jet periphery that grew exponentially in downstream direction. Its amplitude scales linearly with the actuation amplitude, revealing that mode $m = 2$ is convectively unstable. Hence, the outer shear layer acts as a linear amplifier for upstream perturbations – a necessity for efficient active flow control.

The actuated instabilities saturated nonlinearly at $x/D > 0.7$. In this saturation region, coherent energy is transferred from the outer to the inner shear layer, causing a drastic change of the mean flow in the jet interior that results in a significant suppression of the precessing vortex core.

The impact of the forcing on the mean flow was validated by tracking the location of the recirculation bubble for different forcing amplitudes. With increasing amplitude, the size of the recirculation zone is successively decreased and the bubble is displayed downstream. This drastically changes the global stability of the entire flow. A spatio-temporal analysis of the forced flow reveals that the flow becomes globally stable at sufficiently strong forcing amplitudes.

Hence, the receptivity of the outer shear layer allows for stabilization of the global-mode associated precession of the vortex core using low actuation amplitudes. The excited convectively unstable modes amplify to sufficient amplitudes to interact nonlinearly with the mean flow, thereby reducing the absolute growth rate of the $m = 1$ mode. In other words, the actuation at the jet periphery is capable to shift the critical swirl number of the Hopf bifurcation to values beyond $S = 1$.

Moreover, a frequency dependence of the forced mode $m = 2$ and its effectiveness in suppressing the global mode is observed. Waves that reach their maximum amplitude (neutral instability) in the region of inner and outer shear layer interaction are most effective in suppressing the global mode. This scenario is supported by recent theoretical considerations of Pier (2009).

Chapter 8

Concluding Remarks

The swirling jet configuration combines a variety of physical mechanisms whose complex interactions are very challenging. Despite the scientific challenge, the understanding and control of this flow is particularly useful for improving combustion processes (see review articles by [Candel \(2002\)](#); [Huang & Yang \(2009\)](#); [Lieuwen & Yang \(2005\)](#)). The present work is intended to shed some light on the natural and externally controlled coherent structures that evolve in swirling jets below and above the onset of vortex breakdown. Throughout this work, results are collected by means of state-of-the-art experimental methods in conjunction with linear stability analysis.

The theoretical concepts used in this work are rather classic. However, their application is usually restricted to purely theoretical investigations that deal flows obtained from direct numerical simulations at very low Reynolds numbers or from simplified models. In the present work, the analysis is applied to actually measured turbulent flows and the results are quantitatively compared to the experiments. The good agreement between the theoretical and experimental results presented in this thesis confirm that linear stability analysis is more than a tool to predict the laminar-to-turbulent transition. When applied to a turbulent mean flow, this method serves as a theoretical framework to predict the dominant flow dynamics, thereby, intrinsically capturing the involved nonlinearities. This allows to reconstruct reduced order models that are of great importance for active control of turbulent flows.

Previous investigations on swirling jets suffer from the fact that there is no universal swirl configuration. The stability of a swirling base flow depends significantly on the considered velocity profiles, and hence, each proposed swirling jet configuration exhibits different stability mechanisms. This brings up a zoo of different instability modes that are proposed to be crucial in swirling jets. The investigation of the stability of moderately swirling jets described in chapter 6 is, therefore, chosen to be strictly in line with an experimental investigation, thereby, accepting a loss in generality. As a consequence, the derived stability characteristics quantitatively agree with the corresponding experimental results, but they can only be qualitatively related to other swirling jet experiments. Nonetheless, the exhaustive examination of the theoretical results brings up several general statements that should be valid for various types of swirling jet configurations. These are, for instance, the relevance of an azimuthal group velocity that results in a manipulation of the streamwise phase velocity, or the swirl-induced destabilization of steady and streamwise modes. It further clarifies recent theoretical arguments regarding the swirl-enhanced jet spreading.

The major part of this thesis deals with swirling jets undergoing vortex breakdown. State-of-the-art measurement techniques are employed to extract the dynamics that dominate this flow configuration. Theoretical concepts are applied in order to predict the onset of vortex breakdown and the formation of a global mode. The detailed investigation of the formation of vortex breakdown (chapter 4) reveals that vortex core criticality and shear layer instability are two independent mechanisms. With increasing swirl, the jet *first* undergoes vortex breakdown and *then* becomes globally unstable. The corresponding global mode, discussed in detail in chapter 6, is characterized by a single-helical co-rotating counter-winding mode, a robust feature that was observed in numerous previous studies of laminar swirling jets (e.g., see Gallaire et al. 2006; Liang & Maxworthy 2005; Ruith et al. 2003). The precessing vortex core, which is often observed in swirl-stabilized combustor flows, reveals the same characteristic as the presently observed global mode. The comparison of the present results with previous investigations suggest that the flow states that occur during the formation of the spiral-shaped vortex breakdown are universal and do not depend on the initial conditions.

Furthermore, this work reveals control methods that enable this global mode to be locked-in or dampened, thereby, utilizing the receptivity of the outer shear layer. The actuation was applied at the nozzle lip where the outer shear layer is most receptive, ensuring the lowest input cost for the strongest streamwise amplification. However, as described in chapter 7, the source of the natural global mode is located at the jet center and can, therefore, only be indirectly affected by the imposed forcing. A future project will focus on active and passive control methods that act directly on the source of the global instability.

It is surprising to note that the precession of the vortex core that is often observed in combustor flows has so far not been directly related to global stability concepts. This is partly attributed to the poor interconnection between applied research and theoretical work. In the field of combustion, there is still some confusion about the connection between shear layer instabilities and the vortex core dynamics. The previous is assumed to be responsible for the roll-up of the outer shear layer to large-scale flow structures that may significantly effect the flame dynamics. The present work shows that the precessing vortex core corresponds to the wavemaker of the global mode, and it is located upstream of the breakdown bubble. It acts as an internal clockwork, perturbing the convectively unstable outer shear layer. The receptivity of that outer shear layer is related to its radial thickness and so is the streamwise growth rate of the large-scale flow structures. The precession of the vortex core at the jet center and the streamwise growing waves in the jet periphery are synchronized to the same global frequency and both correspond to the same global mode.

Appendix A

Flow Properties of the Swirling Water Jet

A.1 Mean Flow Properties

A.1.1 Velocity Profiles

Dimensionless axial, radial, and azimuthal velocity components are shown in the first three columns of figure A.1 for swirl numbers $S = 0.38, 1.01$ below S_{VB} and the swirl numbers $S = 1.07, 1.12, 1.37$ above S_{VB} . The axial distance between two profiles corresponds to a magnitude of one. Note that the radial velocity V_r is scaled four times larger. Azimuthal vorticity contours ω_θ together with projected streamlines are shown in the right column. The black dots correspond to measurements conducted by Billant et al. (1998) at similar S . The maxima of the profiles agree well, whereas the present data shows thicker shear layers indicating enhanced turbulent diffusion.

V_x -component: For moderate swirl ($S = 0.38$, figure A.1a), the axial velocity profile is jet-like everywhere. The overshoot near the jet axis at $x/D = 0.5$ is created by the rotating flow passing through the contraction (Batchelor 1967). This is consistent with comparable investigations (Billant et al. 1998; Panda & McLaughlin 1994; Shiri et al. 2008; Toh et al. 2010). For higher swirl ($S = 1.01$, figure A.1b), the profiles render a downstream transition from jet-like to wake-like. Upon further increasing swirl, this velocity deficit is enhanced, leading to the appearance of an internal recirculation zone ($S = 1.07$) that moves upstream and grows in axial and radial distance, rendering the profiles wake-like within the entire measurement domain ($S = 1.12, 1.37$). The profiles describe an annular jet with an inner and outer shear layer that strongly spreads in radial direction.

V_r -component: For moderate swirl ($S = 0.38$), negative values for $x/D > 0.5$ indicate entrainment of steady surrounding fluid. For higher swirl ($S = 1.01$), the radial profiles become positive, indicating enhanced jet spreading. For swirl beyond breakdown, V_r is considerably higher upstream of the first stagnation point, where the streamlines indicate highly divergent flow. E.g. for $S = 1.12$ at $x/D = 0.5$, V_r peaks at 20 % of the bulk velocity, forming strong gradients in radial direction. Negative radial velocity for $r/D < 1$ is found downstream of the recirculation region, indicating the closure of the jet.

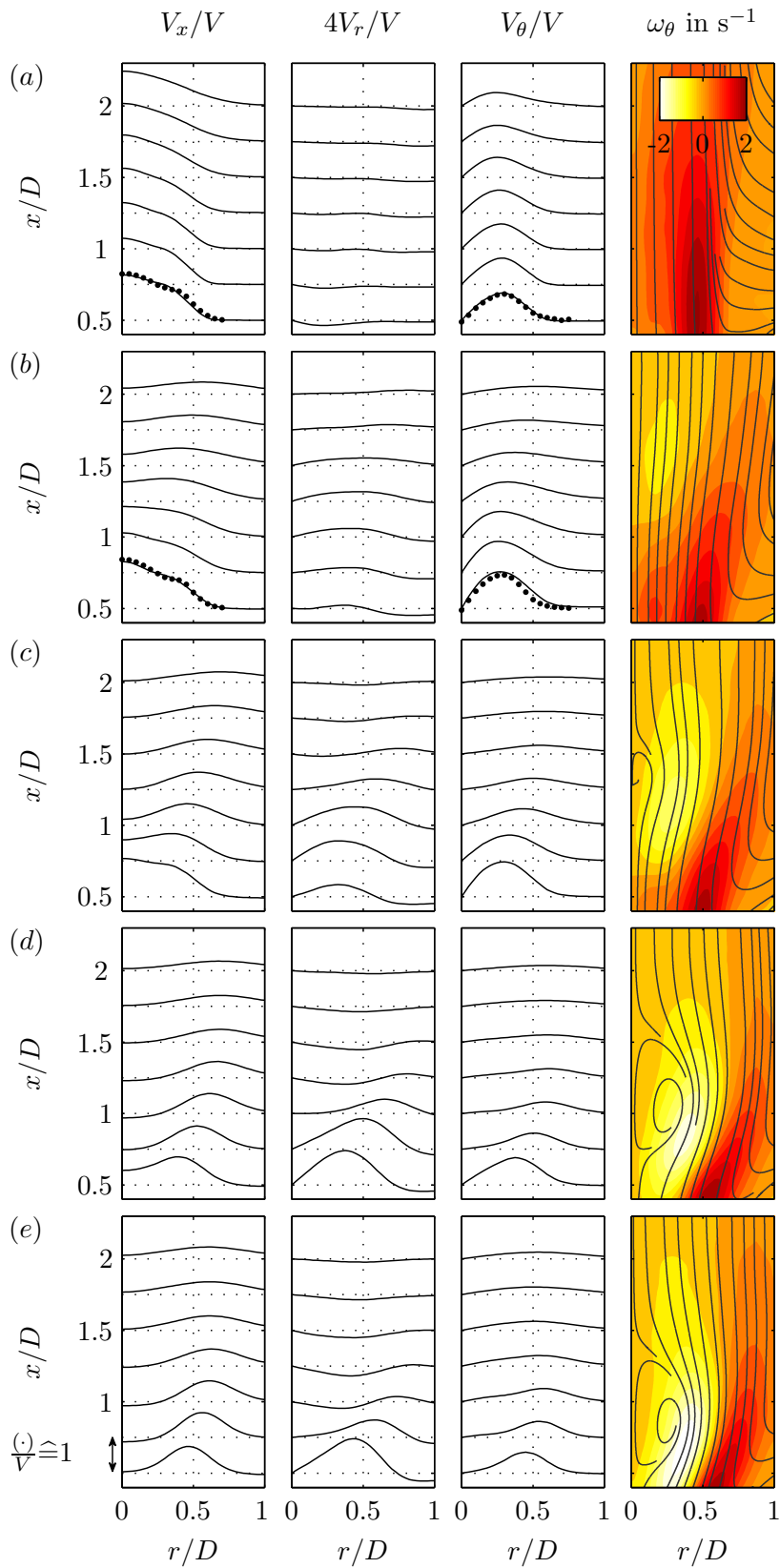


Figure A.1: From left to right: mean axial, radial, azimuthal velocity profiles, and azimuthal vorticity contours with projected streamlines; rows (a-e) represent $S = (0.38, 1.01, 1.07, 1.12, 1.37)$, respectively; black dots represent data recasted from (Billant et al. 1998).

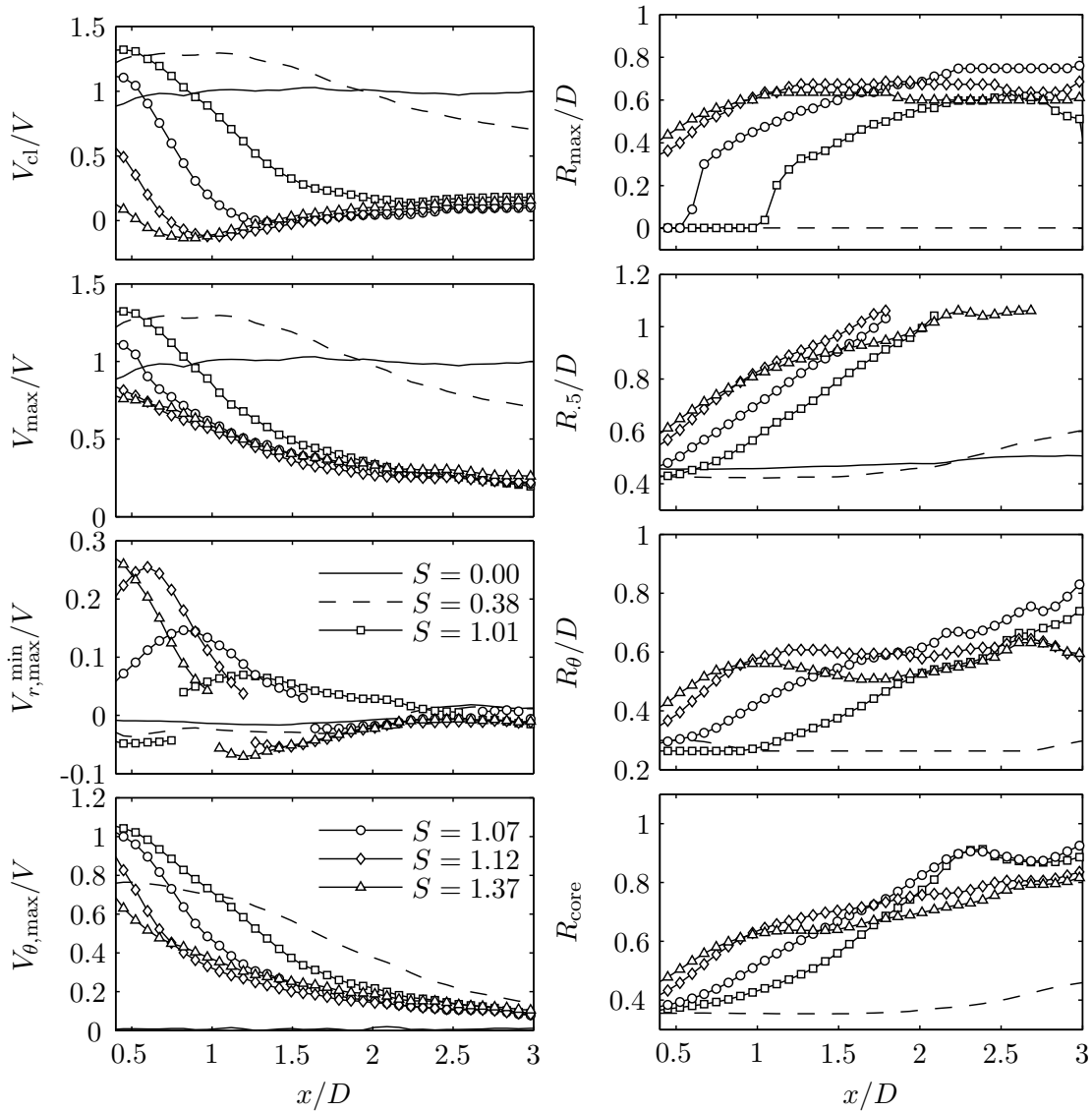


Figure A.2: Characteristic velocity and length scales versus axial distance.

V_θ -component: Below vortex breakdown ($S = 0.38$), the swirl component can be characterized by an inner region where it increases approximately linear with r (solid body rotation) and an outer region where it decays smoothly in outward direction. The decaying region forms an azimuthal shear layer that spreads radially with increasing downstream distance. In the case of vortex breakdown (e.g. $S = 1.12$), the azimuthal component in the recirculation region is very low (e.g. $x/D = 1$). There, the profiles render a concave curvature, revealing a second deflection point in the jet core.

A.1.2 Characteristic Velocity and Length Scales

The spatial development of the mean flow is summarized in figure A.2 for the same swirl numbers as presented in figure A.1. The right column shows the characteristic velocity scales V_{cl} , V_{max} , $V_{r,max}^{min}$, and $V_{\theta,max}$ versus axial distance and the left column shows the quantities R_{max} , R_{5} , and R_θ versus axial distance.

V_x -component: For moderate swirl ($S = 0.38$), the velocity on the centerline decays for $x/D \approx 1.2$, depicting the axial extent of the potential core. The growth rate of the half-width of the jet $R_{.5}$ is comparable to the non-swirling jet. With higher swirl ($S = 1.01$), the decay of V_{cl} is strongly enhanced and a local minimum appears at $x/D \approx 2.25$. The jet half-width increases rapidly with x at an approximately constant growth rate. The radial location of V_{max} is displaced from the jet axis at $x/D \approx 1.1$, indicating the point of jet-wake-transition. Further downstream, R_{max} saturates at $R_{max}/D \approx 0.6$. V_{cl} indicates reversed flow when the swirl is increased to $S = 1.07$. The rapid growth of $R_{.5}$ is initiated further upstream but the growth rate remains equal to $S = 1.01$. The location, where R_{max} is displaced from the jet axis, is shifted upstream. This trend is continued for $S = 1.12$. At $S = 1.37$ the recirculation region has reached the vicinity of the nozzle. The streamwise growth rate of the jet diameter is reduced and develops nonlinearly with x . R_{max} decays for $x/D > 1.5$ indicating the jet-closure downstream of the recirculation region. V_{cl} , V_{max} , and R_{max} converge to the same values at the downstream end of the measurement domain for $S \geq 1.01$, indicating that a change in swirl drastically alters the nearfield but does not substantially influence the flow downstream of $x/D > 2$.

V_r -component: $V_{r,max}^{min}$ corresponds to either the maximum or the minimum of V_r , depending on which quantity has a higher magnitude. The radial component is negative in regions of strong entrainment and positive in regions of strong jet spreading. Symbols on different sides of the abscissa correspond to different characteristic points of the velocity profiles and are, therefore, not connected. For moderate swirl ($S = 0.38$), strong entrainment is indicated by negative radial velocity for $x/D < 2.25$. With 3 % of the bulk velocity, it is approximately four times higher than for non-swirling jets. For higher swirl ($S = 1.01$), the entrainment near the nozzle is enhanced. Downstream of $x/D = 0.76$, jet divergence becomes more pronounced and the outwards directed flow reaches 8 % of the bulk velocity at $x/D = 1.2$. Upon increasing the swirl to $S = 1.07$, this maximum is shifted upstream and increases to 28 % at $x/D = 0.6$. Downstream of $x/D = 1.25$, $V_{r,max}^{min}$ is negative, indicating the inward directed flow downstream of the recirculation region.

V_θ -component: For moderate swirl ($S = 0.38$), the azimuthal component decays downstream of $x/D = 1$. This correlates to the end of the potential core and is presumably attributed to turbulent diffusion. Note that the jet spreading indicated by R_θ and $R_{.5}$ is minor. For higher swirl, the maximum of the swirl component is shifted outwards at the jet-wake transition point. The conservation of tangential momentum requires a rapid downstream decay of $V_{\theta,max}$. In consistency with R_{max} , this point is shifted upstream with a further increase in swirl.

A.2 Turbulent Fluctuations

A.2.1 Turbulent Normal Stress

Dimensionless turbulent normal stresses are shown in the first three columns of figure A.3 for swirl numbers $S = 0.38, 1.01$ below S_{VB} and the swirl numbers $S = 1.07, 1.12, 1.37$ above S_{VB} . The axial distance between two profiles corresponds to a magnitude of 0.25. Contours of the total turbulent kinetic energy together with projected streamlines are shown in the right column.

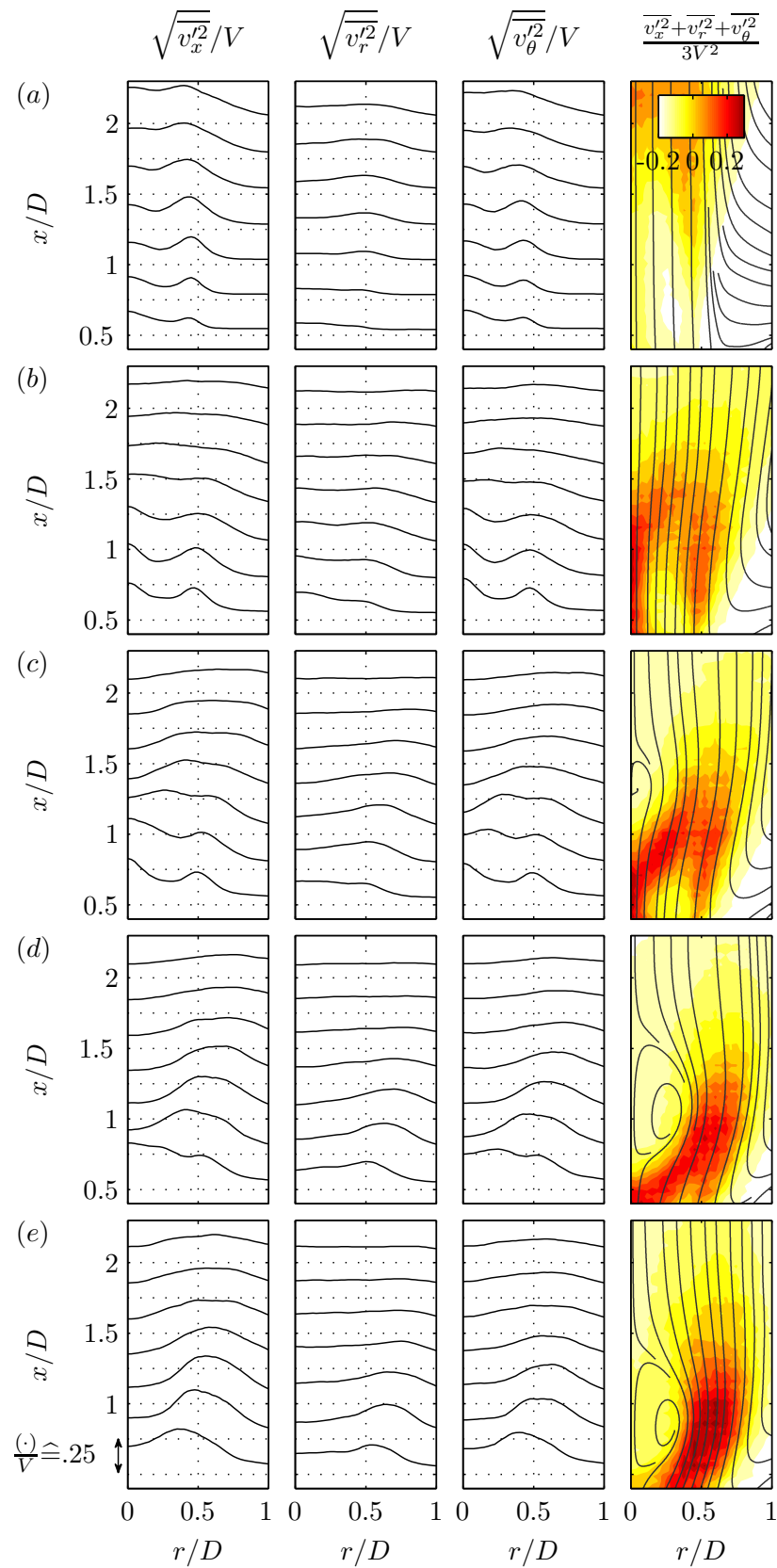


Figure A.3: From left to right: axial, radial, azimuthal profiles of turbulent normal stress, and contours of total turbulent kinetic energy with projected streamlines; rows (a-e) represent $S = (0.38, 1.01, 1.07, 1.12, 1.37)$, respectively.

For all configurations, the axial and azimuthal fluctuations peak at similar magnitude and location. The radial component is always somewhat weaker. Near the nozzle exit upstream of the recirculation region, $\sqrt{v_x'^2}$ and $\sqrt{v_\theta'^2}$ peak on the jet axis and in the center of the outer shear layer. The previous indicates strong oscillation of vortex breakdown and associated meandering of the jet core (e.g. $S = 1.07$, $x/D = 0.5$) while the latter indicates eddies that grow in downstream direction due to the unstable axial and azimuthal shear layer. Approaching the region of vortex breakdown from upstream, the inner peak moves outwards and merges with the peak of the outer shear layer, yielding very weak fluctuations in the recirculation region.

A.2.2 Turbulent Shear Stress

Dimensionless turbulent shear stresses are shown in the first three columns of figure A.4 for swirl numbers $S = 0.38, 1.01$ below S_{VB} and the swirl numbers $S = 1.07, 1.12, 1.37$ above S_{VB} . The axial distance between two profiles corresponds to a magnitude of 0.05. Contours of the total turbulent shear stresses together with projected streamlines are shown in the right column.

For moderate swirl ($S = 0.34$), high levels of $\overline{u'w'}$ are generated due to the coexistence of an axial and an azimuthal shear layer. The peak is located on the inner boundary of the outer shear layer. With incipient breakdown ($S \geq 1.01$), a second peak of $\overline{v_x'v_\theta'}$ appears in the inner shear layer upstream of the recirculation region. It appears that v_x' and v_θ' are strongly correlated in the region of vortex core precessing. In the recirculation region, the turbulent shear stresses diminish completely.

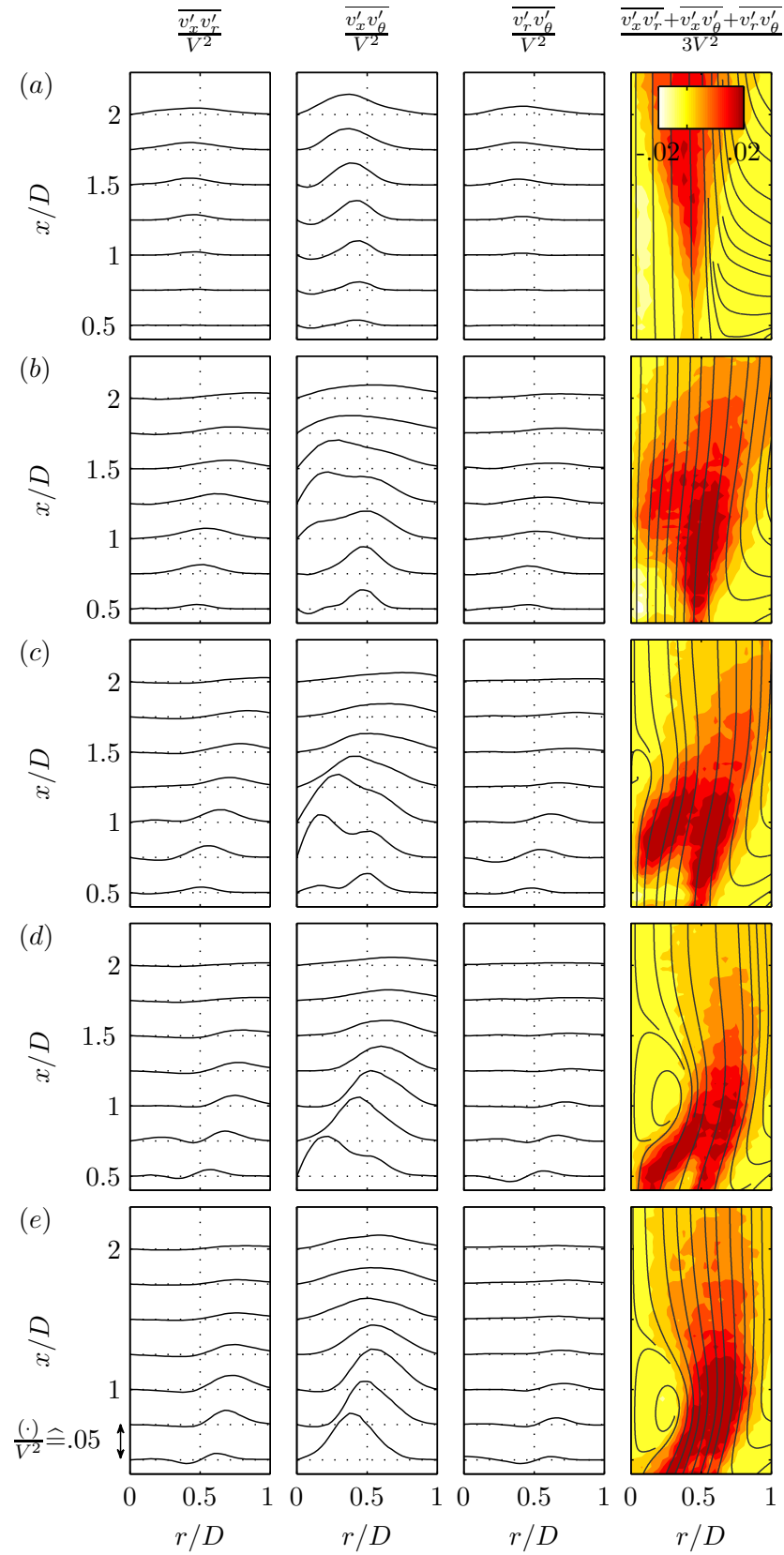


Figure A.4: Profiles of turbulent shear stresses; rows (a-e) represent $S = (0.38, 1.01, 1.07, 1.12, 1.37)$, respectively.

Appendix B

Supplemental Information of the Swirling Air Jet Facility

B.1 The Swirling Jet Facility

The flow enters the facility through two blowers that permit the independent setting of the Reynolds number and the swirl number. The volume flow was derived by measuring the pressure drop across a calibrated orifice. In order to provide constant volume flow for long time measurements, the volume flow was controlled in a closed-loop manner by using a real-time data acquisition setup that allows to re-adjust the blowers automatically and monitor the actual mass flow. A LabView program was written by Moritz Sieber that allows for zeroing the Baratrons connected to the measuring orifices and adjusting the swirl or Reynolds number independently.

After passing a honeycomb, the axial flow concentrically enters the swirl generator. The azimuthal flow enters the swirl chamber through a divider and four symmetrically arranged flexible tubes. Therein, the flow is guided through the slots between four curved and azimuthally displaced guiding plates to the inside of the swirl generator and is merged with the axial flow. In figure B.2 the swirl generator is hidden behind a curved perforated plate which improves the homogeneity of the azimuthal flow. The swirled flow leaves the swirl generator through a 800 mm long duct, before it is converged in a nozzle. The section from the axial blower to the nozzle inlet has a diameter of 154 mm. The diameter of the nozzle outlet is $D = 51$ mm.

The first design depicted in figure B.1 was further improved for the following reason. Measurements of mean velocity profiles of the jet using Laser Doppler Velocimetry revealed an asymmetry of both the non-swirling and swirling jet. Thus, several adjustments on the swirling jet facility have been made. Figure B.1 shows the first state of the experimental setup, and figure B.2 shows the second state. The search for the cause of the asymmetry involved the rotation of the nozzle, the upstream duct, the swirl generator, and the whole swirl chamber. Comparing the asymmetric velocity profiles of each setup, all changes had an influence to a greater or lesser extent but none was solely responsible for the asymmetry. In order to make the azimuthal flow into the swirl generator symmetrical, a divider, four flexible tubes, additional wooden plates in the swirl chamber, and a curved perforated plate surrounding the swirl generator have been added to the setup. Moreover, the four guiding

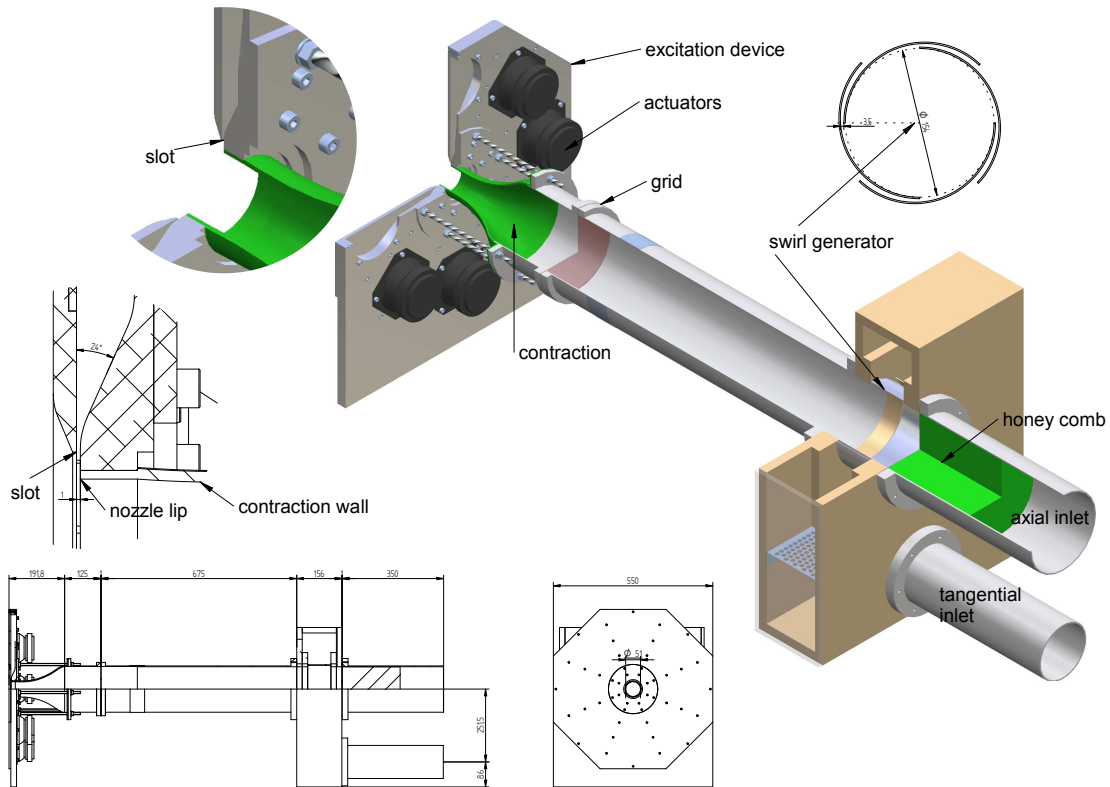


Figure B.1: Sketch of the swirling jet facility (first state)

plates of the swirl generator were glued in place more accurately. The rebuild of the swirl chamber significantly improved the symmetry of the jet. Another perforated plate was added right downstream of the swirl generator. At last, a somewhat wavy grid upstream of the nozzle was removed, which also made an improvement.

B.2 The Actuation Device

The facility allows for zero mass flow excitation at the nozzle lip. Commercial hi-fi speakers are used as actuators that are mounted to a metal plate that houses the wave guides that terminate at slots that are 1 mm thick. The following pages show photographs and technical drawings of the excitation device. It was made from aluminum plates using a CNC-controlled milling machine.

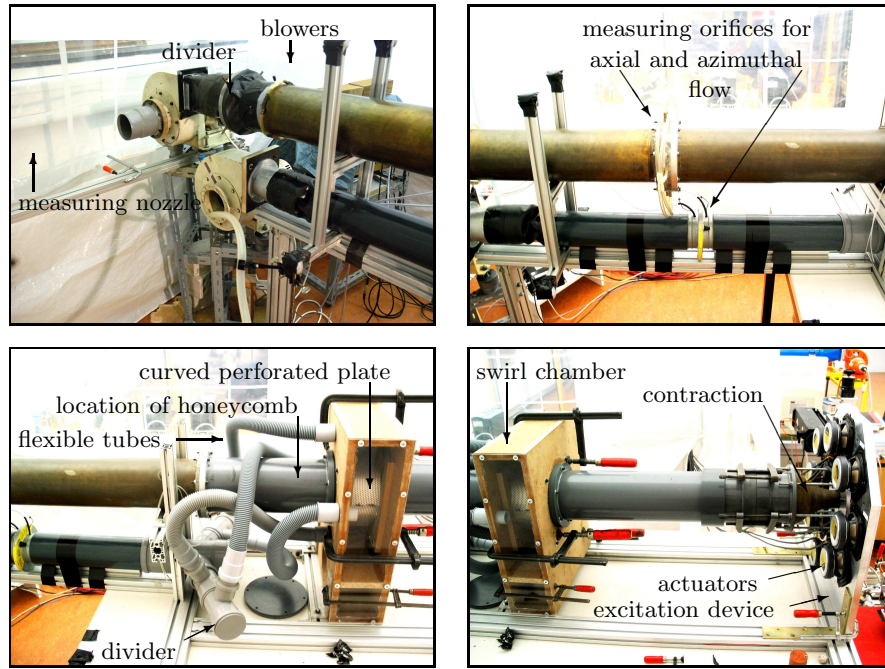


Figure B.2: Photographs of the swirling jet facility (second state)

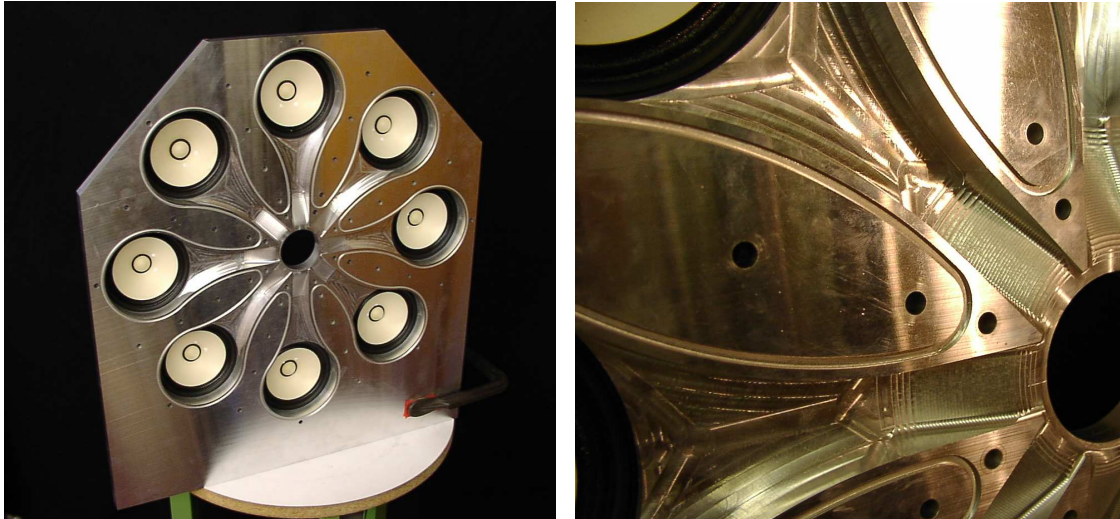


Figure B.3: Photographs of the actuation device with unmounted front plate giving optical excess to the speakers and the wave guides.

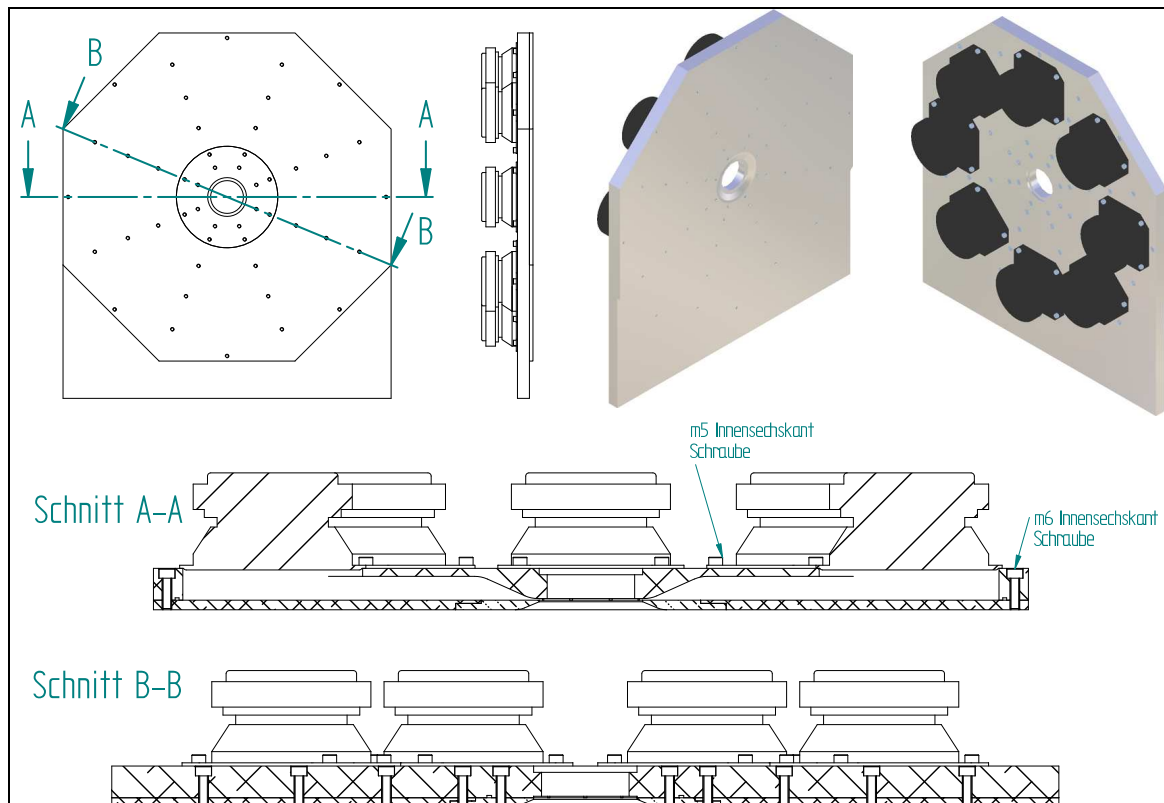


Figure B.4: Technical drawing of the complete excitation device

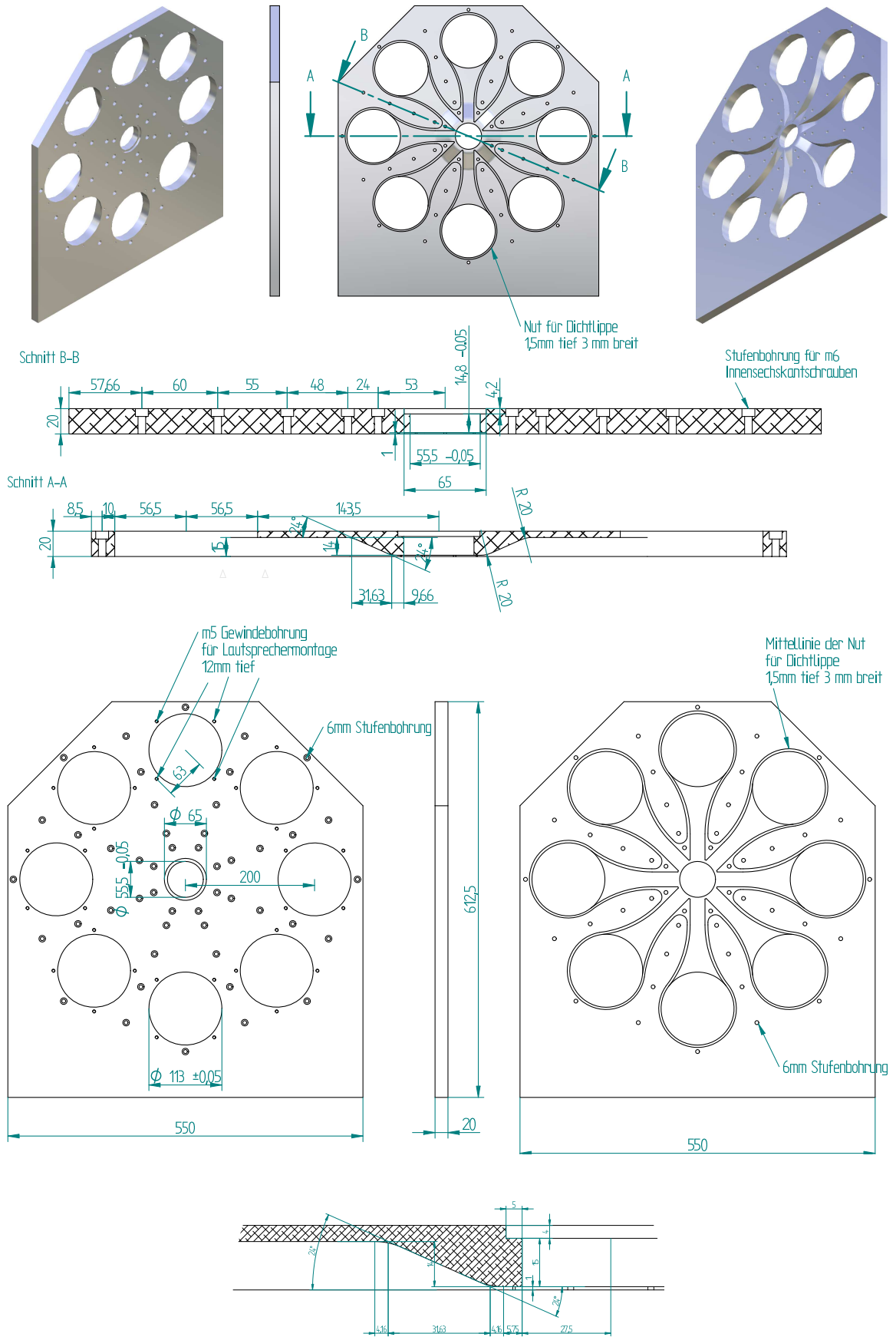


Figure B.5: Technical drawing of the nozzle plate with details on the wave guide geometries.

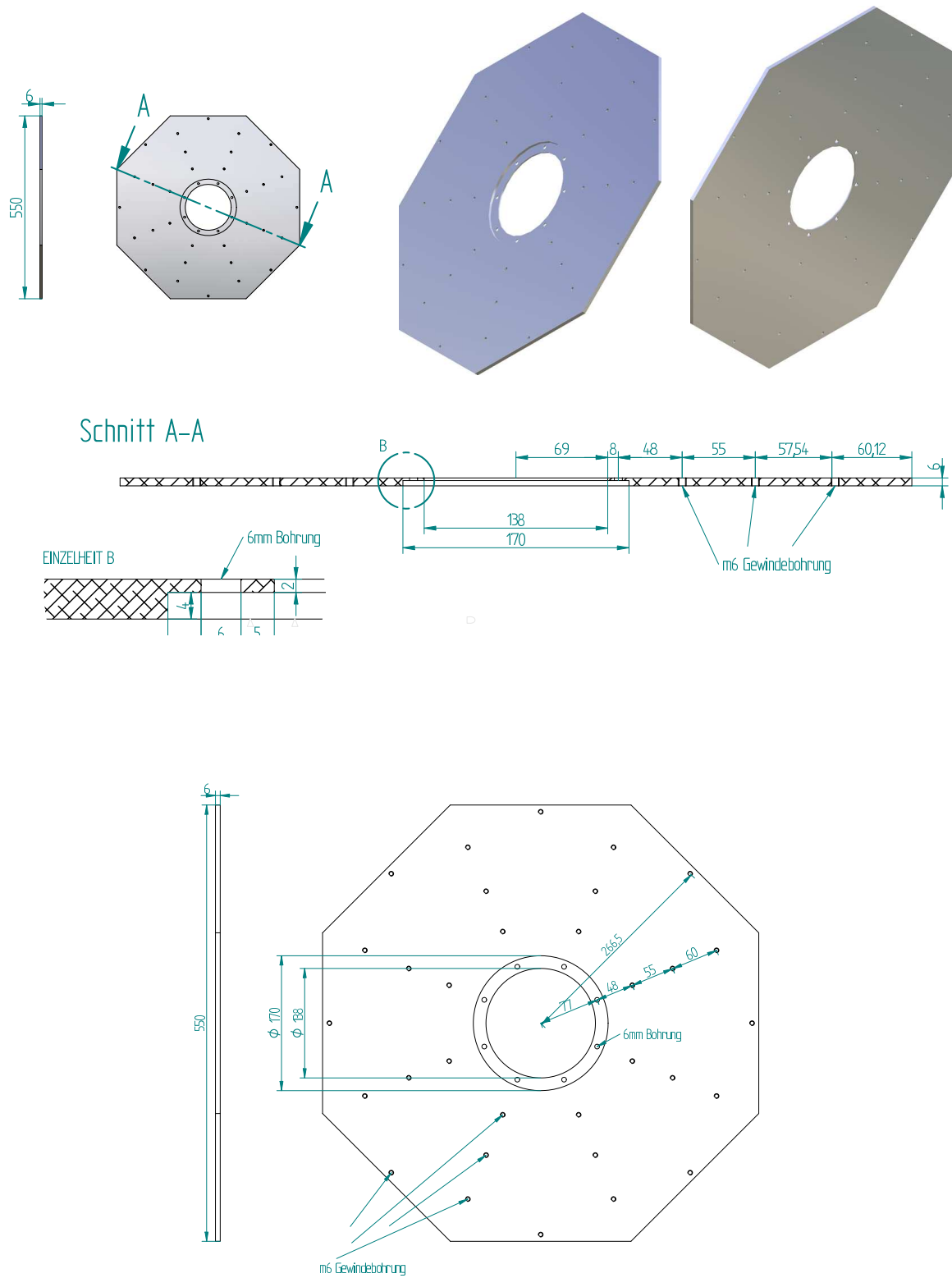


Figure B.6: Technical drawing of the nozzle front plate with details.

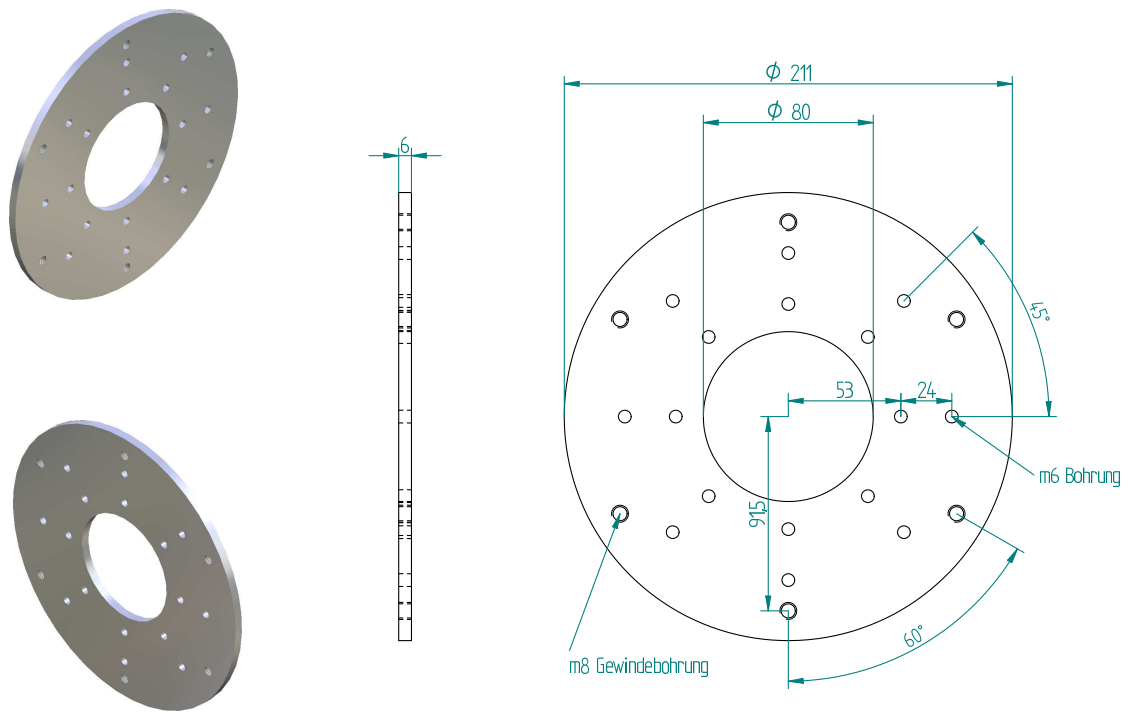


Figure B.7: Technical drawing of the nozzle adapter.

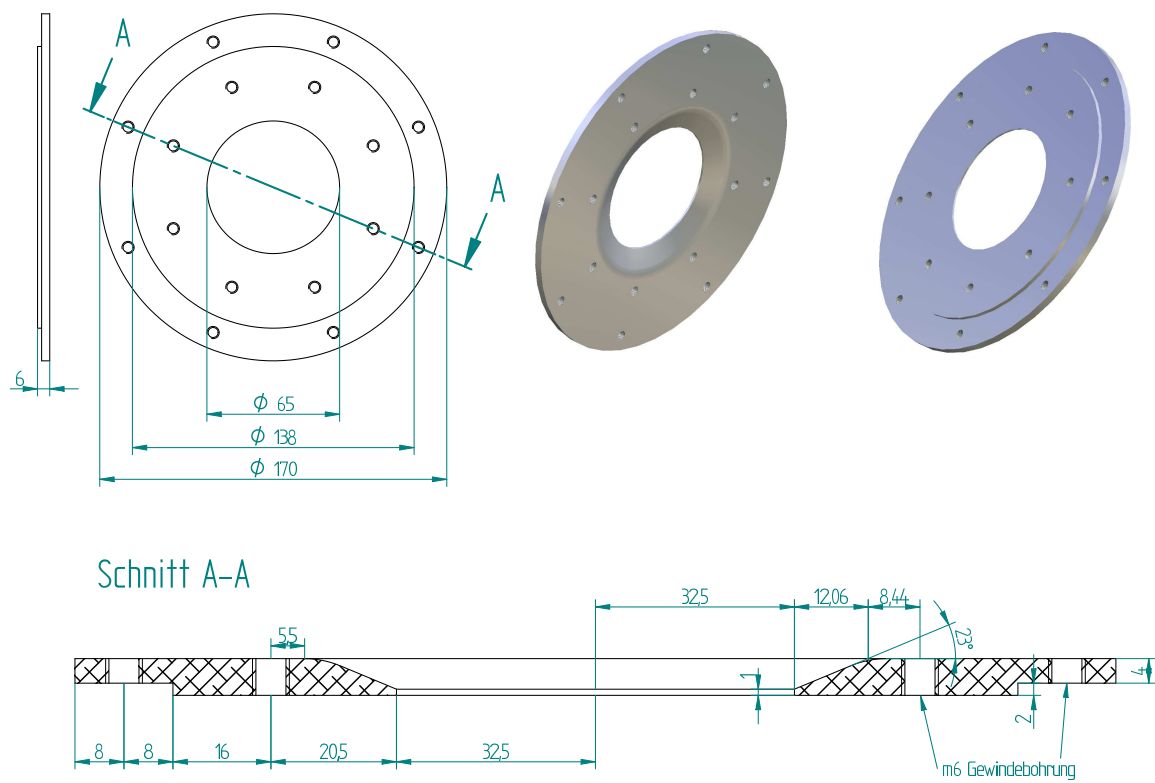
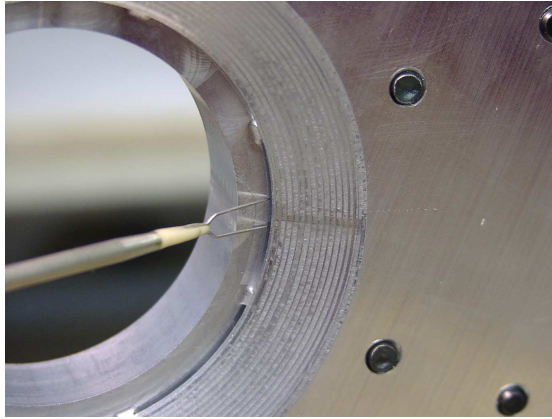


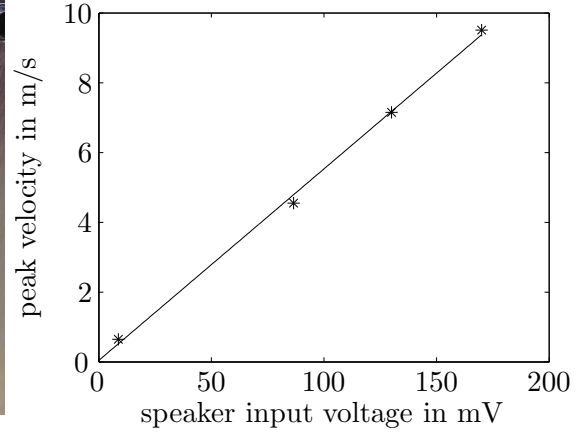
Figure B.8: Technical drawing of the nozzle ring.

input voltage in mV	peak slot velocity in m/s	peak slot mass flow in %
25	1.42	0.23
50	2.79	0.46
75	4.16	0.68
100	5.53	0.9
125	6.9	1.13

Table B.1: Speaker input voltage used for the forced experiments and corresponding peak velocity and slot mass flow relative to the mass flow of the main jet.



(a) Hot-wire measurements



(b) Speaker input voltage versus peak slot velocity for 50 Hz actuation frequency. Symbols refer to hot-wire measurements and black line refers to a linear fit.

Figure B.9: Speaker calibration at no-flow condition

B.3 Actuator Calibration

The peak velocity of the zero mass-flow jet generated by a single actuator was measured at no-flow conditions using a hot-wire probe that was placed at the slot exit (see figure B.9a). This was done for several excitation amplitudes. The frequency that was used for this study was 50 Hz. Figure B.9b shows the linear relation between the speaker input voltage and the peak velocity at the slot exit. Table B.1 lists the values corresponding to the actuation amplitude used in this thesis. The peak slot mass flow is calculated using the area of one slot. Moreover, all eight speakers were adjusted to the same sound pressure level by using a microphone placed at the nozzle exit at $r = 0$.

Appendix C

Visualization of the Global Mode

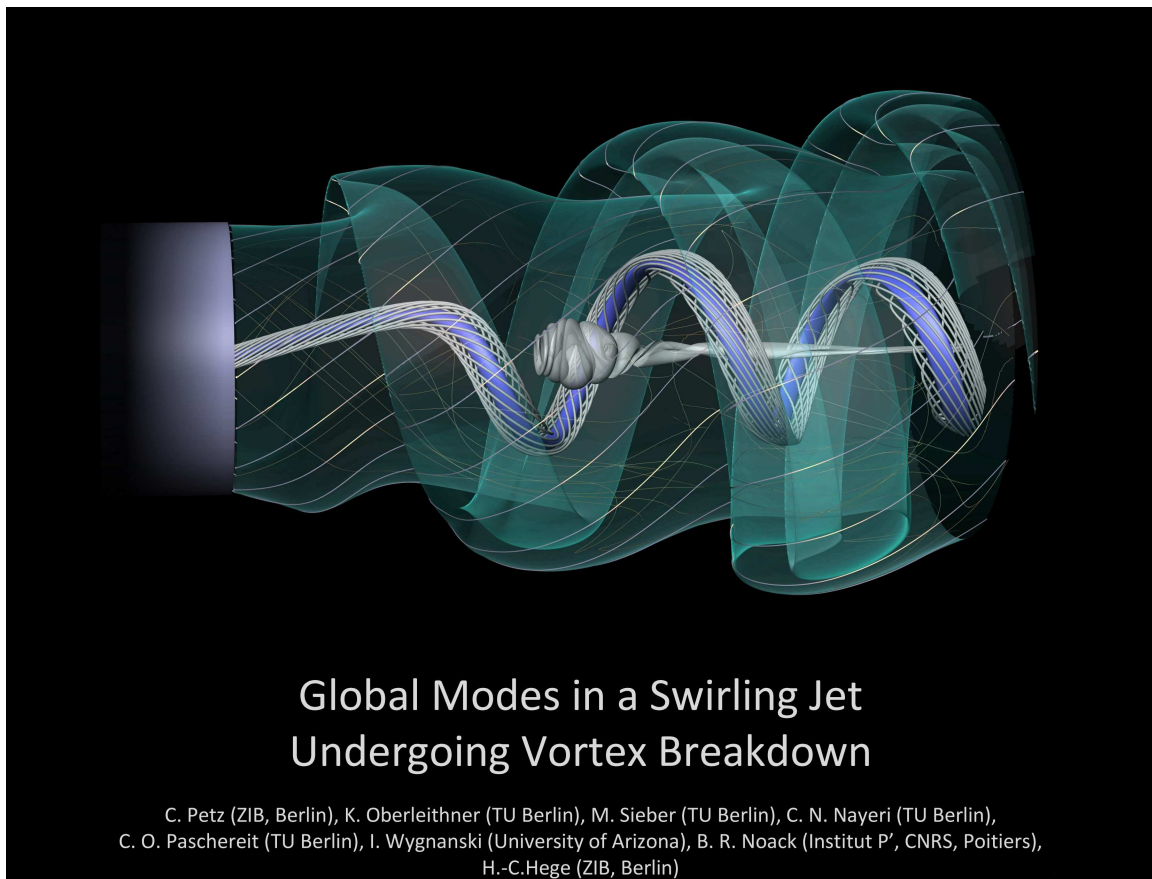


Figure C.1: Visualizations are based on the three-dimensional phase-averaged velocity field ($Re = 20000$) that is constructed from uncorrelated 2D PIV snapshots. Thereby the focus is placed on three flow features: the internal recirculation zone that is characteristic for vortex breakdown (semi-transparent gray pathline-surface in the center); the meandering vortex core that acts as the pacemaker for the global oscillations (central streak-lines and bluish streak-surface); helical waves in the outer shear layer that amplify near the nozzle and roll up to spiral vortices (semi-transparent greenish streak-surface). The visualization was prepared by Christoph Petz using the AIMIRA software environment developed at the Zuse Institute, Berlin. The picture won the gallery of fluid motion award 2011 and is published in *Physics of Fluids* (Petz et al. 2011)

Bibliography

- AKILLI, H., SAHIN, B., & ROCKWELL, D. (2003). “Control of vortex breakdown by a coaxial wire.” *Physics of Fluids*, **15**:123–133.
- BARKLEY, D. (2006). “Linear analysis of the cylinder wake mean flow.” *EPL (Europhysics Letters)*, **75**:750–756.
- BATCHELOR, G. K. (1967). *An Introduction to Fluid Dynamics*. Cambridge University Press.
- BENJAMIN, T. B. (1962). “Theory of the vortex breakdown phenomenon.” *Journal of Fluid Mechanics*, **14**:593–629.
- BERKOOZ, G., HOLMES, P., & LUMLEY, J. L. (1993). “The proper orthogonal decomposition in the analysis of turbulent flows.” *Annual Review of Fluid Mechanics*, **25**:539–575.
- BILLANT, P., CHOMAZ, J.-M., & HUERRE, P. (1998). “Experimental study of vortex breakdown in swirling jets.” *Journal of Fluid Mechanics*, **376**:183–219.
- BRIGGS, R., J. (1964). *Electron-Stream Interaction with Plasmas*. MIT Press, Cambridge, Massachusetts.
- BROWN, G. L. & LOPEZ, J. M. (1990). “Axisymmetric vortex breakdown. II - Physical mechanisms.” *Journal of Fluid Mechanics*, **221**:553–576.
- BRUECKER, C. & ALTHAUS, W. (1995). “Study of vortex breakdown by particle tracking velocimetry (PTV) Part 3: Time-dependent structure and development of breakdown-modes.” *Experiments in Fluids*, **18**:174–186.
- CABRAL, B. & LEEDOM, L. C. (1993). “Imaging vector fields using line integral convolution.” In: *Proceedings of the 20th Annual Conference on Computer Graphics and Interactive Techniques, SIGGRAPH 1993*, pp. 263–270. ACM, New York, NY, USA.
- CANDEL, S. (2002). “Combustion dynamics and control: Progress and challenges.” *Proceedings of the Combustion Institute*, **29**(1):1–28.
- CANTWELL, B. J. (1981). “Organized motion in turbulent flow.” *Annual Review of Fluid Mechanics*, **13**:457–515.
- CARTON, X. & MCWILLIAMS, J. (1989). “Barotropic and baroclinic instabilities of axisymmetric vortices in a quasi-geostrophic model.” In: J. Nihoul & B. Jamart (eds.), *Mesoscale/Synoptic Coherent Structures in Geophysical Turbulence*, p. 225; $\frac{1}{2}$ 244. Elsevier.

- CHIGIER, N. & CHERVINSKY, A. (1965). "Experimental and theoretical study of turbulent swirling jets issuing from a round orifice." *Israel Journal of Technology*, **4**:44–54.
- CHIGIER, N. & CHERVINSKY, A. (1967). "Experimental investigation of swirling vortex motion in jets." *Journal of Applied Mechanics*, **34**:443–451.
- CHIGIER, N. A. & BEER, J. M. (1964). "Velocity and static-pressure distribution in swirling air jets issuing from annular and divergent nozzles." *ASME Journal of Basic Engineering*, **86**:788–796.
- CHOMAZ, J. M. (1992). "Absolute and convective instabilities in nonlinear systems." *Physical Review Letters*, **69**(13):1931–1934.
- CHOMAZ, J.-M. (2005). "Global Instabilities in Spatially Developing Flows: Non-Normality and Nonlinearity." *Annual Review of Fluid Mechanics*, **37**:357–392.
- CHOMAZ, J. M., HUERRE, P., & REDEKOPP, L. G. (1988). "Bifurcations to local and global modes in spatially developing flows." *Physical Review Letters*, **60**:25–28.
- CHOMAZ, J.-M., HUERRE, P., & REDEKOPP, L. G. (1991). "A frequency selection criterion in spatially developing flows." *Studies in Applied Mathematics*, **85**:119.
- COHEN, J. & WYGNANSKI, I. (1987). "The evolution of instabilities in the axisymmetric jet. part 1. the linear growth of disturbances near the nozzle." *Journal of Fluid Mechanics*, **176**:191–219.
- COHEN, J. & WYGNANSKI, I. (1987). "The evolution of instabilities in the axisymmetric jet. Part 2. The flow resulting from the interaction between two waves." *Journal of Fluid Mechanics*, **176**:221–235.
- COHEN, J., MARASLI, B., & LEVINSKI, V. (1994). "Interaction between the mean flow and coherent structures in turbulent mixing layers." *Journal of Fluid Mechanics*, **260**:81–94.
- COOPER, A. J. & PEAKE, N. (2002). "The stability of a slowly diverging swirling jet." *Journal of Fluid Mechanics*, **473**:389–411.
- CRIGHTON, D. G. & GASTER, M. (1976). "Stability of slowly diverging jet flow." *Journal of Fluid Mechanics*, **77**:397–413.
- CUTLER, A. D., KRAUS, D. K., & LEVEY, B. S. (1995). "Near-field flow of supersonic swirling jets." *AIAA Journal*, **33**:876–881.
- DELBENDE, I., CHOMAZ, J.-M., & HUERRE, P. (1998). "Absolute/convective instabilities in the Batchelor vortex: a numerical study of the linear impulse response." *Journal of Fluid Mechanics*, **355**:229–254.
- DEPARDON, S., LASSERRE, J. J., BRIZZI, L. E., & BORÉE, J. (2007). "Automated topology classification method for instantaneous velocity fields." *Experiments in Fluids*, **42**:697–710.
- DUWIG, C. & FUCHS, L. (2007). "Large eddy simulation of vortex breakdown/flame interaction." *Physics of Fluids*, **19**:5103.

- ESCUDIER, M. P. & KELLER, J. J. (1985). "Recirculation in swirling flow - A manifestation of vortex breakdown." *AIAA Journal*, **23**:111–116.
- FALER, J. H. & LEIBOVICH, S. (1978). "An experimental map of the internal structure of a vortex breakdown." *Journal of Fluid Mechanics*, **86**:313–335.
- FREYMUTH, P. (1966). "On transition in a separated laminar boundary layer." *Journal of Fluid Mechanics*, **25**:683–704.
- GALLAIRE, F. & CHOMAZ, J.-M. (2003). "Mode selection in swirling jet experiments: a linear stability analysis." *Journal of Fluid Mechanics*, **494**:223–253.
- GALLAIRE, F., CHOMAZ, J.-M., & HUERRE, P. (2004). "Closed-loop control of vortex breakdown: a model study." *Journal of Fluid Mechanics*, **511**:67–93.
- GALLAIRE, F., ROTT, S., & CHOMAZ, J.-M. (2004). "Experimental study of a free and forced swirling jet." *Physics of Fluids*, **16**:2907–2917.
- GALLAIRE, F., RUIH, M., MEIBURG, E., CHOMAZ, J.-M., & HUERRE, P. (2006). "Spiral vortex breakdown as a global mode." *Journal of Fluid Mechanics*, **549**:71–80.
- GASTER, M. (1974). "On the effects of boundary-layer growth on flow stability." *Journal of Fluid Mechanics*, **66**:465–480.
- GASTER, M. & GRANT, I. (1975). "An experimental investigation of the formation and development of a wave packet in a laminar boundary layer." *Royal Society of London Proceedings Series A*, **347**:253–269.
- GASTER, M., KIT, E., & WYGNANSKI, I. (1985). "Large-scale structures in a forced turbulent mixing layer." *Journal of Fluid Mechanics*, **150**:23–39.
- GREENBLATT, D. & WYGNANSKI, I. J. (2000). "The control of flow separation by periodic excitation." *Progress in Aerospace Sciences*, **36**(7):487 – 545.
- GURSUL, I. & YANG, H. (1995). "On fluctuations of vortex breakdown location." *Physics of Fluids*, **7**:229–231.
- GUTMARK, E. J., SCHADOW, K. C., & YU, K. H. (1995). "Mixing enhancement in supersonic free shear flows." *Annual Review of Fluid Mechanics*, **27**:375–417.
- HALL, M. G. (1972). "Vortex Breakdown." *Annual Review of Fluid Mechanics*, **4**:195–218.
- HO, C.-M. & GUTMARK, E. (1987). "Vortex induction and mass entrainment in a small-aspect-ratio elliptic jet." *Journal of Fluid Mechanics*, **179**:383–405.
- HO, C.-M. & HUERRE, P. (1984). "Perturbed free shear layers." *Annual Review of Fluid Mechanics*, **16**:365–424.
- HOLMES, P., LUMLEY, J. L., & BERKOOZ, G. (1998). *Turbulence, Coherent Structures, Dynamical Systems and Symmetry*. Cambridge University Press.
- HU, G.-H., SUN, D.-J., & YIN, X.-Y. (2001a). "A numerical study of dynamics of a temporally evolving swirling jet." *Physics of Fluids*, **13**:951–965.

- HU, G.-H., SUN, D.-J., YIN, X.-Y., & B., T. (2001*b*). “Studies on stability and dynamics of a swirling jet.” *Acta Mechanica Sinica*, **17**:237–244. 10.1007/BF02486879.
- HUANG, Y. & YANG, V. (2009). “Dynamics and stability of lean-premixed swirl-stabilized combustion.” *Progress in Energy and Combustion Science*, **35**(4):293 – 364.
- HUERRE, P. & MONKEWITZ, P. A. (1990). “Local and global instabilities in spatially developing flows.” *Annual Review of Fluid Mechanics*, **22**:473–537.
- HUSSAIN, A. K. M. F. & REYNOLDS, W. C. (1970). “The mechanics of an organized wave in turbulent shear flow.” *Journal of Fluid Mechanics*, **41**:241–258.
- JUNIPER, M. P., LI, L. K., & NICHOLS, J. W. (2009). “Forcing of self-excited round jet diffusion flames.” *Proceedings of the Combustion Institute*, **32**(1):1191 – 1198.
- JUNIPER, M. P., TAMMISOLA, O., & LUNDELL, F. (2011). “The local and global stability of confined planar wakes at intermediate Reynolds number.” *Journal of Fluid Mechanics*, **686**:218–238.
- KHORRAMI, M. R. (1991). “On the viscous modes of instability of a trailing line vortex.” *Journal of Fluid Mechanics*, **225**:197–212.
- KHORRAMI, M. R., MALIK, M. R., & ASH, R. L. (1989). “Application of spectral collocation techniques to the stability of swirling flows.” *Journal of Computational Physics*, **81**(1):206–229.
- KNOWLES, K. & SADDINGTON, A. J. (2006). “A review of jet mixing enhancement for aircraft propulsion applications.” *Proceedings of the Institution of Mechanical Engineers Part G Journal of Aerospace Engineering*, **220**(2):103–127.
- KUHN, P. (2010). *Untersuchung der räumlichen und zeitlichen Anfachung von akustisch angeregten Instabilitätsmoden in Drallstrahlen*. Bachelorarbeit, TU-Berlin. Bachelorarbeit 897.
- LAMBOURNE, N. & BRYER, D. (1962). “The bursting of leading-edge vortices: some observations and discussion of the phenomenon.” Tech. rep., Ministry of Aviation.
- LANDAU, L. & LIFSHITZ, E. (1987). *Fluid Mechanics, Vol. 6*.
- LAUFER, J. (1975). “New trends in experimental turbulence research.” *Annual Review of Fluid Mechanics*, **7**:307–326.
- LEIBOVICH, S. (1978). “The structure of vortex breakdown.” *Annual Review of Fluid Mechanics*, **10**:221–246.
- LEIBOVICH, S. (1984). “Vortex stability and breakdown - Survey and extension.” *AIAA Journal*, **22**:1192–1206.
- LEIBOVICH, S. & STEWARTSON, K. (1983). “A sufficient condition for the instability of columnar vortices.” *Journal of Fluid Mechanics*, **126**:335–356.
- LESSEN, M., SINGH, P. J., & PAILLET, F. (1974). “The stability of a trailing line vortex. Part 1. Inviscid theory.” *Journal of Fluid Mechanics*, **63**:753–763.

- LIANG, H. & MAXWORTHY, T. (2004). “Vortex Breakdown and Mode Selection of a Swirling Jet in Stationary or Rotating Surroundings.” *APS Meeting Abstracts*, pp. 6–+.
- LIANG, H. & MAXWORTHY, T. (2005). “An experimental investigation of swirling jets.” *Journal of Fluid Mechanics*, **525**:115–159.
- LIEUWEN, T. C. & YANG, V. (eds.) (2005). *Combustion Instabilities in Gas Turbine Engines*, vol. 210 of *Progress in Astronautics and Aeronautics*. AIAA, Inc.
- LIU, J. T. C. (1971). “Nonlinear Development of an Instability Wave in a Turbulent Wake.” *Physics of Fluids*, **14**:2251–2257.
- LIU, J. T. C. (1989). “Coherent structures in transitional and turbulent free shear flows.” *Annual Review of Fluid Mechanics*, **21**:285–315.
- LOISELEUX, T. & CHOMAZ, J.-M. (2003). “Breaking of rotational symmetry in a swirling jet experiment.” *Physics of Fluids*, **15**:511–523.
- LOISELEUX, T., CHOMAZ, J. M., & HUERRE, P. (1998). “The effect of swirl on jets and wakes: Linear instability of the Rankine vortex with axial flow.” *Physics of Fluids*, **10**:1120–1134.
- LOISELEUX, T., DELBENDE, I., & HUERRE, P. (2000). “Absolute and convective instabilities of a swirling jet/wake shear layer.” *Physics of Fluids*, **12**:375–380.
- LONG, T. A. & PETERSEN, R. A. (1992). “Controlled interactions in a forced axisymmetric jet. Part 1. The distortion of the mean flow.” *Journal of Fluid Mechanics*, **235**:37–55.
- LU, G. & LELE, S. K. (1999). “Inviscid instability of compressible swirling mixing layers.” *Physics of Fluids*, **11**:450–461.
- LUCCA-NEGRO, O. & O’DOHERTY, T. (2001). “Vortex breakdown: a review.” *Progress in Energy and Combustion Science*, **27**(4):431 – 481.
- LUCHTENBURG, D. M., GÜNTHER, B., NOACK, B. R., KING, R., & TADMOR, G. (2009). “A generalized mean-field model of the natural and high-frequency actuated flow around a high-lift configuration.” *Journal of Fluid Mechanics*, **623**:283–+.
- LÜCK, M. (2009). *Control of Absolute Instability in Highly Swirled Jets using Azimuthal Forcing*. Diplomarbeit, TU-Berlin. Diplomarbeit 849.
- LUDWIEG, H. (1961). “Ergänzung zu der arbeit: Stabilität der strömung in einem zylindrischen ringraum.” *Z. Flugwiss*, **9**:359.
- LUMLEY, J. L. (1967). *Atmospheric Turbulence and Radio Wave Propagation*. Elsevier Publishing Co., Nauka, Moscow.
- MAGER, A. (1972). “Dissipation and breakdown of a wing-tip vortex.” *Journal of Fluid Mechanics*, **55**:609–628.
- MALIK, M. R., ZANG, T. A., & HUSSAINI, M. Y. (1985). “A spectral collocation method for the Navier-Stokes equations.” *Journal of Computational Physics*, **61**:64–88.

- MARASLI, B., CHAMPAGNE, F. H., & WYGNANSKI, I. J. (1991). “On linear evolution of unstable disturbances in a plane turbulent wake.” *Physics of Fluids*, **3**:665–674.
- MARTIN, J. E. & MEIBURG, E. (1994). “On the stability of the swirling jet shear layer.” *Physics of Fluids*, **6**:424–426.
- MARTIN, J. E. & MEIBURG, E. (1996). “Nonlinear axisymmetric and three-dimensional vorticity dynamics in a swirling jet model.” *Physics of Fluids*, **8**(7):1917–1928.
- MARTIN, J. E. & MEIBURG, E. (1998). “The growth and nonlinear evolution of helical perturbations in a swirling jet model.” *European Journal of Mechanics B Fluids*, **17**:639–651.
- MARTINELLI, F., OLIVANI, A., & COGHE, A. (2007). “Experimental analysis of the precessing vortex core in a free swirling jet.” *Experiments in Fluids*, **42**:841–841.
- MCMANUS K., R., POINSOT, T., & CANDEL S., M. (1993). “A review of active control of combustion instabilities.” *Progress in Energy and Combustion Science*, **19**:1–29.
- MEHTA, R. D., WOOD, D. H., & CLAUSEN, P. D. (1991). “Some effects of swirl on turbulent mixing layer development.” *Physics of Fluids*, **3**:2716–2724.
- MICHALKE, A. (1965). “On spatially growing disturbances in an inviscid shear layer.” *Journal of Fluid Mechanics*, **23**:521–544.
- MICHALKE, A. (1999). “Absolute inviscid instability of a ring jet with back-flow and swirl.” *European Journal of Mechanics*, **18**:3–12.
- MONKEWITZ, P. A. (1988). “The absolute and convective nature of instability in two-dimensional wakes at low Reynolds numbers.” *Physics of Fluids*, **31**:999–1006.
- MONKEWITZ, P. A. & SOHN, K. D. (1988). “Absolute instability in hot jets.” *AIAA Journal*, **26**:911–916.
- MONKEWITZ, P. A., BECHERT, D. W., BARSIKOW, B., & LEHMANN, B. (1990). “Self-excited oscillations and mixing in a heated round jet.” *Journal of Fluid Mechanics*, **213**:611–639.
- MONKEWITZ, P. A., HUERRE, P., & CHOMAZ, J.-M. (1993). “Global linear stability analysis of weakly non-parallel shear flows.” *Journal of Fluid Mechanics*, **251**:1–20.
- MÜLLER, S. B. & KLEISER, L. (2008). “Viscous and inviscid spatial stability analysis of compressible swirling mixing layers.” *Physics of Fluids*, **20**(11):114103–+.
- NAUGHTON, J. W., CATTAFESTA, III, L. N., & SETTLES, G. S. (1997). “An experimental study of compressible turbulent mixing enhancement in swirling jets.” *Journal of Fluid Mechanics*, **330**:271–305.
- NOACK, B. R., AFANASIEV, K., MORZYŃSKI, M., TADMOR, G., & THIELE, F. (2003). “A hierarchy of low-dimensional models for the transient and post-transient cylinder wake.” *Journal of Fluid Mechanics*, **497**:335–363.

- OBERLEITHNER, K. (2006). *Vortex Breakdown in a Swirling Jet with Axial Forcing*. Master's thesis, University of Arizona, Technical University Berlin.
- OBERLEITHNER, K., PASCHEREIT, C. O., & WYGNANSKI, I. (2007). "Vortex breakdown in a swirling jet with axial forcing." In: *18eme Congres Francais de Mechanique, colloquium: Stratified and rotating flows*, 5010.
- OLENDRARU, C. & SELIER, A. (2002). "Viscous effects in the absolute convective instability of the Batchelor vortex." *Journal of Fluid Mechanics*, **459**:371–396.
- ÖRLÜ, R. & ALFREDSSON, P. (2008). "An experimental study of the near-field mixing characteristics of a swirling jet." *Flow, Turbulence and Combustion*, **80**:323–350. 10.1007/s10494-007-9126-y.
- OSTER, D. & WYGNANSKI, I. (1982). "The forced mixing layer between parallel streams." *Journal of Fluid Mechanics*, **123**:91–130.
- PANDA, J. (1990). *Experiments on the instabilities in swirling and non-swirling free jets*. Ph.D. thesis, Pennsylvania State University, USA.
- PANDA, J. & MCLAUGHLIN, D. K. (1994). "Experiments on the instabilities of a swirling jet." *Physics of Fluids*, **6**:263–276.
- PARRAS, L. & FERNANDEZ-FERIA, R. (2007). "Spatial stability and the onset of absolute instability of Batchelor's vortex for high swirl numbers." *Journal of Fluid Mechanics*, **583**:27–+.
- PASCHEREIT, C. O., WYGNANSKI, I., & FIEDLER, H. E. (1995). "Experimental investigation of subharmonic resonance in an axisymmetric jet." *Journal of Fluid Mechanics*, **283**:365–407.
- PETERSEN, R. A. & SAMET, M. M. (1988). "On the preferred mode of jet instability." *Journal of Fluid Mechanics*, **194**:153–173.
- PETZ, C., HEGE, H.-C., OBERLEITHNER, K., SIEBER, M., NAYERI, C. N., PASCHEREIT, C. O., WYGNANSKI, I., & NOACK, B. R. (2011). "Global modes in a swirling jet undergoing vortex breakdown." *Physics of Fluids*, **23**(9):091102.
- PIER, B. (2003). "Open-loop control of absolutely unstable domains." *Proceedings of the Royal Society of London. Series A: Mathematical, Physical and Engineering Sciences*, **459**(2033):1105–1115.
- PIER, B. (2009). "Signalling problem in absolutely unstable systems." *Theoretical and Computational Fluid Dynamics*, pp. 57–+.
- PIER, B. & HUERRE, P. (2001). "Nonlinear self-sustained structures and fronts in spatially developing wake flows." *Journal of Fluid Mechanics*, **435**:145–174.
- PLASCHKO, P. (1979). "Helical instabilities of slowly divergent jets." *Journal of Fluid Mechanics*, **92**:209–215.

- PRATTE, B. D. & KEFFER, J. F. (1972). “The swirling turbulent jet.” *ASME Journal of Basic Engineering*, **93**:739.
- PROVANSAL, M., MATHIS, C., & BOYER, L. (1987). “Benard-von Karman instability: transient and forced regimes.” *Journal of Fluid Mechanics*, **182**:1–22.
- RAJARATNAM, N. (1976). *Turbulent jets (Vol. 5 of Developments in water science)*. Elsevier Scientific Publishing Co.
- REAU, N. & TUMIN, A. (2002). “Harmonic Perturbations in Turbulent Wakes.” *AIAA Journal*, **40**:526–530.
- REES, S. R. (2009). *Hydrodynamic instability of confined jets & wakes and implications for gas turbine fuel injectors*. Ph.D. thesis, University of Cambridge.
- RICHARD, E. (2003). “Swirling jet project.” Tech. rep., University of Arizona.
- ROSHKO, A. (1977). “Errata: Structure of Turbulent Shear Flows: A New Look.” *AIAA Journal*, **15**:768–768.
- ROWLEY, C. (2005). “Model reduction for fluids using balanced proper orthogonal decomposition.” *International Journal of Bifurcation and Chaos*, **15**(3):997–1013.
- ROWLEY, C. W., MEZIĆ, I., BAGHERI, S., SCHLATTER, P., & HENNINGSON, D. S. (2009). “Spectral analysis of nonlinear flows.” *Journal of Fluid Mechanics*, **641**:115–+.
- RUITH, M. R., CHEN, P., MEIBURG, E., & MAXWORTHY, T. (2003). “Three-dimensional vortex breakdown in swirling jets and wakes: direct numerical simulation.” *Journal of Fluid Mechanics*, **486**:331–378.
- RUKES, L. (2010). *Convective/absolute instability transition in swirling jets: linear theory and its application to experimental data*. Diplomarbeit, TU-Berlin. Diplomarbeit 905.
- SARPKAYA, T. (1971). “On stationary and travelling vortex breakdowns.” *Journal of Fluid Mechanics*, **45**:545–559.
- SCHMID, P. J. (2010). “Dynamic mode decomposition of numerical and experimental data.” *Journal of Fluid Mechanics*, **656**:5–28.
- SEELE, R. (2008). *ON THE MEAN PROPERTIES OF THE SWIRLED FLOW*. Master’s thesis, University of Arizona.
- SEMAAN, R., NAUGHTON, J. W., & EWING, D. (2009). “Approach toward similar behavior of a swirling jet flow.” In: *47th AIAA Aerospace Sciences Meeting*.
- SHIRI, A., GEORGE, W. K., & NAUGHTON, J. W. (2008). “Experimental Study of the Far Field of Incompressible Swirling Jets.” *AIAA Journal*, **46**:2002–2009.
- SIEBER, M. (2012). *Closed-loop control of turbulent swirling jets undergoing vortex breakdown: Heuristic design and empirical validation of a reduced order model*. Diplomarbeit, TU-Berlin.

- SIEBER, M., OBERLEITHNER, K., NAYERI, C. N., & PASCHEREIT, C. O. (2011). "Model design and calibration for closed-loop control of swirling jet instabilities." In: *Colloquium FLUID DYNAMICS*. Institute of Thermomechanics AS CR, v.v.i., Prague,.
- SIPP, D. & LEBEDEV, A. (2007). "Global stability of base and mean flows: a general approach and its applications to cylinder and open cavity flows." *Journal of Fluid Mechanics*, **593**:333–358.
- SIROVICH, L. (1987). "Turbulence and the dynamics of coherent structures. part i: Coherent structures." *Quarterly of Applied Mathematics*, **XLV**:561–571.
- SPALL, R. E., GATSKI, T. B., & GROSCH, C. E. (1987). "A criterion for vortex breakdown." *Physics of Fluids*, **30**:3434–3440.
- SREENIVASAN, K. R., RAGHU, S., & KYLE, D. (1989). "Absolute instability in variable density round jets." *Experiments in Fluids*, **7**:309–317.
- STALLING, D. & HEGE, H.-C. (1995). "Fast and resolution independent line integral convolution." In: *Proceedings of the 22nd annual conference on Computer graphics and interactive techniques, SIGGRAPH 1995*, pp. 249–256. ACM, New York, NY, USA.
- STUART, J. (1958). "On the non-linear mechanics of hydrodynamic stability." *Journal of Fluid Mechanics*, **4**:1–21.
- SUSLOV, S. A. (2006). "Numerical aspects of searching convective/absolute instability transition." *Journal of Computational Physics*, **212**:188–217.
- SYRED, N. (2006). "A review of oscillation mechanisms and the role of the precessing vortex core (pvc) in swirl combustion systems." *Progress in Energy and Combustion Science*, **32**(2):93 – 161.
- TOH, I. K., HONNERY, D., & SORIA, J. (2010). "Axial plus tangential entry swirling jet." *Experiments in Fluids*, **48**:309–325.
- TOWNSEND, A. (1956). *The Structure of Turbulent Shear Flow*. Cambridge University Press.
- VAN DYKE, M. (1975). *Perturbation Methods in Fluid Mechanics*. The Parabolic Press, Stanford, annotated edn.
- WEISBROT, I. & WYGNANSKI, I. (1988). "On coherent structures in a highly excited mixing layer." *Journal of Fluid Mechanics*, **195**:137.
- WU, C., FAROKHI, S., & TAGHAVI, R. (1992). "Spatial instability of a swirling jet - Theory and experiment." *AIAA Journal*, **30**:1545–1552.
- WU, J.-Z., MA, H.-Y., & ZHOU, M.-D. (2006). *Vorticity and vortex dynamics*. Springer.
- YANG, X. & ZEBIB, A. (1989). "Absolute and convective instability of a cylinder wake." *Physics of Fluids*, **1**:689–696.
- ZHOU, M. D., HEINE, C., & WYGNANSKI, I. (1996). "The effects of excitation on the coherent and random motion in a plane wall jet." *Journal of Fluid Mechanics*, **310**:1–37.